

Cellular Heterogeneity during Metastatic Colonization of Colorectal Cancer

Investigating phenotypic, transcriptomic, and chromatin
changes over time

Maria Christine Heinz

ISBN: 978-94-6458-622-0
Author: Maria Christine Heinz
Cover: Maria Christine Heinz
Layout: Publiss | www.publiss.nl
Printing: Ridderprint | www.ridderprint.nl

The research described in this thesis was performed in the lab of Dr. Hugo Snippert at the University Medical Center Utrecht, Utrecht, The Netherlands.

Copyright © Maria Christine Heinz. All rights reserved. No part of this thesis may be reproduced, stored or transmitted in any form by any means without prior permission of the author. The copyright of the publications remains with the publishers.

Cellular Heterogeneity during Metastatic Colonization of Colorectal Cancer

Investigating phenotypic, transcriptomic, and chromatin
changes over time

Cellulaire heterogeniteit tijdens metastatische kolonisatie van colorectale kanker

Onderzoek naar fenotypische, transcriptomische en chromatineveranderingen in de
loop van de tijd
(met een samenvatting in het Nederlands)

Proefschrift

ter verkrijging van de graad van doctor aan de
Universiteit Utrecht
op gezag van de
rector magnificus, prof.dr. H.R.B.M. Kummeling,
ingevolge het besluit van het college voor promoties
in het openbaar te verdedigen op
maandag 14 november 2022 des morgens te 10.15 uur

door

Maria Christine Heinz

geboren op 1 april 1992
te Wiesbaden, Duitsland

Promotor:

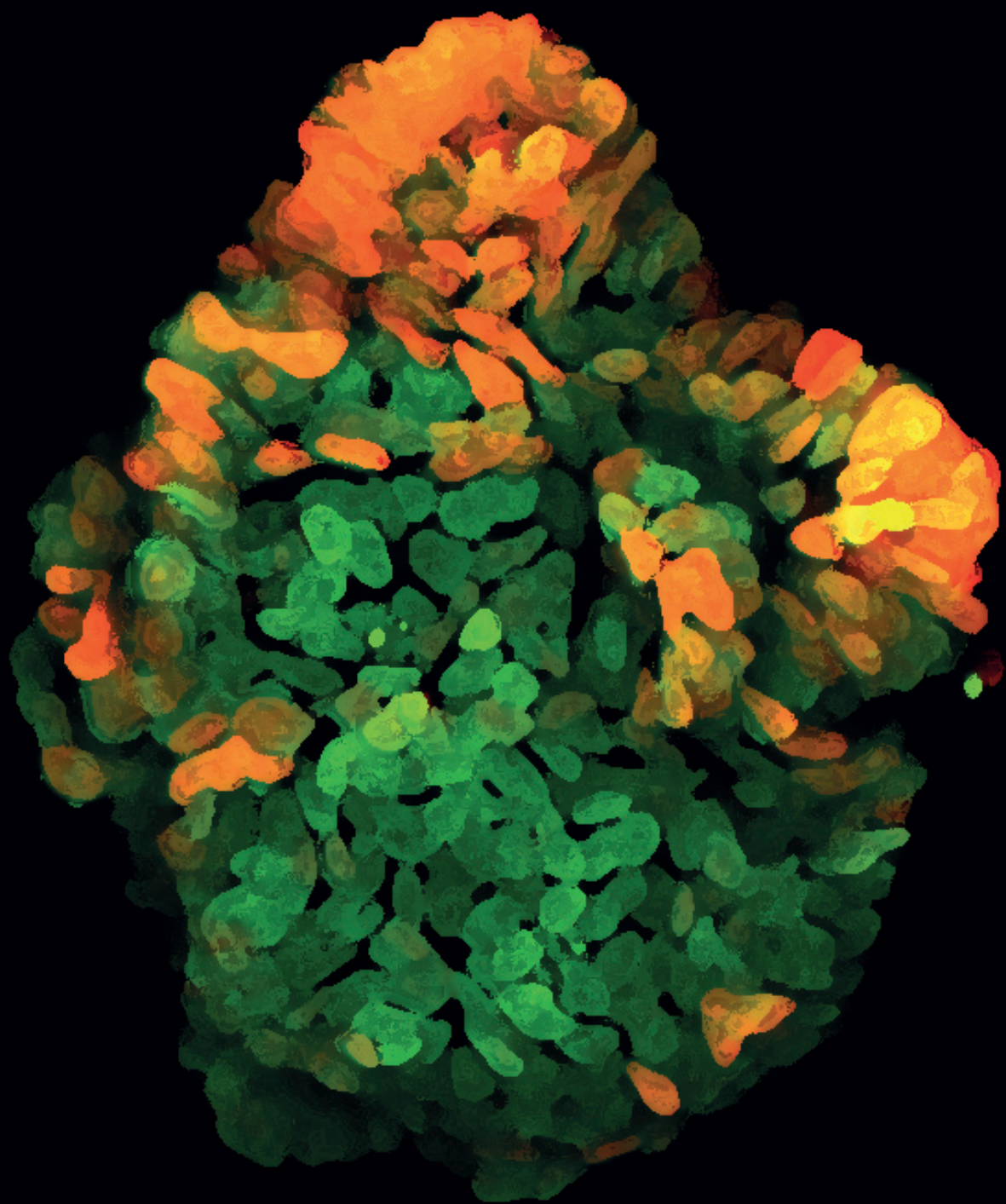
Prof. dr. B.M.T. Burgering

Copromotor:

Dr. H.J.G. Snippert

TABLE OF CONTENTS

Scope of the Thesis		8
Chapter 1	Intestinal Regeneration Regulation by the Microenvironment	16
Chapter 2	Introducing the Stem Cell ASCL2 Reporter STAR into Intestinal Organoids	46
Chapter 3	Liver Colonization by Colorectal Cancer Metastases Requires YAP-Controlled Plasticity at the Micrometastatic Stage	88
Chapter 4	Transcriptome and Chromatin Changes Orchestrating Cellular States during Colorectal Cancer Organoid and Liver Metastasis Outgrowth	144
Chapter 5	Quiescent Cells in Colorectal Cancer Liver Micro- and Macrometastases are Transcriptionally Distinct	184
Chapter 6	Dissecting the Role of Hedgehog Signalling in Advanced Colorectal Cancer	222
Chapter 7	Discussion	258
Appendix	Dutch Summary	280
	German Summary	282
	List of Publications	288
	Curriculum Vitae	289
	Acknowledgements	290



SCOPE OF THE THESIS

S

SCOPE OF THE THESIS

Metastases are the leading cause of mortality in solid cancers. They arise when individual cancer cells detach from the primary tumour site, travel through the body via the lymphatic or the blood system, come to rest at distant sites, and, surviving the hostile environment, grow into macroscopic lesions that impact on the function of the organ in question. Involving many individual steps during which disseminating cancer cells are exposed to various threats and challenges, the entire process is very inefficient. Nevertheless, when successful, it has devastating consequences for patients.

Thus, with the hope of ultimately preventing metastasis formation, there is a great interest in understanding the origin of metastasis. Genomic sequencing efforts on paired primary and metastatic tumours are being conducted with the aim to build phylogenetic trees on the genetic evolution of cancers over time, resolving the similarity of primary tumour cells to metastatic cells and addressing the genetic make-up of clones with metastatic potential (1). Complementary to a genetic background that renders cancer cells less (or even in-) dependent on growth factors provided at the primary tumour site, disseminating cancer cells need to display different behaviour compared to their healthy counterparts. To just mention a few, this includes invasive behaviour at the primary tumour site, survival and immune evasion when travelling through the body, and the capability of breaching the blood or lymph vessel barrier once lodged at a particular site (2). While genetic alterations may facilitate any of these traits, the necessary signalling cascades are linked to specific transcriptomic programmes. Consequently, interfering with the *cellular state* of cells with metastatic competence is an appealing strategy to obtain clinical success.

Various studies have been conducted to define non-genomic characteristics of the *cell-of-origin* of metastasis formation in which metastatic potential is frequently assessed by defining and isolating cancer subpopulations based on expression levels of a single cellular marker and injecting the subpopulations into mice. While these assays determine the potential to survive and grow into tumours when challenged in this way, the assumption that these subpopulations initiate the metastatic cascade in primary tumours would be an unjustified extrapolation. Instead, cells need to be equipped with (additional) different traits to end up in the circulation such as migratory and invasive behaviour. It therefore follows that disseminating cancer cells either have developed a cellular state that supports a whole plethora of traits at once, or, probably more likely, display adaptive behaviour along the way. Thus, profiling cells at different steps of the metastatic cascade most likely leads to very different results.

In this thesis, we focus on investigating the final step of the metastatic cascade, the *colonisation* of a distant organ. The fact that it is considered the rate-limiting event of the entire dissemination procedure (2) highlights yet again that not all cells leaving the primary tumour are equipped with the tools necessary to seed metastasis. As this step provides the last chance to interfere with the formation of clinically significant metastases, we set out to profile phenotypic and transcriptional heterogeneity of metastasized cells during the colonisation process in the context of colorectal cancer (CRC).

In analogy to the healthy intestinal tract where leucine-rich repeat-containing G-protein coupled receptor 5⁺ (LGR5⁺) cells serve as adult stem cells, constantly repopulating the epithelial lining of functionally-specialized differentiated cells (multipotency) and renewing the stem cell pool (self-renewal) (3), LGR5⁺ cancer cells constitute a population of cancer stem cells (CSCs) that fuels cancer growth in many CRC models (4–6). Likewise, Lgr5⁺ CSCs are critical for maintaining and driving metastatic growth (7), yet circulating tumour cells seem to be devoid of Lgr5 expression (8). It thus follows that CSCs have to arise during the last steps of the metastatic cascade by a conversion termed *dedifferentiation*. We therefore decided to incorporate readouts for intestinal stemness in our studies on the earliest steps of CRC liver colonisation. This was achieved by either fluorescently tagging the gene *LGR5* or by using the intestinal STem cell Ascl2 Reporter (STAR), a fluorescent transcriptional reporter of achaete-scute complex homolog 2 (ASCL2), the regulating transcription factor of intestinal stem cell fate and LGR5 (9,10).

To best recapitulate the phenotypic and transcriptional heterogeneity of primary CRC tumours and to dissect those of CRC metastases, we exploit the adult stem cell-derived organoid system that allows to culture and genetically modify patient-derived CRC samples, while representing different cellular states in a single culture condition (11). In combination with fluorescent reporters, microscopy, and transcriptomic readouts, CRC organoids constitute the basis for the research conducted in this thesis.

In **Chapter 1**, we provide a literature background on intestinal biology, focusing on the regeneration of the intestinal stem cell pool upon crypt damage. We summarise the knowledge on which epithelial cell types are capable of dedifferentiating and describe pathways known to be involved. Additionally, we present external cues from the microenvironment that modulate the regenerative response *in vivo*.

To be able to resolve phenotypic heterogeneity at the level of intestinal stemness over an extended timeframe, we modify the STAR reporter to be compatible with long-term time-lapse microscopy (movieSTAR). The whole variety of STAR variants and their applicability

in combination with organoids is described in **Chapter 2**, in which we present methods of introducing STAR into organoids via lentiviruses or a transposase-based approach alongside with potential applications and limitations.

A combination of analyses on patient biopsies and CRC STAR organoids is used in **Chapter 3**, to demonstrate the lack of CSCs in liver micrometastases, lesions that can be dormant on a population level for years in patients. Conversely, macrometastases display heterogeneous SC marker expression. Using intravital microscopy on recently formed metastases, we show that few rounds of proliferation take place before CSCs reappear at a multicellular stage, correlating with sustained growth. We also track lesions devoid of CSCs with limited growth that could well serve as origin of micrometastases. Through single cell outgrowth assays and time-lapse microscopy on STAR organoids, we discover that the phenotypic make-up of metastasis over time is recapitulated in organoids, while spontaneously formed micro-organoids mimic micrometastases. Having developed a size-separation protocol for these organoids, transcriptomic profiling of the different organoid and STAR phenotypes reveals the upregulation of a YAP-driven regenerative response in micro-organoids that is essential for single cell organoid outgrowth and precedes cell type heterogeneity. The verification of a YAP signature in recently formed metastasis concludes this research part.

Chapter 4 comprises a follow-up study in which STAR organoids were exploited in a time-course experiment to model transcriptional and chromatin changes during single cell outgrowth. Both on RNA- and on chromatin-level, the data highlights the vastness of changes happening over time. We report that a proliferation-heavy response involving several E2F family members follows the initial YAP state described in Chapter 3, prior to the establishment of cell type heterogeneity. Interestingly, resulting heterogeneous organoids display again signs of YAP activity, yet presumably involving different target genes, as public gene signatures for regeneration or development are not significantly enriched in this cellular state. Instead, the ATAC sequencing data suggests YAP serving as co-activator of the transcription complex AP-1. Additionally, this data set allows to investigate traits associated to cell fate changes from STAR⁻ to STAR⁺ or the other way around. We find dedifferentiation to be linked to EGF signalling targets and a pro-proliferative phenotype similar to transit amplifying-like (TA-like) cells, suggesting that an upregulation of the MAPK pathway precedes the upregulation of Wnt signalling. Finally, we demonstrate the translatability of transcriptomic findings derived from organoids to metastases by confirming that the organoid states of different time points align with the metastatic states over time, including a temporal peak in proliferation prior to cell type heterogeneity.

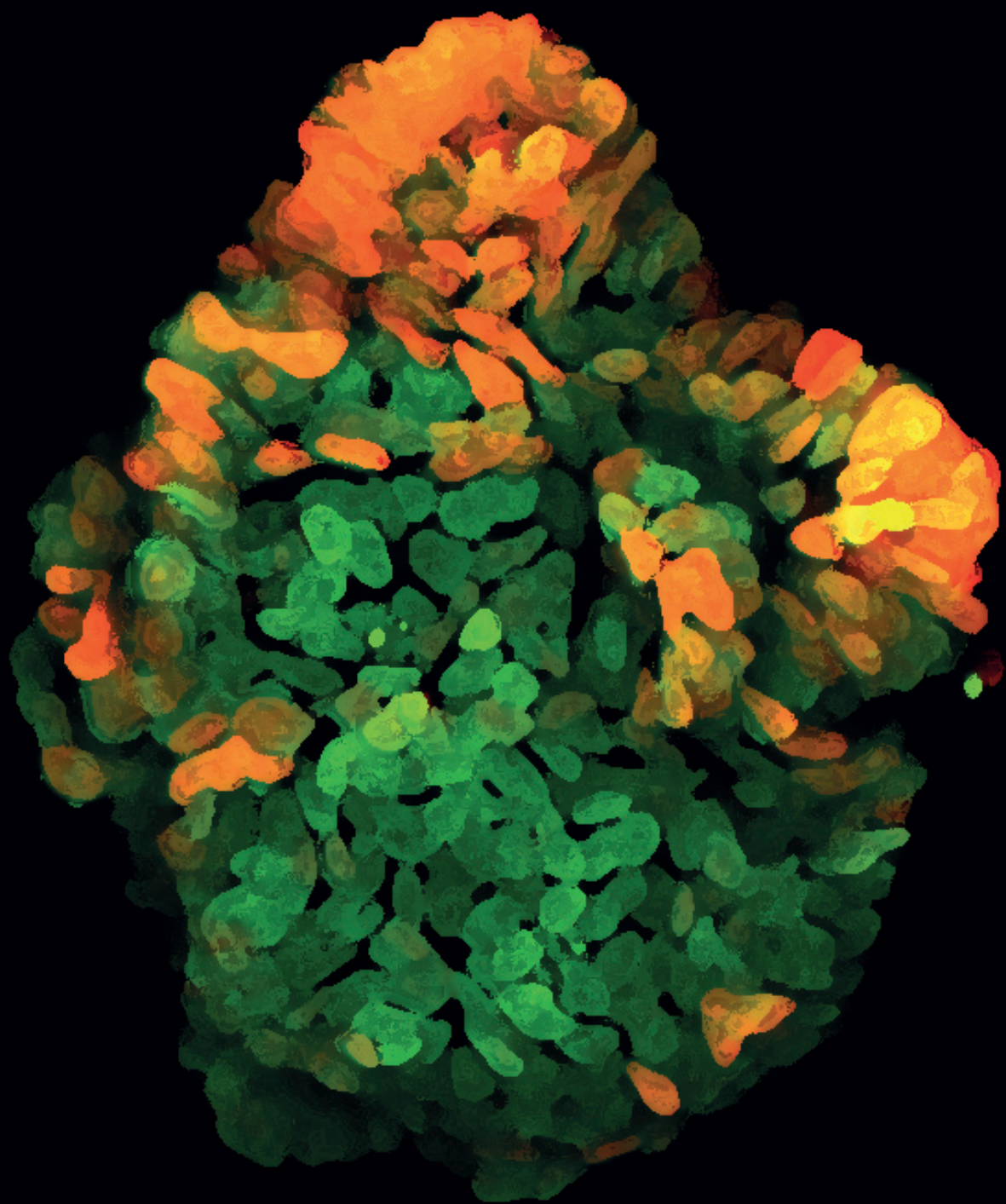
While STAR has enabled us to study cellular heterogeneity at single cell resolution, we were also interested in further defining the role of non-proliferating cancer subpopulations (a fraction of all STAR⁺ cells). To this end, we adapt a quiescence reporter based on high expression levels of P27 (*CDKN1B*) to be able to fluorescently identify cells in the cell cycle phase G₀. Presented in **Chapter 5**, we found the fraction of P27^{high} metastatic cells to vary depending on the CRC model in question, while P27^{high} cells could be detected in metastases of all sizes. Thus, to tell apart quiescent cells in possibly dormant micrometastases from a subpopulation of quiescent cells in macrometastases, additional size fractionation of metastases is required. We suggest to combine an *in vivo* collagenase-based liver perfusion protocol with the subsequent use of cell culture strainers to filter out macrometastases as still intact structures. Using this strategy, we find for our CRC models that micrometastases are either entirely quiescent (P27^{high}) or entirely proliferating (KI67⁺), while macrometastases comprise both proliferating and quiescent cells. In addition, the cellular state of quiescent cells in micro- and macrometastases varies with the latter depicting signs of extracellular matrix remodelling and fibrosis.

In analogy to differentiated Paneth cells exerting a stem cell-supporting role in intestinal homeostasis, we were intrigued by the fact that Hedgehog ligands were upregulated in STAR⁺ cells in heterogeneous organoids. As Hedgehog pathway players are additionally more strongly expressed in STAR⁺ cells, we investigated the role of Hedgehog signalling in advanced CRC in **Chapter 6**. As the mode-of-action of Hedgehog signalling has been under debate in the past decades, we assess the extent of both intra-epithelial “autocrine” and paracrine signalling towards the mesenchyme. CRC organoids as a purely epithelial culture system did not display any measureable signs of Hedgehog signalling. To assess the role of Hedgehog signalling in CRC metastasis formation *in vivo*, we generate a Hedgehog knockout clone (KO) library, in which either one, two or all three Hedgehog ligands were knocked-out through CRISPR/Cas9 technology. However, the capacity for induced liver metastasis formation was comparable between the triple KO line and the parental line, suggesting that Hedgehog signalling is not instrumental for CRC metastasis formation in our model system.

Last but not least, I summarise the findings in **Chapter 7**, highlighting the broader literature context, future prospects and possible therapeutic avenues.

REFERENCES

1. Rogiers A, Lobon I, Spain L, Turajlic S. The Genetic Evolution of Metastasis. *Cancer Res.* 2022;82:1849–57.
2. Massagué J, Obenauf AC. Metastatic colonization by circulating tumour cells. *Nature.* 2016. page 298–306.
3. Barker N, van Es JH, Kuipers J, Kujala P, van den Born M, Cozijnsen M, et al. Identification of stem cells in small intestine and colon by marker gene Lgr5. *Nature.* 2007;449:1003–8.
4. Schepers AG, Snippert HJ, Stange DE, Van Den Born M, Van Es JH, Van De Wetering M, et al. Lineage tracing reveals Lgr5+ stem cell activity in mouse intestinal adenomas. *Science.* 2012;337:730–5.
5. Shimokawa M, Ohta Y, Nishikori S, Matano M, Takano A, Fujii M, et al. Visualization and targeting of LGR5 + human colon cancer stem cells. *Nature [Internet]. Nature Publishing Group;* 2017;545:187–92. Available from: <http://www.nature.com/doi/10.1038/nature22081>
6. Morral C, Stanisavljevic J, Hernando-Momblona X, Mereu E, Álvarez-Varela A, Cortina C, et al. Zonation of Ribosomal DNA Transcription Defines a Stem Cell Hierarchy in Colorectal Cancer. *Cell Stem Cell.* 2020;26:845–861.e12.
7. De Sousa E Melo F, Kurtova A V., Harnoss JM, Kljavin N, Hoek JD, Hung J, et al. A distinct role for Lgr5 + stem cells in primary and metastatic colon cancer. *Nature [Internet]. Nature Publishing Group;* 2017;543:676–80. Available from: <http://www.nature.com/doi/10.1038/nature21713>
8. Fumagalli A, Oost KC, Kester L, Morgner J, Bornes L, Bruens L, et al. Plasticity of Lgr5-Negative Cancer Cells Drives Metastasis in Colorectal Cancer. *Cell Stem Cell [Internet]. Elsevier Inc.;* 2020;26:569–578.e7. Available from: <https://doi.org/10.1016/j.stem.2020.02.008>
9. Schuijers J, Junker JP, Mokry M, Hatzis P, Koo BK, Sasselli V, et al. Ascl2 acts as an R-spondin/wnt-responsive switch to control stemness in intestinal crypts. *Cell Stem Cell [Internet]. Elsevier Inc.;* 2015;16:158–70. Available from: <http://dx.doi.org/10.1016/j.stem.2014.12.006>
10. Oost KC, van Voorthuisen L, Fumagalli A, Lindeboom RGH, Sprangers J, Omerzu M, et al. Specific Labeling of Stem Cell Activity in Human Colorectal Organoids Using an ASCL2-Responsive Minigene. *Cell Rep [Internet]. ElsevierCompany.;* 2018;22:1600–14. Available from: <https://doi.org/10.1016/j.celrep.2018.01.033>
11. Bleijs M, Wetering M van de, Clevers H, Drost J. Xenograft and organoid model systems in cancer research. *EMBO J [Internet]. John Wiley & Sons, Ltd;* 2019 [cited 2022 May 30];38:e101654. Available from: <https://onlinelibrary.wiley.com/doi/full/10.15252/embj.2019101654>



CHAPTER

1

Intestinal Regeneration Regulation by the Microenvironment

Joris H. Hageman¹, Maria C. Heinz¹, Kai Kretzschmar², Jelte van der Vaart³, Hans Clevers⁴, Hugo J. G. Snippert^{5, #}

¹ Molecular Cancer Research, Center for Molecular Medicine, University Medical Center Utrecht, Utrecht University, 3584 CX Utrecht, the Netherlands; Oncode Institute, 3521 AL Utrecht, the Netherlands.

² Oncode Institute, 3521 AL Utrecht, the Netherlands; Hubrecht Institute, Royal Netherlands Academy of Arts and Sciences (KNAW) and UMC Utrecht, 3584 CT Utrecht, the Netherlands; Mildred-Scheel Early Career Centre (MSNZ) for Cancer Research, University Hospital Würzburg, 97080 Würzburg, Germany.

³ Oncode Institute, 3521 AL Utrecht, the Netherlands; Hubrecht Institute, Royal Netherlands Academy of Arts and Sciences (KNAW) and UMC Utrecht, 3584 CT Utrecht, the Netherlands.

⁴ Oncode Institute, 3521 AL Utrecht, the Netherlands; Hubrecht Institute, Royal Netherlands Academy of Arts and Sciences (KNAW) and UMC Utrecht, 3584 CT Utrecht, the Netherlands; Princess Máxima Center for Pediatric Oncology, 3584 CS Utrecht, the Netherlands.

⁵ Molecular Cancer Research, Center for Molecular Medicine, University Medical Center Utrecht, Utrecht University, 3584 CX Utrecht, the Netherlands; Oncode Institute, 3521 AL Utrecht, the Netherlands. Electronic address: h.j.g.snippert@umcutrecht.nl.

#: Lead Contact.

Developmental Cell, doi: 10.1016/j.devcel.2020.07.009.

SUMMARY

Damage to the intestinal stem cell niche can result from mechanical stress, infections, chronic inflammation or cytotoxic therapies. Progenitor cells can compensate for insults to the stem cell population through dedifferentiation. The microenvironment modulates this regenerative response by influencing the activity of signaling pathways, including Wnt, Notch, and YAP/TAZ. For instance, mesenchymal cells and immune cells become more abundant after damage and secrete signaling molecules that promote the regenerative process. Furthermore, regeneration is influenced by the nutritional state, microbiome, and extracellular matrix. Here, we review how all these components cooperate to restore epithelial homeostasis in the intestine after injury.

INTRODUCTION

A striking feature of the intestinal morphology is the epithelial compartmentalization into protruding villi that consist of differentiated cells, and invaginating crypts that harbor stem and progenitor cells at their base (Figure 1). These so-called crypt-villus units are highly repetitive, with estimates suggesting close to a million crypts for the mouse small intestine. The epithelium displays a remarkably high turnover rate as the lifetime of the majority of mature epithelial cells is less than 5 days (Darwich et al., 2014). Crypt base columnar (CBC) cells are the intestinal stem cells, fueling continuous generation of all differentiated cell types, both *in vivo* and *in vitro* (Barker et al., 2007; Sato et al., 2009). CBC cells express *Lgr5* and are intermingled with post-mitotic Paneth cells at the crypt bottom. An alternative stem cell pool has been proposed to be present just above the Paneth cells at the so-called +4 position (Potten and Loeffler, 1990; Sangiorgi and Capecchi, 2008; Takeda et al., 2011), but the function and fate of these cells during homeostasis and injury response is under debate (Barker, 2014).

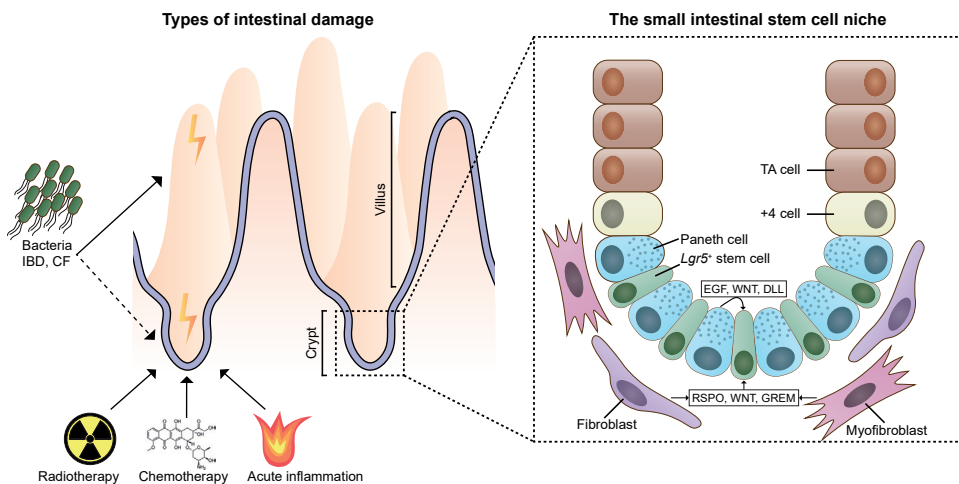


Figure 1: The small intestinal stem cell niche and types of epithelial insults.

The small intestinal epithelium is compartmentalized in crypts and villi. **Left:** different sources of damage are displayed, including the compartments where they are most likely to induce injury (arrows). Damage from the microbiota is mostly restricted to the villi. Severe infection or inflammation, as is the case for inflammatory bowel disease (IBD) and cystic fibrosis (CF), can also involve crypt damage (dashed arrow). Damage by radiotherapy, chemotherapy, or acute inflammation is most detrimental in the crypt region. **Right:** zoom-in of a crypt with *Lgr5*⁺ stem cells that are intermingled with Paneth cells and surrounded by mesenchymal cells. The latter two support stem cell function through various growth factors.

In this review, we discuss how the intestinal epithelium reacts to different types of damage in order to regenerate the stem cell pool. As stem cell fate is largely determined by the activity of signaling pathways, the microenvironment plays a pivotal role in the modulation of plasticity and stem cell function during epithelial repair. We discuss how epithelial damage can be sensed and how alterations in the microenvironment can modulate the regenerative response.

THE INTESTINAL STEM CELL NICHE

Intestinal stem cells are in close physical contact with neighboring cells of both epithelial and mesenchymal origin. These cells and in particular their interplay constitute the intestinal stem cell niche. The proliferative nature of *Lgr5*⁺ stem cells is sustained by signaling factors such as Wnt ligands, EGF, Notch ligands, and bone morphogenetic protein (BMP) inhibitors (Gehart and Clevers, 2019). Stem cells within the niche divide mostly in a symmetrical way and display neutral competition for limited niche space (Lopez-Garcia et al., 2010; Snippert et al., 2010). As a result, cells at the boundary of the niche have a higher probability to be pushed out of the niche (Ritsma et al., 2014; Snippert et al., 2010). Subsequently, diminished exposure to stem cell-promoting factors triggers cellular differentiation into progenitor cells, while they are pushed into the transit-amplifying (TA) zone at the flanks of the crypt compartment. During the differentiation process inside the TA zone, cells undergo multiple rounds of cell division, while migrating out of the crypt toward the villus compartment. The predominant lineage decision involves commitment to either the secretory lineage (comprising enteroendocrine cells, goblet cells, tuft cells, and Paneth cells), or the absorptive lineage (enterocytes and Microfold cells). The main determining factor in this decision is Notch signaling (Koch et al., 2013).

Epithelial Paneth cells produce WNT3, EGF, and DLL4 (Sato et al., 2011a) and they support stem cell metabolism by providing the stem cells with lactate as a substrate for oxidative phosphorylation (Rodríguez-Colman et al., 2017). A decrease in the number of Paneth cells correlates with a decrease in stem cells and their presence is vital for stem cell function *in vitro* (Sato et al., 2011a). Observations that the intestinal epithelium remains largely unaffected when Paneth cells are depleted *in vivo*, suggest that the niche-role of Paneth cells can be adopted by alternative sources (Durand et al., 2012; Kim et al., 2012). Indeed, enteroendocrine and tuft cells can replace ablated Paneth cells to serve as alternative sources of Notch signals (van Es et al., 2019), while the mesenchyme surrounding the intestinal epithelium secretes sufficient levels of Wnt ligands to ensure homeostasis (Farin et al., 2012; Kabiri et al., 2014).

The mesenchymal compartment in the intestine contains fibroblasts, which produce components of the extracellular matrix, and myofibroblasts, which are fibroblasts displaying properties of smooth muscle cells, such as expression of α -SMA (Powell et al., 2011). Recently, different subpopulations of mesenchymal cells have been identified to support stem cells via Wnt activation. These include *Gli1*⁺ cells expressing *Wnt2b* (Degirmenci et al., 2018; Valenta et al., 2016), CD34⁺ cells expressing *Rspo1* and *Wnt2b* (Stzepourginski et al., 2017), *Foxl1*⁺ cells expressing *Wnt2b* and *Rspo3* (Aoki et al., 2016; Shoshkes-Carmel et al., 2018), and *Pdgfra*⁺ myofibroblasts (Greicius et al., 2018). Mesenchymal cells additionally support intestinal stem cell function by establishing a physiological BMP signaling gradient along the crypt-villus axis (Kosinski et al., 2007). At the crypt base, specific *Pdgfra*^{low} mesenchymal cells called trophocytes secrete the BMP inhibitor gremlin 1, while *Pdgfra*^{high} mesenchymal telocytes are predominantly located in the villus where they activate BMP signalling (McCarthy et al., 2020).

Instead of Paneth cells, the colon comprises deep crypt secretory cells that activate Notch signaling in stem cells (Sasaki et al., 2016). The surrounding mesenchyme is an indispensable source of canonical Wnt ligands as these ligands are not produced in the colonic epithelium. Accordingly, when Wnt-secreting *Gli1*⁺ mesenchymal cells are depleted in the colon, the colonic architecture collapses (Degirmenci et al., 2018).

DAMAGE TO THE INTESTINE

The epithelial monolayer of the intestine forms a barrier against the harsh environment of the intestinal tract, with trillions of bacteria, microbes, chemicals, and metabolites, some of which are pathogenic or toxic. A crucial task is therefore to resist the mechanical forces that may otherwise jeopardize the integrity of the epithelium, while simultaneously ensuring intact absorption of nutrients (Gehart and Clevers, 2019). In case of damage, the integrity of the epithelial layer must be rapidly restored in order to prevent infections. Intestinal epithelial damage can occur in different forms: it can be locally restricted to a specific part of the intestine, such as the crypt or villus compartment, or alternatively affect one or multiple crypt-villus units.

In addition to the naturally harsh environment in the intestine, various other factors can cause intestinal damage (Figure 1). For instance, a variety of therapies including radiotherapy, chemotherapeutic agents, and antibiotics can induce intestinal damage in the crypts and villi (Ijiri and Potten, 1987). Considering that differentiated cells at the villi have a limited lifespan of several days at most, it is the damage to the stem and progenitor

cells in the crypts that is most detrimental. Acute inflammation has been shown to ablate *Lgr5*⁺ stem cells in both the small intestine (Schmitt et al., 2018) and colon (Davidson et al., 2012). Bacterial, viral or parasitic infections can affect large areas of the intestine including a multitude of crypt-villus units (Andersson-Rolf et al., 2017). This type of damage can induce the formation of wound-associated epithelial (WAE) cells, which rapidly cover the wound (Miyoshi et al., 2012; Seno et al., 2009). This serves as a temporary solution, since WAE cells do not exert all required intestinal functions. Within a week, WAE cells are replaced by *de novo* formation of functional crypts. Regeneration of lost crypts can be achieved on the large-scale by fission of the newly formed crypts (Cairnie and Millen, 1975; Dekaney et al., 2009), a process that can be counteracted by crypt fusion (Bruens et al., 2017). A chronic medical condition involving such extensive intestinal damage is inflammatory bowel disease (IBD) (de Souza and Fiocchi, 2016). The most prominent types of IBD are Crohn's disease, which can affect the entire gastrointestinal tract, and ulcerative colitis, which mainly affects the large intestine. Although many factors have been described to be involved in IBD pathogenesis, a defect in the epithelial barrier is considered to be one of the early events. The initial damage leads to inflammation, which in turn induces more damage, creating a vicious circle. Cystic fibrosis (CF) is an additional example of a disease involving high levels of intestinal damage. CF, which is characterized by a genetic defect in *CFTR*, results in diminished fluid secretion in epithelial cells (De Lisle and Borowitz, 2013). CF patients have a more static mucus layer that is less potent in protecting against bacterial infections and they display elevated inflammation and damage levels (Smyth et al., 2000).

To study the regenerative response in the intestine, damage can be induced using different strategies. For instance, high-dose radiation depletes *Lgr5*⁺ cells (Barker et al., 2007) and has been used to study the regenerative response (e.g. Montgomery et al., 2011). Additionally, dextran sulphate sodium (DSS), which can induce both acute and chronic colitis in mice (Okayasu et al., 1990), is used to induce crypt loss (e.g. Rakoff-Nahoum et al., 2004). A more refined approach to deplete specific cell types is the targeted knock-in of the diphtheria toxin receptor (DTR) into a cell-type-specific marker gene, such as *Lgr5* (Tian et al., 2011). In this case, the supplementation of diphtheria toxin (DT) induces the specific ablation of *Lgr5*⁺ cells. Although very powerful to study regenerative mechanisms, it should be noted that cell-type-specific ablation does not represent a physiological situation. To model widespread damage in up to 300 crypt-villus units, a biopsy-injury system has been developed (Seno et al., 2009).

PLASTICITY OF EPITHELIAL CELLS

The specific ablation of *Lgr5*⁺ stem cells has virtually no effect on the intestinal architecture (Metcalf et al., 2014; Tian et al., 2011). As *Lgr5*⁺ cells are the multipotent cell source in homeostasis, this suggests that either an additional population of “reserve” stem cells exists that can replenish the epithelium (e.g. +4 cells), or that more differentiated cells have the potential to revert to a stem cell state. Various marker-based lineage tracing studies have investigated the epithelial source of regeneration (Figure 2A). Taken together, these studies demonstrate that the intestinal stem cells are at the apex of a highly dynamic cellular hierarchy, with numerous potential sources for regeneration (Figure 2B).

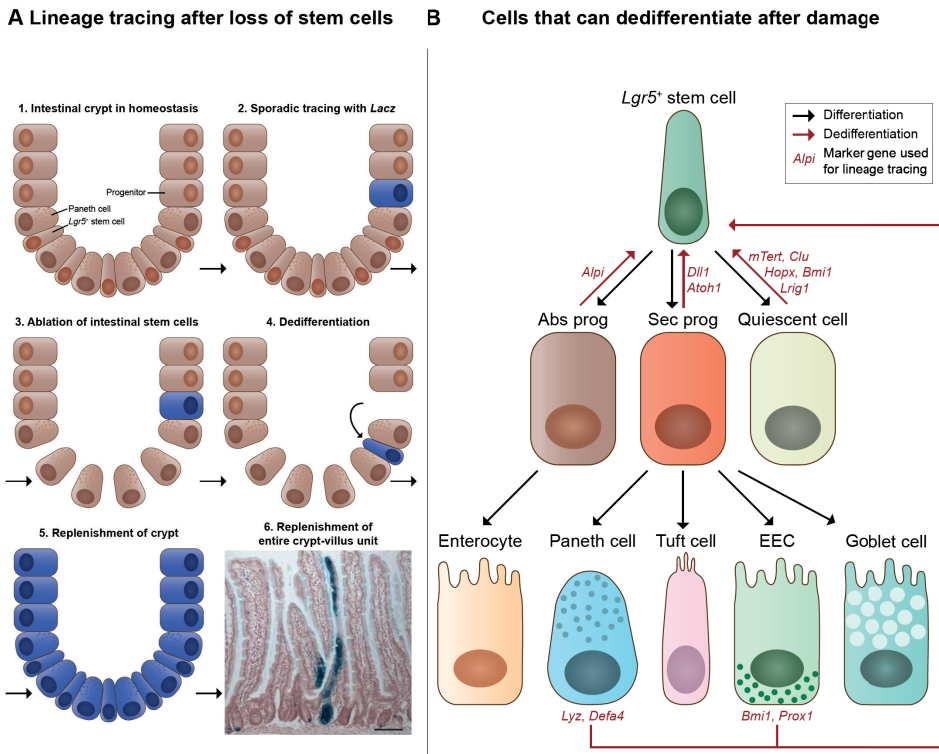


Figure 2: Lineage tracing following stem cell loss.

A. Genetic lineage tracing and stem cell ablation combined can infer dedifferentiation potential. In a normal situation, cells can be marked by activation of Lacz, allowing lineage tracing (blue) (1 and 2). Upon stem cell ablation (3), marked cells can dedifferentiate into a stem cell (4), giving them a possibility to colonize the whole stem cell compartment (5), ultimately giving rise to long-lived traced ‘ribbons’ (6, courtesy: van Es et al., 2012). **B.** Diagram showing the cell types that have been shown to be able to dedifferentiate into *Lgr5*⁺ stem cells following stem cell loss (red arrows). Marker genes used to activate lineage tracing are shown in red. Note that marker genes for differentiated cells might also be expressed in committed progenitors and vice versa. EEC, enteroendocrine cell; Abs prog, absorptive progenitor; Sec prog, secretory progenitor.

Secretory lineage

Cells of the secretory lineage have been shown to be able to revert to stem cells using genetic lineage tracing (van Es et al., 2012). This technique involves the creation of a heritable genetic mark in a specific cell lineage (Kretzschmar and Watt, 2012). The distribution of the mark within tissues can be traced at any time point, revealing continuous propagation or extinction of the lineage. To be able to initiate lineage tracing at will, inducible Cre enzymes are commonly used, which delete loxP-flanked transcriptional roadblocks and hence enable expression of a marker gene. Using this strategy, it was demonstrated that under homeostatic conditions, *Dll1*⁺ cells are committed secretory progenitors with a limited lifespan that can exclusively generate goblet cells, Paneth cells, tuft cells, and enteroendocrine cells, but no enterocytes (van Es et al., 2012). In contrast, single *Dll1*⁺ cells can establish organoids *in vitro* containing *Lgr5*⁺ cells when excessive WNT3A is supplied, highlighting their capacity to revert to the stem cell state under these conditions. Moreover, when challenged *in vivo* upon stem cell depletion by irradiation, *Dll1*⁺ cells can give rise to fully functional *Lgr5*⁺ stem cells that are able to self-renew and generate multicellular progeny. In addition to *Dll1*, secretory progenitors can also be identified by *Atoh1* expression (Castillo-Azofeifa et al., 2019; Ishibashi et al., 2018; Tomic et al., 2018). Lineage tracing of *Atoh1*⁺ secretory progenitor cells confirmed that they can repopulate the intestinal crypts upon damage following irradiation, DTR-mediated stem cell depletion, or DSS treatment (Tomic et al., 2018). Additionally, Paneth cells or their lineage-committed precursors also have the capacity to dedifferentiate, as demonstrated by lineage tracing following irradiation (Yu et al., 2018), DSS treatment (Schmitt et al., 2018), or doxorubicin treatment (Jones et al., 2019). In contrast, *Dclk1*⁺ tuft cells do not contribute to regeneration upon damage, although these cells can sporadically give rise to crypt-villus units under homeostatic conditions (Westphalen et al., 2014).

Absorptive lineage

Absorptive progenitors have been demonstrated to display similar dynamics as secretory progenitors. In the unperturbed intestine, it was shown that *Alpi* expression marks enterocytes and their progenitors (Tetteh et al., 2016). Following the specific depletion of *Lgr5*⁺ cells by the *Lgr5*-DTR technique, *Alpi*⁺ cells provide a source of *de novo* production of functional *Lgr5*⁺ cells. Immuno-histochemistry confirmed that the newly generated stem cell progeny includes all cell types, underpinning the multipotent potential of dedifferentiated *Alpi*⁺ cells of the absorptive lineage.

Quiescent cells

Label-retaining cells (LRCs), which reside just above the Paneth cells at the +4 position, may constitute a reserve stem cell population that can be activated following loss of *Lgr5*⁺ stem cells. Accordingly, lineage tracing indicated that +4 cells, marked by *Bmi1*, *mTert*, *Hopx*, or *Lrig1* regenerate the epithelium after *Lgr5*⁺ cell depletion (Montgomery et al., 2011; Powell et al., 2012; Tian et al., 2011; Yousefi et al., 2016). LRCs express *Uri*, which inhibits Wnt signaling and facilitates low levels of proliferation, rendering LRCs resistant to radiation (Chaves-Pérez et al., 2019). Following irradiation, *Uri* is downregulated, resulting in activation of Wnt signaling, enhanced proliferation levels, and subsequent dedifferentiation and regeneration of the epithelium. However, expression of putative +4 markers *Bmi1*, *mTert*, *Hopx*, and *Lrig1* is not restricted to the +4 position, but these markers display wider expression patterns, frequently including *Lgr5*⁺ stem cells and progenitors (Muñoz et al., 2012; Wong et al., 2012). There is an ongoing debate whether progenitor cells and quiescent +4 cells constitute overlapping cell populations, as lineage-committed progenitor cells can also regenerate the epithelium.

To examine this, Buczacki and colleagues designed a strategy to perform lineage tracing of LRCs based on a functional criterion, being their non-cycling behavior, rather than utilizing marker gene expression (Buczacki et al., 2013). Here, transient, but ubiquitous induction of half the Cre protein was essential, which is exclusively retained by slow- or non-cycling cells over time. These LRCs expressed both *Lgr5* and a number of +4 markers, namely *mTert*, *Lrig1*, and *Hopx*. Subsequently, functional complementation of the split Cre with its other half enabled lineage tracing from LRCs. This revealed that during homeostasis LRCs predominantly differentiate into Paneth or enteroendocrine cells. Upon tissue damage induced by irradiation or chemotherapeutic agents, LRCs are capable to regenerate the entire epithelium, including the *Lgr5*⁺ stem cell compartment. Similarly, cells around the +4 position that are labeled with a *Bmi1*-GFP transgene, express markers of the enteroendocrine lineage, including mature enteroendocrine markers (Jadhav et al., 2017; Yan et al., 2017). Moreover, the chromosome accessibility profiles of secretory progenitors and *Bmi1*-GFP⁺ cells are strikingly similar (Jadhav et al., 2017), indicating that quiescent cells and slowly cycling precursor cells might be overlapping populations.

Recently, a novel population of “revival” stem cells has been identified, which are rare *Clu*-expressing cells observed in intestinal epithelia of irradiated mice (Ayyaz et al., 2019). During homeostasis, *Clu*⁺ cells are most prevalent around the +4 position. Following irradiation, stem cell depletion with DT, or DSS treatment, the *Clu*⁺ cells proliferate and can replenish the intestinal epithelium. Future studies are required to reveal the origin and homeostatic function of these cells.

MECHANISMS OF PLASTICITY

Epigenetic modifications, such as DNA methylation, are fundamental processes during differentiation of the intestinal epithelium (Sheaffer et al., 2014). Yet, the differences between the DNA methylation profiles of intestinal stem cells and differentiated cells are marginal (Kaaij et al., 2013; Yu et al., 2015) and the epigenetic state of the epithelial cells of the intestine is not hard-wired (Jadhav et al., 2017; Kim et al., 2014; Vermeulen and Snippert, 2014). The flexible epigenetic state of intestinal cells makes them susceptible to exposure to trophic factors in the stem cell niche that support stem cell fate. Taken together, this allows cells to dedifferentiate and to recover the intestinal epithelium following insults to the stem cell compartment. As expected, signaling networks known to support stem cell activity, have been reported to be involved in the dedifferentiation process. Wnt signaling, which is pivotal for stem cell proliferation, is intuitively among the primary candidates. Accordingly, the presence of R-spondins, which amplify Wnt signaling (de Lau et al., 2011), protects the intestinal architecture from damage induced by the chemotherapeutic agent 5-FU, DSS or irradiation (Harnack et al., 2019; Kim et al., 2005; Zhao et al., 2007; Zhou et al., 2013). Furthermore, the supplementation of WNT3A to organoid culture medium enables *Dll1*⁺ secretory progenitors to generate organoids, underlining the role of Wnt signaling in dedifferentiation (van Es et al., 2012). Wnt signaling is increased in dedifferentiating Paneth cells following DSS injury (Schmitt et al., 2018) and the Wnt target gene *Ascl2* is essential for the regenerative response (Murata et al., 2020). Conversely, when Wnt ligand secretion is blocked with a porcupine inhibitor in mice, radiation-induced damage cannot be repaired (Kabiri et al., 2014). Likewise, the knockout of the GTPase *Rala* in *Lgr5*⁺ cells suppresses Wnt signalling, resulting in decreased numbers of regenerative crypts following irradiation (Johansson et al., 2019).

A second signaling pathway that plays a pivotal role in regeneration is the Notch pathway. Following DSS-induced damage, the expression of Notch target gene *Hes1* is elevated in the murine intestinal epithelium (Okamoto et al., 2009). Conversely, when DSS treatment is followed by Notch inhibition with a γ -secretase inhibitor, the epithelial layer is disrupted and proliferation is impaired (Okamoto et al., 2009). Likewise, the deletion of the Notch receptors 1 or 2 exacerbates the destructive effects of radiation, resulting in more weight loss and reduced intestinal epithelial proliferation (Carulli et al., 2015). In dedifferentiating Paneth cells (following irradiation), the levels of HES1, NOTCH1, and intracellular Notch domain (NICD) are increased (Yu et al., 2018). In contrast, overexpression of NICD in otherwise unperturbed Paneth cells induces proliferation, which further underscores the role of Notch signaling in regeneration.

A third key player in regeneration is the transcription factors YAP and its homolog TAZ. Although YAP/TAZ were initially identified as downstream targets of the Hippo pathway, it became apparent that multiple other factors, such as Wnt signaling and G protein-coupled receptors, regulate YAP/TAZ activity (Azzolin et al., 2012; Piccolo et al., 2014; Yu et al., 2012). Although entirely dispensable for intestinal homeostasis (Barry et al., 2013; Cai et al., 2010), YAP/TAZ signaling is critical for regeneration. In the colon, DSS-induced damage results in increased YAP activity (Cai et al., 2010). Consequently, a conditional knockout of YAP in combination with DSS treatment results in more weight loss, increased levels of epithelial apoptosis, less proliferation, and decreased survival (Cai et al., 2010). Similar findings have been reported after radiation-induced damage, where YAP is involved in the regenerative response by preventing differentiation (Gregorieff et al., 2015). *In vitro*, YAP overexpression enhances organoid formation and overcomes the need for Wnt ligand supplementation in organoid culture medium during the first days of single cell outgrowth (Serra et al., 2019; Yui et al., 2018). Conversely, YAP inhibition reduces organoid forming efficiency and decreases the number of intestinal stem cells (Gregorieff et al., 2015; Serra et al., 2019). Although it is well-established that Wnt, Notch, and YAP/TAZ are involved in the regenerative response, their exact interplay and relative contributions remain subject of investigation.

MODULATION OF THE REGENERATIVE RESPONSE

Mesenchymal cells

Plasticity within the epithelial layer is not exclusively intrinsically regulated, but requires modulation from non-epithelial components (Figure 3A). The role of mesenchymal cells in intestinal regeneration has been studied by knocking out different mesenchyme-specific factors. Knockout of the microRNAs miR-143/145, which are uniquely expressed in the mesenchyme, results in disorganized myofibroblasts, loss of epithelial proliferation, and decreased survival following DSS treatment (Chivukula et al., 2014). In an additional study, myofibroblasts were shown to express ANGPTL2, which downregulates BMP secretion via the NF- κ B pathway (Horiguchi et al., 2017). After irradiation or DSS treatment, *Angptl2* knockout mice have smaller and less-proliferative colons than wild type mice, which can be attributed to an increase in *Bmp2* and *Bmp7* expression and a decrease in the levels of non-phosphorylated active β -catenin. This suggests that myofibroblasts support regeneration through inhibition of BMP signalling and upregulation of Wnt signaling. Similarly, CD34⁺ mesenchymal cells overexpress the BMP-inhibitor gremlin 1 and the Wnt amplifier R-spondin 1 following DSS treatment (Stzepourginski et al., 2017) and

Gli1⁺ mesenchymal cells produce R-spondin 3 after DSS treatment (Degirmenci et al., 2018). Trophocytes at the crypt bottom that express gremlin 1 potentially also contribute to the regenerative response by inhibiting BMP signaling (McCarthy et al., 2020). An additional factor that is expressed by the mesenchyme and supports regeneration after DSS-induced damage is prostaglandin E2 (PGE2) (Brown et al., 2007). Following DSS-induced damage, *Ptgs2*⁺ mesenchymal cells migrate to the lower crypt regions, where they promote regeneration through the secretion of PGE2. In mouse small intestinal organoids, PGE2 enhances YAP activity through the prostaglandin EP₄ receptor (Roulis et al., 2020), while evidence from human colorectal cancer cell lines suggests that PGE2 promotes regeneration by amplifying both YAP-mediated proliferation (Kim et al., 2017) and Wnt signaling (Castellone et al., 2005).

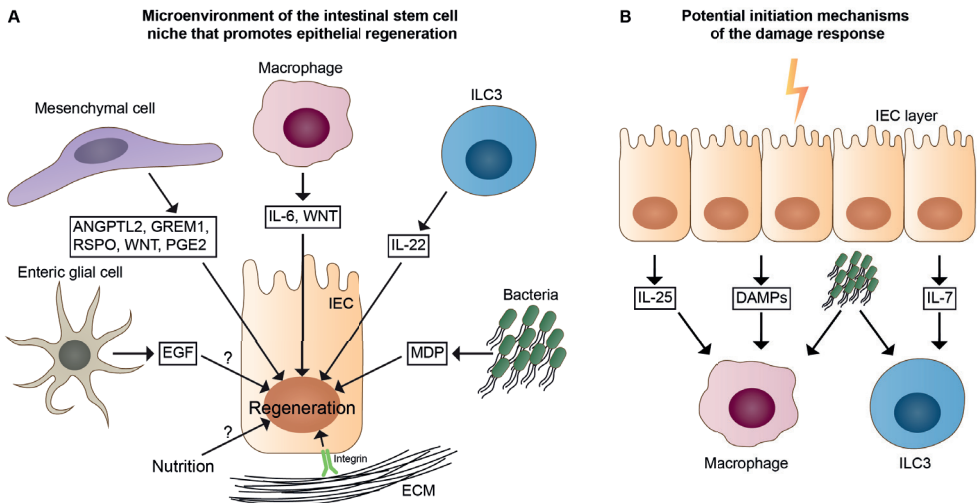


Figure 3: Interplay between intestinal epithelium and non-epithelial components that modulate regeneration.

A. Overview of cellular and non-cellular components that promote regeneration of intestinal epithelial cells (IECs) following injury. The microenvironment provides factors for the epithelium that activate pathways such as Wnt and YAP. ILC3, group 3 innate lymphoid cell; ECM, extracellular matrix. **B.** Potential mechanisms for recruitment of immune cells following injury. Damage-associated molecular patterns (DAMPs), which are released during cell death, activate immune cells such as macrophages. Epithelial cells can signal to macrophages via IL-25, or to ILC3s via IL-7. Alternatively, (bacterial) infections can also activate these immune cells.

In case of large-scale damage to the intestine, the surrounding mesenchymal cells strongly support the formation of WAE cells, which are required to temporarily cover the damaged site prior to replacement by functional epithelial cells (see Damage to

the Intestine). Non-canonical WNT5A, derived from the mesenchyme, facilitates the generation of the WAE layer from adjacent healthy crypts, as demonstrated by lineage tracing (Miyoshi et al., 2012). In addition, large-scale damage, induced by biopsy injury, leads to an increase in the number of *Ptgs2*⁺ mesenchymal cells, which produce PGE2 to promote WAE layer formation (Manieri et al., 2012; Miyoshi et al., 2017).

Immune cells

Damage to the intestine is frequently accompanied by infection or inflammation and, hence, activation of the immune system. Upon activation or recruitment, immune cells, such as wound-healing M2 macrophages, can modulate the regenerative response. For instance, in the injured intestine, macrophages are recruited to the lower crypt region (Pull et al., 2005). In a mouse model lacking macrophages, DSS-induced damage is exacerbated compared with control mice (Pull et al., 2005). Conversely, this differential effect is not observed in mice without neutrophils or lymphocytes. To further examine the mechanism of macrophage-induced regeneration, Wnt ligand secretion was disrupted specifically in macrophages (Saha et al., 2016). As a result, mortality increases and intestinal epithelial architecture is impaired following irradiation. This effect can be rescued by intravenously injecting conditioned medium from wild type macrophage cultures expressing Wnt ligands. These Wnt ligands enhance both β -catenin levels and Wnt target gene expression in the epithelial layer, resulting in increased numbers of *Lgr5*⁺ stem cells. In addition to Wnt ligands, macrophages also secrete interleukin (IL)-6, which can stimulate both YAP and Notch signaling in stem cells via the GP130 receptor (Taniguchi et al., 2015). Additionally, macrophages are also involved in WAE layer formation in the biopsy-injury model (Seno et al., 2009) and they activate Wnt signaling in epithelial cells after incision damage (Quiros et al., 2017).

A second example of immune cells that promote intestinal regeneration are innate lymphoid cells (ILCs). A subset of ILCs expressing IL-22 (referred to as group 3 ILCs, or ILC3s) are of particular interest in the context of regeneration (Aparicio-Domingo et al., 2015; Spits et al., 2013). Bone marrow transplantation can induce graft-versus-host disease (GvHD) which coincides with a decrease in the number of intestinal stem cells (Hanash et al., 2012), likely through T-cell mediated stem cell cytotoxicity (Takashima et al., 2019). GvHD in *Il22* knockout mice leads to a further reduction in the number of stem cells and to an increase in mortality (Hanash et al., 2012). Accordingly, intestinal stem cells express the IL-22 receptor and the expression of this receptor increases during GvHD. IL-22 activates STAT3 signaling, which results in an increase of *Lgr5*⁺ stem

cell numbers and intestinal repair during GvHD, while *in vitro*, IL-22 promotes organoid growth (Lindemans et al., 2015). Alternatively, ILC3s have been suggested to facilitate repair through modulation of epithelial YAP activity, since mice lacking ILC3s display decreased YAP activity (Romera-Hernández et al., 2020). However, it remains unclear whether ILC3s can directly influence epithelial YAP activity.

Bacteria

Bacteria in the intestinal lumen can modulate intestinal repair, for instance via recognition of commensal bacteria by Toll-like receptors (TLRs) that are present on both immune and epithelial cells. Following DSS treatment, mice without commensal bacteria display severe weight loss and colonic bleeding (Rakoff-Nahoum et al., 2004). This phenotype can be rescued by supplementation with the bacterial product lipopolysaccharide in bacteria-free wild type mice, but not in *Tlr4* knockout mice, suggesting an essential role for bacteria recognition in the regenerative response. This could potentially be the result of direct recognition of bacteria by intestinal stem cells, which express TLR4 (Neal et al., 2012). Additionally, intestinal stem cells can recognize bacterial products via the NOD2 receptor. One example is the bacterial product muramyl dipeptide (MDP), which induces decreased levels of reactive oxygen species in intestinal stem cells (Levy et al., 2020). MDP promotes intestinal organoid growth, while *in vivo* it supports repair after injury induced by the chemotherapeutic agent doxorubicin (Nigro et al., 2014). Furthermore, probiotic bacteria secrete proteins that upregulate Akt signaling and prevent apoptosis in the intestinal epithelium (Yan et al., 2007). This constitutes an additional manner by which intestinal regeneration can be promoted directly by bacteria. Moreover, *Citrobacter rodentium* infection results in increased stromal expression of *Rspo2*, which in turn promotes epithelial proliferation (Papapietro et al., 2013). Conversely, bacteria can also negatively influence intestinal regeneration. For example, the bacterial metabolite butyrate decreases the proliferation rate of the recovering epithelium following DSS treatment (Kaiko et al., 2016).

Extracellular matrix

The properties of the extracellular matrix (ECM) affect the state of cells to a large extent. Healthy cells generally do not grow in solution, which indicates that they require anchorage to a solid matrix (Discher et al., 2005). Through receptors such as integrins, cells can sense the stiffness of the ECM and alter their intracellular state accordingly.

This way, the ECM influences cellular behaviors including differentiation. For example, matrix stiffness is a key developmental factor for mesenchymal stem cells to differentiate into neurons, myoblasts, or osteoblasts (Engler et al., 2006). Interestingly, YAP/TAZ, which play a prominent role in intestinal regeneration, are the fundamental effectors of stiffness sensing. *In vitro*, the stiffening of the matrix results in a nuclear translocation and activation of YAP (Dupont et al., 2011), implying that sensing of the ECM can regulate proliferation in stem cells. In mammary epithelial cells, YAP/TAZ activity coordinates the switch to proliferation under the influence of matrix stiffness (Aragona et al., 2013). Similarly, intestinal stem cells require a stiff matrix *in vitro* for optimal proliferation (Gjorevski et al., 2016). Further insights into the link between ECM adherence, YAP signaling, and regeneration in the intestine have been provided by the Jensen group (Yui et al., 2018). Following DSS treatment, the authors detected elevated levels of collagen 1, integrin, and focal adhesions kinase (FAK), a downstream factor of integrin signaling. Moreover, inhibition of FAK impairs the intestinal repair after DSS treatment. Again, YAP was suggested to be an essential player in the sensing of the ECM properties during regeneration because FAK inhibition results in lower levels of active YAP. Thus, sensing of the ECM is an emerging modulating factor in the intestinal regenerative response. It should be noted that additional properties of the ECM, such as porosity, can influence stem cell dynamics as well (Trappmann et al., 2012), but the role of these properties in intestinal regeneration remains largely unexplored.

Enteric nervous system

Although the amount of research into the interplay between the nervous system and intestinal regeneration is limited, there are some indications that the enteric nervous system plays a relevant role. The enteric nervous system is composed of neuronal and glial cells that are involved in intestinal functions, such as blood flow, peristalsis, and interactions between the intestinal epithelium and immune cells (Schneider et al., 2019). Enteric glial cells are in close contact with the intestinal epithelium. DSS-induced damage to the intestine is aggravated when enteric glial cells are depleted (van Landeghem et al., 2011). To study the underlying mechanism *in vitro*, monolayers of intestinal epithelial cells were disrupted in the presence of enteric glial cells. This revealed that EGF secretion by enteric glial cells and subsequent activation of FAK in the intestinal epithelial cells mediates recovery from the epithelial disruptions. *In vivo*, the role of enteric glial cells can be examined after disrupting the small intestinal barrier by steam burning, which severely damages the villi (Costantini et al., 2010). Interestingly, stimulation of the

vagal nerve, which innervates the intestine, mitigates the effects of steam burning via activation of enteric glial cells. Furthermore, a subset of neural cells of the enteric nervous system expresses the hepatocyte growth factor (HGF) receptor MET (Avetisyan et al., 2015). To examine the role of MET in intestinal regeneration, mice with a neural cell-specific inducible knockout of *Met* were used (Avetisyan et al., 2015). Upon DSS treatment, these mice display increased levels of colonic damage and decreased levels of epithelial proliferation, suggesting a role for HGF/MET signaling in neural cells during intestinal regeneration. Accordingly, the administration of HGF attenuates the effects of DSS treatment in rats (Tahara et al., 2003).-

Nutritional state

Stem cell behavior is heavily influenced by the nutritional state. The mammalian target of rapamycin (mTOR) pathway is a key factor in the sensing of the nutritional state and is also involved in proliferation (Sarbasov et al., 2005). Mice on a calorie restricted (CR) diet display an increase in the numbers of both *Lgr5*⁺ stem and Paneth cells, when compared with mice on a control diet (Igarashi and Guarente, 2016; Yilmaz et al., 2012). The CR diet decreases mTOR activity in Paneth cells, which in turn support the stem cells via secretion of cyclic ADP ribose. Colony formation assays confirmed the role of Paneth cells in response to CR, as Paneth cells derived from CR mice enhance the organoid-forming potential of stem cells when compared with Paneth cells derived from control mice (Yilmaz et al., 2012). Notably, the CR diet protects the mice against radiation-induced damage. Moreover, the CR diet diminishes mTOR activity in quiescent *Hopx*⁺ intestinal cells, rendering them more resistant to radiation injury and more prone to contribute to intestinal repair (Yousefi et al., 2018). A potential mechanism for the beneficial effect of the CR diet on intestinal regeneration is a decrease in the secretion of the Wnt inhibitor Notum by Paneth cells as a result of diminished mTOR activity (Pentimikko et al., 2019).

An increase in intestinal stem cell numbers and enhanced organoid-forming capacity of the stem cells can also be observed in mice on a high-fat diet (Beyaz et al., 2016). This diet does not result in an increase in Paneth cells, but exerts its effects directly on the *Lgr5*⁺ stem cells, in which it induces an upregulation of β -catenin target genes, linking the high-fat diet to intestinal regeneration via the Wnt pathway. A ketogenic diet similarly promotes intestinal stem cell function and repair, supposedly by activation of Notch signaling (Cheng et al., 2019).

INITIATION OF THE REGENERATIVE RESPONSE

The observation that a wide variety of non-epithelial factors can modulate the regenerative response in the intestinal epithelium, raises the question as to how damage is sensed. Epithelial injury frequently coincides with an inflammatory response and immune cells that are recruited during inflammation could regulate repair (Figure 3B). A result of epithelial disruption may be the penetration of bacteria through the epithelial layer and subsequent activation of immune cells, which in turn promote restoration of the epithelium. Alternatively, a sterile environment, which does not involve microbes or pathogens, can also evoke inflammation and an immune response (Rock et al., 2010). This can, for instance, be mediated by damage-associated molecular patterns (DAMPs), such as uric acid or extracellular DNA, which are released during cell death and recognized by immune cells.

Inflammation frequently involves the production of tumor necrosis factor (TNF) by macrophages. Interestingly, colonic damage induced with DSS is exacerbated in *Tnf* knockout mice, supporting a role for TNF in regeneration (Naito et al., 2003). TNF activates Wnt signaling in both intestinal organoids and the murine intestine, suggesting that TNF promotes regeneration through activation of Wnt signaling (Bradford et al., 2017). An additional example of an inflammatory cytokine involved in regeneration is interferon-gamma (IFN- γ), which is activated following damage upon helminth infection (Nusse et al., 2018). IFN- γ induces the generation of fetal-like proliferative epithelial cells characterized by *Ly6a* expression, which contribute to repair. Furthermore, it is widely appreciated that the intestinal epithelium signals to cells of the immune system. Although the relevance of this signaling network during regenerative responses has not been directly demonstrated, it is a likely candidate for the recruitment of immune cells during repair. For example, intestinal epithelial tuft cells secrete IL-25 (von Moltke et al., 2016), which promotes differentiation of hematopoietic cells to the macrophage lineage (Saenz et al., 2010). This may in turn promote regeneration, because macrophages play a crucial role in the modulation of repair (see Immune cells). Additionally, bacteria induce the expression of thymic stromal lymphopoietin (TSLP) in primary human intestinal epithelial cells. TSLP activates the secretion of IL-6 in dendritic cells (Rimoldi et al., 2005) and IL-6 promotes repair through Notch and YAP activation in the epithelium (Taniguchi et al., 2015). Furthermore, the production of ILC3-derived IL-22, which is involved in the intestinal repair, is enhanced by the epithelium and bacteria. Intestinal epithelial cells produce IL-7 (Watanabe et al., 1995) and IL-7 stimulates the differentiation of ILC3s and the secretion of IL-22 (Vonarbourg et al., 2010). Moreover, *Citrobacter rodentium* infection activates different subtypes of IL-22 expressing ILC3s (Satoh-Takayama et al.,

2008; Sonnenberg et al., 2011). IL-22 production by ILC3s is essential for immunity to *C. rodentium* (Sonnenberg et al., 2011) and IL-22 may simultaneously be involved in the regenerative response via STAT3 signaling (Lindemans et al., 2015). Thus, the activation of the immune system is a central component in the interplay between the epithelium and the microenvironment to ensure proper initiation of the regenerative response.

CONCLUDING REMARKS AND FUTURE PERSPECTIVES

In the intestinal epithelium, progenitor cells of the absorptive and secretory lineage can repopulate the stem cell compartment following loss of the stem cells. The recent notion that even differentiated cells may have similar capacities (Jones et al., 2019; Schmitt et al., 2018; Yan et al., 2017; Yu et al., 2018), further underscores the highly plastic nature of the intestinal epithelium. There is an ongoing debate on the reserve stem cells at the +4 position. It is compelling that recent progeny of *Lgr5*⁺ stem cells can serve as a reservoir of injury-inducible stem cells (Murata et al., 2020). Whether “reserve stem cells” are progenitor cells on the verge of differentiation, or also include designated (+4) cells whose *raison d’être* is to replace stem cells when necessary, is currently unclear.

Thus far, most studies have focused on whether certain cell types possess the capacity to dedifferentiate. However, how much these cell types contribute to repopulate the stem cell pool in relation to other cell types is yet unspecified. Generally, a decay in stem cell potential along cellular differentiation trajectories is to be expected and it is likely that the relative contributions vary between different types of damage as well. It should not be underestimated that DTR-mediated cell type depletion results in artificial damage, since natural insults are not completely cell-type-specific or entirely effective. Thus, even a limited fraction of *Lgr5*⁺ stem cells that survive natural insults, either by chance, or by a dedicated *Lgr5*⁺ subpopulation (Barriga et al., 2017), should be accounted for as a possible source of cells that can regenerate the epithelium.

An extensive body of research has been performed to study the influence of the microenvironment on intestinal regeneration. Mesenchymal cells, immune cells, bacteria, enteric neuronal cells, the extracellular matrix, and the nutritional state act in concert to establish an environment that facilitates regeneration. The high interconnectivity of several of these components was recently illustrated by the detection of an interesting interplay between the enteric nervous system and ILC3s, which depends on food intake and bacteria (Talbot et al., 2020). Considering the dominant role of the microenvironment during regeneration, it is likely that cellular plasticity is highly regulated by the

microenvironment during epithelial repair. However, it should be noted that the majority of these studies have not demonstrated a direct link between the microenvironment and cellular plasticity.

Human intestinal stem cells of normal and diseased epithelia can be cultured *in vitro* as organoids (Sato et al., 2011b) and these organoids can be xenotransplanted orthotopically into the colonic epithelium, where they locally replace the murine epithelium (Sugimoto et al., 2018). Organoid models, in particular those of human origin, provide a unique platform to study underlying mechanisms of cell fate decisions and lineage specification in genetically normal organoids (Beumer et al., 2020), or to assess the capacity of dedifferentiation at different tumorigenic stages (Oost et al., 2018). Furthermore, organoids can be co-cultured with immune cells, bacteria or fibroblasts (Bar-Ephraim et al., 2019). These co-cultures provide an emerging opportunity to study the contribution of non-epithelial components to human intestinal regeneration in a well-controlled and modular fashion, with the potential to resolve how the regenerative response is initiated or sensed. In the near future, we anticipate that our understanding of the various factors that promote stem cell activity in regenerating cells of the intestine will significantly improve, such that this fundamental knowledge can one day be clinically applied.

ACKNOWLEDGMENTS

We thank Lianne Kraaier for her contributions to the figures. We thank Konradin Müskens and Lotte Bruens for their critical comments on the manuscript. This work was supported by an ERC starting grant.

REFERENCES

1. Andersson-Rolf, A., Zilbauer, M., Koo, B.-K., and Clevers, H. (2017). Stem cells in repair of gastrointestinal epithelia. *Physiology* 32, 278–289.
2. Aoki, R., Shoshkes-Carmel, M., Gao, N., Shin, S., May, C.L., Golson, M.L., Zahm, A.M., Ray, M., Wiser, C.L., Wright, C.V.E., et al. (2016). Foxl1-Expressing Mesenchymal Cells Constitute the Intestinal Stem Cell Niche. *Cmgh* 2, 175–188.
3. Aparicio-Domingo, P., Romera-Hernandez, M., Karrich, J.J., Cornelissen, F., Papazian, N., Lindenbergh-Kortleve, D.J., Butler, J.A., Boon, L., Coles, M.C., Samsom, J.N., et al. (2015). Type 3 innate lymphoid cells maintain intestinal epithelial stem cells after tissue damage. *J. Exp. Med.* 212, 1783–1791.
4. Aragona, M., Panciera, T., Manfrin, A., Giullitti, S., Michielin, F., Elvassore, N., Dupont, S., and Piccolo, S. (2013). A mechanical checkpoint controls multicellular growth through YAP/TAZ regulation by actin-processing factors. *Cell* 154, 1047–1059.
5. Avetisyan, M., Wang, H., Schill, E.M., Bery, S., Grider, J.R., Hassell, J.A., Stappenbeck, T., and Heuckeroth, R.O. (2015). Hepatocyte growth factor and MET support mouse enteric nervous system development, the peristaltic response, and intestinal epithelial proliferation in response to injury. *J. Neurosci.* 35, 11543–11558.
6. Ayyaz, A., Kumar, S., Sangiorgi, B., Ghoshal, B., Gosio, J., Ouladan, S., Fink, M., Barutcu, S., Trcka, D., Shen, J., et al. (2019). Single-cell transcriptomes of the regenerating intestine reveal a revival stem cell. *Nature* 569, 121–125.
7. Azzolin, L., Zanconato, F., Bresolin, S., Forcato, M., Basso, G., Bicciato, S., Cordenonsi, M., and Piccolo, S. (2012). Role of TAZ as mediator of Wnt signaling. *Cell* 151, 1443–1456.
8. Bar-Ephraim, Y.E., Kretzschmar, K., and Clevers, H. (2019). Organoids in immunological research. *Nat. Rev. Immunol.*
9. Barker, N. (2014). Adult intestinal stem cells: critical drivers of epithelial homeostasis and regeneration. *Nat. Rev. Mol. Cell Biol.* 15, 19–33.
10. Barker, N., van Es, J.H., Kuipers, J., Kujala, P., van den Born, M., Cozijnsen, M., Haegerbarth, A., Korving, J., Begthel, H., Peters, P.J., et al. (2007). Identification of stem cells in small intestine and colon by marker gene *Lgr5*. *Nature* 449, 1003–1007.
11. Barriga, F.M., Montagni, E., Mana, M., Mendez-Lago, M., Hernando-Momblona, X., Sevillano, M., Guillaumet-Adkins, A., Rodriguez-Esteban, G., Buczaccki, S.J.A., Gut, M., et al. (2017). *Mex3a* marks a slowly dividing subpopulation of *Lgr5*⁺ intestinal stem cells. *Cell Stem Cell* 20, 801–816.
12. Barry, E.R., Morikawa, T., Butler, B.L., Shrestha, K., De La Rosa, R., Yan, K.S., Fuchs, C.S., Magness, S.T., Smits, R., Ogino, S., et al. (2013). Restriction of intestinal stem cell expansion and the regenerative response by YAP. *Nature* 493, 106–110.
13. Beumer, J., Puschhof, J., Bauzá-Martinez, J., Martínez-Silgado, A., Elmentaite, R., James, K., Ross, A., Hendriks, D., Artegiani, B., Busslinger, G., et al. (2020). High-resolution mRNA and secretome atlas of human enteroendocrine cells. *Cell*, <https://doi.org/10.1016/j.cell.2020.04.036>.
14. Beyaz, S., Mana, M.D., Roper, J., Kedrin, D., Saadatpour, A., Hong, S.-J., Bauer-Rowe, K.E., Xifaras, M.E., Akkad, A., Arias, E., et al. (2016). High-fat diet enhances stemness and tumorigenicity of intestinal progenitors. *Nature* 531, 53–58.
15. Bradford, E.M., Ryu, S.H., Singh, A.P., Lee, G., Goretsky, T., Sinh, P., Williams, D.B., Cloud, A.L., Gounaris, E., Patel, V., et al. (2017). Epithelial TNF receptor signaling promotes mucosal repair in inflammatory bowel disease. *J. Immunol.* 199, 1886–1897.

16. Brown, S.L., Riehl, T.E., Walker, M.R., Geske, M.J., Doherty, J.M., Stenson, W.F., and Stappenbeck, T.S. (2007). Myd88-dependent positioning of Ptg2-expressing stromal cells maintains colonic epithelial proliferation during injury. *J. Clin. Invest.* *117*, 258–269.
17. Bruens, L., Ellenbroek, S.I.J., van Rheenen, J., and Snippert, H.J. (2017). In vivo imaging reveals existence of crypt fission and fusion in adult mouse intestine. *Gastroenterology* *153*, 674–677.
18. Buczacki, S.J.A., Zecchini, H.I., Nicholson, A.M., Russell, R., Vermeulen, L., Kemp, R., and Winton, D.J. (2013). Intestinal label-retaining cells are secretory precursors expressing Lgr5. *Nature* *495*, 65–69.
19. Cai, J., Zhang, N., Zheng, Y., De Wilde, R.F., Maitra, A., and Pan, D. (2010). The Hippo signaling pathway restricts the oncogenic potential of an intestinal regeneration program. *Genes Dev.* *24*, 2383–2388.
20. Cairnie, A.B., and Millen, B.H. (1975). Fission of crypts in the small intestine of the irradiated mouse. *Cell Prolif.* *8*, 189–196.
21. Carulli, A.J., Keeley, T.M., Demitrack, E.S., Chung, J., Maillard, I., and Samuelson, L.C. (2015). Notch receptor regulation of intestinal stem cell homeostasis and crypt regeneration. *Dev. Biol.* *402*, 98–108.
22. Castellone, M.D., Teramoto, H., Williams, B.O., Druey, K.M., and Gutkind, J.S. (2005). Prostaglandin E2 promotes colon cancer cell growth through a Gs-axin-beta-catenin signaling axis. *Science* *310*, 1504–1510.
23. Castillo-Azofeifa, D., Fazio, E.N., Nattiv, R., Good, H.J., Wald, T., Pest, M.A., Sauvage, F.J., Klein, O.D., and Asfaha, S. (2019). Atoh1 + secretory progenitors possess renewal capacity independent of Lgr5 + cells during colonic regeneration. *EMBO J.* *38*, e99984.
24. Chaves-Pérez, A., Yilmaz, M., Perna, C., De La Rosa, S., and Djouder, N. (2019). URI is required to maintain intestinal architecture during ionizing radiation. *Science* *364*, 1165.
25. Cheng, C.W., Biton, M., Haber, A.L., Gunduz, N., Eng, G., Gaynor, L.T., Tripathi, S., Calibasi-Kocal, G., Rickelt, S., Butty, V.L., et al. (2019). Ketone body signaling mediates intestinal stem cell homeostasis and adaptation to diet. *Cell* *178*, 1115–1131.
26. Chivukula, R.R., Shi, G., Acharya, A., Mills, E.W., Zeitels, L.R., Anandam, J.L., Abdelnaby, A.A., Balch, G.C., Mansour, J.C., Yopp, A.C., et al. (2014). An essential mesenchymal function for miR-143/145 in intestinal epithelial regeneration. *Cell* *157*, 1104–1116.
27. Costantini, T.W., Bansal, V., Krzyzaniak, M., Putnam, J.G., Peterson, C.Y., Loomis, W.H., Wolf, P., Baird, A., Eliceiri, B.P., and Coimbra, R. (2010). Vagal nerve stimulation protects against burn-induced intestinal injury through activation of enteric glia cells. *AJP Gastrointest. Liver Physiol.* *299*, G1308–G1318.
28. Darwich, A.S., Aslam, U., Ashcroft, D.M., and Rostami-Hodjegan, A. (2014). Meta-analysis of the turnover of intestinal epithelia in preclinical animal species and humans. *Drug Metab. Dispos.* *42*, 2016–2022.
29. Davidson, L.A., Goldsby, J.S., Callaway, E.S., Shah, M.S., Barker, N., and Chapkin, R.S. (2012). Alteration of colonic stem cell gene signatures during the regenerative response to injury. *Biochim. Biophys. Acta* *1822*, 1600–1607.
30. Degirmenci, B., Valenta, T., Dimitrieva, S., Hausmann, G., and Basler, K. (2018). GLI1-expressing mesenchymal cells form the essential Wnt-secreting niche for colon stem cells. *Nature* *558*, 449–453.
31. Dekaney, C.M., Gulati, A.S., Garrison, A.P., Helmrath, M.A., and Henning, S.J. (2009). Regeneration of intestinal stem/progenitor cells following doxorubicin treatment of mice. *AJP Gastrointest. Liver Physiol.* *297*, G461–G470.

32. Discher, D.E., Janmey, P., and Wang, Y.-L. (2005). Tissue cells feel and respond to the stiffness of their substrate. *Science* *310*, 1139–1143.
33. Dupont, S., Morsut, L., Aragona, M., Enzo, E., Giulitti, S., Cordenonsi, M., Zanconato, F., Le Digabel, J., Forcato, M., Bicciato, S., et al. (2011). Role of YAP/TAZ in mechanotransduction. *Nature* *474*, 179–184.
34. Durand, A., Donahue, B., Peignon, G., Letourneur, F., Cagnard, N., Slomianny, C., Perret, C., Shroyer, N.F., and Romagnolo, B. (2012). Functional intestinal stem cells after Paneth cell ablation induced by the loss of transcription factor Math1 (Atoh1). *Proc. Natl. Acad. Sci. U.S.A.* *109*, 8965–8970.
35. Engler, A.J., Sen, S., Sweeney, H.L., and Discher, D.E. (2006). Matrix elasticity directs stem cell lineage specification. *Cell* *126*, 677–689.
36. van Es, J.H., Sato, T., van de Wetering, M., Lyubimova, A., Yee Nee, A.N., Gregorieff, A., Sasaki, N., Zeinstra, L., van den Born, M., Korving, J., et al. (2012). Dll1+ secretory progenitor cells revert to stem cells upon crypt damage. *Nat. Cell Biol.* *14*, 1099–1104.
37. van Es, J.H., Wiebrands, K., López-Iglesias, C., van de Wetering, M., Zeinstra, L., van den Born, M., Korving, J., Sasaki, N., Peters, P.J., van Oudenaarden, A., et al. (2019). Enteroendocrine and tuft cells support Lgr5 stem cells on Paneth cell depletion. *Proc. Natl. Acad. Sci. U. S. A.* *116*, 26599–26605.
38. Farin, H.F., van Es, J.H., and Clevers, H. (2012). Redundant sources of Wnt regulate intestinal stem cells and promote formation of paneth cells. *Gastroenterology* *143*, 1518–1529.
39. Gehart, H., and Clevers, H. (2019). Tales from the crypt: new insights into intestinal stem cells. *Nat. Rev. Gastroenterol. Hepatol.* *16*, 19–34.
40. Gjorevski, N., Sachs, N., Manfrin, A., Giger, S., Bragina, M.E., Ordóñez-Morán, P., Clevers, H., and Lutolf, M.P. (2016). Designer matrices for intestinal stem cell and organoid culture. *Nature* *539*, 560–564.
41. Gregorieff, A., Liu, Y., Inanlou, M.R., Khomchuk, Y., and Wrana, J.L. (2015). Yap-dependent reprogramming of Lgr5+ stem cells drives intestinal regeneration and cancer. *Nature* *526*, 715–718.
42. Greicius, G., Kabiri, Z., Sigmundsson, K., Liang, C., Bunte, R., Singh, M.K., and Virshup, D.M. (2018). PDGFRα+ pericryptal stromal cells are the critical source of Wnts and RSPO3 for murine intestinal stem cells in vivo. *Proc. Natl. Acad. Sci. U. S. A.* *115*, E3173–E3181.
43. Hanash, A.M., Dudakov, J.A., Hua, G., O'Connor, M.H., Young, L.F., Singer, N. V., West, M.L., Jenq, R.R., Holland, A.M., Kappel, L.W., et al. (2012). Interleukin-22 protects intestinal stem cells from immune-mediated tissue damage and regulates sensitivity to graft versus host disease. *Immunity* *37*, 339–350.
44. Harnack, C., Berger, H., Antanaviciute, A., Vidal, R., Sauer, S., Simmons, A., Meyer, T.F., and Sigal, M. (2019). R-spondin 3 promotes stem cell recovery and epithelial regeneration in the colon. *Nat. Commun.* *10*, 4368.
45. Horiguchi, H., Endo, M., Kawane, K., Kadomatsu, T., Terada, K., Morinaga, J., Araki, K., Miyata, K., and Oike, Y. (2017). ANGPTL2 expression in the intestinal stem cell niche controls epithelial regeneration and homeostasis. *EMBO J.* *36*, 409–424.
46. Igarashi, M., and Guarente, L. (2016). mTORC1 and SIRT1 cooperate to foster expansion of gut adult stem cells during calorie restriction. *Cell* *166*, 536–450.
47. Ijiri, K., and Potten, C.S. (1987). Further studies on the response of intestinal crypt cells of different hierarchical status to eighteen different cytotoxic agents. *Br. J. Cancer* *55*, 113–123.

48. Ishibashi, F., Shimizu, H., Nakata, T., Fujii, S., Suzuki, K., Kawamoto, A., Anzai, S., Kuno, R., Nagata, S., Ito, G., et al. (2018). Contribution of ATOH1+ cells to the homeostasis, repair, and tumorigenesis of the colonic epithelium. *Stem Cell Reports* *10*, 27–42.
49. Jadhav, U., Saxena, M., O'Neill, N.K., Saadatpour, A., Yuan, G.C., Herbert, Z., Murata, K., and Shivdasani, R.A. (2017). Dynamic reorganization of chromatin accessibility signatures during dedifferentiation of secretory precursors into Lgr5+ intestinal stem cells. *Cell Stem Cell* *21*, 65–77.
50. Johansson, J., Naszai, M., Hodder, M.C., Pickering, K.A., Miller, B.W., Ridgway, R.A., Yu, Y., Peschard, P., Brachmann, S., Campbell, A.D., et al. (2019). RAL GTPases drive intestinal stem cell function and regeneration through internalization of WNT signalosomes. *Cell Stem Cell* *24*, 592–607.
51. Jones, J.C., Brindley, C.D., Elder, N.H., Myers, M.G., Rajala, M.W., Dekaney, C.M., McNamee, E.N., Frey, M.R., Shroyer, N.F., and Dempsey, P.J. (2019). Cellular plasticity of Defa4Cre-expressing Paneth cells in response to notch activation and intestinal injury. *Cell. Mol. Gastroenterol. Hepatol.* *7*, 533–554.
52. Kaaij, L.T.J., van de Wetering, M., Fang, F., Decato, B., Molaro, A., van de Werken, H.J.G., van Es, J.H., Schuijers, J., de Wit, E., de Laat, W., et al. (2013). DNA methylation dynamics during intestinal stem cell differentiation reveals enhancers driving gene expression in the villus. *Genome Biol.* *14*, R50.
53. Kabiri, Z., Greicius, G., Madan, B., Biechele, S., Zhong, Z., Zaribafzadeh, H., Edison, Aliyev, J., Wu, Y., Bunte, R., et al. (2014). Stroma provides an intestinal stem cell niche in the absence of epithelial Wnts. *Development* *141*, 2206–2215.
54. Kaiko, G.E., Ryu, S.H., Koues, O.I., Collins, P.L., Solnica-Krezel, L., Pearce, E.J., Pearce, E.L., Oltz, E.M., and Stappenbeck, T.S. (2016). The colonic crypt protects stem cells from microbiota-derived metabolites. *Cell* *165*, 1708–1720.
55. Kim, H.B., Kim, M., Park, Y.S., Park, I., Kim, T., Yang, S.Y., Cho, C.J., Hwang, D.H., Jung, J.H., Markowitz, S.D., et al. (2017). Prostaglandin E2 activates YAP and a positive-signaling loop to promote colon regeneration after colitis but also carcinogenesis in mice. *Gastroenterology* *152*, 616–630.
56. Kim, K.A., Kakitani, M., Zhao, J., Oshima, T., Tang, T., Binnerts, M., Liu, Y., Boyle, B., Park, E., Emtage, P., et al. (2005). Mitogenic influence of human R-spondin1 on the intestinal epithelium. *Science* *309*, 1256–1259.
57. Kim, T.-H., Escudero, S., and Shivdasani, R.A. (2012). Intact function of Lgr5 receptor-expressing intestinal stem cells in the absence of Paneth cells. *Proc. Natl. Acad. Sci. U.S.A.* *109*, 3932–3937.
58. Kim, T.H., Li, F., Ferreiro-Neira, I., Ho, L.L., Luyten, A., Nalapareddy, K., Long, H., Verzi, M., and Shivdasani, R.A. (2014). Broadly permissive intestinal chromatin underlies lateral inhibition and cell plasticity. *Nature* *506*, 511–515.
59. Koch, U., Lehal, R., and Radtke, F. (2013). Stem cells living with a Notch. *Dev.* *140*, 689–704.
60. Kosinski, C., Li, V.S.W., Chan, A.S.Y., Zhang, J., Ho, C., Tsui, W.Y., Chan, T.L., Mifflin, R.C., Powell, D.W., Yuen, S.T., et al. (2007). Gene expression patterns of human colon tops and basal crypts and BMP antagonists as intestinal stem cell niche factors. *Proc. Natl. Acad. Sci. U.S.A.* *104*, 15418–15423.
61. Kretzschmar, K., and Watt, F.M. (2012). Lineage tracing. *Cell* *148*, 33–45.
62. van Landeghem, L., Chevalier, J., Mahe, M.M., Wedel, T., Urvil, P., Derkinderen, P., Savidge, T., and Neunlist, M. (2011). Enteric glia promote intestinal mucosal healing via activation of focal adhesion kinase and release of proEGF. *AJP Gastrointest. Liver Physiol.* *300*, G976–G987.

63. de Lau, W., Barker, N., Low, T.Y., Koo, B.-K., Li, V.S.W., Teunissen, H., Kujala, P., Haegerbarth, A., Peters, P.J., van de Wetering, M., et al. (2011). Lgr5 homologues associate with Wnt receptors and mediate R-spondin signalling. *Nature* 476, 293–297.
64. Levy, A., Stedman, A., Deutsch, E., Donnadieu, F., Virgin, H.W., Sansonetti, P.J., and Nigro, G. (2020). Innate immune receptor NOD2 mediates LGR5+ intestinal stem cell protection against ROS cytotoxicity via mitophagy stimulation. *Proc. Natl. Acad. Sci. U. S. A.* 117, 1994–2003.
65. Lindemans, C.A., Calafiore, M., Mertelsmann, A.M., O'Connor, M.H., Dudakov, J.A., Jenq, R.R., Velardi, E., Young, L.F., Smith, O.M., Lawrence, G., et al. (2015). Interleukin-22 promotes intestinal-stem-cell-mediated epithelial regeneration. *Nature* 528, 560–564.
66. De Lisle, R.C., and Borowitz, D. (2013). The cystic fibrosis intestine. *Cold Spring Harb. Perspect. Med.* 3, 1–17.
67. Lopez-Garcia, C., Klein, A.M., Simons, B.D., and Winton, D.J. (2010). Intestinal stem cell replacement follows a pattern of neutral drift. *Science* 330, 822–825.
68. Manieri, N.A., Drylewicz, M.R., Miyoshi, H., and Stappenbeck, T.S. (2012). Igf2bp1 is required for full induction of Ptg2 mRNA in colonic mesenchymal stem cells in mice. *Gastroenterology* 143, 110–121.
69. McCarthy, N., Manieri, E., Storm, E.E., Saadatpour, A., Luoma, A.M., Kapoor, V.N., Madha, S., Gaynor, L.T., Cox, C., Keerthivasan, S., et al. (2020). Distinct mesenchymal cell populations generate the essential intestinal BMP signaling gradient. *Cell Stem Cell* 26, 391–402.
70. Metcalfe, C., Kljavin, N.M., Ybarra, R., and De Sauvage, F.J. (2014). Lgr5+stem cells are indispensable for radiation-induced intestinal regeneration. *Cell Stem Cell* 14, 149–159.
71. Miyoshi, H., Ajima, R., Luo, C.T., Yamaguchi, T.P., and Stappenbeck, T.S. (2012). Wnt5a potentiates TGF- β signaling to promote colonic crypt regeneration after tissue injury. *Science* 338, 108–113.
72. Miyoshi, H., VanDussen, K.L., Malvin, N.P., Ryu, S.H., Wang, Y., Sonnek, N.M., Lai, C., and Stappenbeck, T.S. (2017). Prostaglandin E2 promotes intestinal repair through an adaptive cellular response of the epithelium. *EMBO J.* 36, 5–24.
73. von Moltke, J., Ji, M., Liang, H.E., and Locksley, R.M. (2016). Tuft-cell-derived IL-25 regulates an intestinal ILC2-epithelial response circuit. *Nature* 529, 221–225.
74. Montgomery, R.K., Carlone, D.L., Richmond, C.A., Farilla, L., Kranendonk, M.E.G., Henderson, D.E., Baffour-Awuah, N.Y., Ambruzs, D.M., Fogli, L.K., Algra, S., et al. (2011). Mouse telomerase reverse transcriptase (mTert) expression marks slowly cycling intestinal stem cells. *Proc. Natl. Acad. Sci. U. S. A.* 108, 179–184.
75. Muñoz, J., Stange, D.E., Schepers, A.G., van de Wetering, M., Koo, B.K., Itzkovitz, S., Volckmann, R., Kung, K.S., Koster, J., Radulescu, S., et al. (2012). The Lgr5 intestinal stem cell signature: Robust expression of proposed quiescent '+4' cell markers. *EMBO J.* 31, 3079–3091.
76. Murata, K., Jadhav, U., Madha, S., van Es, J., Dean, J., Cavazza, A., Wucherpennig, K., Michor, F., Clevers, H., and Shivdasani, R.A. (2020). Ascl2-dependent cell dedifferentiation drives regeneration of ablated intestinal stem cells. *Cell Stem Cell* 26, 377–390.
77. Naito, Y., Takagi, T., Handa, O., Ishikawa, T., Nakagawa, S., Yamaguchi, T., Yoshida, N., Minami, M., Kita, M., Imanishi, J., et al. (2003). Enhanced intestinal inflammation induced by dextran sulfate sodium in tumor necrosis factor-alpha deficient mice. *J. Gastroenterol. Hepatol.* 18, 560–569.
78. Neal, M.D., Sodhi, C.P., Jia, H., Dyer, M., Egan, C.E., Yazji, I., Good, M., Afrazi, A., Marino, R., Slagle, D., et al. (2012). Toll-like receptor 4 is expressed on intestinal stem cells and regulates their proliferation and apoptosis via the p53 up-regulated modulator of apoptosis. *J. Biol. Chem.* 287, 37296–37308.

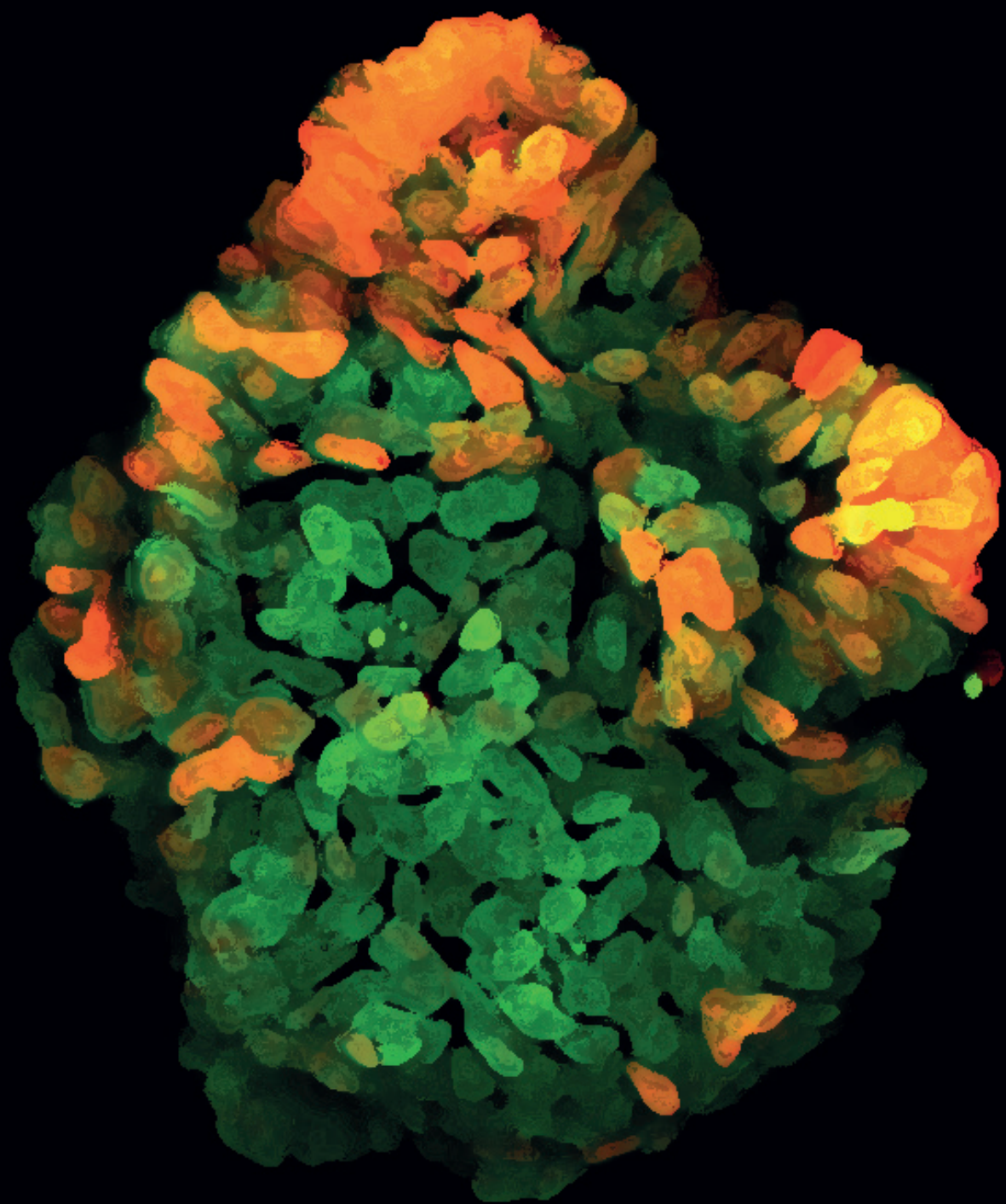
79. Nigro, G., Rossi, R., Commere, P.H., Jay, P., and Sansonetti, P.J. (2014). The cytosolic bacterial peptidoglycan sensor Nod2 affords stem cell protection and links microbes to gut epithelial regeneration. *Cell Host Microbe* *15*, 792–798.
80. Nusse, Y.M., Savage, A.K., Marangoni, P., Rosendahl-Huber, A.K.M., Landman, T.A., De Sauvage, F.J., Locksley, R.M., and Klein, O.D. (2018). Parasitic helminths induce fetal-like reversion in the intestinal stem cell niche. *Nature* *559*, 109–113.
81. Okamoto, R., Tsuchiya, K., Nemoto, Y., Akiyama, J., Nakamura, T., Kanai, T., and Watanabe, M. (2009). Requirement of Notch activation during regeneration of the intestinal epithelia. *AJP Gastrointest. Liver Physiol.* *296*, G23–G35.
82. Okayasu, I., Hatakeyama, S., Yamada, M., Ohkusa, T., Inagaki, Y., and Nakaya, R. (1990). A novel method in the induction of reliable experimental acute and chronic ulcerative colitis in mice. *Gastroenterology* *98*, 694–702.
83. Oost, K.C., van Voorthuisen, L., Fumagalli, A., Lindeboom, R.G.H., Sprangers, J., Omerzu, M., Rodriguez-Colman, M.J., Heinz, M.C., Verlaan-Klink, I., Maurice, M.M., et al. (2018). Specific labeling of stem cell activity in human colorectal organoids using an ASCL2-responsive minigene. *Cell Rep.* *22*, 1600–1614.
84. Papapietro, O., Teatero, S., Thanabalasuriar, A., Yuki, K.E., Diez, E., Zhu, L., Kang, E., Dhillon, S., Muise, A.M., Durocher, Y., et al. (2013). R-Spondin 2 signalling mediates susceptibility to fatal infectious diarrhoea. *Nat. Commun.* *4*, 1–9.
85. Pentimikko, N., Iqbal, S., Mana, M., Andersson, S., Cognetta, A.B., Suci, R.M., Roper, J., Luopajarvi, K., Markelin, E., Gopalakrishnan, S., et al. (2019). Notum produced by Paneth cells attenuates regeneration of aged intestinal epithelium. *Nature* *571*, 398–402.
86. Piccolo, S., Dupont, S., and Cordenonsi, M. (2014). The biology of YAP/TAZ: Hippo signaling and beyond. *Physiol. Rev.* *94*, 1287–1312.
87. Potten, C.S., and Loeffler, M. (1990). Stem cells: attributes, cycles, spirals, pitfalls and uncertainties. Lessons for and from the crypt. *Development* *110*, 1001–1020.
88. Powell, A.E., Wang, Y., Li, Y., Poulin, E.J., Means, A.L., Washington, M.K., Higginbotham, J.N., Juchheim, A., Prasad, N., Levy, S.E., et al. (2012). The pan-ErbB negative regulator Irig1 is an intestinal stem cell marker that functions as a tumor suppressor. *Cell* *149*, 146–158.
89. Powell, D.W., Pinchuk, I.V., Saada, J.I., Chen, X., and Mifflin, R.C. (2011). Mesenchymal cells of the intestinal lamina propria. *Annu. Rev. Physiol.* *73*, 213–237.
90. Pull, S.L., Doherty, J.M., Mills, J.C., Gordon, J.I., and Stappenbeck, T.S. (2005). Activated macrophages are an adaptive element of the colonic epithelial progenitor niche necessary for regenerative responses to injury. *Proc. Natl. Acad. Sci.* *102*, 99–104.
91. Quiros, M., Nishio, H., Neumann, P.A., Siuda, D., Brazil, J.C., Azcutia, V., Hilgarth, R., O’Leary, M.N., Garcia-Hernandez, V., Leoni, G., et al. (2017). Macrophage-derived IL-10 mediates mucosal repair by epithelial WISP-1 signaling. *J. Clin. Invest.* *127*, 3510–3520.
92. Rakoff-Nahoum, S., Paglino, J., Eslami-Varzaneh, F., Edberg, S., and Medzhitov, R. (2004). Recognition of commensal microflora by toll-like receptors is required for intestinal homeostasis. *Cell* *118*, 229–241.
93. Rimoldi, M., Chieppa, M., Salucci, V., Avogadri, F., Sonzogni, A., Sampietro, G.M., Nespoli, A., Viale, G., Allavena, P., and Rescigno, M. (2005). Intestinal immune homeostasis is regulated by the crosstalk between epithelial cells and dendritic cells. *Nat. Immunol.* *6*, 507–514.
94. Ritsma, L., Ellenbroek, S.I.J., Zomer, A., Snippert, H.J., De Sauvage, F.J., Simons, B.D., Clevers, H., and van Rheenen, J. (2014). Intestinal crypt homeostasis revealed at single-stem-cell level by in vivo live imaging. *Nature* *507*, 362–365.

95. Rock, K.L., Latz, E., Ontiveros, F., and Kono, H. (2010). The sterile inflammatory response. *Annu. Rev. Immunol.* *28*, 321–342.
96. Rodríguez-Colman, M.J., Schewe, M., Meerlo, M., Stigter, E., Gerrits, J., Pras-Raves, M., Sacchetti, A., Hornsveld, M., Oost, K.C., Snippert, H.J., et al. (2017). Interplay between metabolic identities in the intestinal crypt supports stem cell function. *Nature* *543*, 424–427.
97. Romera-Hernández, M., Aparicio-Domingo, P., Papazian, N., Karrich, J.J., Cornelissen, F., Hoogenboezem, R.M., Samsom, J.N., and Cupedo, T. (2020). Yap1-driven intestinal repair is controlled by group 3 innate lymphoid cells. *Cell Rep.* *30*, 37–45.
98. Roulis, M., Kaklamanos, A., Scherthanner, M., Bielecki, P., Zhao, J., Kaffe, E., Frommelt, L.-S., Qu, R., Knapp, M.S., Henriques, A., et al. (2020). Paracrine orchestration of intestinal tumorigenesis by a mesenchymal niche. *Nature* <https://doi.org/10.1038/s41586-020-2166-3>.
99. Saenz, S.A., Siracusa, M.C., Perrigoue, J.G., Spencer, S.P., Urban, J.F., Tocker, J.E., Budelsky, A.L., Kleinschek, M.A., Kastelein, R.A., Kambayashi, T., et al. (2010). IL25 elicits a multipotent progenitor cell population that promotes TH2 cytokine responses. *Nature* *464*, 1362–1366.
100. Saha, S., Aranda, E., Hayakawa, Y., Bhanja, P., Atay, S., Brodin, N.P., Li, J., Asfaha, S., Liu, L., Taylor, Y., et al. (2016). Macrophage-derived extracellular vesicle-packaged WNTs rescue intestinal stem cells and enhance survival after radiation injury. *Nat. Commun.* *7*, 1–16.
101. Sangiorgi, E., and Capecchi, M.R. (2008). Bmi1 is expressed in vivo in intestinal stem cells. *Nat. Genet.* *40*, 915–920.
102. Sarbassov, D.D., Ali, S.M., and Sabatini, D.M. (2005). Growing roles for the mTOR pathway. *Curr. Opin. Cell Biol.* *17*, 596–603.
103. Sasaki, N., Sachs, N., Wiebrands, K., Ellenbroek, S.I.J., Fumagalli, A., Lyubimova, A., Begthel, H., van den Born, M., van Es, J.H., Karthaus, W.R., et al. (2016). Reg4+ deep crypt secretory cells function as epithelial niche for Lgr5+ stem cells in colon. *Proc. Natl. Acad. Sci.* *113*, E5399–E5407.
104. Sato, T., Vries, R.G., Snippert, H.J., van de Wetering, M., Barker, N., Stange, D.E., van Es, J.H., Abo, A., Kujala, P., Peters, P.J., et al. (2009). Single Lgr5 stem cells build crypt-villus structures in vitro without a mesenchymal niche. *Nature* *459*, 262–265.
105. Sato, T., van Es, J.H., Snippert, H.J., Stange, D.E., Vries, R.G., van den Born, M., Barker, N., Shroyer, N.F., van de Wetering, M., and Clevers, H. (2011a). Paneth cells constitute the niche for Lgr5 stem cells in intestinal crypts. *Nature* *469*, 415–418.
106. Sato, T., Stange, D.E., Ferrante, M., Vries, R.G.J., van Es, J.H., van den Brink, S., van Houdt, W.J., Pronk, A., van Gorp, J., Siersema, P.D., et al. (2011b). Long-term expansion of epithelial organoids from human colon, adenoma, adenocarcinoma, and Barrett's epithelium. *Gastroenterology* *141*, 1762–1772.
107. Satoh-Takayama, N., Vosshenrich, C.A.J., Lesjean-Pottier, S., Sawa, S., Lochner, M., Rattis, F., Mention, J.J., Thiam, K., Cerf-Bensussan, N., Mandelboim, O., et al. (2008). Microbial flora drives interleukin 22 production in intestinal NKp46+ cells that provide innate mucosal immune defense. *Immunity* *29*, 958–970.
108. Schmitt, M., Schewe, M., Sacchetti, A., Feijtel, D., van de Geer, W.S., Teeuwssen, M., Sleddens, H.F., Joosten, R., van Royen, M.E., van de Werken, H.J.G., et al. (2018). Paneth cells respond to inflammation and contribute to tissue regeneration by acquiring stem-like features through SCF/c-Kit signaling. *Cell Rep.* *24*, 2312–2328.
109. Schneider, S., Wright, C.M., and Heuckeroth, R.O. (2019). Unexpected roles for the second brain: Enteric nervous system as master regulator of bowel function. *Annu. Rev. Physiol.* *81*, 235–259.
110. Seno, H., Miyoshi, H., Brown, S.L., Geske, M.J., Colonna, M., and Stappenbeck, T.S. (2009). Efficient colonic mucosal wound repair requires Trem2 signaling. *Proc. Natl. Acad. Sci.* *106*, 256–261.

111. Serra, D., Mayr, U., Boni, A., Lukonin, I., Rempfler, M., Challet Meylan, L., Stadler, M.B., Strnad, P., Papsaikas, P., Vischi, D., et al. (2019). Self-organization and symmetry breaking in intestinal organoid development. *Nature* 569, 66–72.
112. Sheaffer, K.L., Kim, R., Aoki, R., Elliott, E.N., Schug, J., Burger, L., Schübeler, D., and Kaestner, K.H. (2014). DNA methylation is required for the control of stem cell differentiation in the small intestine. *Genes Dev.* 28, 652–664.
113. Shoshkes-Carmel, M., Wang, Y.J., Wangenstein, K.J., Tóth, B., Kondo, A., Massassa, E.E., Itzkovitz, S., and Kaestner, K.H. (2018). Subepithelial telocytes are an important source of Wnts that supports intestinal crypts. *Nature* 557, 242–246.
114. Smyth, R.L., Croft, N.M., O’Hea, U., Marshall, T.G., and Ferguson, A. (2000). Intestinal inflammation in cystic fibrosis. *Arch. Dis. Child.* 82, 394–399.
115. Snippert, H.J., van der Flier, L.G., Sato, T., van Es, J.H., van den Born, M., Kroon-Veenboer, C., Barker, N., Klein, A.M., van Rheenen, J., Simons, B.D., et al. (2010). Intestinal crypt homeostasis results from neutral competition between symmetrically dividing Lgr5 stem cells. *Cell* 143, 134–144.
116. Sonnenberg, G.F., Monticelli, L.A., Elloslo, M.M., Fouser, L.A., and Artis, D. (2011). CD4⁺ lymphoid tissue-inducer cells promote innate immunity in the gut. *Immunity* 34, 122–134.
117. de Souza, H.S.P., and Fiocchi, C. (2016). Immunopathogenesis of IBD: Current state of the art. *Nat. Rev. Gastroenterol. Hepatol.* 13, 13–27.
118. Spits, H., Artis, D., Colonna, M., Diefenbach, A., Di Santo, J.P., Eberl, G., Koyasu, S., Locksley, R.M., McKenzie, A.N.J., Mebius, R.E., et al. (2013). Innate lymphoid cells—a proposal for uniform nomenclature. *Nat. Rev. Immunol.* 13, 145–149.
119. Stzepourginski, I., Nigro, G., Jacob, J.-M., Dulauroy, S., Sansonetti, P.J., Eberl, G., and Peduto, L. (2017). CD34⁺ mesenchymal cells are a major component of the intestinal stem cells niche at homeostasis and after injury. *Proc. Natl. Acad. Sci.* 114, E506–E513.
120. Sugimoto, S., Ohta, Y., Fujii, M., Matano, M., Shimokawa, M., Nanki, K., Date, S., Nishikori, S., Nakazato, Y., Nakamura, T., et al. (2018). Reconstruction of the Human Colon Epithelium In Vivo. *Cell Stem Cell* 22, 171–176.
121. Tahara, Y., Ido, A., Yamamoto, S., Miyata, Y., Uto, H., Hori, T., Hayashi, K., and Tsubouchi, H. (2003). Hepatocyte growth factor facilitates colonic mucosal repair in experimental ulcerative colitis in rats. *J. Pharmacol. Exp. Ther.* 307, 146–151.
122. Takashima, S., Martin, M.L., Jansen, S.A., Fu, Y., Bos, J., Chandra, D., O’Connor, M.H., Mertelsmann, A.M., Vinci, P., Kuttiyara, J., et al. (2019). T cell-derived interferon- γ programs stem cell death in immune-mediated intestinal damage. *Sci. Immunol.* 4, 8556.
123. Takeda, N., Jain, R., LeBoeuf, M.R., Wang, Q., Lu, M.M., and Epstein, J.A. (2011). Interconversion between intestinal stem cell populations in distinct niches. *Science* 334, 1420–1424.
124. Talbot, J., Hahn, P., Kroehling, L., Nguyen, H., Li, D., and Littman, D.R. (2020). Feeding-dependent VIP neuron–ILC3 circuit regulates the intestinal barrier. *Nature* 579, 575–580.
125. Taniguchi, K., Wu, L.W., Grivnenikov, S.I., De Jong, P.R., Lian, I., Yu, F.X., Wang, K., Ho, S.B., Boland, B.S., Chang, J.T., et al. (2015). A gp130–Src–YAP module links inflammation to epithelial regeneration. *Nature* 519, 57–62.
126. Tetteh, P.W., Basak, O., Farin, H.F., Wiebrands, K., Kretschmar, K., Begthel, H., van den Born, M., Korving, J., de Sauvage, F., van Es, J.H., et al. (2016). Replacement of lost Lgr5-positive stem cells through plasticity of their enterocyte-lineage daughters. *Cell Stem Cell* 18, 203–213.
127. Tian, H., Biehs, B., Warming, S., Leong, K.G., Rangell, L., Klein, O.D., and de Sauvage, F.J. (2011). A reserve stem cell population in small intestine renders Lgr5-positive cells dispensable. *Nature* 478, 255–259.

128. Tomic, G., Morrissey, E., Kozar, S., Ben-Moshe, S., Hoyle, A., Azzarelli, R., Kemp, R., Chilamakuri, C.S.R., Itzkovitz, S., Philpott, A., et al. (2018). Phospho-regulation of ATOH1 is required for plasticity of secretory progenitors and tissue regeneration. *Cell Stem Cell* *23*, 436–443.
129. Trappmann, B., Gautrot, J.E., Connelly, J.T., Strange, D.G.T., Li, Y., Oyen, M.L., Cohen Stuart, M.A., Boehm, H., Li, B., Vogel, V., et al. (2012). Extracellular-matrix tethering regulates stem-cell fate. *Nat. Mater.* *11*, 642–649.
130. Valenta, T., Degirmenci, B., Moor, A.E., Herr, P., Zimmerli, D., Moor, M.B., Hausmann, G., Cantù, C., Aguet, M., and Basler, K. (2016). Wnt ligands secreted by subepithelial mesenchymal cells are essential for the survival of intestinal stem cells and gut homeostasis. *Cell Rep.* *15*, 911–918.
131. Vermeulen, L., and Snippert, H.J. (2014). Stem cell dynamics in homeostasis and cancer of the intestine. *Nat. Rev. Cancer* *14*, 468–480.
132. Vonarbourg, C., Mortha, A., Bui, V.L., Hernandez, P.P., Kiss, E.A., Hoyler, T., Flach, M., Bengsch, B., Thimme, R., Hölscher, C., et al. (2010). Regulated expression of nuclear receptor ROR γ t confers distinct functional fates to NK cell receptor-expressing ROR γ t⁺ innate lymphocytes. *Immunity* *33*, 736–751.
133. Watanabe, M., Ueno, Y., Yajima, T., Iwao, Y., Tsuchiya, M., Ishikawa, H., Aiso, S., Hibi, T., and Ishii, H. (1995). Interleukin 7 is produced by human intestinal epithelial cells and regulates the proliferation of intestinal mucosal lymphocytes. *J. Clin. Invest.* *95*, 2945–2953.
134. Westphalen, C.B., Asfaha, S., Hayakawa, Y., Takemoto, Y., Lukin, D.J., Nuber, A.H., Brandtner, A., Setlik, W., Remotti, H., Muley, A., et al. (2014). Long-lived intestinal tuft cells serve as colon cancer-initiating cells. *J. Clin. Invest.* *124*, 1283–1295.
135. Wong, V.W.Y., Stange, D.E., Page, M.E., Buczacki, S., Wabik, A., Itami, S., van de Wetering, M., Poulosom, R., Wright, N.A., Trotter, M.W.B., et al. (2012). Lrig1 controls intestinal stem-cell homeostasis by negative regulation of ErbB signalling. *Nat. Cell Biol.* *14*, 401–408.
136. Yan, F., Cao, H., Cover, T.L., Whitehead, R., Washington, M.K., and Polk, D.B. (2007). Soluble proteins produced by probiotic bacteria regulate intestinal epithelial cell survival and growth. *Gastroenterology* *132*, 562–575.
137. Yan, K.S., Gevaert, O., Zheng, G.X.Y., Anchang, B., Probert, C.S., Larkin, K.A., Davies, P.S., Cheng, Z., Kaddis, J.S., Han, A., et al. (2017). Intestinal enteroendocrine lineage cells possess homeostatic and injury-inducible stem cell activity. *Cell Stem Cell* *21*, 78–90.
138. Yilmaz, Ö.H., Katajisto, P., Lamming, D.W., Gültekin, Y., Bauer-Rowe, K.E., Sengupta, S., Birsoy, K., Dursun, A., Yilmaz, V.O., Selig, M., et al. (2012). mTORC1 in the Paneth cell niche couples intestinal stem-cell function to calorie intake. *Nature* *486*, 490–495.
139. Yousefi, M., Li, N., Nakauka-Ddamba, A., Wang, S., Davidow, K., Schoenberger, J., Yu, Z., Jensen, S.T., Kharas, M.G., and Lengner, C.J. (2016). Msi RNA-binding proteins control reserve intestinal stem cell quiescence. *J. Cell Biol.* *215*, 401–413.
140. Yousefi, M., Nakauka-Ddamba, A., Berry, C.T., Li, N., Schoenberger, J., Simeonov, K.P., Cedeno, R.J., Yu, Z., and Lengner, C.J. (2018). Calorie restriction governs intestinal epithelial regeneration through cell-autonomous regulation of mTORC1 in reserve stem cells. *Stem Cell Reports* *10*, 703–711.
141. Yu, D.H., Gadkari, M., Zhou, Q., Yu, S., Gao, N., Guan, Y., Schady, D., Roshan, T.N., Chen, M.H., Laritsky, E., et al. (2015). Postnatal epigenetic regulation of intestinal stem cells requires DNA methylation and is guided by the microbiome. *Genome Biol.* *16*, 1–16.
142. Yu, F.X., Zhao, B., Panupinthu, N., Jewell, J.L., Lian, I., Wang, L.H., Zhao, J., Yuan, H., Tumaneng, K., Li, H., et al. (2012). Regulation of the Hippo-YAP pathway by G-protein-coupled receptor signaling. *Cell* *150*, 780–791.

143. Yu, S., Tong, K., Zhao, Y., Balasubramanian, I., Yap, G.S., Ferraris, R.P., Bonder, E.M., Verzi, M.P., and Gao, N. (2018). Paneth cell multipotency induced by Notch activation following injury. *Cell Stem Cell* 23, 1–14.
144. Yui, S., Azzolin, L., Maimets, M., Pedersen, M.T., Fordham, R.P., Hansen, S.L., Larsen, H.L., Guiu, J., Alves, M.R.P., Rundsten, C.F., et al. (2018). YAP/TAZ-dependent reprogramming of colonic epithelium links ECM remodeling to tissue regeneration. *Cell Stem Cell* 22, 35–49.
145. Zhao, J., de Vera, J., Narushima, S., Beck, E.X., Palencia, S., Shinkawa, P., Kim, K., Liu, Y., Levy, M.D., Berg, D.J., et al. (2007). R-spondin1, a novel intestinotrophic mitogen, ameliorates experimental colitis in mice. *Gastroenterology* 132, 1331–1343.
146. Zhou, W.J., Geng, Z.H., Spence, J.R., and Geng, J.G. (2013). Induction of intestinal stem cells by R-spondin 1 and Slit2 augments chemoradioprotection. *Nature* 501, 107–111.



CHAPTER

2

Introducing the Stem Cell ASCL2 Reporter STAR into Intestinal Organoids

Maria C. Heinz^{1,2,*}, Koen C. Oost^{1,2,*}, Hugo J. G. Snippert^{1,2,#}.

¹ Molecular Cancer Research, Center for Molecular
Medicine, University Medical Center Utrecht, University
Utrecht, Utrecht, the Netherlands.

² Oncode Institute, Utrecht, the Netherlands.

*: Equal contribution.

#: Lead Contact.

STAR Protocols, doi: 10.1016/j.xpro.2020.100126.

SUMMARY

Patient-derived organoids maintain functional and phenotypic characteristics of the original tissue such as cell type diversity. Here, we provide protocols on how to label intestinal (cancer) stem cells by integrating the stem cell ASCL2 reporter (STAR) into the human and mouse genome via two different strategies: i) lentiviral transduction or ii) a transposon-based system. Organoid technology, in combination with the user-friendly nature of STAR, will facilitate basic research in human and mouse adult stem cell biology.

For complete details on the use and execution of this protocol, please see Oost *et al.* (Oost et al., 2018).

BEFORE YOU BEGIN

A schematic workflow of the protocol options is provided in Figure 1.

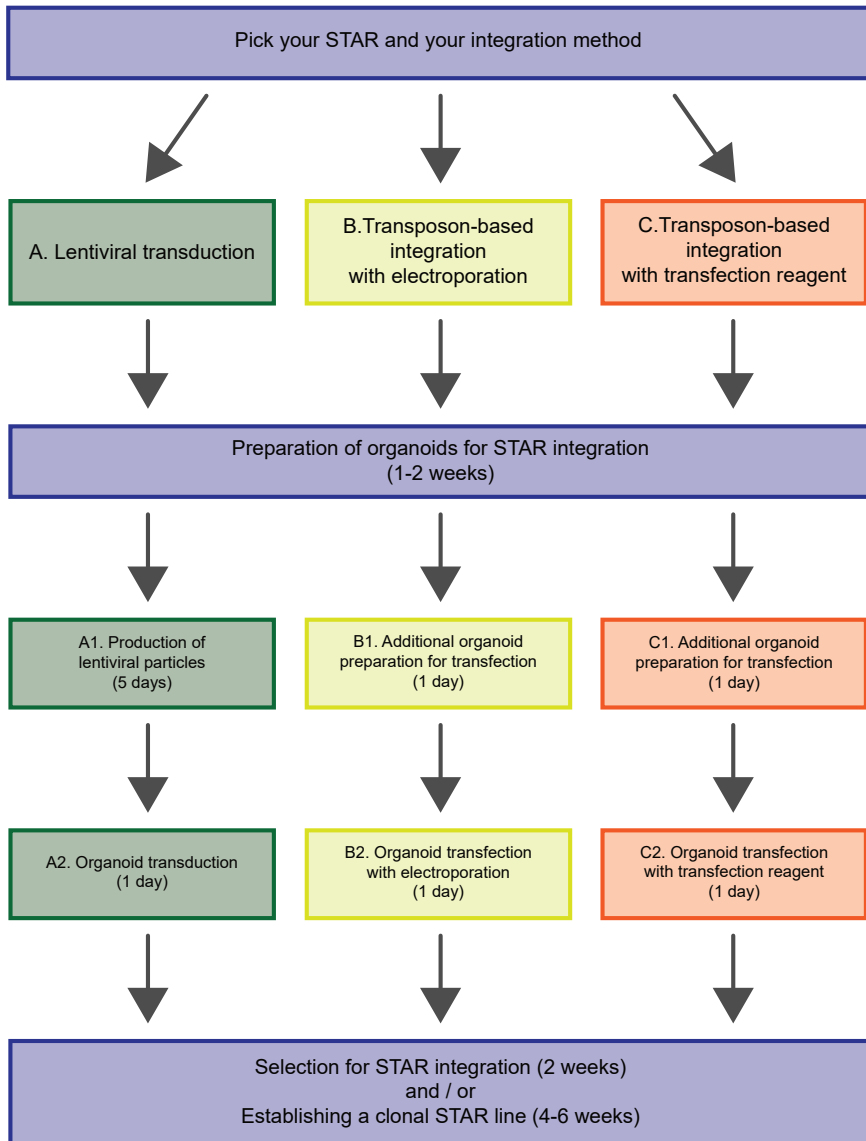


Figure 1: Workflow for integrating STAR into organoids.

Flow chart indicating the key steps with time estimates for the different integration methods provided: lentiviral transduction (protocol A, green), transposon-based integration with electroporation (protocol B, yellow), and transposon-based integration with a transfection reagent (protocol C, red). Protocol steps required for all integration methods are highlighted in blue.

Choosing Your STAR Minigene

The minigene STAR faithfully marks mouse and human intestinal stem cells (Oost et al., 2018) by reporting the transcriptional activity of ASCL2, the master regulator of intestinal cell fate (Schuijers et al., 2015). STAR can be used to identify, track, and study intestinal stem cells using fluorescent labels, which vary in their spectral properties. We have generated STAR constructs with varying fluorescent proteins, subcellular localizations, selection cassettes and integration strategies (Figure 2 and Table 1). The choice of the optimal STAR variant depends on the specific research question and related requirements should be met.

The robustness of a fluorescent reporter is determined by multiple parameters such as expression levels, fluorophore properties, and potentially genomic integration site. In this section, we discuss features to be considered to obtain optimal signal from the STAR minigene.

1. Applicability of the STAR minigene
 - a. STAR can be used to fluorescently label cells with transcriptional activity of ASCL2 in human and murine cells. To our knowledge, it has not been thoroughly tested for other species yet.
 - b. In particular, STAR can be used to faithfully mark small intestinal (SI) and colonic stem cells in both mouse and human organoids, while its expression pattern overlaps with the Lgr5 expression as demonstrated for mouse SI organoids (Oost et al., 2018).
 - c. STAR can also be used to mark stem-like cells in colorectal cancer. Recent evidence suggests that not all patient-derived colorectal cancer cell lines express ASCL2 (Jubb et al., 2006; Ziskin et al., 2013), which constitutes a natural but hitherto not encountered limit.
 - d. STAR might be suitable to reflect the transcriptional activity of ASCL2 in organoid systems beyond the intestine of men and mice. However, this has not been tested yet.
 - e. When STAR is expected to target a non-stem cell population, a ubiquitously expressed selection cassette is preferable. For more details see section ["Selection procedure for STAR organoids"](#).

- f. As Wnt signalling drives ASCL2 expression (Van der Flier et al., 2007), supplementing the organoid medium with exogenous Wnt may lead to a high fraction of STAR+ cells with moderate differences in STAR-level. Cellular differentiation protocols can lead to a higher degree of cellular diversity by reducing the amount of stemness-promoting factors. Consequently, these media induce crypt-(like) budding structures and promote the difference between STAR-high and STAR-negative cells (Sato et al., 2011).
 - g. Studies previously performed using STAR organoids: STAR has been used to study the cellular composition of human colon and patient-derived CRC organoids. Colony formation assays have demonstrated the stem cell properties of single STAR+ cells in human colon organoids. Additionally, STAR has been used to profile tumor subpopulations transcriptomically and to visualize cancer stem cells in xenograft studies (Oost et al., 2018).
2. Comparison of STAR to endogenous labelling of stem cells
 - a. STAR is a very versatile tool, allowing to generate a large number of reporter lines simultaneously in a relatively short time frame with a high success rate (thus maintaining polyclonality).
 - b. As STAR is reporting the transcriptional activity of ASCL2, the brightness of the fluorescent protein is not limited by minimum expression level of an endogenous stem cell marker gene. This makes STAR superior for time-lapse microscopy studies and studies on cell fate conversions (differentiation or plasticity).
 - c. Visualization of intestinal stem cells in human organoids has been performed, for instance by generating a CRISPR/Cas9-mediated knock-in into the LGR5 locus (Fujii et al., 2018). By endogenously tagging the LGR5 protein with a fluorescent protein, both the subcellular localization and interaction partners of LGR5 can be reliably studied.
 - d. Genetic lineage tracing studies provide easy readout for assessing a cell's self-renewal and multipotency potential. Using LoxP-STOP-LoxP-based reporter systems and a knock-in of CreER into the LGR5 locus, this has been successfully performed in human colonic organoids (Shimokawa et al., 2017; Sugimoto et al., 2017).

3. Cellular localization of the fluorescent protein

We have generated STAR plasmids with and without a nuclear localization signal (NLS) fused to the fluorescent protein. Their key features are listed below:

- a. Nuclear localization
 - i. Excellent for quantifications and cell tracking
 - ii. In combination with a bright fluorophore, more difficult to distinguish expressions levels with basic microscopy as the fluorescent proteins are concentrated in a smaller volume
- b. Uniform localization
 - i. Displays cellular morphology (e.g. stem cells are slender cells in mouse small intestinal organoids)
 - ii. Excellent for co-expression studies with cytoplasmic (stem cell) markers

4. Features of fluorescent proteins

- a. To capture ASCL2 dynamics with high accuracy during time-lapse microscopy, the ideal fluorophore would have to have a high extinction coefficient and quantum yield (brightness), high photostability (limited bleaching), a short maturation time, and a high protein turnover. Most of these criteria are met by either mNeonGreen or sTomato, however, depending on the research question a different fluorophore might be more suitable.
- b. When planning to use the STAR lines for in vivo experiments, using a fluorescent protein with an established antibody provides highest flexibility in terms of downstream processing and allows, for instance, for paraffin-embedding or Edu chemistry and subsequent retrieval of the STAR signal.

5. Microscope setup

Generally speaking, the different fluorophores used in this study are suitable for many microscopy techniques as the proteins can be excited with either of the following laser options: 405 nm, 458 nm, 488 nm or 561 nm. If, however, STAR shall be combined with multiple different colors which leads to limited detection windows, it might be preferable to choose bright fluorescent proteins which can be most optimally excited with the available laser equipment.

Table 1: STAR selection at a glance

Resource	Integration method	STAR color	Selection antibiotics	Addgene number
pLV 4xSTAR-mTagBFP2-blast	pLV	TagBFP2	blasticidin	125239
pLV 4xSTAR-mTFP-NLS-blast	pLV	mTFP	blasticidin	136257
pLV 4xSTAR-mNeonGreen-NLS-blast	pLV	mNeonGreen	blasticidin	136258
pLV 4xSTAR-sTomato-NLS-blast	pLV	sTomato	blasticidin	136259
pLV 4xSTAR-mScarletl-NLS-blast	pLV	mScarletl	blasticidin	136260
Tol2 8xSTAR-mNeonGreen. PGK-puro	Tol2	mNeonGreen	puromycin	136255
Tol2 8xSTAR-sTomato. PGK-puro	Tol2	sTomato	puromycin	136264
Tol2 8xSTAR-mScarletl. PGK-puro	Tol2	mScarletl	puromycin	136266
Tol2 8xSTAR-mNeonGreen-NLS. PGK-puro	Tol2	mNeonGreen	puromycin	136262
Tol2 8xSTAR-sTomato-NLS. PGK-puro	Tol2	sTomato	puromycin	136261
Tol2 8xSTAR-mScarletl-NLS. PGK-puro	Tol2	mScarletl	puromycin	136263

List of all available STAR plasmids generated by the Snippert lab and provided to Addgene. Plasmids are either suitable for lentiviral-based (pLV) or transposon-based (Tol2) integration. The fluorescent color reporting STAR activity and selection antibiotics are listed for each plasmid. For a graphical representation of the STAR plasmids see Figure 2.

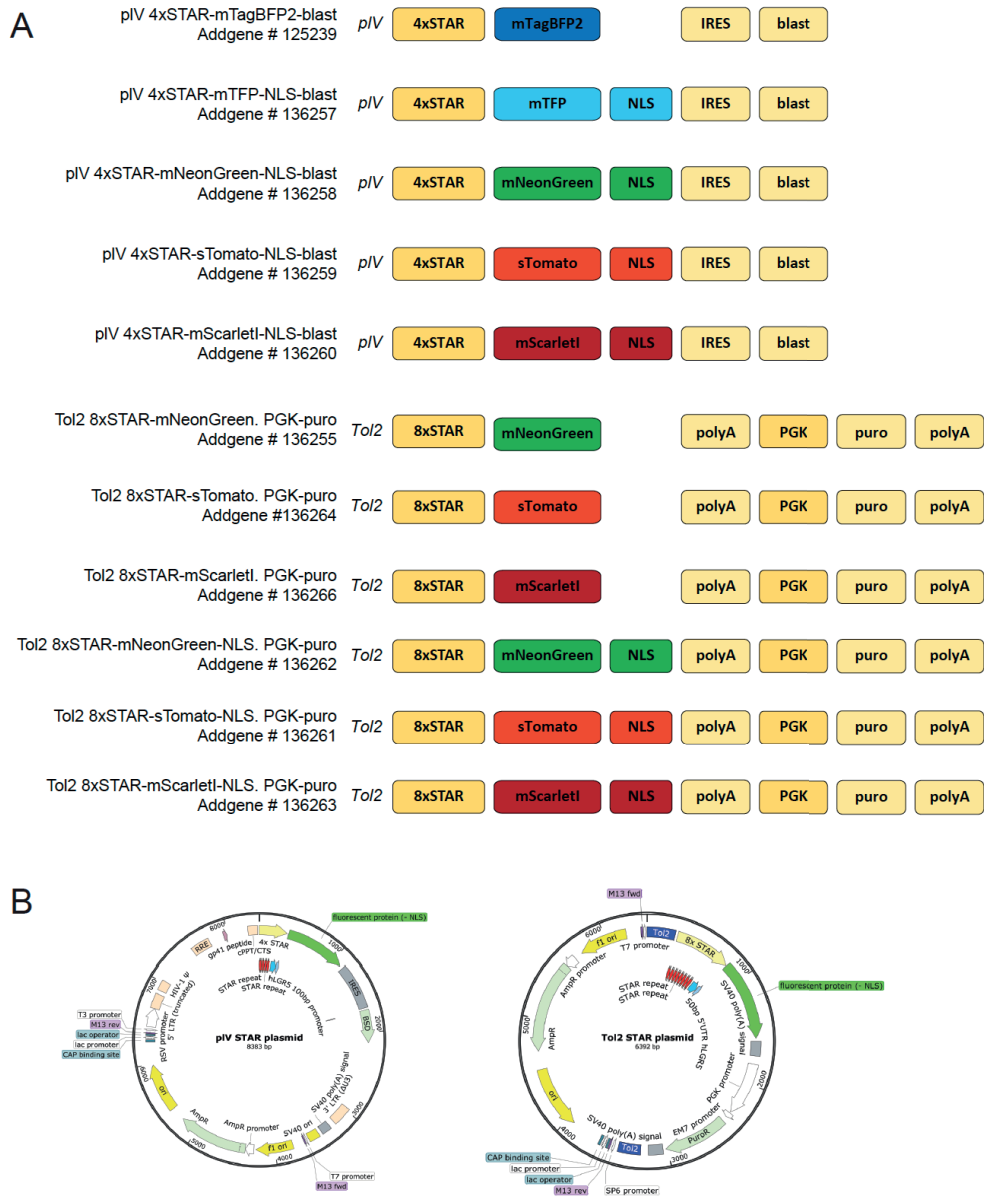


Figure 2: The STAR plasmid selection.

A. Schematic overview of available STAR reporter designs suitable for lentiviral (pIV) or Tol2 transposon-based integration (Tol2). STAR contains either 4 or 8 repeats of the ASCL2 binding motif (4xSTAR and 8xSTAR, respectively). Further features: fluorescent protein, nuclear localisation signal (NLS), selection cassette conferring resistance to puromycin (puro) or blasticidin (blast), internal ribosome entry site (IRES), polyadenylation signal (polyA), and independent, ubiquitously active PGK promoter. Addgene names and numbers of all plasmids are listed. See also Table 1. **B.** Schematic overview of plasmid vector maps (STAR and backbone) for lentiviral (left) and transposon-based (right) integration.

Choosing Your Integration Strategy

We provide STAR plasmids that can be integrated into the genome of organoids either by lentiviral transduction or by transposase-based approaches.

Protocol A: Lentiviral integration

Recommended if high expression levels are desired and for organoids that are very difficult to transfect.

Protocol B: Transposon-based integration with electroporation

Recommended if medium expression levels are desired and for organoids which are difficult to transfect. Expected to lead to fewer integrations than lentiviral approach. Transfection might also be suitable for induced pluripotent stem cells or embryonic stem cell approaches.

Protocol C: Transposon-based integration with transfection reagent

Suitable for organoids that are readily transfectable.

All three integration strategies are suitable for the generation of organoid lines with the following features: species: mouse or human, organ: small intestine or colon, genome: WT or cancerous. In our experience, organoid lines with a WT genome might be more difficult to transfect with a transfection reagent (approach C). Hence, in situations transposon-based integration with electroporation might be superior (approach B). An overview of the experimental workflows is provided in Figure 1.

Preparation of Organoid Cultures

Timing: [1-2 weeks]

To maximize the efficiency of generating stable STAR organoids, the organoids should be in a healthy, **proliferative state** prior to starting any transduction/transfection protocol (Figure 3).

CRITICAL: (for mouse SI organoids) We recommend reverting mouse SI organoids from their regular crypt-like morphology (ENR culture medium) into a highly proliferative state (WENR culture). To get to this state, mouse SI organoids should be cultured in WENR medium (see "[General Organoid Media](#)") after passaging by mechanically shearing off the crypt units. When most of the organoids demonstrates a cystic morphology (usually after 5-10 days), organoids can be used for STAR integration (Figure 3C).

For complete details on the use and execution of this protocol paragraph, please refer to Koo *et al.* and Andersson-Rolf *et al.* for the preparation of mouse SI organoids for transfection or transduction (Andersson-Rolf *et al.*, 2014; Koo *et al.*, 2012).

Note: To obtain **enough starting material**, it is advisable to expand the organoid culture for 1-2 weeks prior to STAR integration. For electroporation-based transfection, the success rate increases significantly if 500,000—1 million cells are being electroporated. This corresponds to organoids growing in approx. 200-400 μ l Matrigel for 7-10 days after the last passage.

CRITICAL: (for transfection-based approaches) As serum hampers the transfection efficiency, organoids should be cultured with **serum-free medium** for the transfection-based approaches (procedures B & C), starting one day in advance. This implies leaving out Penicillin/Streptomycin and replacing the Wnt CM with 10 μ M CHIR99021 (see Step-by-Step Method Details).

Preparation Step	Lentiviruses	Transfection with Electroporation	Transfection with Transfection Reagent
Reverting mouse SI organoids to a proliferative state using WENR medium	recommended	critical	critical
Expanding the culture to get a high cell number (500,000 or more)	obsolete	critical	recommended
Culture in serum-free media prior to STAR integration	obsolete	critical	critical

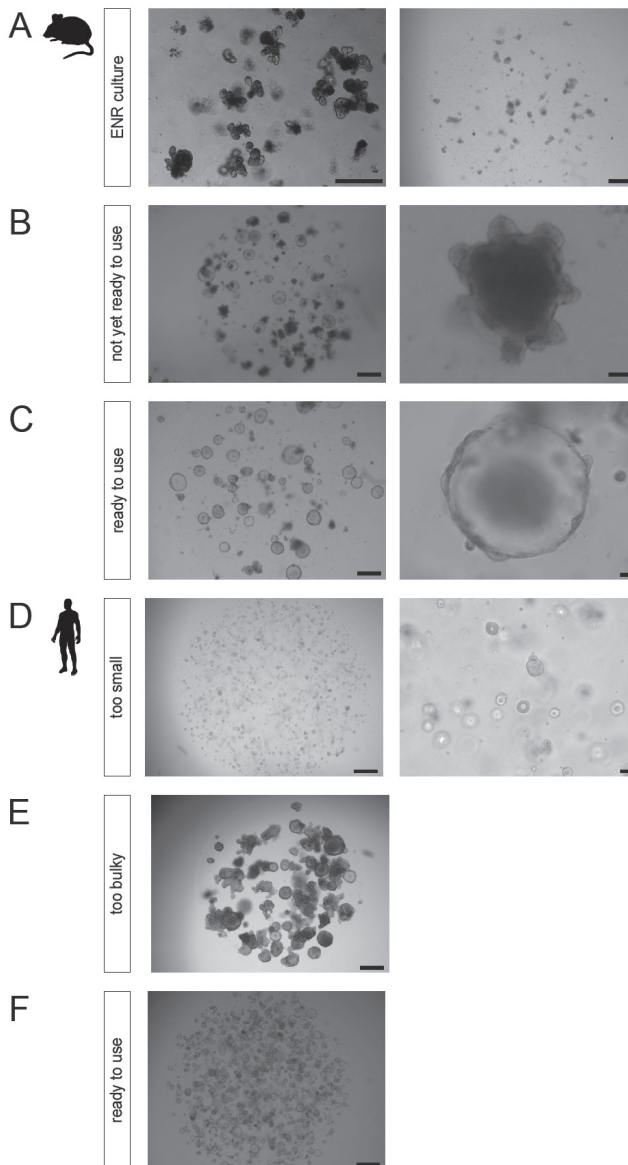


Figure 3: Preparation of organoids prior to STAR integration.

A-C. Mouse small intestinal organoids. (A) Organoids in ENR medium. Mature culture (left) and culture directly after passaging by mechanical fragmentation (right). (B) Changing from ENR to WENR medium yields highly proliferative cyst-like structures over time (right panel = close up (scale bar 50 μ m)). (C) Organoid culture consistently depicting cyst-like phenotypes that is ready to use for STAR integration. (right panel = close up (scale bar 50 μ m)). **D-F.** Human colonic organoids. (D) Organoid culture is not dense enough / organoids are too small to reach sufficient cell numbers. (right panel = close up (scale bar, 50 μ m)). (E) Organoids are too bulky / too much differentiation. (F) Organoids are in a highly proliferative state and ready for STAR integration. Scale bars, 500 μ m unless indicated otherwise.

KEY RESOURCES TABLE

REAGENT or RESOURCE	SOURCE	IDENTIFIER
Chemicals, Peptides, and Recombinant Proteins		
Matrigel	Corning	Cat# 356231
Dispase II	Life Technologies	Cat# 17105041
Trypsin EDTA	Sigma-Aldrich	Cat# 25200056
Trypsin inhibitor	Sigma-Aldrich	Cat# T9003
Opti-MEM	Life Technologies	Cat# 31985054
Advanced DMEM/F-12	Invitrogen	Cat# 12634-028
GlutaMAX	Invitrogen	Cat# 35050-038
HEPES	Invitrogen	Cat# 15630-056
Penicillin/Streptomycin	Lonza	Cat# DE17-602E
EGF (Recombinant Human EGF)	PeproTech	Cat# AF-100-15
B27 supplement	Invitrogen	Cat# 17504001
N-Acetyl-L-Cysteine	Sigma-Aldrich	Cat# A9165
Nicotinamide	Sigma-Aldrich	Cat# N0636
A83-10	Tocris	Cat# 2939/10
SB202190	Gentaur	Cat# A1632
Y-27632	Gentaur	Cat# A3008
Primocin	Invivogen	Cat# ant-pm-2
Puromycin	Sigma-Aldrich	Cat# P7255
Blasticidin	Bio Connect	Cat# ant-bl-1
CHIR99021 (Protocols B and C)	Bio-Techne	Cat# 4423/10
Dulbecco's Modified Eagle's Medium (DMEM) – high glucose (Protocol A)	Sigma-Aldrich	Cat# D6429
Fetal bovine serum (FBS, Protocol A)	Fisher Scientific	Cat# 10309433
Polybrene / Hexadimethrine bromide (Protocol A)	Merck	Cat# 107689
Experimental Models: Cell Lines		
HA-RSpondin1-Fc 293T cell line to make R-Spondin CM	In-house production	N/A
HEK293-mNoggin-Fc cell line to make Noggin CM	In-house production	N/A
L-Wnt3A cell line to make Wnt CM	In-house production	N/A
HEK293T cell line (Protocol A)	N/A	N/A
Recombinant DNA		
Envelope plasmid for lentiviral production pHDM-G	PlasmID by DF/HCC DNA Resource Core at Harvard Medical School	PlasmID clone ID EvNO00061607
Helper plasmid for lentiviral production pHDM-Hgpm2	PlasmID by DF/HCC DNA Resource Core at Harvard Medical School	PlasmID clone ID EvNO00061606
Helper plasmid for lentiviral production pRC-CMV-rev1b	PlasmID by DF/HCC DNA Resource Core at Harvard Medical School	PlasmID clone ID EvNO00061616
CMV-Tol2 transposase (Protocols B and C)	Addgene	Addgene 158774
Other		
24-well tissue culture plates	Magazijn	Cat# 3524
Cell culture dishes, 100mm x 20 mm	Greiner	Cat# 664160
X-tremeGENE 9 DNA transfection reagent	Life Technologies	Cat# 6365779001
Sterile 50 mL concentric luer-lock syringe (Protocol A)	BD Plastipak	Cat# 300865
Sterile 0.45 µm syringe filter (Protocol A)	Satorius	Cat# 16555-K
Ultracentrifuges tubes, e.g. Thinwall Polypropylene Tube, 25x89mm (Protocol A)	Beckman Coulter	Cat# 326823
BTX electroporation solution (Protocol B)	Fisher Scientific	Cat# 15417350
Electroporation cuvette Plus, BTX, 2mm gap (Protocol B)	Fisher Scientific	Cat# 15447270

MATERIALS AND EQUIPMENT

The STAR Selection

A selection of STAR plasmids for either lentiviral or Tol2 transposon-based integration has been generated and is depicted in Figure 2 and Table 1. The plasmid sequences at base-pair resolution are available on Addgene.

General Organoid Media

The organoid culture media were established by Sato *et al.* (Sato et al., 2009, 2011).

Ingredient	Mouse SI organoids, ENR culture	Mouse SI organoids, WENR culture	Human SI / colon WT culture
Advanced DMEM/F12 supplemented with GlutaMAX, HEPES, Pen/Strep			
Wnt 3A CM		50 %	50 %
R-Spondin CM	5 %	20 %	20 %
Noggin CM	10 %	10 %	10 %
EGF (Recombinant Human EGF)	50 ng/mL	50 ng/mL	50 ng/mL
B27 supplement	2 %	2 %	2 %
N-Acetyl-L-Cysteine	1.25 mM	1.25 mM	1.25 mM
Nicotinamide		10 μ M	10 μ M
A83-01			500 nM
SB202190			3 μ M

Note: In case of organoid lines with pathway-activating mutations, certain culture ingredients can be left out (Drost et al., 2015).

Troubleshoot 9: [Access to conditioned media](#)

Additional Organoid Media Required for Lentiviral Transduction (Protocol A)

Transduction medium: Adjust standard organoid medium as follows

- Add 10 μ M Y-27632
- Add 8 μ g/mL polybrene

Optional: Freezing medium for lentiviruses: Adjust standard organoid medium as follows

- If standard organoid medium contains Wnt CM, replace it by 10 μ M CHIR99021
- Add 10 μ M Y-27632
- Add 8 μ g/mL polybrene

Additional Organoid Media Required for Transposon-Based Integration (Protocols B and C)

CRITICAL: Transfection medium should be serum-free. Due to the dissociation procedure, the following adaptations are recommended:

Transfection medium: Adjust standard organoid medium as follows

- Use Advanced DMEM/F12 supplemented with GlutaMAX and HEPES (but without Pen/Strep)
- If standard organoid medium contains Wnt CM, replace it by 10 μ M CHIR99021
- Add 10 μ M Y-27632

Additional Equipment Required for Lentiviral Integration (Protocol A)

- Ultracentrifuge, e.g. Beckman Coulter with SW32Ti rotor

Alternatives: If you do not have access to an ultracentrifuge, you can also concentrate the virus using the Lenti-X™ concentrator according to the manufacturer's instructions (Takara, Cat. No.: 631231) with which we have limited but good experience.

Additional Equipment Required for Electroporation-Based Integration (Protocol B)

- Electroporation machine, e.g. Nepa Gene NEPA21

STEP-BY-STEP METHOD DETAILS

Integration of STAR into the Genome

The protocols below describe the integration of STAR via (A) lentiviral transduction, (B) transposase-based integration with electroporation, and (C) transposase-based integration using a transfection reagent.

Protocol A: Lentiviral Transduction

Timing: 5 days

For complete details on the use and execution of this part of the protocol, please refer to Van Lidth de Jeude *et al.* for the organoid transduction protocol with lentiviruses (Van Lidth de Jeude *et al.*, 2015).

Protocol A1: Production of Lentiviral Particles

This protocol describes the production of lentiviral particles using VSV-G envelopes. All lentiviral STAR plasmids listed in Table 1 are suitable for 3rd generation lentivirus making with VSV-G envelopes and the packaging vectors gag, pol, and rev. Transduced stem cells will generate STAR organoids.

CRITICAL: Protocol steps involving lentiviral particles must be performed in a BSL-2 lab (indicated below). This involves careful attention to BSL-2 regulations on sample handling and disposal of plasticware and media.

Day 1:

Timing: 30 min

1. Split HEK293T cells to 25%-30% confluency in T75 flask or 100mm petri dish and plate in DMEM supplemented with 10% foetal bovine serum (DMEM/FBS).

Note: Each plate at 80% confluency can be split over 4 plates.

Day 2:

Timing: 25 min

2. Prepare transfection solution as indicated in the table below. Troubleshoot 2: No access to indicated lentiviral packaging plasmids or transfection reagent
3. Mix transfection solution thoroughly, and incubate at 20°C for 15 min.

CRITICAL: Do not incubate the transfection mixture for more than 30 min.

Reagent	For 1 dish	For 2 dishes	For 4 dishes
Opti-MEM	100 µL	200 µL	400 µL
DNA STAR reporter, stock concentration at 1 µg/µL	5 µL	10 µL	20 µL
DNA pMDLg/pRRRE, stock concentration at 1 µg/µL	1 µL	2 µL	4 µL
DNA pRSV-Rev, stock concentration at 1 µg/µL	1 µL	2 µL	4 µL
DNA pMD2.G, stock concentration at 1 µg/µL	2 µL	4 µL	8 µL
X-tremeGENE 9	18 µL	36 µL	72 µL

CRITICAL: The following step must be performed in a BSL-2 lab.

4. Drip 127 µL DNA transfection solution onto HEK293T cells growing in DMEM/FBS and store them in a humidified cell culture incubator at 37 °C.

Day 3:

Timing: 5 min

CRITICAL: The following step must be performed in a BSL-2 lab.

5. Carefully aspirate medium from HEK293T culture plates and add 8 mL DMEM/FBS to each plate.

Note: This culture media volume allows to pool the virus suspension of up to 4 plates into one bucket for ultracentrifugation on Day 5.

Day 5:

Timing: 3.5 h, including 2.5 h centrifugation

CRITICAL: The following steps must be performed in a BSL-2 lab.

6. Before you begin:
 - a. Pre-cool ultracentrifuge to 4°C
 - b. Prepare transduction medium as described in section "[Additional Organoid Media Required for Lentiviral Transduction \(Protocol A\)](#)"
 - c. **Optional:** Prepare freezing medium for lentiviruses as described in section "[Additional Organoid Media Required for Lentiviral Transduction \(Protocol A\)](#)"
7. **Optional:** If dead cells are floating in the culture medium, collect supernatant in 15 mL flask and centrifuge for 5 min at 500 x g. Continue with supernatant.
8. Collect the culture medium from the plates and push it through a 0.45 µm filter using a large 60 ml syringe.
9. Load ultracentrifuge buckets with tubes and pipet virus suspension into the tube.

Note: Culture media of up to 4 plates can be combined into one ultracentrifugation bucket.

10. Carefully equal balance opposite buckets (lids included) by topping up with DMEM/FBS. Afterwards, carefully cap buckets with corresponding lids.
11. Centrifuge for 2.5 h at 170,000 x g at 4°C.
12. In the meantime, prepare N*550 µL transduction medium with N being the total number of flasks or plates in which virus has been produced.

13. Transfer ultracentrifuge buckets very carefully into a laminar flow hood, remembering the orientation of the tube inside the centrifuge.
14. Open bucket containing ultracentrifuge tube and decant medium carefully in such orientation that the opaque brown pellet is on the upper side of the tube. Take a micropipette and remove leftover medium, while taking care not to agitate the pellet.
15. Resuspend the virus pellet in $N \times 500 \mu\text{L}$ of organoid transduction medium.
16. Use $250 \mu\text{L}$ virus suspension ($N/2$) to transduce organoids grown in $50\text{-}100 \mu\text{L}$ Matrigel (see protocol A2). Residual virus suspension can be aliquoted in single-use fractions ($250 \mu\text{L}$ each) and frozen at -80°C .

Pause Point: The lentivirus can be frozen at -80°C and transduction can be done on a different day with a minor loss in efficiency.

Note: In our experience, 2-year old virus stocks are suitable for high efficiency transductions (minor loss compared to fresh virus), when previously stored as single-use aliquots at -80°C .

Protocol A2: Lentiviral Transduction of Organoids

Timing: 3.5-6.5 h, including 1h centrifugation and 1-4 h incubation

CRITICAL: Protocol steps involving lentiviral particles must be performed in a BSL-2 lab (indicated below). This involves careful attention to BSL-2 regulations on sample handling and disposal of plasticware and media.

17. Before you begin:
 - a. Pre-heat water bath to 37°C
 - b. Pre-cool centrifuge to 4°C
18. Harvest organoids with ice-cold medium and transfer into a 15 mL tube.

Note: For one transduction, $50\text{-}100 \mu\text{L}$ of Matrigel containing approx. 5,000 - 20,000 organoids which were passaged 7-10 days ago should suffice.
19. Top up to 10 mL with ice-cold Advanced DMEM and spin at 4°C , $300 \times g$ for 5 min.

Note: Ice-cold medium will dissolve the Matrigel.
20. Discard supernatant.

21. **Optional:** If residual Matrigel is visible (not a clean pellet), repeat steps 19 and 20.
22. Discard supernatant and resuspend pellet in 500 μ L trypsin. Incubate for about 3 min in a 37 °C water bath until organoid have dissociated into single cells or small fragments.

Note: (Non-cancerous) Organoids might have reduced outgrowth potential when trypsinized to single cells.

23. Inactivate trypsin by adding 500 μ L trypsin inhibitor (1:1 ratio with trypsin), top up to 10 mL with Advanced DMEM, and spin at 4°C, 500 x g for 5 min.
24. Discard the supernatant and resuspend pellet in 20 μ L transduction medium.

CRITICAL: The following steps have to be performed in a BSL-2 lab.

25. Add 250 μ L virus suspension to the organoids and spin at RT, 75 x g for 1 h.
26. Incubate samples in a 37°C incubator for 1-4 h with a loosened lid.

Note: Prolonged incubation of up to 4 h may increase the transduction rate significantly.

27. In the meantime, thaw Matrigel on ice and keep on ice after thawing.
28. Spin samples at RT, 500 x g for 5 min.
29. Take off supernatant and resuspend cell pellet in 100-200 μ L Matrigel. Plate in 10 μ L droplets onto a pre-warmed 24-well plate with 4-5 droplets per well.
30. Incubate plate upside-down in the incubator for 10-20 min until the Matrigel has solidified.

Note: Turning the plate upside-down prevents organoids from sinking to the bottom of the culture plate and attaching to the plastic.

31. Add 500 μ L organoid medium supplemented with 10 μ M Y-27632 to each well.

Start with selection procedure, 3 days after transduction (see section "[Selection procedure for STAR organoids](#)").

[Troubleshoot 1: STAR integration by lentiviruses](#)

[Troubleshoot 3: Cell death upon transduction](#)

Protocol B: Transposon-Based Integration with Electroporation**Timing: 3 days**

For complete details on the use and execution of this part of the protocol, please refer to Fujii *et al.* for the organoid electroporation protocol (Fujii *et al.*, 2015).

32. Pre-heat water bath to 37°C
33. Pre-cool centrifuge to 4°C
34. Thaw Matrigel on ice
35. Prepare electroporation mixture as follows: For each electroporation condition mix 100 μ L BTX electroporation solution + 10 μ L STAR reporter DNA (stock concentration 1 μ g / mL) + 5 μ L miniTol2 transposase (stock concentration 1 μ g / mL).
36. Label collection tubes for after electroporation.
37. Prepare 100X dispase: Dilute 0.05 g Dispase II in 500 μ L Advanced DMEM/F12 and mix well by pipetting and vortexing until completely dissolved.
38. Prepare 1X dispase (inside a flow cabinet): Add 100 μ L of 100X dispase stock to 9.9 mL Advanced DMEM/F12 and mix by vortexing briefly.

Note: Dispase stocks (100X and 1X) can be stored at 4°C but dispase is most active during the first days after preparation.

39. Prepare transfection medium as described in section "[Additional Organoid Media Required for Transposon-Based Integration \(Protocols B and C\)](#)"

Protocol B1: Preparation of Organoids for Transfection

Day 1:

Timing: 5 min

40. Replace organoid medium with transfection medium while using 500 μ L transfection medium for each well of a 24-well plate.

Note: 200-400 μ L Matrigel containing organoids grown for 7-10 days after the last passage should suffice for one electroporation.

Day 2:

Timing: 1-1.5 h

41. Add 1.25 % v/v DMSO to the transfection medium.
42. Keep organoids in the incubator for 2-4 h.
43. Take off medium, collect organoid droplets using 1X dispase, and transfer into a 15 mL tube.
44. Incubate in 37°C water bath for 3-10 min until Matrigel is properly dissolved.

Alternatives to steps 43 and 44: Harvest organoids with ice-cold medium and transfer into 15 mL tube. This approach might require additional washing / centrifugation steps as indicated in step 46.

45. Top up to 10 mL with cold Advanced DMEM/F12 and spin at 4°C, 300 x g for 5 min.
46. If a clean organoid pellet is visible, discard the supernatant. Otherwise, carefully take off the clear supernatant on top of the Matrigel cloud (approx. 8 mL of supernatant). Then, repeat steps 45 and 46.
47. Resuspend pellet in 1 mL of trypsin. Incubate for about 3 min in a 37 °C water bath until organoid have dissociated into small fragments.

Note: Dissociation to small fragments, rather than to single cells, will increase the survival and outgrowth potential upon electroporation.

48. Inactivate trypsin by adding 1 mL of trypsin inhibitor (1:1 ratio with trypsin), top up to 10 mL with Advanced DMEM/F12, and spin at 4°C, 500 x g for 5 min.
49. **Optional:** Discard the supernatant, resuspend the pellet in 1mL Advanced DMEM/F12, and roughly estimate the cell number by counting. 500,000-1 million cells are recommended for one electroporation. Afterwards, pellet cells again by spinning at 4°C, 500 x g for 5 min.
50. Discard the supernatant and put tube on ice.

Protocol B2: Transfection of Organoids Using Electroporation

Timing: 45 min

51. Set up the electroporator. During the subsequent steps, avoid prolonged incubation of the cells in electroporation buffer.

52. Resuspend cell pellet in 115 μ L electroporation mixture and transfer 100 μ L into electroporation cuvette.
53. Cap the cuvette with its lid and place the electroporation cuvette in the cuvette holder of the electroporator.
54. Measure the impedance and adjust if value outside 30-55.

Note: Increasing the volume in the cuvette will lower the impedance.

55. **Optional:** If impedance is larger than 30, add residual cell suspension to the cuvette to increase the number of cells which are being electroporated.
56. Electroporate cells with the settings indicated in the table below. [Troubleshoot 4: Cell death upon electroporation](#)
57. Add 400 μ L of Opti-MEM supplemented with 10 μ M Y-27632 to the electroporation cuvette.
58. Use the plastic pipette provided with the cuvette to transfer the cells from the cuvette into an Eppendorf tube and put on ice.
59. Rest cells for 10-20 min on ice.
60. Spin tubes at 4°C, 500 x g for 5 min.
61. Take off supernatant.
62. Resuspend pellet in approx. 200 μ L Matrigel and plate cells at high density in 10 μ L droplets onto a pre-warmed 24-well plate with 4-5 droplets per well.

Note: A significant fraction of cells won't survive this harsh procedure. Hence, cells can be plated more densely than usual for maintenance of the organoid line.

63. Incubate the plate upside-down in the incubator for 10 min until the Matrigel has solidified.
64. Add 500 μ L transfection medium + 1.25% DMSO per well for at least 30-60 min.
65. Refresh each well with 500 μ L transfection medium without DMSO.

	Poring pulse	Transfer Pulse
Voltage	175 V	20 V
Pulse Length	5 msec	50 msec
Pulse interval	50 msec	50 msec
Number of pulses	2	5
Decay rate	10 %	40 %
Polarity	+	+/-

Day 3:

Timing: 5 min

66. Replace medium with 500 μ L standard culture medium.

Start with selection procedure, 3-7 days after transfection (see section "[Selection procedure for STAR organoids](#)").

Troubleshoot 1: Transposon-based STAR integration via electroporation

Protocol C: Transposon-Based Integration Using a Transfection Reagent

The protocol for organoid transfection with transfection reagents was inspired by a transfection protocol using liposomes of Schwank *et al.* (Schwank et al., 2013), while the key transfection step was adapted by the Snippert lab.

67. Pre-heat water bath to 37°C
68. Pre-cool centrifuge to 4°C
69. Prepare 100X dispase: Dilute 0.05 g Dispase II in 500 μ L Advanced DMEM/F12 and mix well by pipetting and vortexing until completely dissolved.
70. Prepare 1X dispase (inside a flow cabinet): Add 100 μ L of 100X dispase stock to 9.9 mL Advanced DMEM/F12 and mix by vortexing briefly.

Note: Dispase stocks (100X and 1X) can be stored at 4°C but dispase is most active during the first days after preparation.

71. Prepare transfection medium as described in section "Materials and Equipment/ Media Compositions"

Protocol C1: Preparation of Organoids for Transfection

Timing: 3 days

Note: Protocol is written for the transfection of one well of a 24-well plate containing 50 μ L Matrigel. Sufficient organoid amounts for successful transfection are between 4 and 8 wells of a 24-wells (approx. 200-400 μ L Matrigel).

Day 1:

Timing: 5 min

72. Replace organoid medium with 500 μ L transfection medium per well.

Day 2:

Timing: 1-1.5 h

73. Take off medium, collect organoid droplets using 1X dispase, and transfer into a 15 mL tube.
74. Incubate in 37°C water bath for 3-10 min until Matrigel is properly dissolved.

Alternatives to steps 73 and 74: Harvest organoids with ice-cold medium and transfer into 15 mL tube. This approach might require additional washing / centrifugation steps as indicated in step 76.

75. Top up to 10 mL with Advanced DMEM and spin at 4°C, 300 x g for 5 min.
76. If a clean organoid pellet is visible, discard the supernatant. Otherwise, carefully take off the clear supernatant on top of the Matrigel cloud (approx. 8 mL of supernatant). Then, repeat steps 75 and 76.
77. Discard supernatant and resuspend pellet in 250 µL of trypsin. Incubate for about 3 min in a 37 °C water bath until organoid have dissociated into single cells or small fragments.

Note: (Non-cancerous) Organoids might have reduced outgrowth potential when trypsinized to single cells.

78. Inactivate trypsin by adding 250 µL of trypsin inhibitor (1:1 ratio with trypsin), top up to 10 mL with Advanced DMEM, and spin at 4°C, 500 x g for 5 min.
79. Take off supernatant and put cells on ice.

Protocol C2: Transfection of Organoids with a Transfection Reagent

Timing: 6-7 h, including 5-6 h incubation

80. Prepare transfection mixture as follows: For one well mix 50 µL Opti-MEM + 0.5 µL STAR reporter DNA at 1 µg/mL + 0.25 µL miniTol2 transposase at 1 µg/mL + 2.25 µL X-tremeGENE 9. [Troubleshoot 2: No access to transfection reagent](#)

Recommended: If more wells are used for transfection, scale transfection mixture linearly.

81. Mix transfection mixture well by vortexing, spin the tube briefly to remove drops from the lid or the side of the tube, then incubate for 15 min at RT.

CRITICAL: Do not incubate the transfection mixture for more than 30 min.

82. Resuspend cell pellet in 225 μ L transfection medium (previously prepared as described at the beginning of this protocol).
83. Add $N \times 53 \mu$ L transfection mixture to the cell suspension with N being the total number of wells the organoids were derived from and mix well by pipetting up and down.
84. Incubate for 5-6 h in the incubator with a loosened lid.
85. Towards the end of the incubation period, thaw Matrigel on ice and keep on ice after thawing.
86. Spin tubes at 4°C, 500 x g for 5 min.
87. Take off supernatant.
88. Resuspend pellet in Matrigel and plate cells in 10 μ L droplets onto a pre-warmed 24-well plate with 4-5 droplets per well.
89. Incubate the plate upside-down in the incubator for 10 min until the Matrigel has solidified.
90. Add 500 μ L transfection medium to each well.

Day3:

Timing: 5 min

91. Replace medium with 500 μ L standard culture medium.

Start with selection procedure, 3 days after transfection (see section "[Selection procedure for STAR organoids](#)").

Troubleshoot 1: Transposon-based STAR integration via transfection reagent

SELECTION PROCEDURE FOR STAR ORGANOIDS

Timing: 3 days – 2 weeks

Start selecting for STAR organoids as early as 3 days post integration. If viability is low (usually after electroporation), start selecting 7 days post integration to not further disturb the outgrowth process. Representative figures of organoids prior, during, and after selection are depicted in Figure 4. (The fraction of surviving organoids is representative for STAR integration by transfection. Lentiviral transduction rates usually are between 20-80 % in our hands.)

Timing: 5 min

92. Refresh medium and supplement with the appropriate selection antibiotic (puromycin at 1-4 $\mu\text{g}/\text{mL}$ and blasticidin at 2-50 $\mu\text{g}/\text{mL}$).

Optional: As the sensitivity to the drugs might vary across lines, a dose-response test on non-transduced/transfected organoids might be informative.

Note: We usually use concentrations which kill off negative clones within 3 and 7 days for puromycin and blasticidin, respectively. In our experience, organoid lines with a WT genome can be selected for using drug concentrations at the lower end of the indicated spectrum, while cancerous organoids might require higher concentrations.

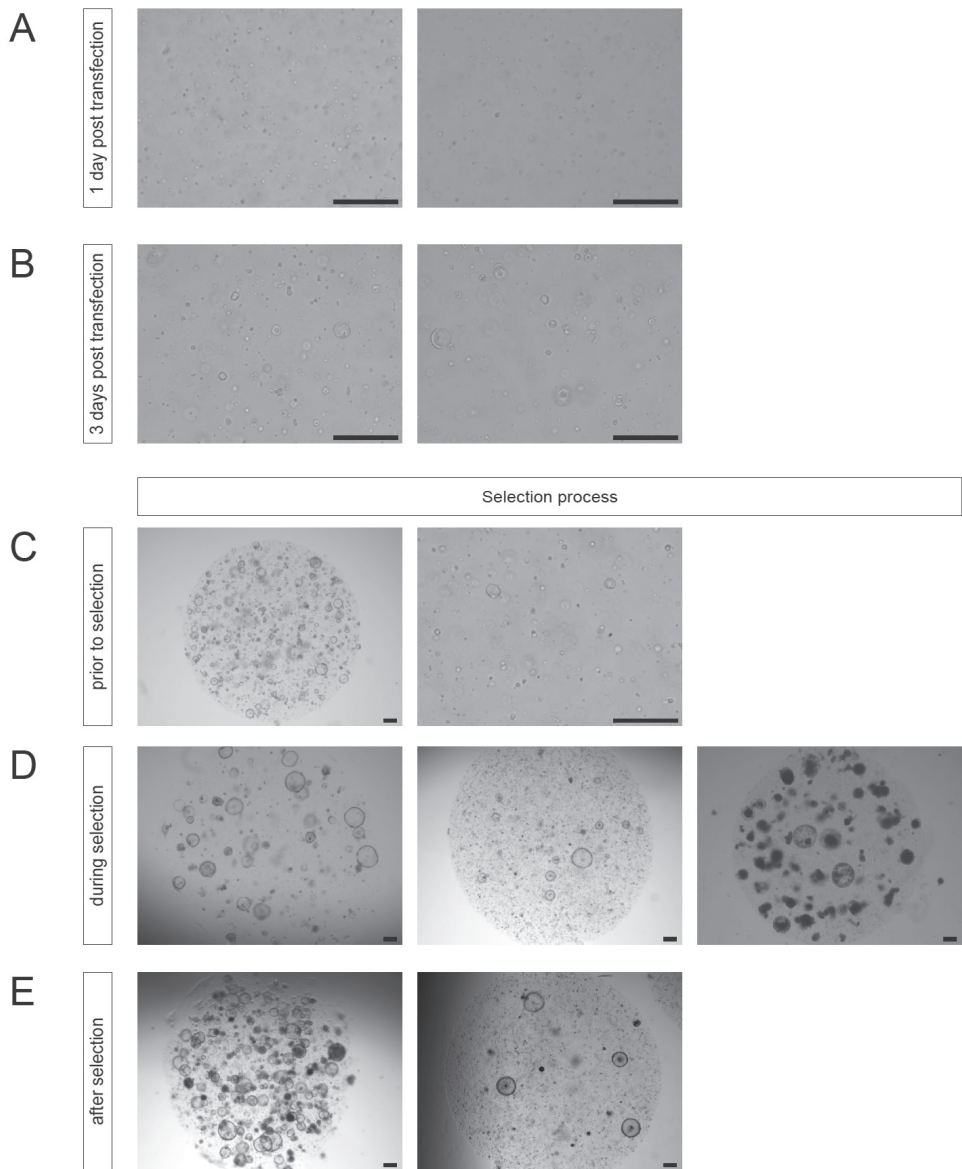


Figure 4: Organoids during STAR integration.

A-C. Electroporated organoid culture prior to selection. (A) Individual cells, one day after electroporation. (B) Small organoid structures at day 3. (C) Representative image of 4-7 day old viable organoids on which selection can be applied. **D.** Organoid cultures during the selection process. Efficiency of integration may fluctuate per condition (high on the left, low in the middle). Late administration of selection antibiotics (e.g. day 7) results in dead organoid structures (right panel), rather than dead single cells. **E.** Organoids having survived the selection procedure for high (left) and low (right) STAR integration efficiency. Scale bars, 250 μm .

Selection in case of a Ubiquitously Expressed Resistance Cassette

Timing: 1-2 weeks

93. Keep organoids on selection medium for at least 1-2 passages to ensure proper selection

Note: Organoids are most vulnerable at a single cell state which is why passaging organoids to single cells during the selection process is recommendable. Exceptions to this may be organoid lines with a poor single cell outgrowth efficiency.

94. **Optional:** FACS-purify STAR⁺ cells and grow them into a culture.

Note: This procedure is suitable in particular if a polyclonal line shall be used for future experiments. (For more detail, see first note below.)

95. **Optional:** Pick individual organoids grown from a single cell state to establish a clonal culture [see section "[Establishing a clonal STAR organoid line](#)"].

Selection in case of a STAR-Driven Resistance Cassette

Timing: 1-2 weeks

96. Keep organoids on selection medium for about 3-5 days to enrich for STAR⁺ cells.
97. Continue to culture organoids in the absence of the selection drug.
98. **Recommended:** FACS-purify STAR⁺ cells and grow them into a line.

Note: This procedure is suitable to establish a polyclonal line and could be used for future experiments. (For more detail, see first note below.)

99. **Optional:** Pick individual organoids grown from a single cell state to establish a clonal culture [see section "[Establishing a clonal STAR organoid line](#)"].

Note: We recommend to perform this step after FACS-purifying STAR⁺ cells (step 98) to ensure that reporter-positive clones are picked.

Note: FACS purification of STAR⁺ cells is suitable for all organoid lines in which STAR⁺ cells constitute the stem cell population and therefore regenerate the organoid culture. It further ensures proper selection for cells having integrated the reporter which is particularly reassuring in cases of transient antibiotics

selection. In designs in which a separate promoter drives the expression of a selection cassette, FACS purification of STAR⁺ cells rules out partial silencing of the reporter at the STAR sites.

Note: When infecting mouse SI organoids, keep organoids on WENR medium during the selection process. Passaging mouse WENR organoids can be performed by mechanical fragmentation using stacked pipet tips (e.g. stack a p200 tip on top of a p1000 tip and vigorously pipet up and down). Subsequently, organoids can be reverted to a crypt-like state in a 2-step process: First, culture organoids for 2-7 days in medium consisting of 50% WENR and 50% ENR. As soon as Paneth cells have reformed (recognizable by their dark and granular appearance inside small budding structures on a bright field table top microscope), the organoids can be maintained in ENR medium. As not all organoids revert at the same speed, it is advisable to carefully monitor the culture daily and base the timing of media change on the average organoid morphology. Different stages of reverting organoids are depicted in Figure 5.

Troubleshoot 5: STAR signal in resistant organoids

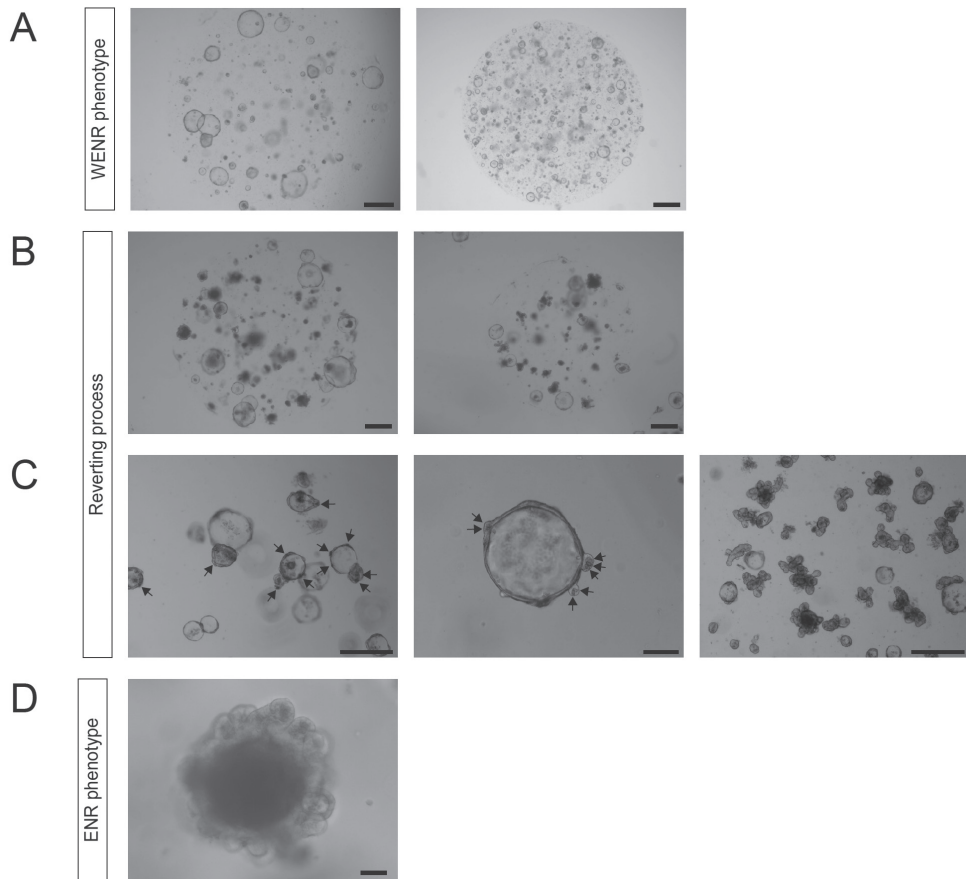


Figure 5: Mouse small intestinal organoids reverting from a cyst-like state to a crypt-villus architecture.

A. Cyst-like organoid structures growing at two different densities in WENR medium. Scale bars, 500 μm. **B-C.** Various examples of organoid cultures during the reversion process towards 'budding organoids'. **(B)** Upon downscaling of WNT (50% WENR + 50% ENR medium), organoids start to shed cells. Some organoids may already revert to crypt morphology. Scale bars, 500 μm. **(C)** Re-appearance of Paneth cells (arrows) in small buds indicates that the organoids can be passaged on ENR medium. Right: after first passage most organoids reverted back to ENR state. Scale bars: left/ right 250 μm and middle 50 μm. **D.** Mature organoid with crypt-villus phenotype. Scale bar, 50 μm.

ESTABLISHING A CLONAL STAR ORGANOID LINE

The outgrowth of isolated single cells into organoids is a highly inefficient process. Therefore, organoids need to be grown at a low-to-intermediate density prior to picking to ensure outgrowth while maintaining clonality. (A plating density of approximately 2,000-10,000 cells / 100 μL Matrigel is recommended.)

CRITICAL: The organoid density should be monitored carefully to ensure that no organoids are fusing during the outgrowth process. For organoid lines which are very sensitive to density, this process might involve plating cells at a density supporting single cell outgrowth and over the course of the next weeks replating intact organoid structures (without disruption) into larger volumes to ensure sufficient space for clonal organoid growth.

CRITICAL: The organoid should exceed a size of 300 cells prior to picking, to ensure successful passaging (approx. size depicted in Figure 4E, right panel). Growing the organoids as big as possible while ensuring their clonality and suitable culturing conditions will increase the success rate in establishing clonal organoid lines.

There are three time points at which a clonal organoid can be picked (ordered according to our preference):

- after selection on the initial plating

Note: This option does not require dissociation to single cells. Therefore, it is very suitable for sensitive lines and can also be applied to mouse SI organoids which are growing in their regular crypt-like budding structure (ENR medium).

- after selection and subsequent FACS-purification of single STAR⁺ cells

Note: Broadly applicable strategy given that STAR⁺ cells constitute the stem cell population, i.e. can regenerate the organoid culture.

- after selection and subsequent thorough trypsinisation to single cells.

Note: This option is preferable in organoid systems in which STAR⁺ cells do not constitute the (sole) stem cell population. For instance, some lung and stomach cancers show upregulation of ASCL2, while it is not expressed during homeostasis (Hu et al., 2015; Huang et al., 2018; Zuo et al., 2018). Thus, the nature of STAR⁺ cells in respective cancer organoids is not well defined yet.

Note: Before you start: Label Eppendorf collection tubes and put them on ice

Optional: Add 10 μ L of Advanced DMEM/F12 into each collection tube to more easily release the organoids into medium.

Timing: 1 h (may be longer if multiple clones are picked)

100. Select a Matrigel droplet with a big STAR fluorescent organoid using a tabletop microscope.

101. Discard culture medium of the selected culture well.
102. Use 50 μ L ice-cold (4°C) Advanced DMEM/F12 to dissolve selected Matrigel droplet by tilting the culture plate and placing a pipette-tip (200 μ L) above the droplet.
103. Take up the Matrigel droplet and transfer it into a 15 mL falcon tube.
104. **Optional:** Add 200 μ L 1X dispase to the tube and incubate at 37°C for 5 min until Matrigel is properly dissolved.
105. Top up to 10 mL with ice-cold Advanced DMEM/F12 and carefully pellet organoids by spinning at 300 x g at 4°C for 4 min.
106. Take off medium and carefully resuspend organoids in 100 μ L Advanced DMEM/F12.

Note: If there are many organoids, increase the volume of Advanced DMEM/F12 to facilitate the next steps.

107. Spot organoid suspension onto the inside of the lid of a 10 cm culture dish, while making droplets of approximately 20 μ L volume (Figure 6C).
108. Locate organoids using a table-top or stereomicroscope.
109. For droplets having just one organoid, take up the medium droplet and transfer the organoid into a separate collection tube by carefully pipetting up and down. Verify that the organoid is transferred. If multiple organoids are in the same droplet, carefully take up single organoids using a 20 μ L pipet, while checking through the oculars that the other organoids stay put. Transfer organoid into an Eppendorf tube (Figure 6C).
110. Keep Eppendorf tubes on ice while picking.
111. Add 100 μ L fresh Trypsin EDTA and incubate at 37°C for 5 min, while vortexing every minute.

Note: This step is recommended for most organoid lines as it allows for the highest plating density. Mouse SI organoids, however, and organoids with a low single cell plating efficiency may benefit from mechanical disruption instead.

Alternative: (to step 114) *Mechanically disrupt organoid by adding 200 μ L cold Advanced DMEM and pipetting up and down with a p200 tip several times.*

112. Check under the microscope that the organoids has dissociated into small fragments/single cells. Otherwise, prolong the trypsin incubation step.

113. Add 100 μL trypsin inhibitor and top up to 1 mL with Advanced DMEM.
114. Spin Eppendorf tube at 4°C, 500 x g for 5 minutes.
115. Carefully take of supernatant, while leaving 5-10 μL supernatant to not agitate the pellet

Troubleshoot 6: Cell loss when picking clonal organoids

116. Add 30-50 μL Matrigel and mix gently by pipetting up and down.
117. Plate Matrigel in 2 droplets onto a pre-warmed 48-well plate with one droplet per well.

Note: Efficient clonal outgrowth requires at least 5 crypt-like structures (mouse small intestinal organoids in ENR state) or 100 single cells per Matrigel droplet of 10 μL .

118. Incubate the plate upside-down in the incubator for 10-25 min until the Matrigel has solidified
119. Add 250 μL organoid medium with 10 μM Y-27632 and 100 $\mu\text{g}/\text{mL}$ primocin (since clonal organoids has been exposed to an environment outside the hood).

Note: In case of a low yield or organoid lines that are particularly sensitive to low density, it may be conceivable to plate STAR⁺ cells together with reporter-negative cells to support organoid growth. FACS purification can be subsequently used to isolate all STAR⁺ cells. Troubleshoot 7: Cell death after passaging clonal organoids

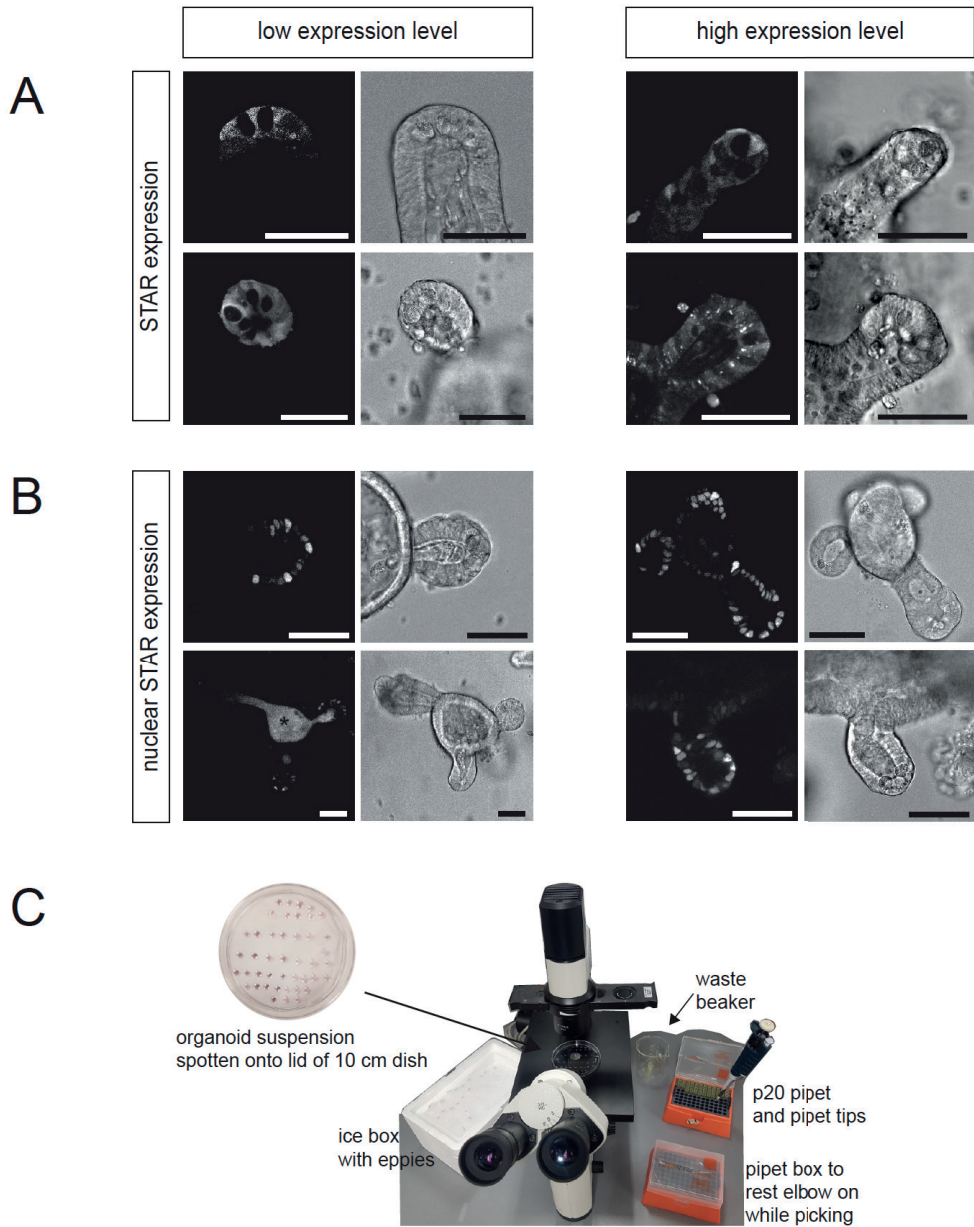


Figure 6: Selecting and picking a clonal STAR organoid.

A-B. Organoids with low and high STAR expression levels (white) are depicted on the left and right, respectively. (A) Four examples of crypt structures with STAR expression (uniform cell labelling) that demonstrate clear separation between stem cell niche and TA-region and exclusion of Paneth cells. (B) Four examples of clonal organoids with nuclear STAR expression. (*) auto-fluorescence. Scale bars, 50 μ m. **C.** Example set-up for picking of clonal organoids using a benchtop microscope.

EXPECTED OUTCOMES

STAR activity reflects the transcriptional activity of the intestinal stem cell specific transcription factor ASCL2. Hence, STAR labels intestinal stem cells and, with decreasing intensity along the crypt-villus axis, transit amplifying cells (but not differentiated cells). The overall intensity levels depend on the number of ASCL2-binding motif repeats (STAR repeats, compare Figure 2), the brightness of the fluorophore, and the laser intensity used for exposure. While the nature of the STAR intensity gradient along the crypt-villus axis is independent of these parameters, the absolute intensity impacts on the visual manifestation of the gradient (Figure 6A-B). We therefore recommend analyzing multiple clonal organoids and compare their STAR expression to get the best fit for your research question.

1. Plate clonal STAR organoid cultures on glass for live-cell microscopy.

Note: It is convenient to have multiple clonal lines (> 3 clonal lines) to compare them with each other. In the end the aim is to report both reliable and efficient ASCL2 activity in stem cells.

2. Image STAR expression levels and pick your favorite. The range of STAR patterning in clonal organoids is depicted in Figure 6 A-B.

LIMITATIONS

STAR reports the transcriptional activity of ASCL2, thus its application is limited to tissues that express ASCL2 (such as the small and large intestine, placenta, and several tumor tissues (Jubb *et al.*, 2006, Proteinatlas 2020). The recent discovery of ASCL2 controlling the LGR5⁺ stem cell state in the intestine, makes STAR a versatile tool to report intestinal stemness which partially overlaps but is more exclusive than Wnt activity (Murata *et al.*, 2020; Oost *et al.*, 2018; Schuijers *et al.*, 2015). While STAR has been successfully applied in mouse and human intestinal tissues, extending the range to other species and tissues is hitherto untested. Furthermore, for tissues in which ASCL2 is expressed by a differentiated cell type rather than the stem cell compartment, reporter plasmids with STAR-driven expression of the antibiotic selection cassette are not suitable. It is advisable therefore to choose reporter plasmids with an independent, uniform promoter which drives the expression of a selection cassette and works in parallel to STAR (see Table 1).

When analyzing cell type conversions, it is important to note that while the STAR signal is maintained by ongoing ASCL2 transcriptional activity, its decay is mainly determined by the half-life of the fluorescent protein itself and not directly related to the stability

of ASCL2. Additionally, expansion media for organoids are generally rich in stem cell supporting factors which, in turn, can lead to widespread STAR activity at varying levels within a single organoid. For instance, with respect to the intestine, this reflects the stemness gradient from the crypt bottoms up to the transit amplifying zone. Please note, conditions that favor cellular differentiation, either by modulating the media composition or xenotransplantation in mice which provides a more native micro-environment, facilitates cellular diversity and might be desirable depending on the organoid system and the research question (Fumagalli et al., 2020; Oost et al., 2018).

TROUBLESHOOTING

Problem 1:

STAR won't integrate into the genome.

Potential Solution for Lentiviral Approach (Protocol A):

Infecting organoids requires a much higher virus titer than most cell lines. Therefore, concentration of the virus prior to transduction and the addition of polybrene may be key to success. To test for successful virus production, a cell line of choice can be transduced alongside with the organoids (using a small split of the virus suspension). The STAR signal should be visible after 1-2 days. If the cell line does not express ASCL2, transient transfection of ASCL2 (and oncogenic beta-catenin) is required to test for successful transduction (see [Troubleshoot 8: How to functionally test the STAR plasmid](#)). Note, however, that while this test can be easily performed alongside with the actual transduction, it is inconclusive on the amount of virus particles being produced.

Potential Solution for Transposon-Based Approach with Electroporation (Protocol B):

Double (or triple) the amount of STAR reporter DNA and of Tol2 transposase. When viability is not the limiting step, you may increase the poring pulse (up to 220 Ω in steps of 10 Ω for instance) and/or poring pulse length (up to 10 msec, in steps of 1 msec).

Potential Solution for Transposon-Based Approach with Transfection Reagent (Protocol C):

If transfection with a transfection reagent does not work well, consider using the transfection with electroporation protocol (protocol B).

Problem 2:

No access to the indicated lentiviral envelope, packaging vectors or transfection reagent.

Potential Solution:

The three plasmids pHDM-G, pHDM-Hgpm2, and pRC-CMV-rev1b lead to the expression of VSV-G, gag and pol, and rev, respectively. Alternative plasmids containing these functional elements are commercially available, for instance on Addgene.

Alternatively to X-tremeGENE 9, the authors have successfully used TransIT-LT1 (Sopachem, MIR 2360) for the transfection of 293T cells during virus making (protocol A1, with a ratio of 2 μ l transfection reagent for 1 μ g of DNA). However, the transfection of STAR into organoids using a transfection reagent (protocol C2) has so far only been performed with X-tremeGENE 9 by the authors. While other transfection reagents might be suitable as well, we cannot comment on necessary adaptations to the existing protocol.

Problem 3:

The cells die upon transduction with STAR lentiviruses.

Potential Solution:

The virus titre might be too high. We suggest to set-up a small dilution range of the virus (following ultracentrifugation) and transduce cells with different virus titers. If the cells are readily transducible, like some cell lines, ultracentrifugation is obsolete as the viral supernatant can be directly harvested of the virus-producing 293T cells, filtered with a 45 μ m strainer (see protocol A step 9), supplemented with 8 μ g/mL polybrene, and added on top of the receiving cells.

Problem 4:

Electroporation kills all cells.

Potential Solution:

Use up to 1 million cells per electroporation (while ensuring that the impedance is within the limits of 30-55 Ω). If still unsuccessful, lower the poring voltage and/or poring pulse length to make the procedure less harsh.

Problem 5:

The cells are resistant to the selection antibiotic but there is no STAR signal.

Potential Solution:

For plasmids in which the antibiotics selection cassette is controlled by an independent promoter, it is conceivable that expression of the reporter gene is compromised by epigenetic silencing of the STAR promoter/enhancer site, while the ubiquitous promoter is still active. If this applies to a subculture, FACS purification of STAR⁺ cells or establishing a clonal line from STAR⁺ cells may solve the problem. Otherwise, when working with colorectal cancer organoids, make sure ASCL2 is still expressed in this tissue. You may also consider to integrate insulator sequences around the reporter to reduce the risk of epigenetic silencing (Ramezani et al., 2003). Note, however, that insulator sequences might be detrimental for the virus titer (Hanawa et al., 2009).

Problem 6:

Loss of cells while picking clonal organoids.

Potential Solution:

Pre-coat Eppendorf tubes with 10 % fetal bovine serum or 1% BSA to prevent the cells from sticking to the plastic. If the cells easily stick to the pipet tip (check under the microscope), consider to pre-coat the tips as well. After trypsinizing the organoid and spinning down the single cell suspension, check under a table-top microscope to identify the location of the pellet. Carefully tilt the Eppendorf tube and take off media in multiple steps while checking that the pellet stays intact after each pipetting step. Collect supernatant in second Eppendorf tube to make sure the cells can be recovered in case the pellet is loose. Alternatively use 15 mL falcon tubes to get a cleaner pellet.

Problem 7:

When generating clonal lines, the cells derived from a single organoid have difficulties surviving after the first passage.

Potential Solution:

Organoid cells require a minimum density for successful outgrowth. Consider plating the cells in the presence of STAR-negative supporter cells of the same line to increase

the plating density. This step requires subsequent purification of STAR⁺ cells at a later time-point (e.g. by FACS).

Problem 8:

How to functionally test the STAR plasmid.

Potential Solution:

Transiently transfect a cell line of your choice with the STAR plasmid. If the cells express ASCL2, the fluorescent protein should be visible under a confocal laser microscope. As 293T cells do not express ASCL2, STAR plasmids can be tested by co-transfecting ASCL2 (and oncogenic beta-catenin) to stimulate ASCL2 activity. For suitable plasmids, see Schuijers et al (Schuijers et al., 2015).

Problem 9:

No access to growth factor conditioned media.

Potential Solution:

Wnt 3A, Noggin, and R-Spondin 1 conditioned media can be replaced by the Wnt Surrogate-Fc fusion protein, the Noggin-FC fusion protein conditioned medium, and the R-Spondin 3-FC fusion protein conditioned medium, respectively (U-Protein Express, Cat. No. #N001, #N002, and #R001, respectively).

The recommended concentration of the Wnt Surrogate-Fc fusion protein (U-protein Express, Cat.No. #N001) is around 0.1-0.5 μ M. It should be noted, however, that the optimal concentration might vary per organoid line. The recombinant Noggin and R-Spondin 3 may be used 1:100.

Other recombinant proteins are commercially available and might be suitable as well but the authors do not have any experience with them.

RESOURCE AVAILABILITY

Lead Contact

Further information and requests for resources and reagents should be directed to and will be fulfilled by the Lead Contact, Dr Hugo Snippert (H.J.G.Snippert@umcutrecht.nl).

Materials Availability

STAR plasmids referred to this study have been deposited to Addgene as listed in the Table 1. Additional plasmids required to perform the protocols are commercially available (Addgene or plasmID) and are listed in the key resource table.

Data and Code Availability

The sequences of the STAR plasmids and the Tol2 transposase are available on Addgene via the Addgene numbers indicated in Table 1 and the Key Resource Table.

ACKNOWLEDGMENTS

We thank all members of the Snippert lab for valuable discussions and practical input, in particular Ingrid Verlaan-Klink for her help in testing different transfection reagents. We also thank Jeroen van Velzen and Pien van der Burght of the Flow Core cytometry Facility in the UMC Utrecht for support. This work was supported by a KWF fellowship from the Dutch Cancer Society (UU 2013-6070) and an ERC Starting Grant (IntratumoraNiche - 803608). This work is part of the Oncode Institute which is partly financed by the Dutch Cancer Society.

AUTHOR CONTRIBUTIONS

M.C.H. and K.C.O. cloned the STAR plasmids and optimized the protocols. H.J.G.S. supervised the research. All authors wrote the manuscript.

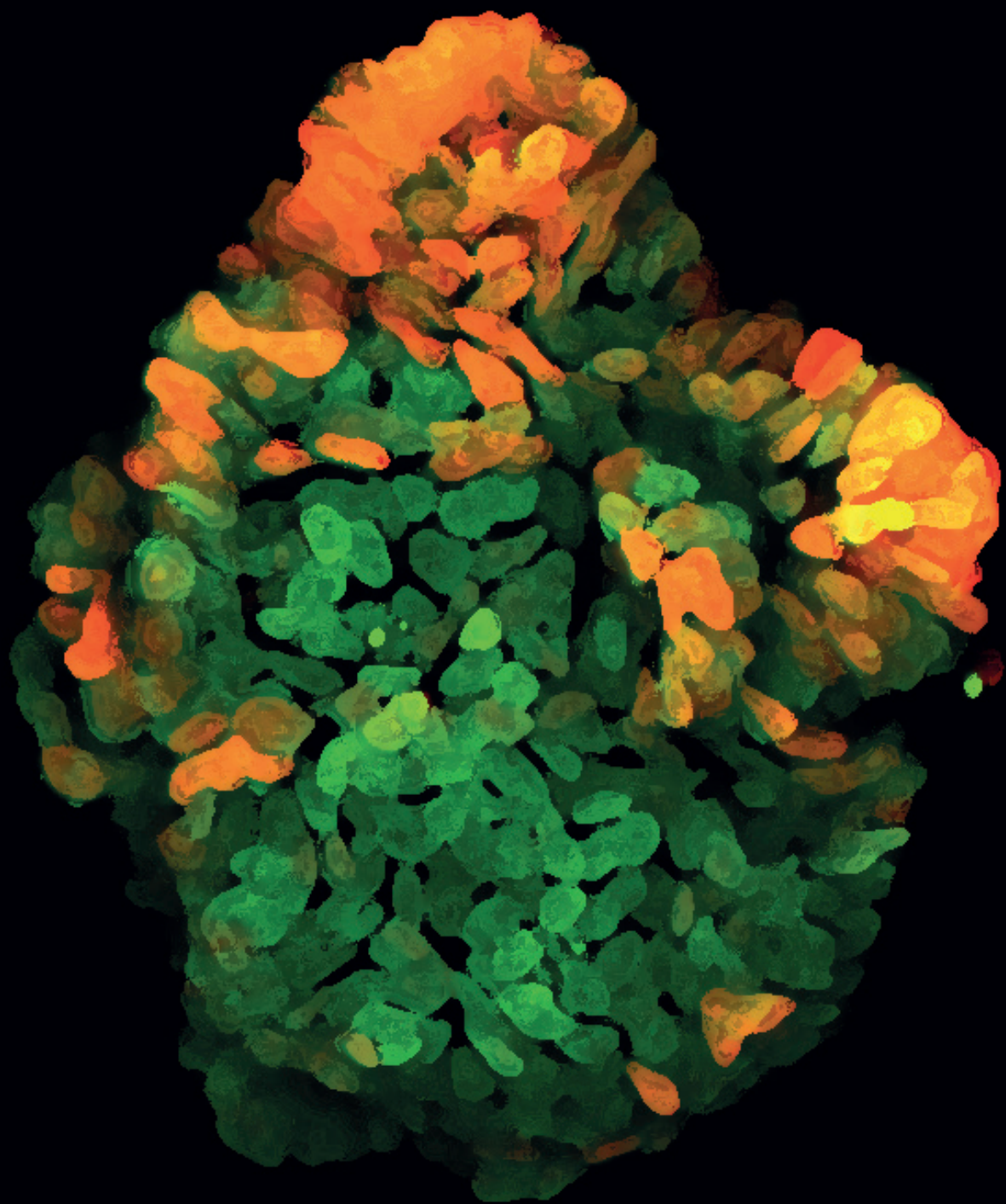
DECLARATION OF INTERESTS

H.J.G.S. and K.C.O. filed a patent concerning applications of STAR (ASCL2-responsive reporters for labelling of intestinal stem cell activity; WO Patent WO/2020/020,471).

REFERENCES

1. Andersson-Rolf, A., Fink, J., Mustata, R.C., and Koo, B.K. (2014). A video protocol of retroviral infection in primary intestinal Organoid culture. *J. Vis. Exp.* 1–8.
2. Drost, J., van Jaarsveld, R.H., Ponsioen, B., Zimmerlin, C., van Boxtel, R., Buijs, A., Sachs, N., Overmeer, R.M., Offerhaus, G.J., Begthel, H., et al. (2015). Sequential cancer mutations in cultured human intestinal stem cells. *Nature* 521, 43–47.
3. Van der Flier, L.G., Sabates-Bellver, J., Oving, I., Haegerbarth, A., De Palo, M., Anti, M., Van Gijn, M.E., Suijkerbuijk, S., Van de Wetering, M., Marra, G., et al. (2007). The Intestinal Wnt/TCF Signature. *Gastroenterology* 132, 628–632.
4. Fujii, M., Matano, M., Nanki, K., and Sato, T. (2015). Efficient genetic engineering of human intestinal organoids using electroporation. *Nat. Protoc.* 10, 1400–1474.
5. Fujii, M., Matano, M., Toshimitsu, K., Takano, A., Mikami, Y., Nishikori, S., Sugimoto, S., and Sato, T. (2018). Human Intestinal Organoids Maintain Self-Renewal Capacity and Cellular Diversity in Niche-Inspired Culture Condition. *Cell Stem Cell* 23, 787–793.e6.
6. Fumagalli, A., Oost, K.C., Kester, L., Morgner, J., Bornes, L., Bruens, L., Spaargaren, L., Azkanaz, M., Schelfhorst, T., Beerling, E., et al. (2020). Plasticity of Lgr5-Negative Cancer Cells Drives Metastasis in Colorectal Cancer. *Cell Stem Cell* 26, 569–578.e7.
7. Hanawa, H., Yamamoto, M., Zhao, H., Shimada, T., and Persons, D.A. (2009). Optimized Lentiviral Vector Design Improves Titer and Transgene Expression of Vectors Containing the Chicken β -Globin Locus HS4 Insulator Element. *Mol. Ther.* 17, 667–674.
8. Hu, X., Chen, L., Wang, Q., Zhao, X., Tan, J., Cui, Y., Liu, X., Zhang, X., and Bian, X. (2015). Elevated expression of ASCL2 is an independent prognostic indicator in lung squamous cell carcinoma. *J. Clin. Pathol.* jclinpath-2015-203025.
9. Huang, Y.H., Klingbeil, O., He, X.Y., Wu, X.S., Arun, G., Lu, B., Somerville, T.D.D., Milazzo, J.P., Wilkinson, J.E., Demerdash, O.E., et al. (2018). POU2F3 is a master regulator of a tuft cell-like variant of small cell lung cancer. *Genes Dev.* 32, 915–928.
10. Jubb, A., Chalasani, S., Frantz, G., Smits, R., Grabsch, H., Kavi, V., Maughan, N., Hillan, K., Quirke, P., and Koeppen, H. (2006). Achaete-scute like 2 (*ascl2*) is a target of Wnt signalling and is upregulated in intestinal neoplasia. *Oncogene* 2, 3445–3457.
11. Koo, B.K., Stange, D.E., Sato, T., Karthaus, W., Farin, H.F., Huch, M., Van Es, J.H., and Clevers, H. (2012). Controlled gene expression in primary Lgr5 organoid cultures. *Nat. Methods* 9, 81–83.
12. Van Lidth de Jeude, J.F., Vermeulen, J.L.M., Montenegro-Miranda, P.S., Van den Brink, G.R., and Heijmans, J. (2015). A protocol for lentiviral transduction and downstream analysis of intestinal organoids. *J. Vis. Exp.* 2015.
13. Murata, K., Jadhav, U., Madha, S., van Es, J., Dean, J., Cavazza, A., Wucherpennig, K., Michor, F., Clevers, H., Shivdasani, R.A., et al. (2020). *Ascl2*-Dependent Cell Dedifferentiation Drives Regeneration of Ablated Intestinal Stem Cells. *Cell Stem Cell* 1–14.
14. Oost, K.C., van Voorthuisen, L., Fumagalli, A., Lindeboom, R.G.H., Sprangers, J., Omerzu, M., Rodriguez-Colman, M.J., Heinz, M.C., Verlaan-Klink, I., Maurice, M.M., et al. (2018). Specific Labeling of Stem Cell Activity in Human Colorectal Organoids Using an ASCL2-Responsive Minigene. *Cell Rep.* 22, 1600–1614.
15. Ramezani, A., Hawley, T.S., and Hawley, R.G. (2003). Performance- and safety-enhanced lentiviral vectors containing the human interferon- β scaffold attachment region and the chicken β -globin insulator. *Blood* 101, 4717–4724.

16. Sato, T., Vries, R.G., Snippert, H.J., van de Wetering, M., Barker, N., Stange, D.E., van Es, J.H., Abo, A., Kujala, P., Peters, P.J., et al. (2009). Single Lgr5 stem cells build crypt-villus structures in vitro without a mesenchymal niche. *Nature* 459, 262–265.
17. Sato, T., Stange, D.E., Ferrante, M., Vries, R.G.J., van Es, J.H., van Den Brink, S., van Houdt, W.J., Pronk, A., van Gorp, J., Siersema, P.D., et al. (2011). Long-term expansion of epithelial organoids from human colon, adenoma, adenocarcinoma, and Barrett's epithelium. *Gastroenterology* 141, 1762–1772.
18. Schuijers, J., Junker, J.P., Mokry, M., Hatzis, P., Koo, B.K., Sasselli, V., Van Der Flier, L.G., Cuppen, E., Van Oudenaarden, A., and Clevers, H. (2015). Ascl2 acts as an R-spondin/wnt-responsive switch to control stemness in intestinal crypts. *Cell Stem Cell* 16, 158–170.
19. Schwank, G., Andersson-Rolf, A., Koo, B.-K., Sasaki, N., and Clevers, H. (2013). Generation of BAC Transgenic Epithelial Organoids. *PLoS One* 8, 6–11.
20. Shimokawa, M., Ohta, Y., Nishikori, S., Matano, M., Takano, A., Fujii, M., Date, S., Sugimoto, S., Kanai, T., and Sato, T. (2017). Visualization and targeting of LGR5+ human colon cancer stem cells. *Nature* 1–21.
21. Sugimoto, S., Ohta, Y., Fujii, M., Matano, M., Shimokawa, M., Nanki, K., Date, S., Nishikori, S., Nakazato, Y., Nakamura, T., et al. (2017). Reconstruction of the Human Colon Epithelium In Vivo. *Cell Stem Cell* 1–6.
22. Ziskin, J.L., Dunlap, D., Yaylaoglu, M., Fodor, I.K., Forrest, W.F., Patel, R., Ge, N., Hutchins, G.G., Pine, J.K., Quirke, P., et al. (2013). In situ validation of an intestinal stem cell signature in colorectal cancer. *Gut* 62, 1012–1023.
23. Zuo, Q., Wang, J., Chen, C., Zhang, Y., Feng, D.-X., Zhao, R., and Chen, T. (2018). ASCL2 expression contributes to gastric tumor migration and invasion by downregulating miR223 and inducing EMT. *Mol. Med. Rep.* 3751–3759.



CHAPTER

3

Liver Colonization by Colorectal Cancer Metastases Requires YAP-Controlled Plasticity at the Micrometastatic Stage

Maria C. Heinz^{1,2,*}, Niek A. Peters^{3,*}, Koen C. Oost^{1,2}, Rik G. H. Lindeboom^{2,4,5}, Lisa van Voorthuijsen^{2,4,5}, Arianna Fumagalli^{2,5,§}, Mirjam C. van der Net¹, Gustavo de Medeiros⁶, Joris H. Hageman^{1,2}, Ingrid Verlaan-Klink^{1,2}, Inne H. M. Borel Rinkes⁷, Prisca Liberali^{6,8}, Martijn Gloerich¹, Jacco van Rheenen^{2,5}, Michiel Vermeulen^{2,4}, Onno Kranenburg^{3,#}, Hugo J. G. Snippert^{1,2,#}

¹ Center for Molecular Medicine, University Medical Center Utrecht, Utrecht, the Netherlands.

² Oncode Institute, the Netherlands.

³ Division of Imaging and Cancer, University Medical Center Utrecht, Utrecht, the Netherlands.

⁴ Department of Molecular Biology, Faculty of Science, Radboud Institute for Molecular Life Sciences, Radboud University Nijmegen, Nijmegen, the Netherlands.

⁵ Department of Molecular Pathology, Netherlands Cancer Institute, Amsterdam, the Netherlands.

⁶ Quantitative Biology, Friedrich Miescher Institute for Biomedical Research (FMI), Basel, Switzerland.

⁷ Department of Surgery, University Medical Center Utrecht, Utrecht, the Netherlands.

⁸ University of Basel, Basel, Switzerland.

*: Equal contribution. †: Equal contribution.

#: Lead Contact.

Cancer Research, doi: 10.1158/0008-5472.CAN-21-0933.

SUMMARY

Micrometastases of colorectal cancer (CRC) can remain dormant for years prior to the formation of actively growing, clinically detectable lesions (i.e., colonization). A better understanding of this step in the metastatic cascade could help improve metastasis prevention and treatment. Here we analyzed liver specimens of CRC patients and monitored real-time metastasis formation in mouse livers using intravital microscopy to reveal that micrometastatic lesions are devoid of cancer stem cells (CSC). However, lesions that grow into overt metastases demonstrated appearance of *de novo* CSCs through cellular plasticity at a multicellular stage. Clonal outgrowth of patient-derived CRC organoids phenocopied the cellular and transcriptomic changes observed during *in vivo* metastasis formation. First, formation of mature CSCs occurred at a multicellular stage and promoted growth. Conversely, failure of immature CSCs to generate more differentiated cells arrested growth, implying that cellular heterogeneity is required for continuous growth. Second, early stage YAP activity was required for the survival of organoid-forming cells. However, subsequent attenuation of early stage YAP activity was essential to allow for the formation of cell type heterogeneity, while persistent YAP signalling locked micro-organoids in a cellularly homogenous and growth-stalled state. Analysis of metastasis formation in mouse livers using single cell RNA-sequencing confirmed the transient presence of early stage YAP activity followed by emergence of CSC and non-CSC phenotypes, irrespective of the initial phenotype of the metastatic cell of origin. Thus, establishment of cellular heterogeneity after an initial YAP-controlled outgrowth phase marks the transition to continuously growing macrometastases.

STATEMENT OF SIGNIFICANCE

Characterization of the cell type dynamics, composition, and transcriptome of early colorectal cancer liver metastases reveals that failure to establish cellular heterogeneity through YAP-controlled epithelial self-organization prohibits the outgrowth of micrometastases.

INTRODUCTION

Epithelial tissue turnover is fuelled by a small pool of self-renewing stem cells (SCs) that give rise to a large population of differentiated cells. Colorectal cancers (CRC) comprise similar cell populations to the healthy intestine, including cell types reminiscent of cycling SCs as well as differentiated cells (1–4). Furthermore, the cellular hierarchy observed in normal epithelium is vastly maintained in tumours where so-called cancer stem cells (CSCs), marked by *Lgr5*, constitute a self-renewing population that fuels cancer growth by generating all epithelial cell types present in CRCs (3,5). Both in intestinal homeostasis and cancers, genetic lineage tracing experiments have revealed a high degree of plasticity where more differentiated cells regain SC potential often triggered by external cues (6).

The main cause of CRC-related mortality is metastatic spread to distant organs such as the liver and lungs. Metastases exhibit cellular heterogeneity resembling the tissue of origin (7). Similarly to primary CRCs, *Lgr5*⁺ CSCs are indispensable for metastatic growth and maintenance in murine models (5,8). Considering the central role of CSCs within the cellular organisation of tumours and metastases, it has been a long-held belief that CRC metastases are seeded by CSCs. However, using mouse models it was recently demonstrated that the vast majority of disseminating CRC tumour cells are *Lgr5*⁻, while *Lgr5*⁺ CSCs reappear at the distant site (8).

Metastatic colonisation, that is the successful outgrowth of a (dormant) micrometastasis into an actively growing overt lesion, is a rate limiting step in the metastatic cascade (9,10). Illustrative of this is the phenomenon of metastatic latency in CRC patients. Micrometastases can remain dormant and undetected in the liver for years after surgical removal of the primary tumour, eventually regaining proliferative behaviour and resulting in overt metastases (11). Yet, their small size and inactive nature make micrometastases difficult to detect and study. As a result, it remains elusive as to how a single metastasizing cell grows out into a heterogeneous cell mass, and which features are critical for its success (7). Although the microenvironment has been previously implicated in population dormancy (12,13), the epithelial side underlying cellular dormancy is poorly understood.

Adult SC-derived organoids have emerged as a tool to study both normal and cancerous tissue physiology (14,15). In particular, their genetic tractability and accessibility allow detailed studies on cellular differentiation trajectories in human and mouse intestinal tissue (16–18) and permit detailed insights into the intrinsic nature of epithelial self-organisation.

In this study, we are using a combination of patient biopsies, functional patient-derived xenografts (PDX) and mouse models of CRC to study plasticity at different stages of *in vivo* metastasis formation in the liver. We demonstrate a close resemblance in cellular organisation and patterning between liver metastasis formation *in vivo* and clonal outgrowth of patient-derived CRC organoids (PDOs). Through detailed imaging and transcriptomic analysis, our organoid and *in vivo* data reveal that epithelial self-organisation involving attenuation of high levels of YAP activity followed by the formation of cell type heterogeneity is required to transition from the micrometastatic stage to overt liver colonisation.

RESULTS

Liver micrometastases of human colorectal cancers are devoid of classical stem cell markers

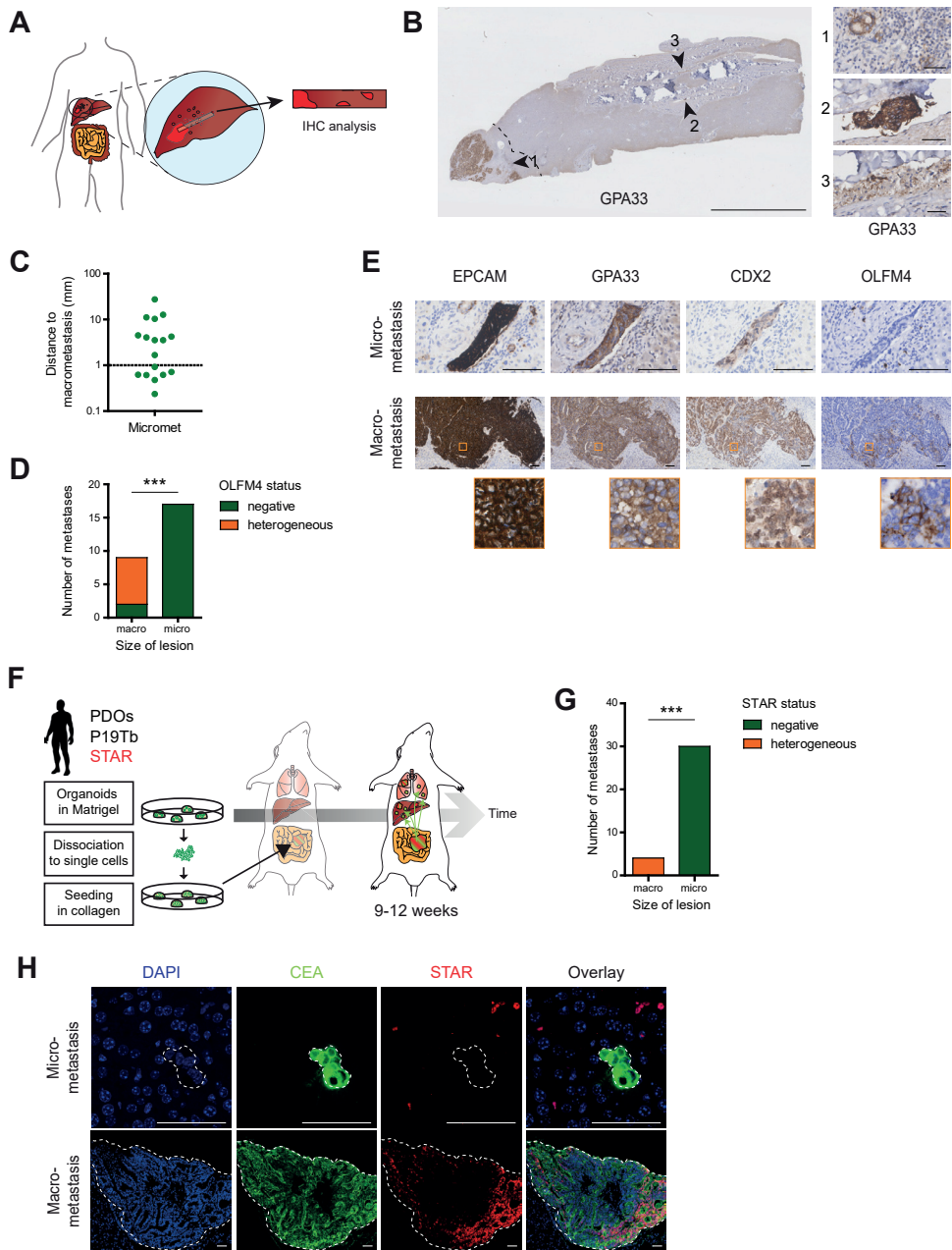
Recent data suggests that metastatic growth requires CSCs (5,8). Yet, examining the presence of CSCs in patient micrometastases is challenging due to their small size and sporadic appearance. Therefore, we collected liver tissue strips of patients undergoing surgical removal of CRC liver metastases (Table S1), which start at the clinically detectable metastatic lesion and extend 5-10 cm into the adjacent liver tissue (Figure 1A-B). Using immunohistochemistry (IHC) against three colonic markers (EPCAM, GPA33, and CDX2, Table S2), we could faithfully identify 17 micrometastatic lesions in 18 patients. (Figures 1B, S1A-H).

We ensured that the micrometastatic lesions are independent entities by demonstrating the absence of branches towards macrometastases using IHC on consecutive sections. Additionally, most micrometastases exceeded 1mm in distance to the macrometastatic lesion (Figure 1C), which is the margin used for radical resection in the clinic (35).

To examine the cellular composition of micrometastases, we set out to perform IHC analysis for intestinal SC markers. Frequently used intestinal SC markers comprise LGR5, ASCL2, and OLFM4 (29,36–39). Due to the lack of proven antibodies against human LGR5 or ASCL2, we stained human liver metastases with an OLFM4 antibody whose suitability we confirmed on human colonic sections (Figure S1D). Most macroscopic lesions displayed a heterogeneous expression pattern, reminiscent of a subpopulation of OLFM4⁺ CSCs. Conversely, all micrometastatic lesions were completely devoid of OLFM4 (Figure 1D-E, Figure S1G-H), suggesting the lack of OLFM4⁺ CSCs at the micrometastatic stage.

Compromised by limited availability of IHC-compatible SC-markers, we decided to corroborate the OLFM-based patient data with the analysis of spontaneously formed liver metastases upon orthotopic transplantation of human CRC organoids into the caecum of mice (Figure 1F). In these metastases, we assessed activity of our previously developed intestinal SC reporter STAR (40) that reflects the transcriptional activity of ASCL2, the master regulator of intestinal SC fate (37,39).

While the number of macrometastases was limited (n = 4, humane endpoint after 9-12 weeks), micrometastatic lesions identified through expression of human CEA were very abundant (n = 30). CSC activity, visualised with STAR-driven sTomato (Figure S11-J), showed a heterogeneous expression pattern in macroscopic metastases, while being enriched at the rim of the tumour where most actively growing clones reside (41). In contrast, no STAR signal could be detected in any microscopic lesion (Figure 1G-H), indicating that classical CSCs are absent in liver micrometastases of human CRC.



◀Figure 1: Liver micrometastases of human colorectal cancers are devoid of classical stem cell markers

A. Graphical representation of liver tissue strips extending from macrometastases into adjacent liver tissue. **B.** Liver tissue strip stained for GPA33 to identify macro- and micrometastases (arrowheads). Dashed lines indicates 1mm distance to macrometastasis. Scale bar, 5mm (50µm in close-ups). **C.** Distance of identified micrometastases to their respective macrometastasis. Each dot represents one lesion. **D.** Bar graph summarising OLFM4 expression patterns in all macro- and micrometastases as either completely absent (green) or heterogeneous (orange). **E.** Representative IHC stainings of a macro- and micrometastasis of the same patient. Macrometastasis shows heterogeneous OLFM4 expression. Close-ups, orange boxes. Scale bars, 100 µm. **F.** Experimental setup for spontaneous metastasis formation in mice using orthotopic transplantation of human CRC PDOs with analysis after 9-12 weeks. **G.** Bar graph depicting the presence of STAR⁺ CSCs in liver macro- or micrometastases, identified and classified (size) through IHC against human CEA. **H.** Representative images related to G. STAR minigene is unique to xenotransplanted cancer line. Signal outside CEA-marked metastasis is background. Scale bars, 50 µm.

Lgr5⁺ CSCs appear at micrometastatic stages and mark the transition towards successful metastatic colonisation

To understand the relationship between CSC appearance and growth kinetics of liver metastases, we set out to monitor these parameters for individual metastatic lesions over time by intravital microscopy (IVM). To monitor live metastatic outgrowth, we turned to a well-known mouse CRC cancer model (*Apc*, *Kras*, and *Tp53* mutant) (8), in which we used the Lgr5-DTR-eGFP knock-in allele as SC marker. As circulating tumour cells of this model have previously been shown to be Lgr5⁺ (8), we FACS-purified Lgr5⁺ tumour cells as previously described (8) and injected them into the mesenteric vein to synchronise seeding of liver metastases (Figure 2A). After surgical implantation of an abdominal imaging window (22,42) (Day 5), we could track the outgrowth of multiple metastatic lesions over time (3-10 days), while assessing their size and cellular composition (Figure 2B-E). Most lesions were first entirely Lgr5⁻ with *de novo* Lgr5⁺ cells appearing during the next days. Notably, this *symmetry break* in terms of spontaneous CSC appearance coincided with a burst in growth (Figure 2C-D). In strong contrast, microscopic lesions without appearance of Lgr5⁺ cells displayed limited to no growth (Figures 2E, S1K). Thus, the establishment of a SC-driven cellular organisation defines the transition towards continuous, colonising growth.

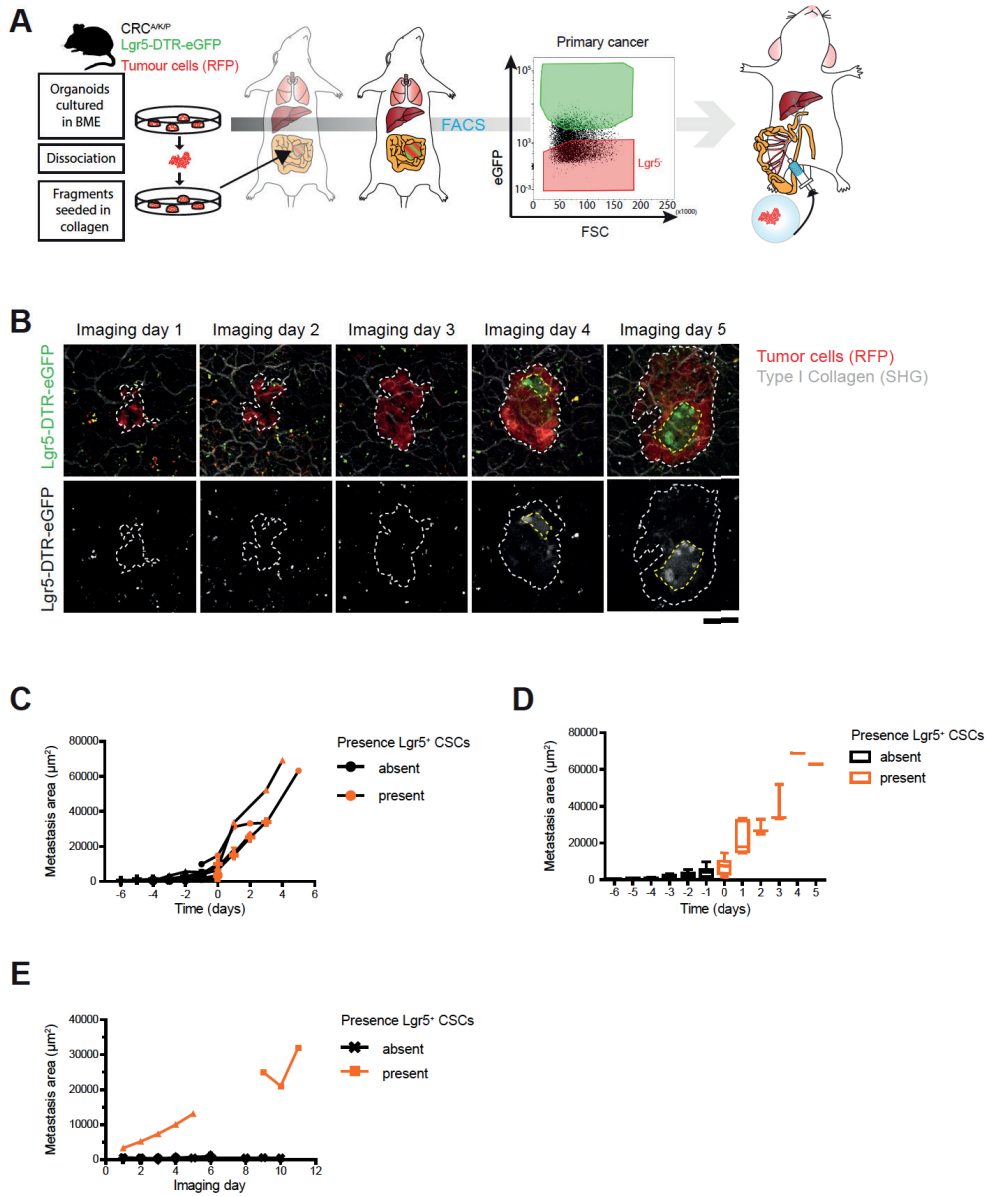


Figure 2: Lgr5⁺ CSCs appear at micrometastatic stages and mark the transition towards successful metastatic colonisation

A. Experimental setup for timed metastasis formation assay in mice: RFP⁺ murine *Apc*^{FL/FL}/*Kras*^{G12D/+}/*Tp53*^{KO/KO} cancer organoids were orthotopically transplanted into mice to form primary cancers. After 8-10 weeks, Lgr5⁺ primary tumour cells were collected by FACS and injected into the mesenteric vein of recipient mice. Growth kinetics and cellular dynamics of growing liver metastases were monitored

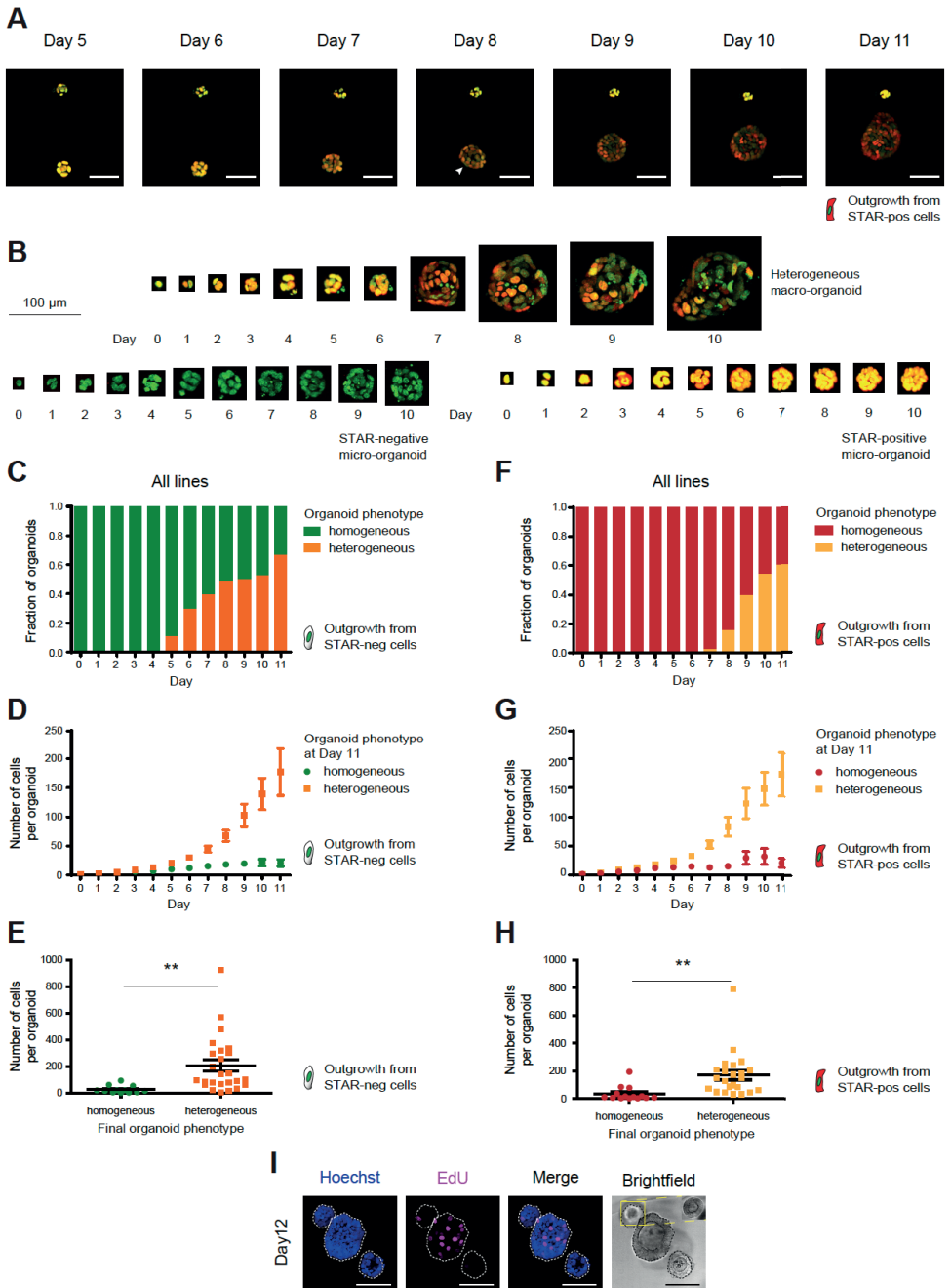
by intravital microscopy (IVM). Stem cells are labelled by endogenous Lgr5-DTR-eGFP expression. **B.** Representative IVM images of one liver metastasis taken on consecutive days. Top: RFP⁺ tumour cells (red) visualising tumour mass, Lgr5-DTR-eGFP expression (green) marking CSCs. Bottom: Identical panels in false colours. Dashed line: Metastasis border. Scale bar, 50 μm . **C.** Traces depicting the size of individual metastatic lesions that develop cellular heterogeneity over time. Day 0: time of *de novo* appearance of Lgr5⁺ CSCs. Black and orange symbols refer to time points prior to and post symmetry break, respectively. **D.** As in C, with the mean metastasis size of all lesions represented by a box plot. Whiskers representing min to max. **E.** Traces showing the size of individual metastatic lesions over time with no symmetry break event during the course of imaging. Lesion without Lgr5⁺ CSCs (black), lesions with Lgr5 expression before start of IVM (orange).

CRC organoids phenocopy the cellular dynamics during metastatic outgrowth

Organoids are known for their self-organising capacity (43). To study early development of human CRC liver metastases in more detail, we tested if their growth kinetics and corresponding cellular composition are recapitulated by clonal outgrowth of human CRC organoids.

Using the STAR reporter to label endogenous ASCL2-driven stem cell activity (nuclear sTomato, Figure S11) in lines with diverse genetic background, we noticed behaviour closely resembling our *in vivo* observations (Figure 3A-B). Foremost, STAR⁺ cells gave rise to multicellular structures in the absence of CSCs. After about 5 to 6 days of culture, heterogeneity arose in the majority of the organoids (Figures 3C, S2A, Video S1). When correlating organoid size to phenotypes, it became clear that organoids with a heterogeneous cellular composition were efficiently growing, while organoids that failed to generate CSCs remained restricted in size (Figures 3D-E, S2B). Intriguingly, when plating single STAR⁺ cells, we observed similar growth kinetics, timing of symmetry break (corrected for fluorophore decay), and organoid sizes in relation to cellular composition (Figures 3F-H, S2C-G). Indeed, homogeneous STAR⁺ organoids that failed to break symmetry by differentiation remained growth-restricted similar to their homogeneous STAR⁻ counterparts that lacked CSCs (Figure 3E,H).

To further consolidate these findings, STAR was introduced into a set of eight independent colonic organoid lines with diverse sets of driver mutations (representative of either normal, adenoma or malignant state). Again, analysis confirmed that organoids which failed to develop cell type heterogeneity, being pure CSC or non-CSC organoids, became growth stagnated (Figure S3A-B). The difference in the proliferative behaviour between macro- and micro-organoids was further demonstrated by EdU incorporation on Day 11 (Figure 3I). Importantly, using a computed growth rate per cell, we confirmed that generating cellular heterogeneity is functionally supportive of organoid growth rather than being a stochastic result linked to higher cell numbers (Figure S2F-G).



◀Figure 3: CRC organoids phenocopy the cellular dynamics during metastatic outgrowth

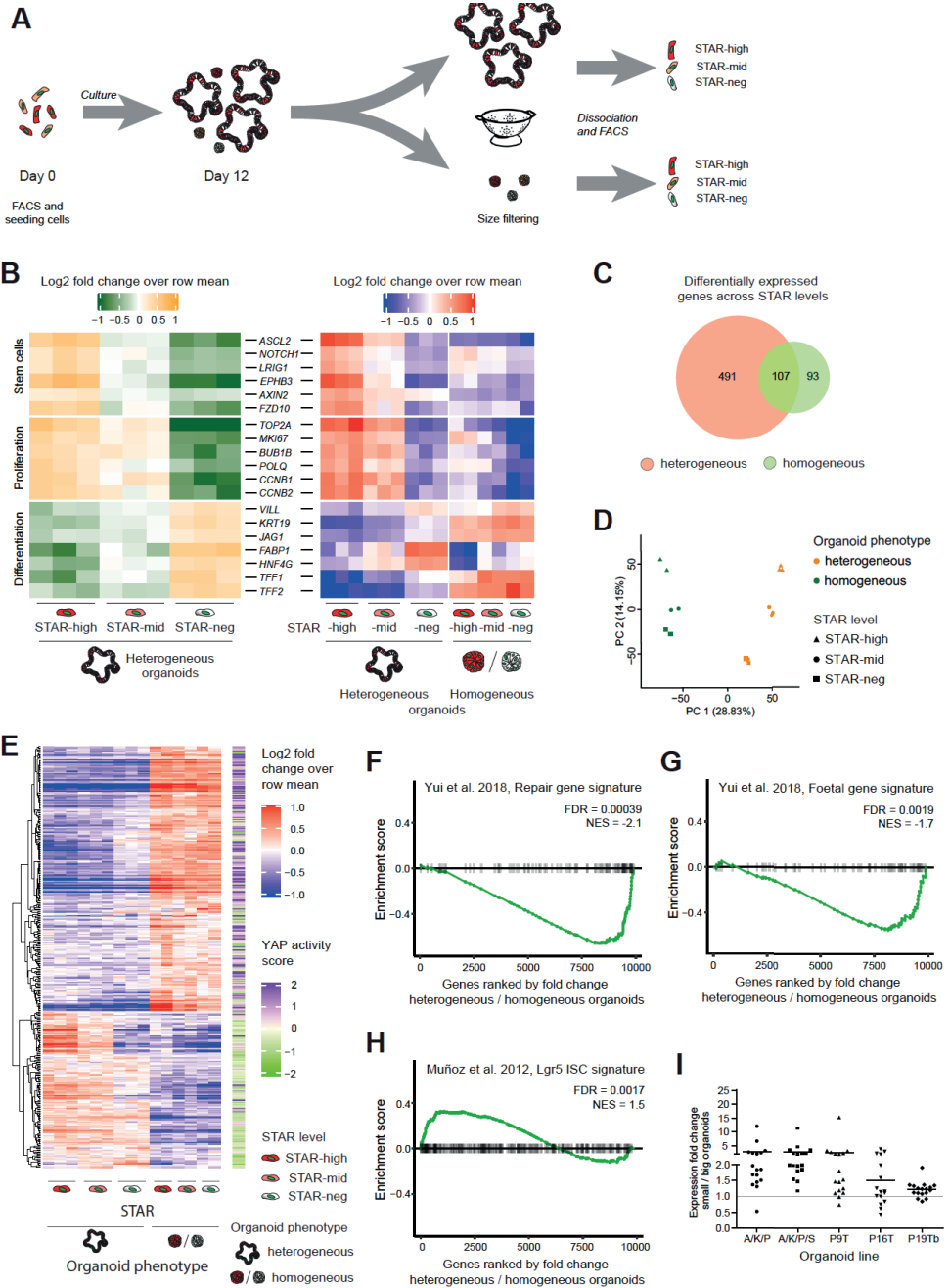
A. Stills from live-cell recordings of A/K/P/S mutant organoid formation (Day 5 to 11) from single nuclear STAR⁺ cells (red). Top: organoid fails to establish heterogeneity and stagnates in growth. Bottom: organoid develops cellular heterogeneity indicated by varying STAR levels and continues to grow. Nuclei are marked with a chromatin tag (green). Colour hues are red/green overlaid (resulting in yellow to dark orange). Arrowhead: symmetry break. Scale bars, 50 μ m. **B.** 3D-rendered pictures of single cells growing into either a heterogeneous organoid (top) or into homogeneous STAR-neg (bottom left) or STAR-pos (bottom right) micro-organoids. Nuclei (green), STAR (nuclear, red), overlay (yellow). Scale bar, 100 μ m. **C-H.** Pooled data of four human CRC organoid lines: Engineered *APC^{KO/KO}/KRAS^{G12D/-}/TP53^{KO/KO}* (A/K/P), *APC^{KO/KO}/KRAS^{G12D/-}/TP53^{KO/KO}/SMAD^{KO/KO}* (A/K/P/S), PDO P16T, and PDO P19bT. Data is stratified by STAR identity at the time of plating. (C-E/F-H) Outgrowth of STAR⁻/STAR⁺ cells with homogeneously STAR-neg (green)/STAR-pos (red) organoids and heterogeneous organoids (orange/yellow). (C/F): Graph representing the fraction of organoid phenotypes per indicated time point during the outgrowth of STAR⁻/STAR⁺ CRC cells. (D/G): Graph representing the size (mean cell number + SEM) of developing organoids from single STAR⁻/STAR⁺ cells, stratified by final phenotype. (E/H): Organoid size per final phenotype for the outgrowth of single STAR⁻/STAR⁺ cells. Two-tailed Student's t-test (p-value 0.0070 / 0.0045) indicates significant difference. **I.** Three 12-day-old organoids with EdU incorporation (pink) to label proliferative cells. Counterstain Hoechst 33342 (blue). Selection (yellow) shows optimal bright-field cross-section. Scale bars, 100 μ m.

Next, we assessed the pattern by which *de novo* CSCs emerged during plasticity events in live-cell recordings of organoid outgrowth with respect to their preceding mitosis (Figure S3C, Video S1). We found no link when comparing STAR levels in the first emerging STAR⁺ CSCs to their direct sisters, which were either diverging or comparable (Figure S3D-F vs. S3G-I). Likewise, the onset of STAR level increase seemed uncoupled to the timing of the preceding mitosis (Figure S3D-E vs. S3F,I).

Growth-restricted micro-organoids are in a YAP state

To understand why the development of cell type heterogeneity coincides with sustained growth, we set out to transcriptionally profile cells with various STAR levels from either growth-stagnated (micro) organoids or from cellular heterogeneous (large) organoids (Figure 4A). We chose A/K/P/S organoids as they depict a pronounced size difference between organoid phenotypes which enables their separation by size (Figure S2B,D, S4A). Moreover, they grow in the absence of niche-derived growth factors, which suggests that the growth stagnation of micro-organoids is a tumour intrinsic failure.

Transcriptomic analysis demonstrated anticipated expression patterns in heterogeneous (large) organoids: The STAR-high population was enriched for SC-markers/ Wnt targets (such as *ASCL2*, *AXIN2*, *NOTCH1*) and proliferation markers (*MKI67*, *CCNB1*, *CCNB2*), while the STAR-neg population showed increased expression of differentiation markers such as *VILL*, *KRT19*, *JAG1*, *TFE2*, and *HNF4G* (Figure 4B). Furthermore, in contrast to the differential expression of mature cell type markers, the cellular states within the homogeneous micro-organoids seemed to be less diverse, with immature CSCs and high expression of some differentiation markers (Figure 4B-C, S4B-C). In line with this, principle component



◀Figure 4: Growth restricted micro-organoids are in a YAP state

A. Experimental setup: single STAR⁺ cells were cultured for 12 days. Organoids were size separated and STAR-high, STAR-mid, and STAR-neg cells were collected by FACS for each organoid subfraction for prospective expression analysis. **B.** Heatmap representing expression levels of intestinal markers for SCs, proliferation, and differentiation (log₂ fold change over row mean). Left: relative expression per STAR population of only heterogeneous organoids. Right: both organoid types. **C.** Venn diagram depicting the number of differentially expressed genes across STAR populations (FDR < 0.01 in at least one comparison) in heterogeneous (orange) and homogeneous (green) organoids. **D.** Principal component analysis of the expression patterns across STAR populations and organoid phenotypes. **E.** Heatmap showing all 369 differentially expressed genes between small (homogeneous) and large (heterogeneous) organoids (fold change > 1.5, FDR < 0.05) for which the assigned YAP score (right side) represents at least a 10% change (YAP score < 0.9 (green) or > 1.1 (purple), score from (28)). **F-H.** Gene set enrichment analyses demonstrating the similarity of (homogeneous) micro-organoids to (F) the regenerative state of mouse intestine (30), (G) the foetal state of mouse intestine (30) or of large (heterogeneous) organoids to (H) intestinal SCs (29). **I.** Expression pattern (by qPCR) of 17 *micro-organoid associated genes* across five lines. Horizontal bar per line: mean fold change of all genes. Individual values depicted in Figure S5A.

analysis of all samples revealed that the strongest source of biological variance related to the organoid phenotype, directly followed by the level of SC activity (Figure 4D).

Next, unbiased analysis of the differentially expressed genes between big and small organoids (1,985 genes, fold change > 1.5, FDR < 0.05) suggested YAP signalling as the strongest enriched signature in micro-organoids (FDR < 2.1*10⁻⁶, Figure S4D). Moreover, the addition of a computed YAP score that is based on *in vivo* perturbation studies (28), indicated that 40% of these genes show a high probability to be target genes of YAP activity (Figure 4E, S4E). Additionally, gene signatures derived from previous YAP/TAZ studies (16,30), in contrast to an intestinal SC signature, positively correlate with the expression pattern in growth-stalled micro-organoids (Figure 4F-H).

Reassuring, a set of these genes (Table S3) was generally enriched in micro-organoids across different lines (Figure 4I, S5A), confirming similar YAP activity in micro-organoids regardless of the mutational background.

Micro-organoids are in a pseudo-stable state and resemble dormant micrometastases

Growth-stalled micro-organoids and dormant micrometastases both lack mature CSCs and demonstrate limited proliferative behaviour. Assessing whether micro-organoids are also transcriptionally similar to micrometastases is challenging due to their elusive nature and lack of CRC micrometastatic model systems. As closest alternative, we exploited expression data of *latency competent cells* (LCCs) from lung adenocarcinoma and breast tumour models that can only form small metastatic foci in mice (13). We found strong

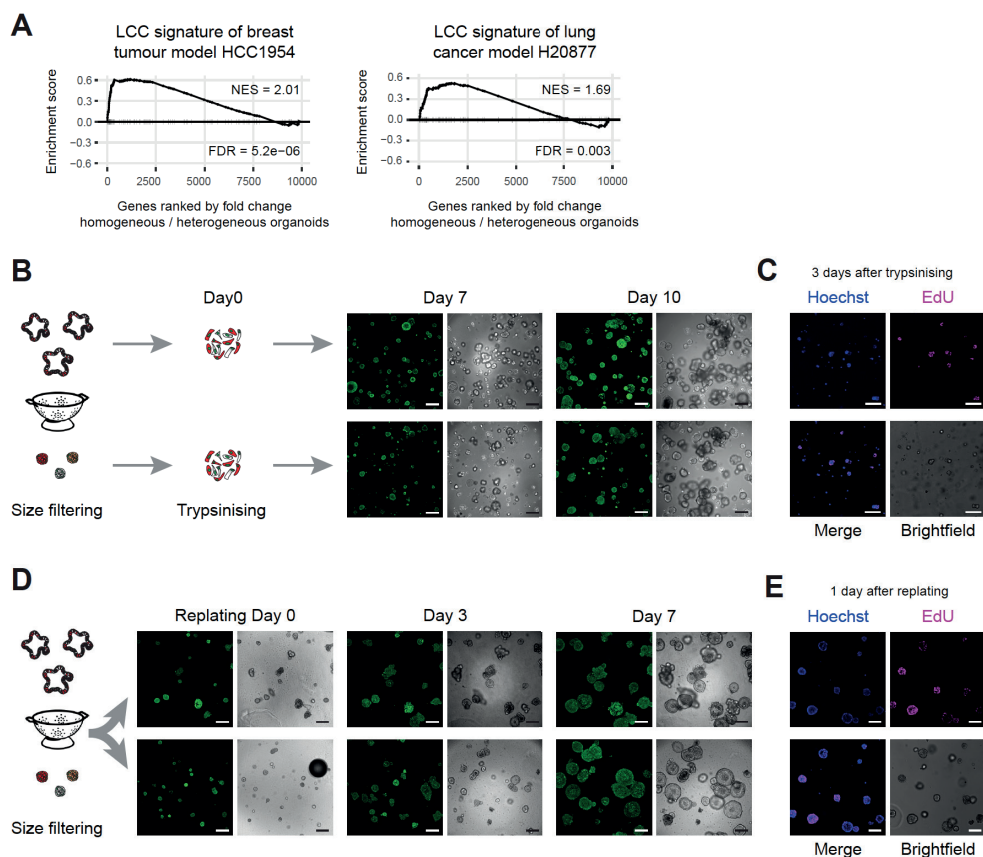


Figure 5: Micro-organoids are in a pseudo-stable state and resemble dormant micrometastases

A. Gene set enrichment analyses demonstrating similarity of micro-organoids to alternative models of *metastatic dormancy* (13) (breast tumour line HCC1954 and lung adenocarcinoma line H20877). **B.** Outgrowth potential of single cells derived from micro- or macro-organoids (A/K/P/S) isolated after 12 days of culturing. H2B (green). Scale bars, 200 μ m. **C.** EdU incorporation (pink) indicates proliferating cells 3 days after plating single cells derived from micro-organoids. Counterstain Hoechst 33342 (blue). Scale bars, 100 μ m. **D.** Growth potential of 12-day-old micro- and macro-organoids (A/K/P/S) upon isolation and replating as intact structures. H2B (green). Scale bars, 200 μ m. **E.** EdU incorporation (pink) indicates regained proliferative activity of micro-organoids 1 day after replating. Counterstain Hoechst 33342 (blue). Scale bars, 100 μ m.

similarity in expression patterns between our micro-organoids and LCCs (Figure 5A), corroborating the extent of similarity between micro-organoids and micrometastases.

An additional functional property of CRC micrometastases in livers is their capacity to re-initiate growth after years of being dormant. Using organoid formation capacity of micro-organoid-derived cells, we demonstrated renewed proliferation in virtual all cells as shown

by the incorporation of EdU within 16h (Figure 5B-C). Moreover, over time, they generated large organoid structures that are indistinguishable from a normal culture (Figure 5B), supporting the notion that tumour cells in micro-organoids are intrinsically fine, yet remain in a pseudo-stable, non-proliferative state. Likewise, isolation and replating of intact micro-organoids revealed again their capacity to re-enter a proliferative state and transition to mature organoids (Figure 5D-E), while YAP activity decreased (Figure S5B).

Dynamic YAP activity is required for the outgrowth of CRC organoids

To understand the origin of active YAP/TAZ signalling in growth-stagnated micro-organoids, we assessed the temporal expression patterns of micro-organoid-related YAP genes during clonal organoid formation. As observed in mouse organoids (16), most YAP genes demonstrated highest expression levels during the earliest stage of outgrowth which subsequently decreased over time (Figures 6A, S5C), suggesting that the transcriptional state of micro-organoids mimics the earliest stages of organoid outgrowth prior to symmetry break.

To assess if persistent YAP signalling is related to the homogeneous nature of micro-organoids, we measured SC activity upon perturbing YAP signalling activity. Inducible expression of YAP^{55A}, a constitutively active YAP mutant, led to transcriptional downregulation of intestinal SC markers in multiple lines, while overexpression of the inactive mutant YAP^{594A} had no effect (Figure S5D). To confirm this on protein level, we chose flow cytometry analysis over Western Blot, due to low expression levels of intestinal SC markers and a lack of proven antibodies. As expected, expressing YAP^{55A} for 48h in different CRC organoids prior to symmetry break induced a loss of STAR-high CSCs, while STAR-low cells became more frequent (Figure S5E). Conversely, upon inducible expression of YAP inhibitor YTIP (44), the fraction of CSCs increased at the expense of the STAR-low population (Figure S5E).

Next, to activate Yap signalling activity to more physiological levels, we made use of the MST1/2 inhibitor XMU-MP-1, which prevents inactivation of YAP by LATS1/2 (45). Across multiple lines, organoids treated with XMU-MP-1 at functional, non-toxic levels were smaller in size (Figures 6B, S5F-I) and showed reduced EdU incorporation (Figure 6C) compared to controls. Additionally, these YAP-activated organoids revealed a similar reduction in STAR-high CSCs (Figure 6D), as seen previously through active Yap^{55A} overexpression. Thus, counteracting the physiological decay of early-stage YAP activity

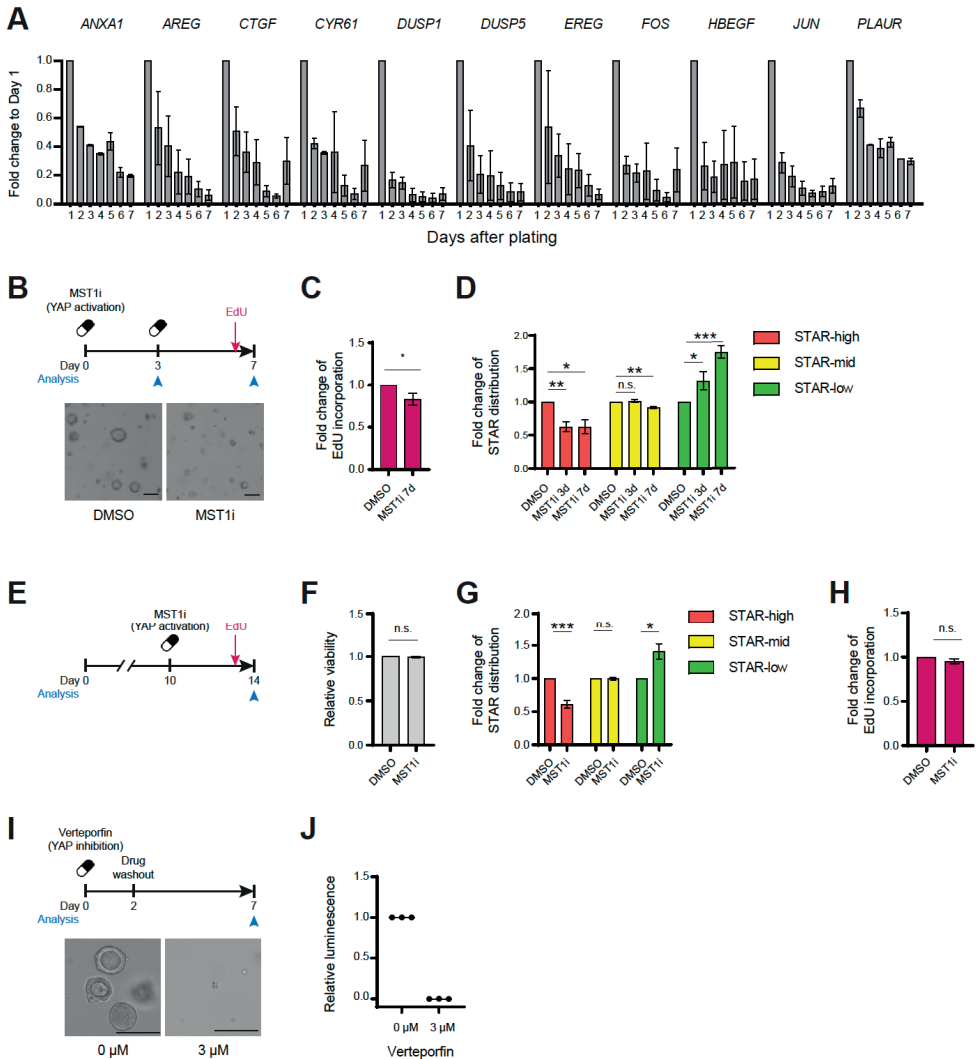


Figure 6: Dynamic YAP activity is required for the outgrowth of CRC organoids

A. Diminishing expression of *micro-organoid associated genes* during the first 7 days of A/K/P/S organoid outgrowth. Gene expression, represented as mean + SEM, is normalised to Day 1. **B-D.** Single A/K/P/S cells treated with 500nM XMU-MP-1 (MST1/2 inhibitor) for 3 or 7 days. (B) Schematic of experimental setup (top) and representative organoid overview after 7 days of culture (bottom). Scale bars, 100 µm. (C) Relative fraction of EdU incorporating cells. (D) Flow analysis of STAR levels. (C-D) Data is normalised to DMSO control. **E-H.** 10-day-old A/K/P/S organoids were treated with 500nM XMU-MP-1 and analysed after 96 h by flow cytometry. (E) Experimental setup. (F) Relative viability assessed by DAPI. (G) Relative change in STAR populations. (H) Relative fraction of EdU incorporating cells. (F-H) Data is normalised to their respective DMSO control. **I-J.** 3µM verteporfin was added to single A/K/P/S cells for 48h prior to wash out. Organoids were analysed after 7 days. (I) Schematic of experimental setup (top) and representative organoid overview after 7 days of culture (bottom). Scale bars, 100 µm. (J) Relative viability as assessed by CellTiter-Glo. Data is normalised to DMSO control.

in CRC PDOs compromises the formation of mature CSCs and persistent YAP activity can induce growth-stalled micro-organoids.

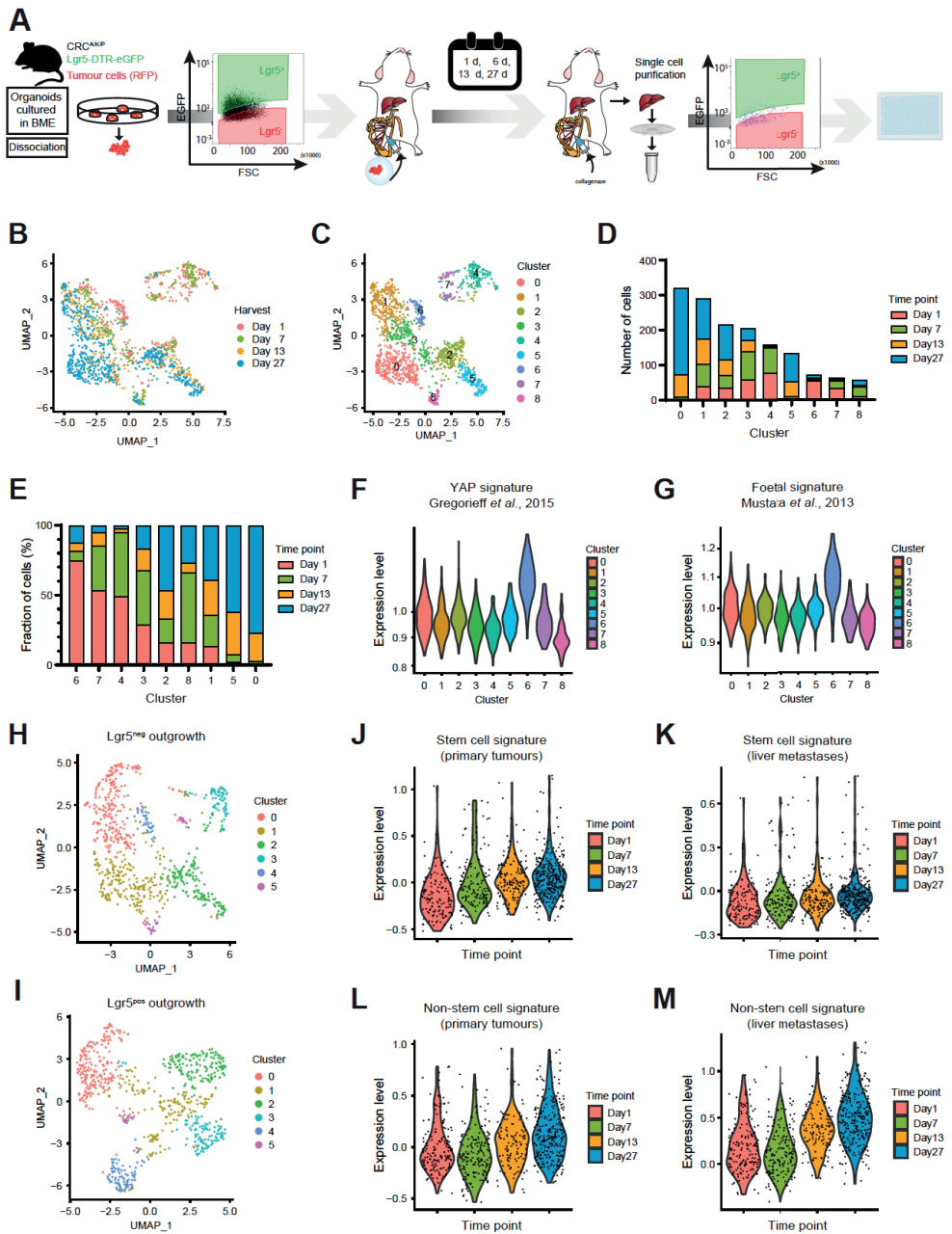
Next, we treated 8-day-old A/K/P/S organoids with XMU-MP-1 (Figure 6E-F). In these mature CRC organoids we scored again a reduction in CSC numbers (Figure 6G). However, in contrast to the organoid formation data, proliferation both overall and stratified by STAR population, was not affected at this stage (Figure 6H, Figure S5J-K). Finally, we tested the consequence of inhibiting the early-stage YAP activity wave using verteporfin at non-toxic levels (Figure S5L). As previously described for low-grade APC^{KO} CRC lines (30), preventing YAP activity during the first 2 days of outgrowth entirely blocked organoid formation (Figure 6I-J). Thus, YAP activity is essential for single CRC cells, yet needs to decay over time to enable the formation of CSCs and to sustain proliferation.

Mapping cellular phenotypes during *in vivo* formation of CRC liver metastases

To assess if the dynamic expression patterns underlying CRC organoid formation can be translated to a metastatic setting, we investigated the cellular composition during liver metastasis formation over time by single-cell RNA-sequencing (scRNA-seq, Figure 7A).

First, we noticed that *Lgr5* constitutes a suitable SC marker in this cancer model, considering its co-expression with other SC markers (Figure S6A-B). Next, in agreement with the fact that both *Lgr5*⁺ CSC and *Lgr5*⁻ non-CSC are capable of forming metastases in injection assays (8), we noticed that the initial *Lgr5* status at the time of injection does not majorly influence the transcriptomic phenotype of metastatic cells (Figure S6C). Conversely, the age of the metastases (1, 7, 14 and 27 days) strongly correlates with transcriptional changes in our data set (Figure 7B), indicating major changes in cellular phenotypes during liver colonisation by CRC metastases.

Unsupervised clustering of all cells resulted in nine distinct clusters (Figure 7C-D), which were subsequently ranked by their relative abundance of cells per time-point (Figure 7E). Cluster 6, the cluster predominantly made up of cells from Day 1, revealed an enrichment for many known YAP target genes (e.g. *Edn*, *Mln*, *Amotl2*) including those enriched in micro-organoids (*Ctgf*, *Cyr61*, *Ankrd1*, Figure S6D) and also associates most strongly with published YAP signatures (Figure 7F-G). Conversely, gene expression patterns of cells arising late during metastatic outgrowth (clusters 0, 5 and 1) (Figure 7E), showed particular enrichment of SC markers (*Lgr5*, *DTR-eGFP*, *Smoc2*) and SC-associated genes (*Hes1*, *Hnf4a*) in the dominant late-stage clusters 0 and 1 (Figure S6E).



◀Figure 7: Mapping cellular phenotypes during *in vivo* formation of CRC liver metastases

A. Experimental design of scRNA-seq analysis of metastatic cells at specific time points during *in vivo* liver metastasis formation initiated by either Lgr5⁺ or Lgr5⁻ CRC cells. **B-C.** UMAP of scRNA-seq data colour-coded by (B) time of harvest and (C) clusters resulting from unsupervised hierarchical clustering. **D-E.** Composition of clusters colour-coded by time of harvest. (D) Absolute number of cells. (E) Relative composition of clusters ranked (in descending order) according to highest relative contribution from Day 1. **F-G.** Expression levels of YAP-associated gene signatures by cluster for (F) YAP overexpression in murine intestine (28) and (G) foetal intestinal organoids (33). **H-I.** UMAP after unsupervised hierarchical clustering of all (H) Lgr5⁻ and (I) Lgr5⁺ injected cells. **J-M.** Expression levels of (J-K) SC and (L-M) non-SC gene signatures over time. Signatures are derived from (J,L) primary tumours (8) and (K,M) liver metastases (8). Data input: (J-K) Lgr5⁻ and (L-M) Lgr5⁺ injected cells.

3

Next, we stratified the data set by the Lgr5 status at the time of injection and analysed the developing cellular phenotypes separately (Figure 7H-I). In line with the need for Lgr5⁺ CSC for metastatic growth (5), we found that *Lgr5* and *Ascl2* are becoming more widely expressed over time in metastases originating from Lgr5⁻ cells (Figure S6F-G), as well as previously obtained (8) gene expression signatures of Lgr5⁺ CSCs (Figure 7J-K). Interestingly, also gene expression signatures for non-CSCs increased slightly over time (Figure S6H-I), suggesting that non-CSCs in older metastases start matching those of primary tumours. Similarly, signatures for non-CSCs became more pronounced over time during metastasis formation by Lgr5⁺ CSC (Figure 7L-M).

Thus, regardless of the metastatic cell of origin, also *in vivo* cellular heterogeneity is generated over time and is preceded by YAP activity at the earliest stage.

DISCUSSION

The metastatic cascade is a multi-step cell-biological process that includes cell migration, intravasation, metastatic seeding and outgrowth (46). The process of outgrowth, or metastatic colonisation, is a highly inefficient, rate-limiting step that depends on complex interactions between tumour cells and the microenvironment (10). Yet, the cell-intrinsic properties underlying successful transition to metastatic colonisation and developmental trajectory of cells are poorly understood. Among others, due to their sporadic occurrence and limited size, micrometastases are difficult to identify and characterise. Foremost, functional studies are hampered as the number of appropriate model systems is limited.

In this study, we used patient biopsies, CRC PDOs, mouse models of CRC, and human tumour xenografts to investigate at high spatial and temporal resolution the phenotypic and transcriptional changes taking place during the transition from micrometastases to successful liver colonisation (Figure 8).

Our patient-related data is in agreement with previous mouse studies demonstrating the ultimate need for Lgr5⁺ colorectal CSCs for metastatic outgrowth (5,8). Additionally, our study is complementary to the previous finding that the majority of metastases is seeded by Lgr5⁻ cells (8). However, irrespective of the identity of the seeding cell, our *in vitro* and *in vivo* data indicate that both CSC and non-CSC have the capacity to establish cell type heterogeneity and form successfully growing metastases. Moreover, our data shows that generation of cell type heterogeneity through epithelial self-organisation is essential, as pure CSC or non-CSC organoids become growth stagnated. In analogy to the SC support that is provided by differentiated Paneth cells in the normal intestine (47), it is conceivable that non-CSCs fulfil a similar role in promoting CSC function, even in a highly mutated background. Furthermore, our data is in line with L1CAM⁺ cells being essential for metastatic colonisation of CRC (48), since L1CAM is known to induce YAP/TAZ activity in lung and breast cancer models (49).

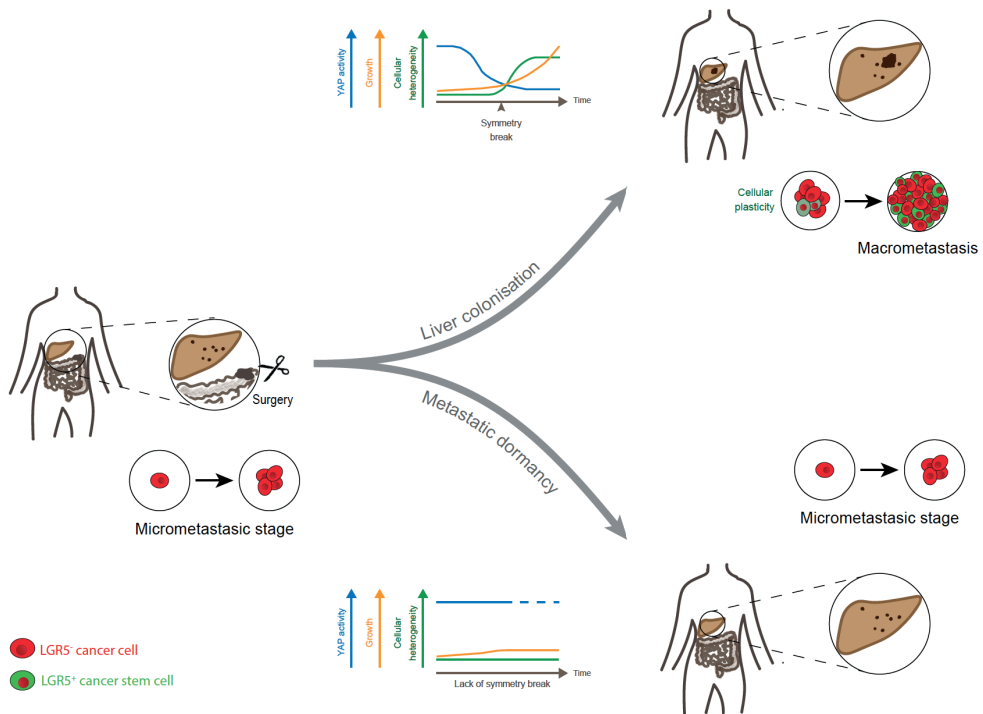


Figure 8: Summarising model

Intriguingly, the cellular dynamics and transcriptomic changes during metastatic outgrowth is accurately phenocopied by clonal outgrowth of CRC PDOs. Moreover, the processes underlying cell type maturation and CSC appearance at a multicellular stage draw similarities to the symmetry break in mouse small intestinal organoids during which an initial YAP high/proliferative state precedes the reappearance of Lgr5⁺ SCs and subsequent crypt formation (16). We show that this level of epithelial self-organisation is shared across multiple CRC PDOs, making organoid formation by CRC PDOs a tractable disease model to study live-cell biology during early stage liver metastasis formation.

We also scored a fraction of CRC micro-organoids that failed to establish cellular heterogeneity and was compromised in growth. These micro-organoids contain a homogeneous population of immature cell types with strong expression of transcriptional YAP targets. This finding is in line with the notion that YAP activity represses in particular target genes requiring high Wnt levels like SC genes, while more progenitor-associated Wnt target genes, and as a consequence proliferative behaviour, seem preserved (Figure 6G-H) (28,30,50,51). Persistent YAP activity in micro-organoids most likely originates from the physiological and essential YAP spike during the earliest stages of organoid formation. Moreover, we demonstrate that its subsequent decay is critical, as maturation and growth of CRC organoids is otherwise prohibited. These transcriptional changes are in line with our *in vivo* experiments and are functionally supported by earlier studies demonstrating that YAP activation in murine CRC cells prevents liver metastases (50). While our data supports a preceding role for YAP activity during cellular plasticity, future studies are warranted to resolve the underlying molecular mechanisms in full detail.

Several publications have linked YAP/TAZ activity in primary cancers to poor patient survival (52–54). More specifically in CRCs, YAP activity and migratory behaviour are linked to cell populations (Lgr5⁻ or L1CAM⁺) that are endowed with metastasis-initiating capacity (8,48,49,55), providing an explanation for YAP as a biomarker based on primary CRC tissues. Complementary to this, we show that that early-stage YAP promotes single cell survival and that loss of YAP activity at the metastatic site is essential to enable CSC formation, subsequent maturation, and growth of the lesion.

In analogy to our experimental data, it is conceivable that failure to establish epithelial self-organisation at the micrometastatic stage constitutes an epithelial, tumour-intrinsic cause underlying the formation of dormant micrometastases in the liver of CRC patients. As the microenvironment constitutes a further strong determinant of metastatic colonisation (13,56), it will be of interest to study its influence on the propensity of micrometastases

to establish cellular reorganisation. The conceptual idea that dormant micrometastases are stuck during their early developmental trajectory is a novel perspective that provides a possible explanation for their state of cellular quiescence.

ACKNOWLEDGEMENTS

We thank all colleagues, the UMCU Flow Core Cytometry Facility and the UMCU tissue facility (Department of Pathology) for continuous support and many fruitful discussions.

This work was supported by a KWF fellowship from the Dutch Cancer Society (UU 2013-6070) and an ERC Starting Grant (IntratumoralNiche - 803608), both awarded to H.J.G. Snippert. J. van Rheenen was supported by the Doctor Josef Steiner Foundation. This work is part of the Oncode Institute which is partly financed by the Dutch Cancer Society.

AUTHOR CONTRIBUTIONS

M.C.H. and H.J.G.S conceived the study and M.C.H. performed and analysed most *in vitro* organoid experiments. N.A.P., O.K., and I.H.M.B.R. developed the micrometastasis detection protocol in human liver specimens. N.A.P performed the spontaneous metastasis formation experiment, IHC on liver metastases, and together with M.C.H. the *in vivo* time-course experiment. M.C.H. analysed the single-cell RNA-sequencing data. K.C.O., A.F., and J.v.R performed the IVM metastases studies. M.C.H. and K.C.O were equally involved in the organoid tracking experiments. The bulk RNA-sequencing experiment was designed and conducted by M.C.H., K.C.O., L.v.V., R.G.H.L., M.V. and H.J.G.S. with R.G.H.L. performing the transcriptomic analyses. G.d.M. and P.L. conducted the light-sheet microscopy experiments. M.C.H. and K.C.O generated the STAR reporter plasmids and M.C.H. and I.V.K., generated most human organoid lines. M.C.v.d.N. and M.G. helped with YAP perturbation experiments. M.C.H. and J.H.H. performed the RT-PCR experiments and J.H.H. did the organoid stainings. M.C.H. and H.J.G.S. wrote the manuscript. The manuscript has been approved by all authors.

DECLARATION OF INTERESTS

The authors declare no potential conflicts of interest.

MATERIALS AND METHODS

Human CRC liver metastases

The collection and processing of human tissue from residual material of liver resection specimens was performed in accordance with the Declaration of Helsinki and approved by the Biobank Research Ethics Committee (TCBio; protocol 16-651) of the University Medical Center Utrecht, The Netherlands. This tissue is classified as 'residual material' and the collection and processing of this biological material is in accordance with the 'no objection' procedure defining the release of anonymised residual material without broad consent under strict conditions and approval under aforementioned Research Ethics Committee.

Liver tissue strips from colorectal cancer patients (Table S1) measuring 5-10 cm x 2 cm and extending from a macrometastasis into healthy peripheral liver tissue were formalin-fixed paraffin embedded (FFPE) and consecutively cut. When no macrometastasis was available for diagnostic reasons, a liver tissue strip was obtained from a part of the liver unrelated to a macro-metastasis.

Immunohistochemistry

FFPE sections were deparaffinised in xylene (Klinipath) and subsequently rehydrated in a graded alcohol series (100% ethanol to 70% ethanol). For patient liver tissue sections, epitope retrieval was performed by cooking the slides for 20 minutes in citrate buffer (Alfa Aesar, pH 6.0), followed by blocking of endogenous peroxidase in 1.5% H₂O₂ in PBS, and antibody incubation. Subsequently, slides were developed with diaminobenzidine (Fluka) followed by hematoxylin counterstaining, air-dried, and mounted on cover slips. For tyramide multiplex IHC, epitope retrieval was carried out in 10 mM Sodium Citrate (pH 6.0) or 1 mM EDTA (pH 9.0) depending on the antibody. Endogenous peroxidase was inactivated and sections were blocked in 10% normal goat serum prior to antibody incubation. Sections were developed using Alexa Fluor conjugated tyramides. Same species antibodies were applied after 10 minutes of heat-mediated stripping of the antibody complex in 10 Mm sodium citrate (pH 6.0) buffer. Slides were counterstained with DAPI (Sigma-Aldrich, 600X).

Antibodies were incubated overnight at 4°C (details listed in Table S2) and poly-HRP antibodies were used in both cases for signal amplification. Automated stainings were performed for CDX2 and EPCAM using the Ventana Bench Ultra at the department of pathology at the UMCU.

For identified metastases, the correlation between metastatic size (micro or macro) and SC marker expression (absent or heterogeneous) was assessed using a Fisher's exact test.

Mouse experiments

All mouse experiments were performed in accordance with protocols approved by the Institutional Animal Care and Use Committees of our institutions: the Animal Welfare Committees of the Animal Welfare Body Utrecht, the Royal Netherlands Academy of Arts and Sciences, and the Netherlands Cancer Institute. Animals were kept at animal facilities of the Central Laboratory Animal Research Facility (Gemeenschappelijk Dierenlaboratorium, GDL), the Hubrecht Institute or the Netherlands Cancer Institute.

For transplantation experiments, 8-14-week-old male and/or female NOD.Cg-Prkdc^{SCID} Il2rg^{tm1Wjl}/SzJ mice, obtained from Charles River (NSG, Charles River strain code 614) or The Jackson Laboratory (NSG, The Jackson Laboratory Cat. No. 005557) were used as acceptors.

Orthotopic transplantation of CRC organoids

Orthotopic transplantation of PDOs was performed as previously described (19). Mice were sedated and type I collagen blobs (Corning, Cat# 354249) containing approximately 250,000 and 150,000 cells for the murine and human CRC model, respectively, were transplanted into the caecal subserosa of recipient mice.

Murine livers of 15 mice were analysed for the presence of human metastases after 3 weeks (3 mice, 1 micrometastasis) or 9-12 weeks (12 mice, all but 1 metastasis).

Mesenteric or portal vein injection of murine CRC cells

Lgr5⁺ and Lgr5⁻ cells were collected by FACS and injected in 100 μ l PBS into recipient mice. For IVM experiments, 10,000 Lgr5⁻ cells were collected from murine CRCs grown for 7-10 weeks upon orthotopic transplantation and injected into the mesenteric vein (8,20). For the scRNA-seq experiment, Lgr5⁺ and Lgr5⁻ subpopulations were isolated from CRC organoids. Approximately, 400k, 200k, 200k, and 50k cells were injected into the portal vein and harvested after 1, 7, 13, and 27 days, respectively.

Intravital imaging on liver metastases

An abdominal imaging window was applied onto the liver of sedated mice and daily tracking of metastases through IVM was performed as previously described (8,21,22).

Collagenase liver perfusion

For the isolation of CRC cells, a two-step liver perfusion protocol was adopted and modified (23). In brief, the portal vein or subhepatic vena cava was cannulated with a 24G IV catheter (BD Insyte Autoguard Shielded IV catheter; BD 381412) to perfuse first, 70 mL HBSS (Gibco) with 0.5 mM EGTA, 25 mM HEPES, and NaOH to reach a pH of 7.4 at 37°C. Next, 80 mL digestion medium consisting of DMEM-low glucose (Corning) with 15 mM HEPES, Penn-Strep, collagenase type IV (Gibco) in sufficient quantity for 120 Collagenase Digestive Units (CDU)/ml at 37°C) was perfused.

The liver was excised, minced in a 15 cm petri dish with 10 mL digestion medium, resuspended in 25 mL isolation medium (DMEM-High/F-12, Gibco with 10% FBS), and filtered through a 70 µm strainer. The supernatant of two initial washing steps (centrifugation at 50xg for 2 minutes) was washed twice more with 25 mL isolation medium (centrifugation at 500xg for 3 min). Then, DRAQ7 (Cell Signaling Technology) was added and single, alive, RFP⁺ cells were FACS-sorted into 384-well collection plates for scRNA-seq.

Organoid cultures

Organoid lines were maintained in Matrigel (Corning) as previously described (24,25). Culture medium was adapted per line depending on the presence of oncogenic mutations that render growth factors obsolete: Loss of *APC*, *SMAD4*, and oncogenic *KRAS^{G12D}* were attributed by leaving out R-Spondin, Noggin, and EGF, respectively. For details on the lines, see supplementaries.

For experiments, single cells were plated at a density of 250-1,000 cells / µl Matrigel. Perturbation studies were performed using doxycycline (Bio-Connect), verteporfin (Bio-Techne), XMU-MP-1 (Sigma) at indicated concentrations with corresponding DMSO controls (VWR).

Flow analysis of organoids

Viability readouts were performed upon addition of DAPI (Sigma) 30 min prior to the sort. STAR gates were defined as STAR-high (top 15%), STAR-low (bottom 15%), and STAR-mid (remaining 70%) based on the DMSO sample using FlowJo 10.6.1 (<https://www.flowjo.com>). EdU incorporation assays were performed after fixation with 4% paraformaldehyde for 15 min at RT. Significance levels were assessed by two-tailed Student's t-tests compared to DMSO control.

Organoid tracking experiment

STAR-high and STAR-neg cells were collected by FACS from 2-week-old organoids and plated onto 384-well imaging plates (Corning). Organoid size per phenotype (homogeneous and heterogeneous) was compared using a two-tailed Student's t-test. For the organoid growth rate r , a proliferation model with uniform growth of all cells over time was assumed: $N(t) = N_0 \cdot \exp(r \cdot t)$, with number of cells per organoid N and time in days t . Paired organoid data of Day 6 (N_0) and Day 10-11 ($N(t)$) were used for the analysis.

Size filtering of organoids

Organoids were harvested with 1 mg/mL Dispase II (Life Technologies), and pelleted by gentle spinning at 300xg, 4 min, 4°C. The organoid suspension was first applied onto a 100 μm strainer (VWR), while organoids passing the filter were collected in a 50 mL falcon tube. Organoids trapped in the filter ($>100\mu\text{m}$) were isolated using 10 mL of Advanced DMEM/F12, pelleted and kept on ice. Next, to collect organoids of 40-70 μm in diameter, the flow-through of the 100 μm strainer was subjected first to a 70 μm strainer (VWR) and subsequently to a 40 μm strainer (VWR). Organoids trapped in the 40 μm strainer were washed out with 10 mL of Advanced DMEM/F12, pelleted, and kept on ice until processed further.

Organoid staining

Antibody staining was performed as previously described (26). Briefly, 10-14-day-old organoids were fixed in 4% PFA, incubated in PBT (PBS with 0.1% Tween 20), and blocked with OWB (0.1% Triton X100 and 0.2% BSA). Antibodies (Table S2) were incubated overnight at 4 °C. Organoids were imaged in clearing agent (60% glycerol and 2.5 M fructose).

CellTiter-Glo

Organoids were grown in white-walled 96-well tissue culture plates (Merck). For analysis, 50% v/v CellTiter-Glo reagent (Promega) was added to each well. The plate was shaken rigorously for 30 min and afterwards analysed using a SpectraMax M5 microplate reader (Molecular Devices). Background levels (average of cell-free wells) were subtracted and data was normalised to the respective DMSO control.

EdU incorporation assay

EdU incorporation assays were performed after adding 500 nM EdU for 16 h to cells and processed according to the manufacturer's instructions (Click-iT™ EdU Cell Proliferation Kit for Imaging, ThermoFisher).

RT-qPCR analysis

Samples frozen in 350 µl RLT buffer were processed using the RNeasy Mini Kit (Qiagen) according to the manufacturer's instructions including DNaseI treatment (Qiagen). cDNA was reverse transcribed (iScript™ cDNA Synthesis Kit, Bio-Rad) with 1 µg RNA input. 4 µl of cDNA input (diluted to 220 total volume) was mixed with 5 µl FastStart Universal SYBR Green Master (Sigma-Aldrich) and 0.5 µM forward and reverse primer each (Table S3). Gene expression was normalised to the mean of the housekeeping genes ACTB (Fw: CATTCCAAATATGAGATGCGTTGT; Rv: TGTGGACTTGGGAGAGGACT) and B2M (Fw: GAGGCTATCCAGCGTACTCCA; Rv: CGGCAGGCATACTCATCTTTT). Data is represented as mean + SEM.

Bulk RNA sequencing sample preparation

Twelve-day-old organoids, grown from single STAR⁺ cells, were size filtered as described above. Subcultures were trypsinized and STAR-high, STAR-mid, and STAR-neg cells were collected by FACS in technical duplicates or triplicates (10-20 k cells each), then snap-frozen.

RNA sequencing libraries were prepared as previously described (15) with the following adaptations: Up to 73ng RNA was used as input material. The library was amplified in 13 cycles and subsequent clean-up was performed using a 0.8x bead-based clean-up. Sequencing was performed using an Illumina NextSeq500 with 50-bp paired-end reads.

Bulk RNA sequencing analysis

Sequencing reads mapped to the pre-indexed hg38 genome assembly. Differential gene expression analysis was performed with the DESeq2 package (27). Genes with no reads mapped in any of the samples were filtered prior to differential gene expression (DGE) analysis (Wald test with Benjamini-Hochberg correction). For investigations on STAR dynamics (Figures 4C and S4B), equal numbers of replicates (N=2) of each biological condition were used and significantly changing genes were identified with a likelihood-ratio test.

The YAP activity score is based on Yap perturbation studies in mice (28). It is computed as mean of two expression level fold changes: Yap knockout/control and the inverse of Yap overexpression/control. Genes which were not picked up reliably in both studies, were not assigned a YAP score.

Gene set enrichment analysis (GSEA) was performed using the fgsea R package (Korotkevich G, Sukhov V, and Sergushichev A. 2019. Fast gene set enrichment analysis. bioRxiv doi: <https://doi.org/10.1101/060012>) of an intestinal SC signature (29), foetal and repair gene signature (30), and LCC signature (13).

Micro-organoid-related genes were extracted based on their high YAP score and/or a high fold change in expression between micro- and macro-organoids (see supplementary methods and Table S3).

Single-cell RNA-sequencing

ScRNA-seq was performed according to the Sort-seq protocol (31). Libraries were sequenced on an Illumina NextSeq500 at paired-end 60 and 26 bp read length and 75,000 reads per cell.

Single-cell RNA-sequencing data analysis

Reads were mapped to the mm10 genome assembly including the DTR-eGFP and tDimer2 reporter transcripts. Analysis was performed with the R-package Seurat (32) (version 4.0.4). Cells with >200 unique transcripts and <10% mitochondrial reads were included into the analysis. Gene signature expression levels were computed using the AddModuleScore function (ctrl = 5) for the following gene sets: YAP signature (28) and foetal signature (33) (as previously extracted (34)); CSC and non-CSC signatures (8) extracted upon differential gene expression of Lgr5⁺ and Lgr5⁻ cells located in primary or metastatic tumours.

Quantification and Statistical analysis

Statistical analysis was performed using GraphPad Prism (software version 6) unless specified otherwise. Results with p-values smaller than 0.05 were considered statistically significant (*). P-values smaller than 0.01 and 0.001 were indicated by (**) and (***), respectively.

Data and Code availability

The single-cell and bulk RNA-seq data generated in this study are publicly available in Gene Expression Omnibus (GEO) at GSE189987 and GSE193248, respectively.

REFERENCES

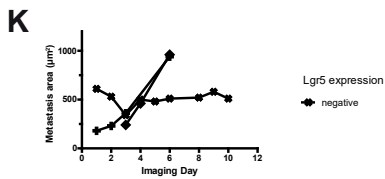
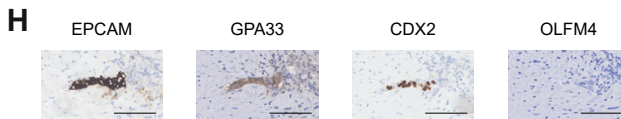
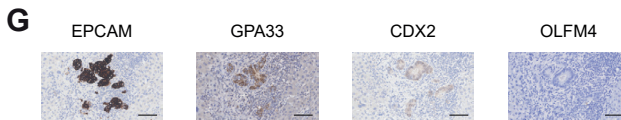
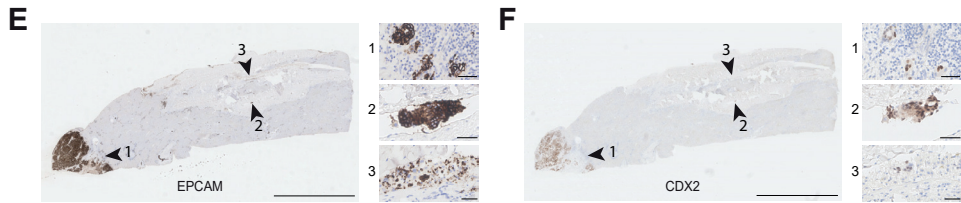
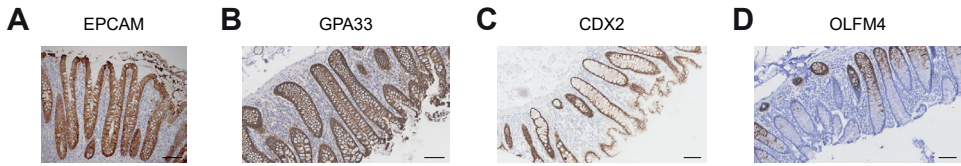
1. Schepers AG, Snippert HJ, Stange DE, Van Den Born M, Van Es JH, Van De Wetering M, et al. Lineage tracing reveals Lgr5+ stem cell activity in mouse intestinal adenomas. *Science*. 2012;337:730–5.
2. Humphries A, Cereser B, Gay LJ, Miller DSJ, Das B, Gutteridge A, et al. Lineage tracing reveals multipotent stem cells maintain human adenomas and the pattern of clonal expansion in tumor evolution. *Proc Natl Acad Sci U S A* [Internet]. 2013;110:E2490–9. Available from: <http://www.pnas.org/cgi/doi/10.1073/pnas.1220353110>
3. Shimokawa M, Ohta Y, Nishikori S, Matano M, Takano A, Fujii M, et al. Visualization and targeting of LGR5 + human colon cancer stem cells. *Nature* [Internet]. Nature Publishing Group; 2017;545:187–92. Available from: <http://www.nature.com/doi/10.1038/nature22081>
4. Morral C, Stanisavljevic J, Hernando-Momblona X, Mereu E, Álvarez-Varela A, Cortina C, et al. Zonation of Ribosomal DNA Transcription Defines a Stem Cell Hierarchy in Colorectal Cancer. *Cell Stem Cell*. 2020;26:845–861.e12.
5. De Sousa E Melo F, Kurtova A V., Harnoss JM, Kljavin N, Hoeck JD, Hung J, et al. A distinct role for Lgr5 + stem cells in primary and metastatic colon cancer. *Nature* [Internet]. Nature Publishing Group; 2017;543:676–80. Available from: <http://www.nature.com/doi/10.1038/nature21713>
6. Hageman JH, Heinz MC, Kretschmar K, van der Vaart J, Clevers H, Snippert HJG. Intestinal Regeneration: Regulation by the Microenvironment. *Dev Cell* [Internet]. Elsevier Inc.; 2020;54:435–46. Available from: <https://doi.org/10.1016/j.devcel.2020.07.009>
7. Tauriello DVF, Calon A, Lonardo E, Batlle E. Determinants of metastatic competency in colorectal cancer. *Mol Oncol*. 2017;11:97–119.
8. Fumagalli A, Oost KC, Kester L, Morgner J, Bornes L, Bruens L, et al. Plasticity of Lgr5-Negative Cancer Cells Drives Metastasis in Colorectal Cancer. *Cell Stem Cell* [Internet]. Elsevier Inc.; 2020;26:569–578.e7. Available from: <https://doi.org/10.1016/j.stem.2020.02.008>
9. Obenauf AC, Massagué J. Surviving at a Distance: Organ-Specific Metastasis. *Trends in Cancer* [Internet]. Elsevier Ltd; 2015;1:76–91. Available from: <http://dx.doi.org/10.1016/j.trecan.2015.07.009>
10. Massagué J, Obenauf AC. Metastatic colonization by circulating tumour cells. *Nature*. 2016. page 298–306.
11. Sosa MS, Bragado P, Aguirre-Ghiso JA. Mechanisms of disseminated cancer cell dormancy: An awakening field. *Nat Rev Cancer*. Nature Publishing Group; 2014;14:611–22.
12. Tauriello DVF, Palomo-Ponce S, Stork D, Berenguer-Llargo A, Badia-Ramentol J, Iglesias M, et al. TGFβ drives immune evasion in genetically reconstituted colon cancer metastasis. *Nature* [Internet]. Nature Publishing Group; 2018;554:538–43. Available from: <http://dx.doi.org/10.1038/nature25492>
13. Malladi S, Macalinao DG, Jin X, He L, Basnet H, Zou Y, et al. Metastatic Latency and Immune Evasion through Autocrine Inhibition of WNT. *Cell*. 2016;165:45–60.
14. Yuki K, Cheng N, Nakano M, Kuo CJ. Organoid Models of Tumor Immunology. *Trends Immunol* [Internet]. The Authors; 2020;41:652–64. Available from: <https://doi.org/10.1016/j.it.2020.06.010>
15. Lindeboom RG, Voorthuisen L van, Oost KC, Rodríguez-Colman MJ, Luna-Velez M V, Furlan C, et al. Integrative multi-omics analysis of intestinal organoid differentiation. *Mol Syst Biol* [Internet]. 2018;14:e8227. Available from: <http://msb.embopress.org/content/14/6/e8227>

16. Serra D, Mayr U, Boni A, Lukonin I, Rempfler M, Challet Meylan L, et al. Self-organization and symmetry breaking in intestinal organoid development. *Nature* [Internet]. Springer US; 2019;569:66–72. Available from: <http://dx.doi.org/10.1038/s41586-019-1146-y>
17. Basak O, Beumer J, Wiebrands K, Seno H, van Oudenaarden A, Clevers H. Induced Quiescence of Lgr5+ Stem Cells in Intestinal Organoids Enables Differentiation of Hormone-Producing Enteroendocrine Cells. *Cell Stem Cell* [Internet]. Elsevier Inc.; 2017;20:177-190.e4. Available from: <http://dx.doi.org/10.1016/j.stem.2016.11.001>
18. Beumer J, Puschhof J, Bauzá-Martinez J, Martínez-Silgado A, Elmentaite R, James KR, et al. High-Resolution mRNA and Secretome Atlas of Human Enteroendocrine Cells. *Cell*. 2020;181:1291–306.
19. Fumagalli A, Suijkerbuijk SJE, Begthel H, Beerling E, Oost KC, Snippert HJ, et al. A surgical orthotopic organoid transplantation approach in mice to visualize and study colorectal cancer progression. *Nat Protoc* [Internet]. Nature Publishing Group; 2018;13:235–47. Available from: <http://www.nature.com/doifinder/10.1038/nprot.2017.137>
20. van der Bij GJ, Bögels M, Otten MA, Oosterling SJ, Kuppen PJ, Meijer S, et al. Experimentally induced liver metastases from colorectal cancer can be prevented by mononuclear phagocyte-mediated monoclonal antibody therapy. *J Hepatol* [Internet]. Elsevier; 2010;53:677–85. Available from: <https://doi.org/10.1016/j.jhep.2010.04.023>
21. Ritsma L, Steller EJA, Ellenbroek SJJ, Kranenburg O, Borel Rinkes IHM, Van Rheenen J. Surgical implantation of an abdominal imaging window for intravital microscopy. *Nat Protoc*. Nature Publishing Group; 2013;8:583–94.
22. Ritsma L, Steller EJA, Beerling E, Loomans CJM, Zomer A, Gerlach C, et al. Intravital Microscopy Through an Abdominal Imaging Window Reveals a Pre-Micrometastasis Stage During Liver Metastasis. *Sci Transl Med* [Internet]. 2012;4:158ra145 LP-158ra145. Available from: <http://stm.sciencemag.org/content/4/158/158ra145.abstract>
23. Klaunig JE, Goldblatt PJ, Hinton DE, Lipsky MM, Trump BF. Mouse Liver Cell Culture . I . Hepatocyte Isolation. *In Vitro*. 1981;17:913–25.
24. Drost J, van Jaarsveld RH, Ponsioen B, Zimmerlin C, van Boxtel R, Buijs A, et al. Sequential cancer mutations in cultured human intestinal stem cells. *Nature* [Internet]. 2015;521:43–7. Available from: <http://dx.doi.org/10.1038/nature14415>
25. van de Wetering M, Francies HE, Francis JM, Bounova G, Iorio F, Pronk A, et al. Prospective Derivation of a Living Organoid Biobank of Colorectal Cancer Patients. *Cell* [Internet]. Elsevier Inc.; 2015;161:933–45. Available from: <http://dx.doi.org/10.1016/j.cell.2015.03.053>
26. Dekkers JF, Alieva M, Wellens LM, Ariese HCR, Jamieson PR, Vonk AM, et al. High-resolution 3D imaging of fixed and cleared organoids. *Nat Protoc* [Internet]. Springer US; 2019;14:1756–71. Available from: <http://dx.doi.org/10.1038/s41596-019-0160-8>
27. Love MI, Huber W, Anders S. Moderated estimation of fold change and dispersion for RNA-seq data with DESeq2. *Genome Biol*. 2014;15:1–21.
28. Gregorieff A, Liu Y, Inanlou MR, Khomchuk Y, Wrana JL. Yap-dependent reprogramming of Lgr5+ stem cells drives intestinal regeneration and cancer. *Nature* [Internet]. 2015;526:715–8. Available from: <http://www.ncbi.nlm.nih.gov/pubmed/26503053>
29. Muñoz J, Stange DE, Schepers AG, Van De Wetering M, Koo BK, Itzkovitz S, et al. The Lgr5 intestinal stem cell signature: Robust expression of proposed quiescent ' +4 ' cell markers. *EMBO J*. 2012;31:3079–91.

30. Yui S, Azzolin L, Maimets M, Pedersen MT, Fordham RP, Hansen SL, et al. YAP/TAZ-Dependent Reprogramming of Colonic Epithelium Links ECM Remodeling to Tissue Regeneration. *Cell Stem Cell* [Internet]. Elsevier Inc.; 2018;22:35-49.e7. Available from: <https://doi.org/10.1016/j.stem.2017.11.001>
31. Muraro MJ, Dharmadhikari G, Grün D, Groen N, Dielen T, Jansen E, et al. A Single-Cell Transcriptome Atlas of the Human Pancreas. *Cell Syst*. 2016;3:385-394.e3.
32. Stuart T, Butler A, Hoffman P, Hafemeister C, Papalexi E, Mauck WM, et al. Comprehensive Integration of Single-Cell Data. *Cell* [Internet]. Elsevier Inc.; 2019;177:1888-1902.e21. Available from: <https://doi.org/10.1016/j.cell.2019.05.031>
33. Mustata RC, Vasile G, Fernandez-Vallone V, Strollo S, Lefort A, Libert F, et al. Identification of Lgr5-Independent Spheroid-Generating Progenitors of the Mouse Fetal Intestinal Epithelium. *Cell Rep*. 2013;5:421–32.
34. Tallapragada NP, Cambra HM, Wald T, Keough Jalbert S, Abraham DM, Klein OD, et al. Inflation-collapse dynamics drive patterning and morphogenesis in intestinal organoids. *Cell Stem Cell* [Internet]. Elsevier Inc.; 2021;28:1516-1532.e14. Available from: <https://doi.org/10.1016/j.stem.2021.04.002>
35. Postriganova N, Kazaryan AM, Røsok BI, Fretland ÅA, Barkhatov L, Edwin B. Margin status after laparoscopic resection of colorectal liver metastases: Does a narrow resection margin have an influence on survival and local recurrence? *Hpb* [Internet]. Elsevier Masson SAS; 2014;16:822–9. Available from: <http://dx.doi.org/10.1111/hpb.12204>
36. Barker N, van Es JH, Kuipers J, Kujala P, van den Born M, Cozijnsen M, et al. Identification of stem cells in small intestine and colon by marker gene Lgr5. *Nature*. 2007;449:1003–8.
37. Schuijers J, Junker JP, Mokry M, Hatzis P, Koo BK, Sasselli V, et al. Ascl2 acts as an R-spondin/wnt-responsive switch to control stemness in intestinal crypts. *Cell Stem Cell* [Internet]. Elsevier Inc.; 2015;16:158–70. Available from: <http://dx.doi.org/10.1016/j.stem.2014.12.006>
38. van der Flier LG, Haegebarth A, Stange DE, van de Wetering M, Clevers H. OLFM4 Is a Robust Marker for Stem Cells in Human Intestine and Marks a Subset of Colorectal Cancer Cells. *Gastroenterology* [Internet]. AGA Institute American Gastroenterological Association; 2009;137:15–7. Available from: <http://dx.doi.org/10.1053/j.gastro.2009.05.035>
39. van der Flier LG, van Gijn ME, Hatzis P, Kujala P, Haegebar A, Stange DE, et al. Transcription Factor Achaete Scute-Like 2 Controls Intestinal Stem Cell Fate. *Cell* [Internet]. Elsevier Ltd; 2009;136:903–12. Available from: <http://dx.doi.org/10.1016/j.cell.2009.01.031>
40. Oost KC, van Voorthuijsen L, Fumagalli A, Lindeboom RGH, Sprangers J, Omerzu M, et al. Specific Labeling of Stem Cell Activity in Human Colorectal Organoids Using an ASCL2-Responsive Minigene. *Cell Rep* [Internet]. ElsevierCompany.; 2018;22:1600–14. Available from: <https://doi.org/10.1016/j.celrep.2018.01.033>
41. Van Der Heijden M, Miedema DM, Waclaw B, Veenstra VL, Lecca MC, Nijman LE, et al. Spatiotemporal regulation of clonogenicity in colorectal cancer xenografts. *Proc Natl Acad Sci U S A*. 2019;116:6140–5.
42. Ritsma L, Ellenbroek SJ, Zomer A, Snippert HJ, De Sauvage FJ, Simons BD, et al. Intestinal crypt homeostasis revealed at single-stem-cell level by in vivo live imaging. *Nature* [Internet]. Nature Publishing Group; 2014;507:362–5. Available from: <http://dx.doi.org/10.1038/nature12972>
43. Xavier da Silveira dos Santos A, Liberali P. From single cells to tissue self-organization. *FEBS J*. 2019. page 1495–513.

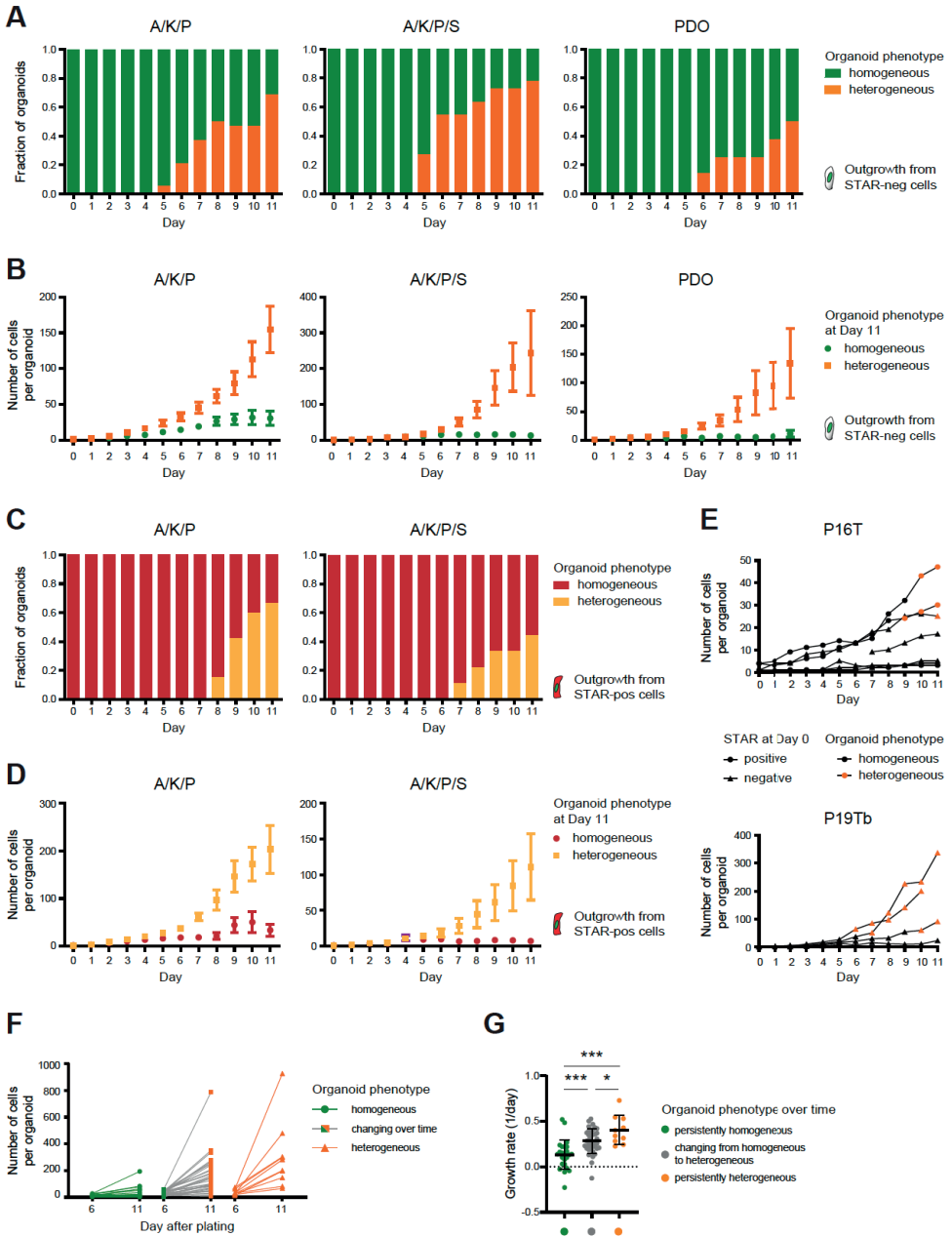
44. Von Gise A, Lin Z, Schlegelmilch K, Honor LB, Pan GM, Buck JN, et al. YAP1, the nuclear target of Hippo signaling, stimulates heart growth through cardiomyocyte proliferation but not hypertrophy. *Proc Natl Acad Sci U S A*. 2012;109:2394–9.
45. Fan F, He Z, Kong LL, Chen Q, Yuan Q, Zhang S, et al. Pharmacological targeting of kinases MST1 and MST2 augments tissue repair and regeneration. *Sci Transl Med*. 2016;8.
46. Valastyan S, Weinberg RA. Tumor metastasis: Molecular insights and evolving paradigms. *Cell* [Internet]. Elsevier Inc.; 2011;147:275–92. Available from: <http://dx.doi.org/10.1016/j.cell.2011.09.024>
47. Sato T, van Es JH, Snippert HJ, Stange DE, Vries RG, van den Born M, et al. Paneth cells constitute the niche for Lgr5 stem cells in intestinal crypts. *Nature* [Internet]. Nature Publishing Group; 2011;469:415–8. Available from: <http://www.pubmedcentral.nih.gov/articlerender.fcgi?artid=3547360&tool=pmcentrez&rendertype=abstract%5Cnhttp://www.nature.com/doi/10.1038/nature09637>
48. Ganesh K, Basnet H, Kaygusuz Y, Laughney AM, He L, Sharma R, et al. L1CAM defines the regenerative origin of metastasis-initiating cells in colorectal cancer. *Nat Cancer* [Internet]. Springer US; 2020;1:28–45. Available from: <http://dx.doi.org/10.1038/s43018-019-0006-x>
49. Er EE, Valiente M, Ganesh K, Zou Y, Agrawal S, Hu J, et al. Pericyte-like spreading by disseminated cancer cells activates YAP and MRTF for metastatic colonization. *Nat Cell Biol*. 2018;20:966–78.
50. Cheung P, Xiol J, Dill MT, Yuan WC, Panero R, Roper J, et al. Regenerative Reprogramming of the Intestinal Stem Cell State via Hippo Signaling Suppresses Metastatic Colorectal Cancer. *Cell Stem Cell* [Internet]. 2020;27:590-604.e9. Available from: <http://www.ncbi.nlm.nih.gov/pubmed/32730753>
51. Guillermin O, Angelis N, Sidor CM, Ridgway R, Baulies A, Kucharska A, et al. Wnt and Src signals converge on YAP-TEAD to drive intestinal regeneration. *EMBO J*. 2021;40:1–19.
52. Bernal C, Silvano M, Taponnier Y, Anand S, Angulo C, Ruiz i Altaba A. Functional Pro-metastatic Heterogeneity Revealed by Spiked-scRNAseq Is Shaped by Cancer Cell Interactions and Restricted by VSIG1. *Cell Rep* [Internet]. ElsevierCompany.; 2020;33:108372. Available from: <https://doi.org/10.1016/j.celrep.2020.108372>
53. Xu Z, Wang H, Gao L, Zhang H, Wang X. YAP levels combined with plasma CEA levels are prognostic biomarkers for early-clinical-stage patients of colorectal cancer. *Biomed Res Int*. 2019;2019.
54. Yuen HF, McCrudden CM, Huang YH, Tham JM, Zhang X, Zeng Q, et al. TAZ Expression as a Prognostic Indicator in Colorectal Cancer. *PLoS One*. 2013;8.
55. Kiefel H, Bondong S, Hazin J, Ridinger J, Schirmer U, Riedle S, et al. L1CAM: A major driver for tumor cell invasion and motility. *Cell Adhes Migr*. 2012;6:374–84.
56. Laughney AM, Hu J, Campbell NR, Bakhoun SF, Setty M, Lavallée VP, et al. Regenerative lineages and immune-mediated pruning in lung cancer metastasis. *Nat Med* [Internet]. Springer US; 2020;26:259–69. Available from: <http://dx.doi.org/10.1038/s41591-019-0750-6>

SUPPLEMENTARY MATERIAL



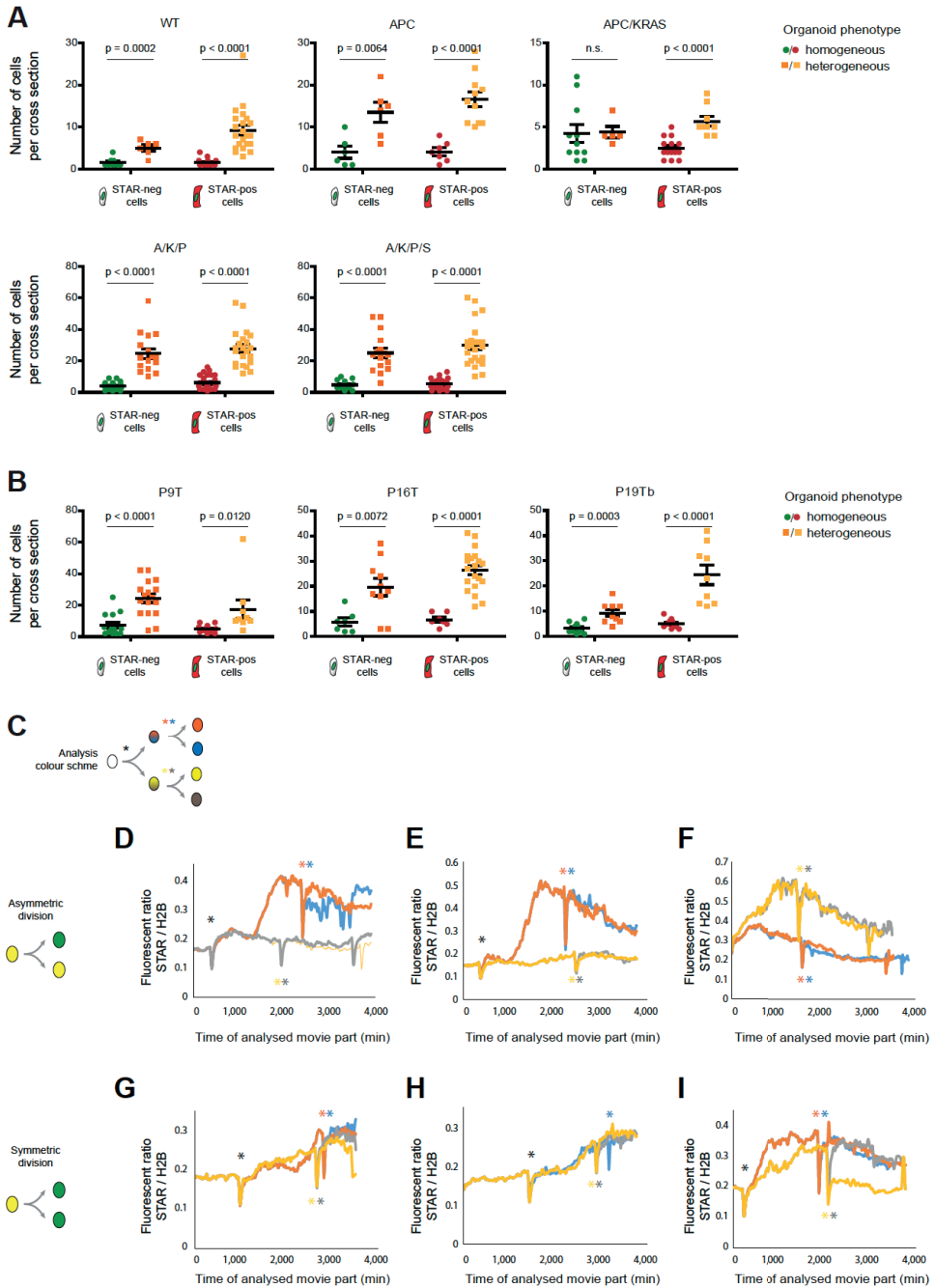
◀Figure S1: Related to Figures 1 and 2

A-D. Representative images of antibody stainings on human colon sections for (A) EPCAM, (B) GPA33, (C) CDX2, and (D) OLFM4. Scale bars, 100 μm . **E-F.** Patient-derived liver tissue strip stained for (E) EPCAM and (F) CDX2 to identify cells of colonic origin. The positions of micrometastases (positive for EPCAM, CDX2, and GPA33) are indicated by arrowheads. Scale bars, 5 mm (in close ups, 50 μm). Related to Figure 1B. **G-H.** Two examples of micrometastases identified by stainings for EPCAM, GPA33, and CDX2. Micrometastases are completely devoid of the SC marker OLFM4. Scale bars, 100 μm . **I.** Schematic of STAR reporter design suitable for Tol2 transposon-based integration. Having 8 repeats of an ASCL2 motif (8xSTAR) upfront, transcriptional activity of ASCL2 is reported by nuclear expression of sTomato. Additionally, ubiquitous expression of H2B fused to mNeonGreen is driven by an independent, ubiquitously active PGK promoter. Other elements: insulator sequence preventing 5' methylation (cHS4 insulator), polyadenylation signal (polyA), 2A self-cleavage peptide (P2A), puromycin selection cassette (puroR). This STAR is a derivative of the previously published STAR (Figure S1J) (40). **J.** Design of the STAR reporter as previously published (40). 4xSTAR indicating 4 repeats of the ASCL2 binding site. Other elements: Internal ribosome entry site (IRES) and blasticidin selection cassette (BSD). **K.** Traces of individual metastases that are devoid of Lgr5 expression during the whole course of IVM, depicting the size of the lesions over time. This data is a subset of the data depicted in Figure 2E but with a different scale.



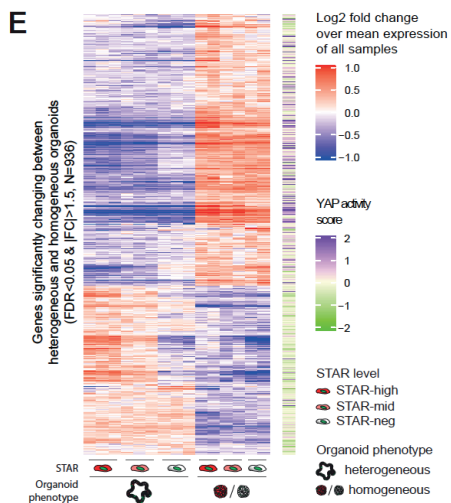
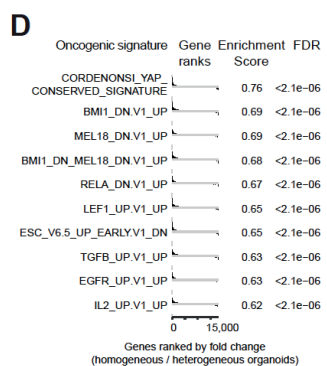
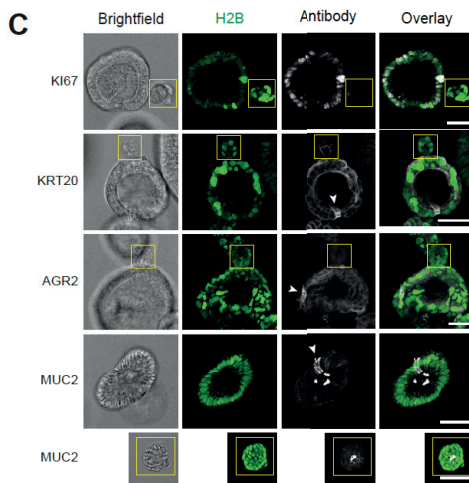
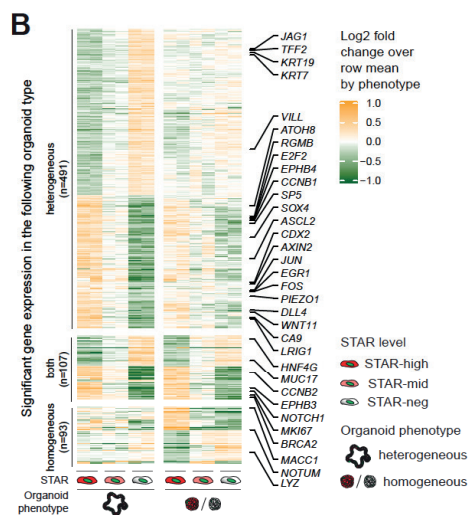
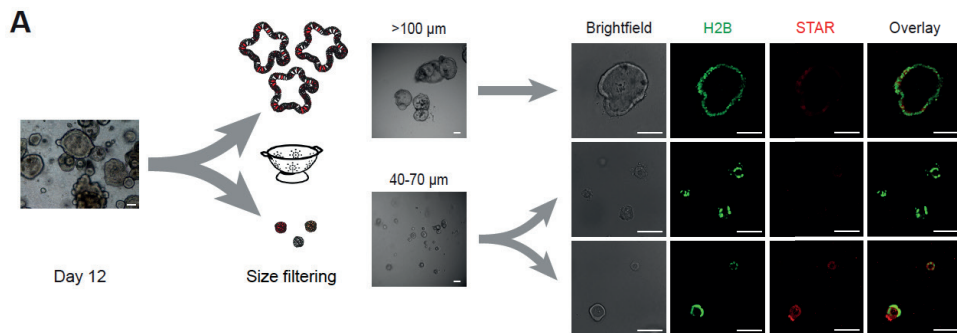
◀Figure S2: Related to Figure 3

Quantification of the outgrowth behaviour of human CRC organoid lines over time with respect to cellular composition. (A-E) The data is stratified by organoid line. Engineered CRC with $APC^{KO}/KRAS^{G12D}/TP53^{KO/KO}$ (A/K/P); engineered, metastatic A/K/P with additional $SMAD4^{KO/KO}$ (A/K/P/S); PDOs P16T and P19Tb pooled (PDO). The pooled data of all lines is presented in Figure 3. **A.** Graph representing the fraction of organoid phenotypes (homogeneous versus heterogeneous) per indicated time point during the outgrowth of STAR⁻ CRC cells. **B.** Number of cells per organoid over time, stratified by organoid phenotype at the final day of tracking. Graph represents the mean size + SEM for the outgrowth of STAR⁻ cells. **C.** Graph representing the fraction of organoid phenotypes (homogeneous versus heterogeneous) per indicated time point during the outgrowth of STAR⁺ CRC cells. **D.** Number of cells per organoid over time, stratified by organoid phenotype at the final day of tracking. Graph represents the mean size + SEM for the outgrowth of STAR⁺ cells. **E.** Single PDO outgrowth traces over time depicting the organoid phenotypes to be either homogeneous organoids (black) or heterogeneous (orange). Outgrowth of single STAR⁻ (triangle) or STAR⁺ cells (dots). PDOs: P16T (top) and P19Tb (bottom). **F.** Paired data of individual organoids at Day 6 and 11 of culturing. Number of cells per organoid is plotted and the organoid phenotype is indicated by colour for each time point to be either homogeneous (green) or heterogeneous (orange). **G.** Computed growth rate of individual organoids plotted in panel F. The growth rate distributions of the three phenotype groups was compared with a two-tailed Student's t-test (p-value < 0.0001 for comparisons left vs. middle and left vs. right and 0.0002 for comparison middle vs right).



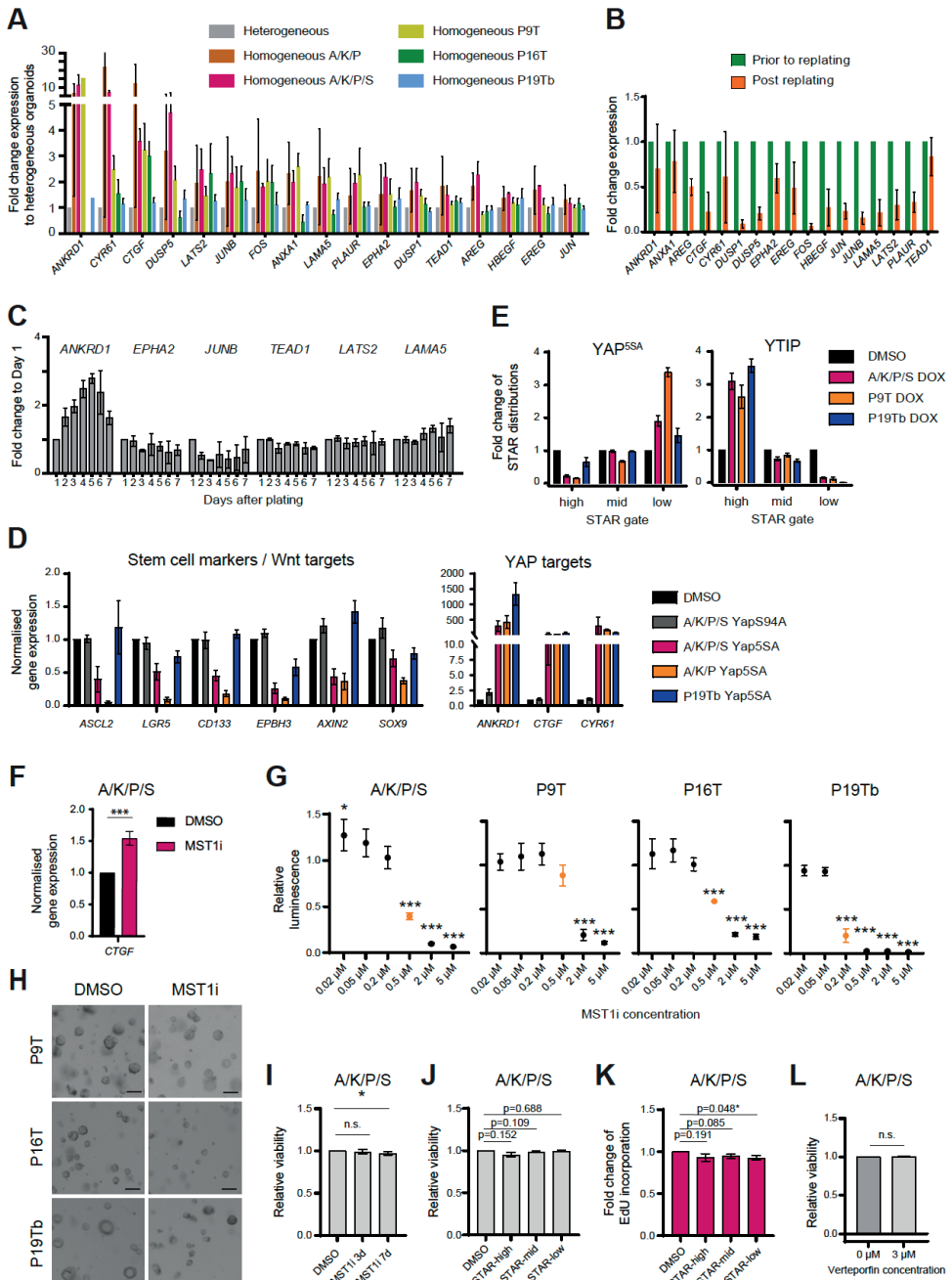
◀Figure S3: Related to Figure 3

A-B. Organoid size after 10 days of culturing is depicted as the number of nuclei per organoid cross section at its widest position. Single STAR⁺/STAR⁻ cells grew either into homogeneous structures (green/red) or into heterogeneous structures (orange/yellow). Organoid size stratified by phenotype was compared using a two-tailed Student's t-test. (A) Data generated with human colon WT and engineered human CRC lines with the following mutations: loss of *APC* (APC or A), *TP53* (P), *SMAD4* (S), and oncogenic *KRAS*^{G12D/-} (KRAS or K). (B) Data generated with PDOs P9T, P16T and P19Tb. **C-I.** Analysis of early cell plasticity events during PDO outgrowth starting at preceding mitosis (black asterisk) up until 1-2 mitoses later (coloured asterisks). Ratio intensities of measured nuclear STAR over H2B signal are plotted for the individual cells. Mitoses coincide with dips in ratio plot due to dilution of STAR signal during nuclear envelope breakdown. (C) Schematic of colour/lineage assignment. (D-F) and (G-I) show plasticity events with asymmetric and symmetric divisions in division round 1, respectively.



◀Figure S4: Related to Figures 4

A. Representative images of organoids prior to and after size filtering with STAR-neg and STAR-pos micro-organoids (40-70 μm , centre and bottom row, respectively). H2B chromatin-tag (green), STAR (red). Scale bars, 100 μm . **B.** Heatmap depicting genes being differentially expressed for at least one comparison between STAR-high, STAR-mid, and STAR-neg samples with $\text{FDR} < 0.01$. Genes are grouped to be dynamically expressed in heterogeneous (top), homogeneous (bottom), or both organoid phenotypes (mid). Gene expression was normalised to the row mean of samples of the respective organoid phenotype. Equal numbers of replicates ($N=2$) were considered for each biological condition in this analysis. **C.** Representative images of small and large A/K/P/S or P16T organoids stained for the proliferation marker KI67 and differentiation markers KRT20, AGR2, and MUC2. Micro-organoids are outlined by a yellow box. Cells positive for the differentiation markers are indicated with an arrowhead. Scale bars, 50 μm . **D.** Comparison of the homogeneous organoid signature (gene expression of homogeneous over heterogeneous organoids, ranked by fold change) to the oncogenic signatures of Molecular Signature Database (MSigDB). Enrichment score and FDR is depicted for the top 10 hits. Ranking starts with genes upregulated in homogeneous micro-organoids (left). **E.** Heatmap showing all differentially expressed genes between homogeneous and heterogeneous organoids (fold change (FC) > 1.5 , $\text{FDR} < 0.05$) to which a YAP score could be assigned.



◀Figure S5: Related to Figures 4-6

A. Expression pattern of *micro-organoid associated genes* across engineered and patient-derived CRC organoid lines after size filtering for small (homogeneous) and large (heterogeneous) organoids. Gene expression, assessed by qPCR, is normalised to heterogeneous organoids. Data shows mean + SEM of 2-4 independent experiments. Related to Figure 4I. **B.** Gene expression of A/K/P/S micro-organoids isolated from a 12 day culture with (orange) or without (green) replating intact organoids into new Matrigel and harvesting after another 16h. Mean expression + SEM of three independent experiments is indicated. **C.** Gene expression over time in A/K/P/S organoids growing from single cells for a selection of genes being upregulated in micro-organoids. Gene expression is normalised to Day 1. Data shows mean + SEM of two independent experiments. **D.** Gene expression of YAP targets and SC markers / Wnt targets upon overexpression of either constitutively active YAP^{55A} or a TEAD-binding-dead mutant YAP^{S94A}. qPCR data was normalised to housekeeping genes and data is represented as fold change to DMSO treated samples (mean + SEM of 3-4 independent experiments). **E.** Flow analysis of STAR levels in 3 different CRC organoid lines upon perturbation of YAP activity via inducible overexpression (48 hrs) of the constitutively active YAP mutant YAP^{55A} or the YAP mimetic YTIP. Inhibiting YAP activity skews cells towards high STAR levels, at the expense of cells with low to medium levels of SC activity. Conversely, stimulating YAP activity skews cells towards low STAR levels, at the expense of cells with high levels of SC activity. Analysis at Day 5 of outgrowth. Data represents the change for each STAR population compared to DMSO as mean + SEM. **F.** Gene expression data of YAP targets in A/K/P/S organoids treated for 48h with 500 nM of the MST1/2 inhibitor XMU-MP-1. qPCR data was normalised to housekeeping genes and is represented as fold change to DMSO treated samples (mean + SEM of 4 independent experiments). **G.** Relative viability of CRC organoids treated with a concentration range of the MST1/2 inhibitor for 7 days after plating single cells. CellTiter-Glo data is normalised to DMSO control. The level of significance of the difference between MST1i-treated cells and the DMSO control was assessed using a two-tailed Student's t-test. **H.** Representative images of CRC organoids after 7 days of MST1/2 inhibitor treatment (500 nM for P9T and P16T and 200 nM for P19Tb). Scale bars, 100 μ m. **I-L.** Flow analysis of A/K/P/S organoids with respect to (I-J, L) viability and (K) EdU incorporation upon the following drug treatments: (I) 500 nM MST1/2 inhibitor was added for 3 or 7 days to single cells. (J-K) 500 nM MST1/2 inhibitor was added for 96 h to 10-day-old organoids. (L) 3 μ M verteporfin was added for 48 h to single cells. Viability readout was assessed upon DAPI wash-in before flow analysis. EdU incorporation was assessed after addition of 500 nM EdU to the culture for the last 16 h. All data is normalised to the respective DMSO control and significance levels were assessed by two-tailed Student's t-test.

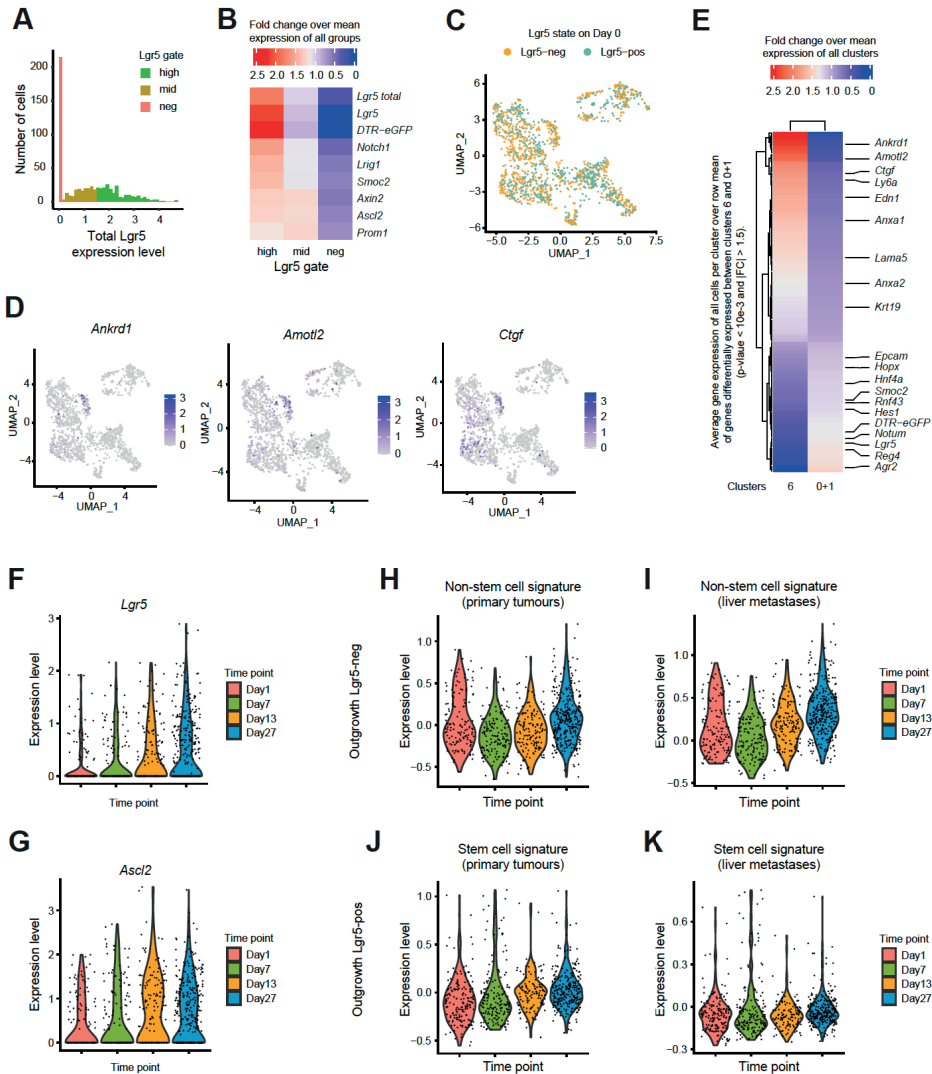


Figure S6: Related to Figure 7

A. Histogram of total Lgr5 expression computed as the sum of both alleles (WT and DTR-eGFP) after normalization of the data. Lgr5-high (green), -mid (orange), and -neg (red) subpopulations are determined by total expression level > 1.5 (37.5 % of all cells), < 1.5 but > 0 (27.5 % of all cells), zero (35.0 % of all cells). **B.** Heatmap of selected SC markers and Wnt targets stratified by Lgr5 populations defined in (A). Data is represented as fold change over row mean for each gene. **C.** UMAP of scRNA-seq data colour-coded by the Lgr5 state at the time of injection. **D.** UMAP with colour-coded gene expression levels of the following Yap target genes: *Ankrd1*, *Amotl2*, and *Ctgf*. **E.** Average gene expression for all differentially expressed genes between cluster 6 and clusters 0 and 1 (p -value $< 10e-3$ and $|FC| > 1.5$). Expression value is normalised by row mean and candidate genes are annotated. **F-G.** Gene expression of (F) *Lgr5* and (G) *Ascl2* over time of all cells being Lgr5⁺ at time of injection. **H-K.** Expression levels of (H-I) non-SC signature and (J-K) SC signature over time for (H-I) Lgr5⁻ and (J-K) Lgr5⁺ injected cells. Signature is based on cells growing in (H/J) primary tumours and (I/K) liver metastases (8).

Patient	Age	Gender	Primary CRC TNM	Primary CRC Location	Diagnosis	Pre-operative chemotherapy	Pre-operative Intra-arterial therapy	Surgery	RAS mutational status	BRAF mutational status	MMR status	Number of micro-metastases
MM1	72	M	pT3N1	Rectum	Adenocarcinoma	FOLFOX + bevacuzimab	no	Left hemihepatectomy	KRASmut	BRAF-wt	MSS	n.d.
MM2	71	M	pT3N1	Left colon	Adenocarcinoma	FOLFOXIRI + bevacuzimab	no	Right hemihepatectomy	KRASmut	BRAF-wt	MSS	n.d.
MM3	60	M	NA	Left colon	Adenocarcinoma	FOLFOXIRI + bevacuzimab	TARE / SIRT	Ext. right hemihepatectomy	KRASmut	BRAF-wt	MSS	n.d.
MM4	74	M	pT4N1	Left colon	Adenocarcinoma	FOLFOX + panitumumab	no	Right hemihepatectomy + Wedge S4b	KRAS-wt HRAS-wt NRAS-wt	BRAF-wt	MSS	6
MM5	66	M	pT3N0	Rectum	Adenocarcinoma	CAPOX	no	Left hemihepatectomy	-	-	-	n.d.
MM6	52	F	cT4aN2	Rectum	Adenocarcinoma	CAPOX + bevacuzimab	no	Right hemihepatectomy	KRAS-wt HRAS-wt NRAS-wt	BRAF-wt	MSS	n.d.
MM7	58	M	pT3N1	Rectum	Adenocarcinoma	FOLFIRI + bevacuzimab	no	Right hemihepatectomy	KRASmut	BRAF-wt	MSS	n.d.
MM8	53	F	pT3N1a	Rectum	Adenocarcinoma	-	no	Robotic Right hemihepatectomy	-	-	MSS	n.d.
MM9	59	M	pT3N1a	Left colon	Adenocarcinoma	-	no	Left hemihepatectomy	KRASmut	BRAF-wt	MSS	3
MM10	57	M	cT4N1	Rectum	Adenocarcinoma	FOLFOXIRI + bevacuzimab	no	Right hemihepatectomy + Wedge S3	KRASmut	BRAF-wt	MSS	n.d.
MM11	52	F	pT4N0	Rectum	Adenocarcinoma	Capecitabine	no	Robotic Right hemihepatectomy	KRAS-wt HRAS-wt NRAS-wt	BRAF-wt	MSS	3
MM12	52	F	ypT3N0	Left colon	Adenocarcinoma	FOLFOX + bevacuzimab	no	Right hemihepatectomy	KRAS-wt HRAS-wt NRAS-wt	BRAF-wt	-	n.d.
MM13	61	F	pT4N1b	Left colon	Adenocarcinoma	-	no	Left hemihepatectomy	-	-	MSS	n.d.
MM14	69	M	ypT3N0	Left colon	Adenocarcinoma	FOLFOXIRI + bevacuzimab	no	Right hemihepatectomy	KRAS-wt HRAS-wt NRAS-wt	BRAF-wt	MSS	1
MM15	60	M	cT3N2	Rectum	Adenocarcinoma	CAPOX + bevacuzimab	TARE / SIRT	Right hemihepatectomy	KRAS-wt HRAS-wt NRAS-wt	BRAF-wt	MSS	3
MM16	63	M	pT3N2a	Left colon	Adenocarcinoma	CAPOX + bevacuzimab	no	Right hemihepatectomy	KRASmut	BRAF-wt	MSS	1
MM17	67	F	ypT3N1b	Right colon	Adenocarcinoma	FOLFOX + bevacuzimab	no	Right hemihepatectomy + S1 resection	KRAS-wt HRAS-wt NRAS-wt	BRAFmut	MSI	n.d.
MM18	77	M	pT3N1a	Left colon	Adenocarcinoma	FOLFIRI + bevacuzimab	no	Right hemihepatectomy	KRASmut	BRAF-wt	MSS	n.d.

Table S1: Characteristics of patients included for liver specimen collection. Related to Figure 1

Basic characteristics of CRC patients undergoing resection for liver metastases which were included for liver specimen collection and subsequent immunohistochemistry analysis for the presence of micro-metastases. Abbreviations: Mismatch repair (MMR), transarterial radioembolization (TARE), selective internal radiation therapy (SIRT), microsatellite stable (MMS), microsatellite unstable (MSI), not detected (n.d.).



Antibody	Company	Catalogue number	Concentration	Application
EPCAM	Abcam, clone BER-EP4	ab7504	80 X	Fluorescent IHC
GPA33	Atlas Antibodies	HPA018858,	250 X	Fluorescent IHC
CDX2	Immunologic, clone EPR2764Y	ILM2353-C1	200 X	Fluorescent IHC
OLFM4	Cell Signaling Technology	CST14369	100 X	Fluorescent IHC
anti-RFP	Rockland	600-401-379	200 X	Fluorescent multiplex IHC
anti-CEA	Abcam	ab75685	600 X	Fluorescent multiplex IHC
Goat-anti-Rb-poly-HRP	PowerVision	PV6119	<i>according to manual</i>	Fluorescent (multiplex) IHC
Goat-anti-Ms-poly-HRP	PowerVision	PV6114	<i>according to manual</i>	Fluorescent (multiplex) IHC
Alexa Fluor 488	Invitrogen Tyramide SuperBoost™ Kit	B40943	<i>according to manual</i>	Fluorescent multiplex IHC
Alexa Fluor 647	Invitrogen Tyramide SuperBoost™ Kit	B40916	<i>according to manual</i>	Fluorescent multiplex IHC
AGR2	Abcam	ab56703	500 X	Organoid staining
KI67	Abcam	ab15580	1,000 X	Organoid staining
KRT20	Abcam	ab854	100 X	Organoid staining
MUC2	Santa Cruz	sc-15334	500 X	Organoid staining
Alexa Fluor 405 goat anti-mouse	Life technologies	A31553	500 X	Organoid staining
Alexa Fluor 647 goat anti-rabbit	Fisher scientific	10739574	500 X	Organoid staining
Alexa Fluor 647 donkey anti-goat	Fisher scientific	10493402	500 X	Organoid staining

Table S2: Details on antibodies used in this study.

Transcript ID	Gene Symbol	FDR Size	YAP score	Rank YAP Filtering	FC small / big	Rank FC Filtering	RT-qPCR Fw primer	RT-qPCR Rv primer
NM_014391	ANKRD1	2.15E-15	NA	NA	5.1	20	GCTTGAATCCACAGCCATCCAC	GCACTCATAGTGGCCAGTCC
NM_000700	ANXA1	2.49E-09	4.58	15	3.51	63	CTAAGCGAAACAATGCACAGC	CCTCCTCAAGGTGACCTGTAA
NM_001657	AREG	5.80E-13	NA	NA	4.35	32	GATTCAGTCAGAGTTGAACAGG	CCATTTTTGCCTCCCTTTTTTC
NM_001901	CTGF	2.75E-64	NA	NA	4.82	24	ACCGACTGGAAGACACCGTTTG	CCAGGTCAAGCTTCGCAAGG
NM_001554	CYR61	1.24E-57	NA	NA	4.47	30	GATCTGCAGAGCTCAGTCAGAG	CCATCAATACATGTGCACCTG
NM_004417	DUSP1	6.80E-118	5.03	12	4.97	22	ACCACCACCGTGTCCAACCTTC	TGGGAGAGGTCGTAATGGGG
NM_004419	DUSP5	2.80E-33	1.68	92	9.69	6	GCGACCCACTACACTACAAA	CTTCATAAGGTAAGCCATGCAGA
NM_004431	EPHA2	2.45E-22	6.73	8	2.46	NA	TGGCTCACACACCCCGTATG	GTCGCCAGACATCACGTTG
NM_001432	EREG	7.91E-10	NA	NA	5.06	21	GGACAGTGCATCTATCTGGTGG	TTGGTGGACGGTTAAAAAAGAAGT
NM_005252	FOS	1.43E-33	2.56	46	2.05	NA	GGGGCAAGGTGGAAACAGTTAT	CCGCTTGGAGTGTATCAGTCA
NM_001945	HBEGF	3.80E-198	3.03	39	5.5	17	ATCGTGGGGCTTCTCATGTTT	TTAGTCATGCCCAACTTCACCTT
NM_002228	JUN	1.32E-23	1.62	100	1.93	NA	TCCAAGTGCCGAAAAAGGAAG	CGAGTTCTGAGCTTTCAAGGT
NM_002229	JUNB	1.67E-28	1.71	91	2.69	NA	ACGACTATACACAGCTACGG	GCTCGGTTTCAGGAGTTTGTAGT
NM_005560	LAMA5	8.71E-18	5.46	10	2	NA	CCCACCGAGGACCTTTACTG	GGTGTGCCTTGTGTCTGTT
NM_014572	LATS2	2.61E-39	3.91	21	2.05	NA	ACTTTTCTGCCACGACTTATTC	GATGGCTGTTTTAACCCCTCA
NM_001005376	PLAUR	2.01E-11	8.09	7	2.32	NA	GAGCTATCGGACTGGCTTGAA	CGGCTTCGGGAATAGGTGAC
NM_021961	TEAD1	8.48E-07	1.87	78	1.35	NA	ATGCCAACCACTTCTACAGTGAC	ACAGTTCTTTAAGCCACCTTTC

Table S3: Key features of micro-organoid genes. Related to Figures 4 and 5

Selection of genes upregulated in micro-organoids in RNAseq (Figure 4). Genes were selected due to a high YAP score and/or to a high fold change in expression between homogeneous and heterogeneous organoids (FC small / big). Selection of genes due to their YAP score was performed after filtering genes for (1) FDR size comparison < 0.001 (FDR Size), (2) YAP score > 1.5 (non-NA), and (3) mean expression of all samples > 9. Rank of genes after sorting final list by decreasing YAP score is indicated (Rank YAP Filtering). Selection of genes due to their expression fold change was performed after filtering genes for (1) FDR size comparison < 0.001, (2) expression fold change homogeneous / heterogeneous organoids > 3, and (3) mean expression of all samples > 9. Rank of genes after sorting final list by decreasing fold change is indicated (Rank FC Filtering). Forward and reverse primer sequences of each gene used in RT-qPCR experiments are indicated.

Supplementary material and methods

Collagenase liver perfusion

Collagenase liver perfusion was performed as described in the main document. To expose the cannulation site, a midline laparotomy was performed and the intestines were mobilized to the left. After successful cannulation the catheter was connected to the perfusion line. After the first perfusion, the subhepatic vena cava was cut allowing the drainage of the perfusate prior to perfusion of the digestion medium. When portal vein cannulation failed or proved difficult, the subhepatic vena cava was used instead as cannulation site. In this fashion, after successful cannulation the suprahepatic vena cava was clamped and the portal vein was cut to allow a retro-grade perfusion of the liver.

Plasmid designs

The STAR reporter used in this study (unless indicated otherwise) is an optimized version of the original reporter (1), enabling high-throughput imaging with easy quantifications, high sensitivity, and is well suitable for *in vivo* studies. The optimized STAR technology, termed movieSTAR, is based on a transposase-based integration method (movieSTAR: Tol2 insulator-8xSTAR-min.pLGR5-sTomato-NLS-pA-PGK-H2BmNeonGreen-2A-Puro, Figure S1I-J). A tandem cHS4 insulator precedes 8xSTAR repeats followed by a sTomato with a nuclear localisation signal (NLS) and a polyA sequence. Additionally, the murine PGK promoter is driving the expression of a H2B-mNeonGreen fusion protein alongside with a 2A sequence and a puromycin resistance cassette.

Experiments depicted in Figures 4, S3A-B, and S4 were performed with the previously published STAR version suitable for lentiviral integration (1): A blue or red STAR reporter in which 4xSTAR repeats are followed by TagBFP2 or tagRFP, an IRES sequence, and a blasticidin selection cassette (pLV-4xSTAR-min.pLGR5-TagBFP2-IRES-Blast or pLV-4xSTAR-min.pLGR5-TagRFP-IRES-Blast, Figure S1J). These reporters were combined with CMV-driven expression of an H2B-mNeonGreen fusion protein, a 2A sequence, and a puromycin selection cassette (pLV-CMV-H2BmNeonGreen-2A-Puro).

Inducible YAP and YTIP overexpression plasmids were cloned into a modified pInducer backbone which contains a ubiquitously expressed resistance cassette. YAP activation and inhibition was achieved by overexpression of the constitutively active YAP^{55A} (pLV-pTREG-YAP^{55A}-Ubc-rtTA-IRES-Blast) and the YAP mimetic YTIP (2) together with the fluorescent protein mMaroon1 (pLV-pTREG-mMaroon-NLS-2A-YTIP-Ubc-rtTA-IRES-Blast), respectively.

Plasmids were stably integrated into the genome of organoids as previously described (3). Plasmids generated in this study can either be found on Addgene or are available upon request.

Intravital imaging on liver metastases

Stage coordinates and visual landmarks inside the liver (such as blood vessels) were used for orientation. Metastases were identified and size-measured through RFP expression. Lesions were included into the analysis if tracked on at least 3 days.

Metastatic size and phenotype calling

IHC for human CEA was used to identify and measure the size of P19Tb-derived liver metastases. The stem cell expression pattern was assessed upon staining for RFP to be either heterogeneous or negative. Lesions smaller than 5,000 μm^2 were classified to be micrometastases. A Fisher's exact test was used to test the contingency between metastatic size and the stem cell expression pattern.

Organoid cultures

PDO lines used in this study are listed on COSMIC and comprise P19Tb (COSMIC: I2L-P19Tb-Tumor-Organoid, ID 2433500), P16T (COSMIC: I2L-P16-Tumor-Organoid, ID 2433496), and P9T (COSMIC: I2L-P9-Tumor-Organoid, ID 2433492). Additionally, the following engineered human CRC and colon WT lines were used: A/K/P/S ($APC^{KO/KO}; KRAS^{G12D/-}; TP53^{KO/KO}; SMAD4^{KO/KO}$), A/K/P ($APC^{KO/KO}; KRAS^{G12D/-}; TP53^{KO/KO}$), APC/KRAS ($APC^{KO/KO}; KRAS^{G12D/-}$), APC ($APC^{KO/KO}$), and WT (4).

Human organoid lines were maintained in Matrigel (Corning, Cat# 356231) as previously described (4,5), with culture medium containing Advanced DMEM/F12 (Invitrogen, Cat# 12634-028) supplemented with 10 mM Hepes (Invitrogen, Cat# 15630-056), 1% GlutaMAX (Invitrogen, Cat# 35050-038), 1% Penicillin-Streptomycin (Lonza, Cat# DE17-602E) as well as 1x B27 supplement (Invitrogen, Cat# 17504001), 1.25 mM N-Acetyl-L-cysteine (Sigma-Aldrich, Cat# A9165), 10 mM Nicotinamide (Sigma-Aldrich, Cat# N0636), 500 nM A83-01 (Tocris, Cat# 2939/10), 10 μM SB202190 (Gentaur, Cat# A1632), 10% R-Spondin1 conditioned medium, 10% Noggin conditioned medium, and 50 ng/mL human EGF (PeproTech).

For organoid splitting, the Matrigel was degraded through incubation with 1 mg/mL Dispase II (Life Technologies, Cat# 17105041) for 10 min at 37°C and organoids were

enzymatically dissociated using Trypsin-EDTA (Sigma-Aldrich, Cat# 25200056). Trypsin activity was subsequently abrogated through trypsin inhibitor (Sigma-Aldrich, Cat# T9003) in a 1:1 ratio. For maintenance, organoids were cultured in the presence of 10 μ M Y-27632 (Gentaur, Cat# A3008) during the first two days.

The murine CRC model of the genetic background *VillinCre-ER^{T2}; Apc^{FL/FL}; Kras^{LSL-G12D/+}; Tp53^{KO/KO}; R26R-Confetti; Lgr5^{DTR-eGFP}* was generated as previously described, while RFP⁺ confetti clones were isolated by FACS in order to generate the corresponding organoid line (6). This line was cultured in BME (AMS Bio), growing in Advanced DMEM/F12 with HEPES, GlutaMAX, B27, N-Acetyl-L-cysteine, and Noggin at concentrations specified above.

Absence of microplasm and the identity of all organoid lines was confirmed in regular intervals by targeted PCRs and sequencing of identifying loci, respectively.

Time-lapse microscopy of organoid outgrowth

Light-sheet recordings were performed using a LS1 light-sheet microscope from Viventis Microscopy equipped with temperature control at 37°C and 5.0% CO₂ overflow. CRC organoids were dissociated to small fragments and plated in Matrigel inside the light-sheet chamber. Organoids were imaged every 10 min for 7-13 days, while re-adjusting the stage position every couple of days (small jump in movies). For each channel, the data was background subtracted and a maximum intensity projection was performed for each time point. Data is represented with constant intensity scale over the entire movie.

Analysis of STAR dynamics around plasticity events

Plasticity events were selected by sudden appearance of STAR signal in time-lapse movies recording the outgrowth of p19Tb STAR organoids. Analysis was performed from the preceding mitosis up until two mitoses later. All 4 cells were analysed backwards in time down to t=0, so that each mother cell has at least 2 overlapping traces describing the same cell. STAR and H2B intensities were measured, the ratio STAR/H2B calculated, and the ratio is plotted as rolling average of 3 time points. Mitoses can be recognized by a sudden dip in the ratio which is affected by the nuclear envelope breakdown leading to dilution of STAR over the entire cell. The third round of mitoses is not outlined by asterisks but can be recognized by the shape. Cells for which the analysis could not be reliably conducted, are excluded from the plots.

FACS isolation of STAR populations

Two-week-old organoid were dissociated to single cells, incubated with 1.5 μ M DRAQ7 (Cell Signaling Technology), and sorted using an Aria III machine (Becton Dickinson). STAR populations were collected in organoid medium with 100 μ g/mL primocin and 2 % v/v Matrigel.

Flow analysis of STAR expression

3-day-old organoids grown from single cells were treated with either 2 μ g/mL doxycycline (Bio-Connect, Cat# 0219504401) or with DMSO (VWR). 48 h later, organoids were dissociated to single cells and fixed using 1mL of 4% paraformaldehyde (VWR, Cat# 47377.9L) for 15 min at RT. Samples were kept at 4°C in PBS with 0.05% Tween (VWR, Cat# 8221840500) until analysis.

For each line, 20,000-200,000 single, alive cells were analysed (gating on scattering properties and H2B-mNeonGreen expression) on a BD FACSCelesta™ flow cytometer. For YTIP overexpression lines, additional gating on mMaroon1⁺ cells was performed. STAR gates were defined as STAR-high (top 15%), STAR-low (bottom 15%), and STAR-mid (remaining 70%) based on the DMSO sample using FlowJo 10.6.1 (<https://www.flowjo.com>). The fraction of cells within each STAR gate was plotted as mean + SEM of 3-4 independent experiments for each line.

Relative viability and proliferation was assessed by comparing the number of DAPI-negative and EdU-positive cells, respectively, in drug-treated samples to their respective DMSO control.

Organoid tracking experiment

Organoids were scanned daily with a 40X water objective (HC PL APO CS2; NA 1.1) on a Leica SP8X confocal microscope equipped with a culture chamber held at 37°C with 5.0% CO₂ overflow. The images were analysed with Imaris (v9.3, Oxford Instruments) and organoids with at least 5 time points were included into the analysis.

For the data represented in Figure S3, organoid size is represented as the number of nuclei per organoid cross-section at its widest position, while STAR fate was assessed after investigating the entire organoid in 3D in Fiji (<https://imagej.nih.gov/ij/>).

EdU incorporation assay

Intact organoids were fixed inside Matrigel using 4% paraformaldehyde with 0.25% glutaraldehyde for 15 min at RT and subsequent washing with PBS. Background signal was quenched with 1 % sodium borohydride (Sigma- Aldrich, Cat# 480886) for 10 min at RT thrice, followed by 3 PBS washing steps. Click-iT™ EdU Cell Proliferation Kit for Imaging (ThermoFisher, Cat# 12043795) was used with a 647 nm dye according to the manufacturer's instructions.

Fluorescent image analysis

Fluorescent images were imported into Fiji (<https://imagej.nih.gov/ij/>) for analysis (unless indicated otherwise). If necessary, background subtraction, correction for bleed through, smoothing, cropping / rotating, and linear contrast adjustment were applied.

Bulk RNA sequencing analysis

Sequencing reads were aligned with Hisat2 version 2.0.4 (7) to the provided and pre-indexed hg38 transcript assembly from UCSC, with alignment tailoring for transcript assemblers enabled. Reads per gene were counted with the htseq-count script from the Hisat2 software suite using the GTF file corresponding to the transcript assembly, with strandness disabled and identification attribute set to gene_id. The Wald test followed by correction for multiple testing using Benjamini-Hochberg method was used to identify significantly changing genes. The 'rlogTransformation' function in DESeq2 was used to normalise, \log_2 transform and noise-stabilize the expression data for visualisation purposes. Heatmaps were created with the ComplexHeatmap package (version 4.2.4) (8).

Gene set enrichment analyses were run with the following parameters: Nominal p-values were determined by 1000000 gene-set permutations. The repair gene signature was defined by upregulated genes with a p-value < 0.01 and fold change of at least 1.5. The foetal gene signature included genes that were significant at p-value < 0.01 and with a fold change of at least 3. Both LCC signatures were defined as genes with a fold change of at least 2 and an adjusted p-value < 0.05.

Micro-organoid gene selection

Bulk RNA-seq data was mined for genes with a high YAP score and/or a high fold change in expression between micro- and macro-organoids using two different strategies. Filtering strategy 1: (1) FDR size comparison < 0.001, (2) normalised mean sample expression > 9,

(3) YAP score > 1.5. Filtering strategy 2: (1) FDR size comparison < 0.001, (2) normalized mean sample expression > 9, (3) fold change expression micro-/macro-organoid samples > 3. Gene lists were ranked by decreasing YAP score (strategy 1) or decreasing fold change in expression (strategy 2). From these list, 17 *micro-organoid-related genes* were manually selected (Table S3).

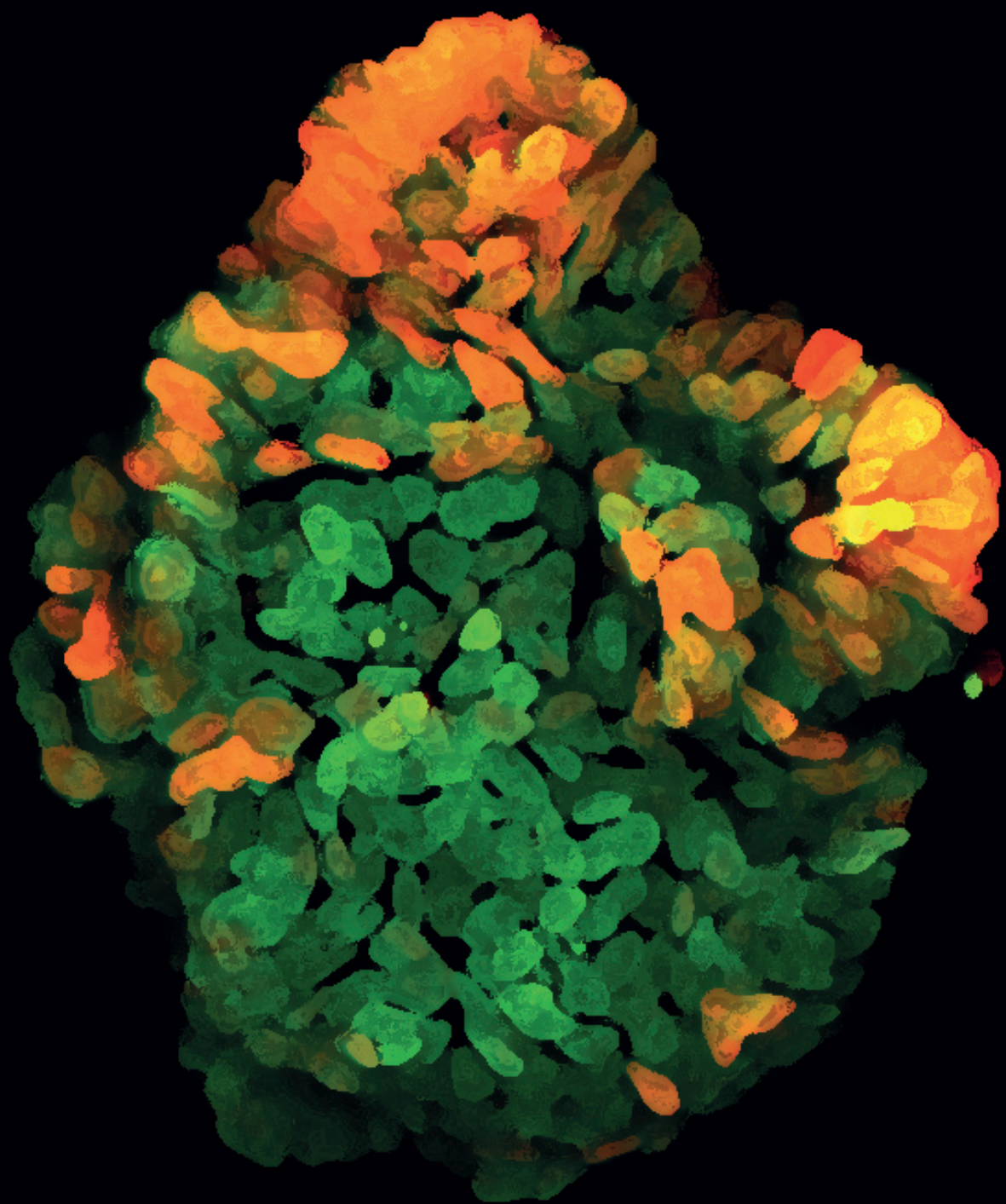
Single-cell RNA-sequencing data analysis

After mapping of the reads, cells with >200 unique transcripts and <10% mitochondrial reads were included into the analysis. The first 16 principle components were used for unsupervised hierarchical clustering (default settings at resolution 0.5). Differential gene expression was performed using a wilcox test (FindMarkers with min.pct = 0.25) and genes with adjusted p-value < 10e-3 and absolute average log2 fold change > 0.58 are displayed.

The co-expression of Lgr5 with other SC markers was tested for cells harvested on Day 27. The expression of both Lgr5 alleles (WT and DTR-eGFP gene fusion) were summed up and cells were grouped by their normalised expression value into three classes: negative (zero), mid (up to 1.5), and high (above 1.5). For each class, the mean expression of indicated SC markers was computed and depicted as mean over row mean in Figure S7B (R package ComplexHeatmap version 2.6.2).

Supplementary references

1. Oost KC, van Voorthuijsen L, Fumagalli A, Lindeboom RGH, Sprangers J, Omerzu M, et al. Specific Labeling of Stem Cell Activity in Human Colorectal Organoids Using an ASCL2-Responsive Minigene. *Cell Rep* [Internet]. Elsevier Company.; 2018;22:1600–14. Available from: <https://doi.org/10.1016/j.celrep.2018.01.033>
2. Von Gise A, Lin Z, Schlegelmilch K, Honor LB, Pan GM, Buck JN, et al. YAP1, the nuclear target of Hippo signaling, stimulates heart growth through cardiomyocyte proliferation but not hypertrophy. *Proc Natl Acad Sci U S A*. 2012;109:2394–9.
3. Heinz MC, Oost KC, Snippert HJG. Introducing the Stem Cell ASCL2 Reporter STAR into Intestinal Organoids. *STAR Protoc* [Internet]. The Author(s); 2020;100126. Available from: <https://doi.org/10.1016/j.xpro.2020.100126>
4. Drost J, van Jaarsveld RH, Ponsioen B, Zimmerlin C, van Boxtel R, Buijs A, et al. Sequential cancer mutations in cultured human intestinal stem cells. *Nature* [Internet]. 2015;521:43–7. Available from: <http://dx.doi.org/10.1038/nature14415>
5. van de Wetering M, Francies HE, Francis JM, Bounova G, Iorio F, Pronk A, et al. Prospective Derivation of a Living Organoid Biobank of Colorectal Cancer Patients. *Cell* [Internet]. Elsevier Inc.; 2015;161:933–45. Available from: <http://dx.doi.org/10.1016/j.cell.2015.03.053>
6. Fumagalli A, Oost KC, Kester L, Morgner J, Bornes L, Bruens L, et al. Plasticity of Lgr5-Negative Cancer Cells Drives Metastasis in Colorectal Cancer. *Cell Stem Cell* [Internet]. Elsevier Inc.; 2020;26:569-578.e7. Available from: <https://doi.org/10.1016/j.stem.2020.02.008>
7. Kim D, Langmead B, Salzberg SL. HISAT: A fast spliced aligner with low memory requirements. *Nat Methods*. 2015;12:357–60.
8. Gu Z, Eils R, Schlesner M. Complex heatmaps reveal patterns and correlations in multidimensional genomic data. *Bioinformatics*. 2016;32:2847–9.



CHAPTER

4

Transcriptome and Chromatin Changes Orchestrating Cellular States during Colorectal Cancer Organoid and Liver Metastasis Outgrowth

Maria C. Heinz^{1,2}, Rik G. H. Lindeboom^{2,3}, Koen C.
Oost^{1,2}, Lisa van Voorthuijsen^{2,3}, Michiel Vermeulen^{2,3},
Hugo J. G. Snippert^{1,2,#}

¹ Center for Molecular Medicine, University Medical
Center Utrecht, Utrecht, the Netherlands.

² Oncode Institute, the Netherlands.

³ Department of Molecular Biology, Faculty of Science,
Radboud Institute for Molecular Life Sciences, Radboud
University Nijmegen, Nijmegen, the Netherlands.

#: Lead Contact.

In preparation.

SUMMARY

Lgr5⁺ cancer stem cells (CSCs) are vital for metastatic growth in colorectal cancer (CRC), yet metastasis-initiating cells are devoid of Lgr5 expression. Thus, during metastatic colonisation, de novo Lgr5⁺ CSCs have to emerge by means of dedifferentiation. We have previously demonstrated that this occurs at the micrometastatic stage and embodies a critical transition step in the metastatic cascade towards overt metastasis and liver colonisation. However, the transcriptional changes associated with dedifferentiation and the transition to a heterogeneous cell population are poorly understood.

Here we exploit clonal outgrowth of CRC organoids whose transcriptome and phenotypic changes reflect the elusive early stages of liver metastasis formation, to profile transcriptome and chromatin changes at the time of cell fate conversions. We found that late-stage organoids show enhanced cell type diversity and upregulation of YAP targets with open chromatin sites containing AP-1 motifs. As this cellular state is distinct from YAP/TEAD-driven regenerative (developmental) programs, YAP likely serves as co-activator to the AP-1 transcriptional complex. We reveal that AP-1, and members of the HNF4 and PPAR subfamilies are of particular importance in cells without stem cell activity. At the time of dedifferentiation, the cells are highly proliferative, as indicated by the activity of the E2F family of transcription factors. Moreover, dedifferentiation events are coupled to upregulation of developmental-related EGF-like ligands *AREG* and *EREG*, suggesting that upregulation of MAPK signalling supports dedifferentiation.

INTRODUCTION

The severity of colorectal cancer (CRC) lies in metastasis that primarily form in the liver or the lungs. In analogy to multipotent Lgr5⁺ adult stem cells in the intestine which constantly renew all cell types of the epithelial lining through proliferation and differentiation, it is a population of Lgr5⁺ cancer stem cells (CSCs) that is essential for metastatic maintenance and growth (1). Yet, this does not imply that Lgr5⁺ CSCs originating from the primary tumour also acts as cell-of-origin for metastases. On the contrary, it has recently been shown that the vast majority of circulating tumour cells are negative for Lgr5 (2), and that when injected into the blood stream of mice, Lgr5⁻ cells are capable of generating metastases comprised of a mixed population of cell types, including CSCs (1,2). It thus follows that at some point during metastasis formation, new Lgr5⁺ CSCs are generated, a process that is known as *dedifferentiation*.

The metastatic cascade, a framework comprising 7 key steps that cells have to complete in order to metastasize, has been studied on many levels (3). Yet, the last hurdle, that is the successful outgrowth of metastasized cells into an overt lesion, is not well understood (4). Underlying reasons for this are, among others, that metastatic events are rare, the lesions involved are of microscopic size, and the transition point at which micrometastases turn into over overt, growing lesions varies in time. Only in the last years, emerging technologies have allowed to study these elusive early stages from novel perspectives, for instance through transcriptional profiling using single-cell sequencing approaches or phenotypically through intravital time-lapse microscopy, in combination with novel mouse models that recapitulate the human disease. Using these methods, we have recently analysed growing metastases *in vivo* and derived that dedifferentiation into Lgr5⁺ CSCs only happens at the multicellular stage, and that failure to do so impedes metastatic growth (5).

Next to *in vivo* studies, the self-renewal and multipotency characteristics of adult stem cells (SCs) can be studied using organoid technology (6–9). When derived from diseased tissue, organoids thus provide an attractive model to study disease/tissue physiology *in vitro* at the level of (live-) cell biology, while key functional and phenotypic properties of the original tissue are being maintained (6). We have previously demonstrated that the organoid model system reflects the poorly understood events underlying the early stages of metastatic colonisation, with features such as cell type composition, dynamics of phenotypic states, and transcriptomic profiles over time being recapitulated by CRC organoid outgrowth (5). For instance, we detected pronounced but transient YAP activity

in the first 1-2 days of clonal CRC organoid outgrowth, that is furthermore required for survival of single CRC cells (5). Likewise, we could detect YAP activity in 1-day-old CRC metastases in murine livers (5). During the next few days, gradual decay of early YAP levels is a prerequisite for efficient organoid outgrowth (4), which is very much in line with recent publications using genetic mouse models, showing that overexpression of YAP in CRCs only leads to the formation of micrometastases (10).

Despite the clinical relevance of the transition point between micrometastasis formation and successful outgrowth into macrometastases, the transcriptomic changes that are happening in tumour cells right after YAP activity has declined, including changes leading to dedifferentiation towards CSCs, have not yet been resolved in detail. In particular, questions remain as to what transcriptional states cells experience once the loss of early YAP activity permits cells to change fate and mature (e.g. to turn into Lgr5⁺ CSC) and which are the transcription factors orchestrating the diverse phenotypic states.

Here, we exploited the organoid system to gain in-depth insights into tumour cells' transcriptome and the chromatin states (RNA-seq, and ATAC-seq, resp.) right at the moment of epithelial self-organisation, that is after YAP levels have declined and when diverse cell fates, including CSCs, start to appear.

RESULTS

The transcriptome of PDOs is fundamentally changing over time

As we have shown that metastasis formation is accurately reflected by the outgrowth of patient-derived CRC organoids (PDOs) (5), we utilized PDOs to study the transcriptional processes underlying epithelial self-organisation. More specifically, we have used a genetically engineered CRC model with metastatic potential, containing the sequentially introduced key driver mutations *APC*^{KO/KO}; *KRAS*^{G12D/-}; *TP53*^{KO/KO}; *SMAD4*^{KO/KO} (A/K/P/S) (11,12). We chose two time points to analyse clonal organoid outgrowth: Day 5 at which the majority of organoids is at the verge of developing cell type heterogeneity and Day 12 which represents a mature organoid culture (Fig 1A).

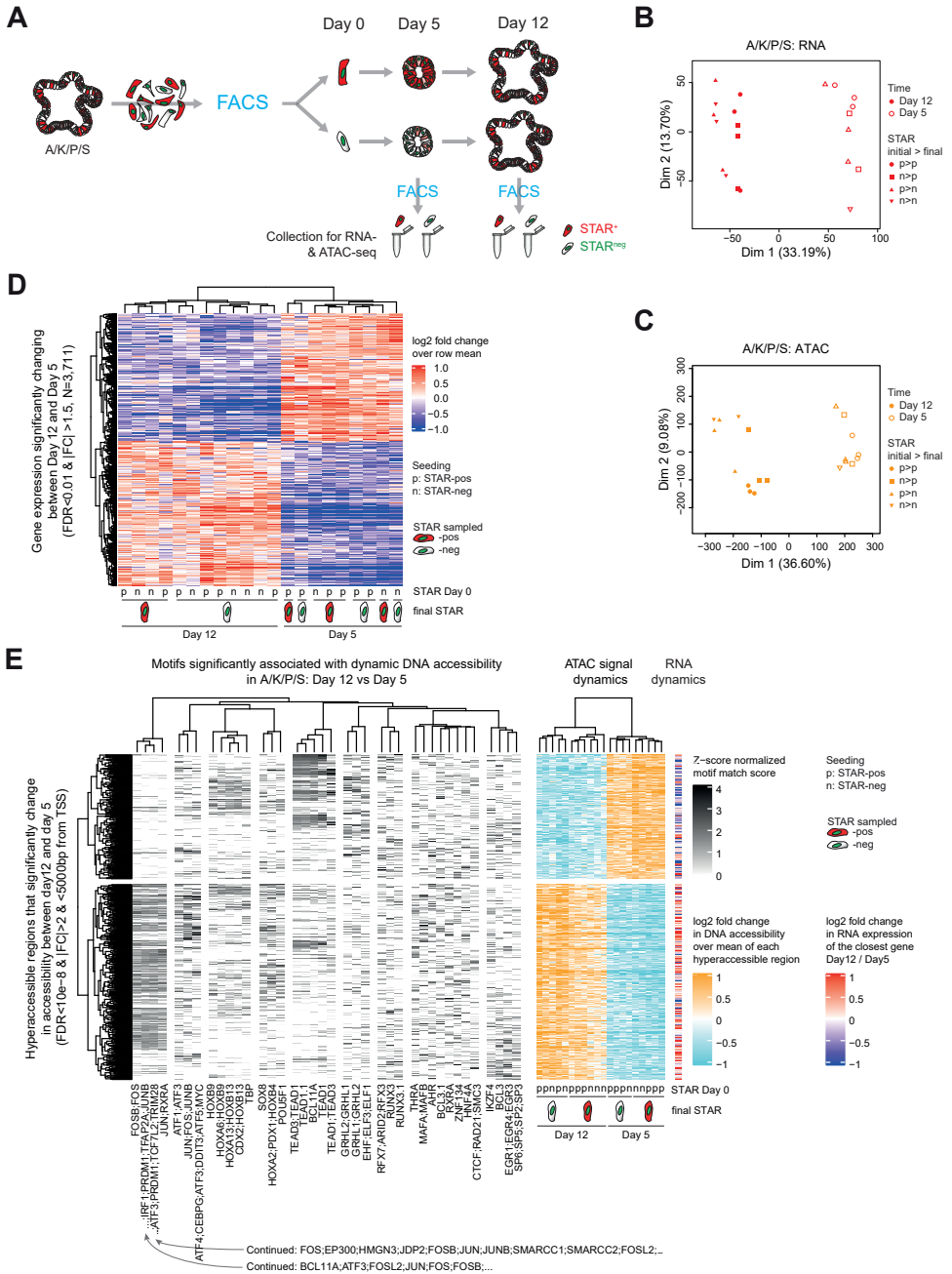
While the vast majority of circulating tumour cells has been described to be Lgr5⁺, Lgr5⁺ cells have a higher capacity to form metastases when compared side-by-side (2), raising the question if in practice metastasis-initiating cells always originate of the same population. We therefore decided to perform the outgrowth study starting with either cancer SCs or non-SCs. Of note, the phenotypic outgrowth trajectory of CSCs parallels those of cancer

non-SCs with *differentiation* being the process leading to cell type heterogeneity (5). To monitor live intestinal stemness, we have introduced the fluorescent stem cell ASCL2 reporter (STAR) into PDOs which faithfully reports transcriptional activity of ASCL2, the key transcription factor regulating intestinal stemness (5,13–15) (Fig 1A).

After validating robustness of the assay (similarity between replicates, Fig Times-S_A-B), we performed principal component analysis (PCA) which revealed organoid age as the strongest determinant of the dataset in both assays (Fig 1B-C). Accordingly, 32 % of the sequenced transcriptome was dynamically expressed between Day 5 and Day 12 (Fig 1D, $FDR < 0.01$, $|FC| > 1.5$) and 40 % of all chromatin sites significantly changed in accessibility between Day 5 and Day 12 ($FDR < 0.01$, $|FC| > 1.5$), indicating major changes in gene expression over time.

We next integrated the changes in chromatin accessibility and gene expression by taking the closest gene to each hyperaccessible region and computing the fold change in expression level, which revealed a strong correlation for each time point (Fig 1E). Computational prediction of transcription factor (TF) binding at the hyperaccessible sites was performed to gain further insight into the underlying biological processes (Fig 1E) and was used in the subsequent analyses.

To ensure that this is not a line-specific result, we repeated the experiment for the outgrowth of STAR⁺ cells of the related CRC organoid line A/K/P. Reassuring, we again found the transcriptome to be dynamically changing over time at high technical robustness (Fig S1C-E).



◀**Figure 1: The transcriptome of PDOs is fundamentally changing over time**

A. Schematic of experimental setup. Single STAR⁺ and STAR⁻ A/K/P/S cells were collected by FACS and cultured separately. After 5 and after 12 days, organoids were dissociated to single cells and STAR⁺ and STAR⁻ cells were collected in technical duplicates or triplicates of 10-20 k and 75-100 k cells for bulk RNA-seq and bulk ATAC-seq, respectively. **B-C.** Principal component analyses of A/K/P/S (B) RNA-seq and (C) ATAC-seq samples. STAR⁺ (p) and STAR⁻ (n) populations of Day 0 (initial) and of Day 5/12 (final) are depicted by different symbols. **D.** Heatmap of dynamically expressed genes between Day 12 and Day 5 in A/K/P/S organoid samples (FDR < 0.01, |FC| > 1.5). Data is represented as log₂ fold change over row mean. **E.** Representation of DNA hyperaccessibility with dynamically changing regions over time (FDR < 10e-8, |FC| > 2, and distance to transcriptional start site (TSS) < 5 kb). Left: Prediction of TF binding at hyperaccessible regions based on motif scores. Center: Fold change in DNA accessibility. Right: Heatmap of the expression of the closest gene depicted as log₂ fold change in expression levels on Day 12 / Day 5.

4

In a combined analysis with the A/K/P/S data, we found that organoid age is reflected by the first principal component (PC), despite the fact that the organoids were grown on different media (A/K/P organoids require supplementation of Noggin) (Fig S1F). Moreover, 50-71 % of dynamically expressed transcripts were shared between the two lines (Fig S1G), underlining the robustness of transcriptomic changes during organoid outgrowth.

Expression differences between STAR⁺ and STAR⁻ cells increase over time

Next, we focused on transcriptional and chromatin changes in STAR⁺ versus STAR⁻ cells as they also contribute to the variation described in the datasets (Fig S2A-C). Differential gene expression (DGE) analysis demonstrated that 618 genes vary in expression levels across all samples (FDR<0.01, Fig 2A). According to STAR reflecting stemness, gene set enrichment analysis (GSEA) revealed that public signatures of intestinal SCs correlate with STAR⁺ cells (Fig S2D-E), while an enterocyte signature is significantly enriched in STAR⁻ cells (Fig S2F). Next, we regressed out the difference over time to facilitate comparisons of gene expression within samples of the same time point and visualized the data side-by-side (Fig STAR-A). Genes with significant expression differences between SCs and non-SCs at both time points include for instance the SC markers *ASCL2*, *EPHB3*, *NOTCH1*, while many other Wnt/proliferation markers (e.g. *AXIN2*, *MKI67*, *CCNB1/2*, *POLQ*, *TOP2A*, *BUB1B*) or differentiation markers (e.g. *VILL*, *KRT19*, *TFF2*, *JAG1*) only show differential expression patterns at Day 12 (Fig 2A, STAR-S_G). This fits to the overall finding that the number of differentially expressed genes between STAR⁺ and STAR⁻ cells increases over time (Fig 2B). Additionally, cell type diversification during organoid outgrowth was confirmed through GSEA, as a signature for a cycling population of transit-amplifying (TA) cells strongly correlates with gene expression on Day 5 (Fig S2H), while markers for differentiation cell types such as enterocytes and Paneth cells are enriched on Day 12 (Fig S2I-J).

◀**Figure 2: Expression differences between STAR⁺ and STAR⁻ cells increase over time**

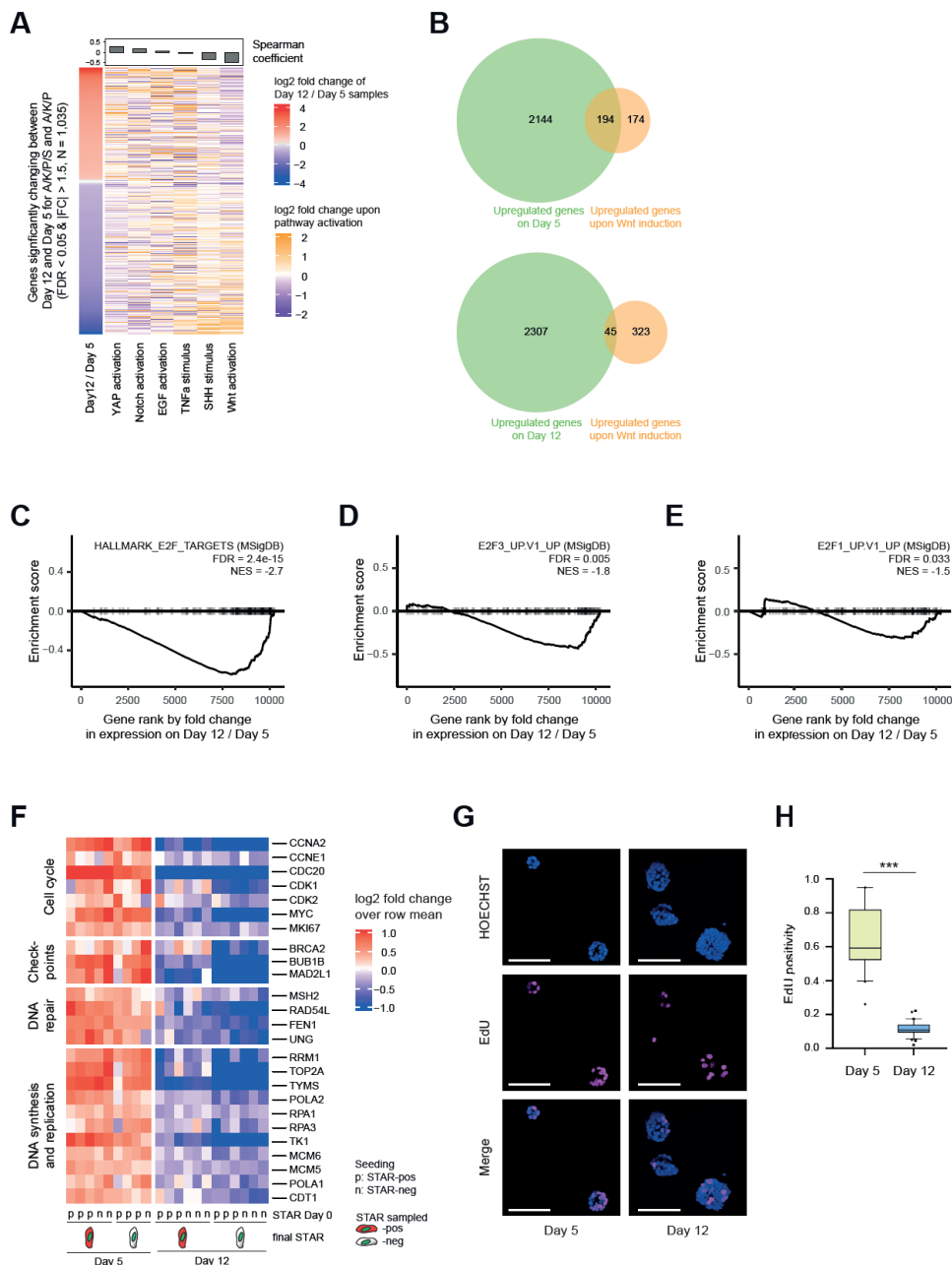
A. Heatmap of genes differentially expressed in A/K/P/S organoids across STAR significant at Day 5 (bottom), Day 12 (center), or both (top) (FDR < 0.01). Data is represented as log₂ fold change over row mean of all samples (left) or all samples of each time point (right). **B.** Venn diagram depicting the number of differentially expressed genes across STAR to be 1.33 fold higher on Day 12 (red) than on Day 5 (blue) organoids. For a fair comparison, equal numbers of samples per time point were used for each line (N = 10 each, FDR < 0.01). **C.** Representation of DNA hyperaccessibility with dynamically changing regions across STAR (FDR < 0.05, |FC| > 1.25, and distance to transcriptional start site (TSS) < 5 kb). Left: Prediction of TF binding at hyperaccessible regions based on motif scores. Center: Fold change in DNA accessibility. Right: Heatmap of the expression of the closest gene depicted as log₂ fold change in expression levels of STAR⁺ / STAR⁻.

Next, mapping open chromatin loci by ATAC-seq as a proxy for differential epigenetic states provided further support of cell type diversification during organoid outgrowth. After regressing out the differences in time, differences in chromatin states now clearly clustered by STAR fate and correlated with the expression patterns of the associated genes (Fig 2C). As expected, using TF binding prediction on open chromatin loci in STAR⁺ CSCs, we detected enhanced numbers of binding motifs for both *ASCL2* and its heterodimeric binding partner *TCF3* (14,16). Conversely, genes associated with STAR⁻ cells seem to be regulated by few classes of TFs, prominent among which was the HNF4 subfamily that has previously been implicated in enterocyte differentiation and brush border formation (8,17). Accordingly, both an enterocyte cell type signature and a brush border gene list demonstrate an enrichment in STAR⁻ cells, yet only in 12-day-old organoids (FDR < 0.05) (Fig S3A-B). Furthermore, the chromatin data suggested enhanced activity of *PPARA* and *PPARG* in STAR⁻ cells (Fig 2C), which together with *HNF4A* have been described as modulators of intestinal lipid metabolism (18–20). Accordingly, we find many genes related to fatty acid binding or brush borders upregulated in the STAR⁻ cells (Fig S3C), while GSEA of publically available signatures registered at Molecular Signature Database (MSigDB) also hints at many metabolic pathways enriched in this population (Fig S3D-E).

Thus, both on transcriptional and on chromatin level, our data reveals robust diversification of cell types during organoid outgrowth.

Day 5 is characterized by hyperproliferation and Wnt activity

To better understand the significance of the chromatin accessibility and gene expression changes during organoid outgrowth, we compared our gene expression states to target genes of specific signalling pathways. This revealed Wnt target genes to be most enriched during early outgrowth (Fig 3A).



◀**Figure 3: Day 5 is characterized by hyperproliferation and Wnt activity**

A. Correlation between gene expression and pathway signatures. Left: Dynamically expressed genes between Day 12 and Day 5 in A/K/P/S and A/K/P organoids are represented as log₂ fold change (FC) in expression (FDR < 0.05, |FC| > 1.5). Right: Log₂ FC in gene expression upon pathway perturbations. Top: Spearman coefficient ranging from -0.34 to 0.23 for YAP and Wnt signalling, respectively. **B.** Venn diagrams depicting the overlap between Wnt target genes of a public signature (FC > 1.5, derived from (52)) and differentially upregulated genes on Day 5 (top) or Day 12 (bottom) in A/K/P/S organoids (FDR < 0.01). **C-E.** GSEA of ranked gene expression on Day 12 versus Day 5 in A/K/P/S organoids with gene sets registered at MolSigDB. (C) Hallmark signature: *Hallmark_E2F_Targets*, (D) Oncogenic signature: *E2F3_UP.V1.UP*, and (E) Oncogenic signature: *E2F1_UP.V1.UP*. **F.** Heatmap of E2F family target genes and cell cycle-related genes grouped by function. Data is represented as log₂ fold change over row mean. **G.** Representative images of 5-day-old and 12-day-old A/K/P/S organoids with 500 nM EdU incorporation for the last 16 h. EdU (pink), Hoechst33342 (blue). Scale bars, 100 μm. **H.** Quantification of EdU incorporation on Day 5 and Day 12. EdU positivity was computed as ratio of EdU⁺ / H2B-mNeonGreen⁺ pixels.

When interrogating Wnt target genes in our dataset in closer detail (Fig S4A), we noted an enrichment of cell cycle-related genes. Notably, 52 % of all Wnt target genes are also upregulated on Day 5 (FDR < 0.01), while only 13 % of those are downregulated on Day 5 (Fig 3B). In line with this, GSEAs using MSigDB Hallmark signatures demonstrated that gene expression at Day 5 is characterized by proliferation-associated signatures (Fig S4B). Most strongly enriched are targets of the E2F family of transcription factors (Fig 3C) that are known to regulate the expression of cyclins, CDKs, checkpoint regulators, DNA repair proteins, and chromosomal replication proteins (21). In agreement with this, we found oncogenic signatures associated with E2F3 and E2F1 overexpression to be among the most significant gene sets (Fig 3D-E, Fig S4C) and many E2F family member binding sites being in promoter regions of genes significantly enriched on Day 5 (Fig S4D). Consequently, many well-known E2F target genes, that are involved in cell cycle regulation, checkpoints, DNA repair, synthesis, and replication among others (21), were enriched on Day 5 in our dataset (Fig 3F).

Furthermore, we functionally validated the leads towards enhanced proliferation at Day 5 using EdU incorporation. Microscopy analysis and quantification of EdU⁺ nuclei confirmed that the vast majority of cells in 5-day-old organoids are cycling, while the proliferative fraction in 12-day-old organoids is strongly reduced (Fig 3G-H).

Next, computation analysis of transcription factor motifs in hyperaccessible regions at Day 5 revealed in particular the families of HOX and TEAD TFs to be likely regulators of gene expression (Fig Time-E). In agreement with this finding, a HOXA9-based gene expression signature was the second most enriched oncogenic signature (MSigDB) for the gene expression on Day 5 (Fig S4C). Both family of transcription factors, HOX and TEAD, are well known for their pivotal roles in development (22,23). Moreover, transient YAP

transcriptional activity via TEAD is critical during the initial growth phase of mouse small intestinal and human CRC organoids (5,7). It is thus conceivable that some hyperaccessible regions in 5-day-old organoids are a remnant of the initial phase of organoid outgrowth.

Early dedifferentiation events display upregulation of EGF pathway activity

Our experimental set-up offers the opportunity to investigate the transcriptional underpinning of cell fate plasticity in organoids, comparing gene expression of dedifferentiated, newly emerged STAR⁺ CSCs on Day 5 (seeded as STAR⁻ cell) versus pre-existing STAR⁺ CSCs (seeded as STAR⁺ cell) (Fig 4A). While we found SC-associated genes to be enriched in the pre-existing STAR⁺ CSCs (*ASCL2*, *HES1*, *TCF7*), two ErbB family receptor ligands (*AREG*, *EREG*) are among the most strongly enriched genes in the newly emerged CSCs. Intrigued by this observation, we looked into general enrichment of MAPK targets in dedifferentiating cells using a public dataset that describes the response of genes to EGF stimulation. In line with the upregulation of *AREG* and *EREG*, Spearman correlation indicates enrichment of EGF signalling in the dedifferentiating cells (Fig 4B, correlation coefficient = -0.38). To rule out that the higher levels of EGF targets are a remnant from the dedifferentiating cells' previous states (STAR⁻ at Day 0), we tested for EGF target enrichment in STAR⁻ versus STAR⁺ cells at Day 5 and as expected found no correlation (Spearman coefficient -0.06, data not shown). Thus, it is suggestive that reactivation of MAPK signalling through the development-related ligands supports the transition to a more stem-like state.

We also noted that newly emerged CSCs depicted upregulation of several cell cycle-related genes such as *MKI67*, *CCNA2*, *POLQ*, and *TOP2A* (Fig 4A). As regenerative and developmental processes in the gut are also related to proliferation, we tested if they are linked to dedifferentiation using GSEA with public signatures (24) (Fig S5A-B). No correlation was found (FDR > 0.35), suggesting that regenerative / developmental responses are either only very transiently involved or that these processes are unrelated. On the other hand, it has been previously shown that lowering Wnt activity in intestinal SCs leads to the transition to TA cells including upregulation of MAPK signalling (25). We are therefore tempted to speculate that during dedifferentiation, cells go through a TA-like state at which most of them were captured during this experiment.

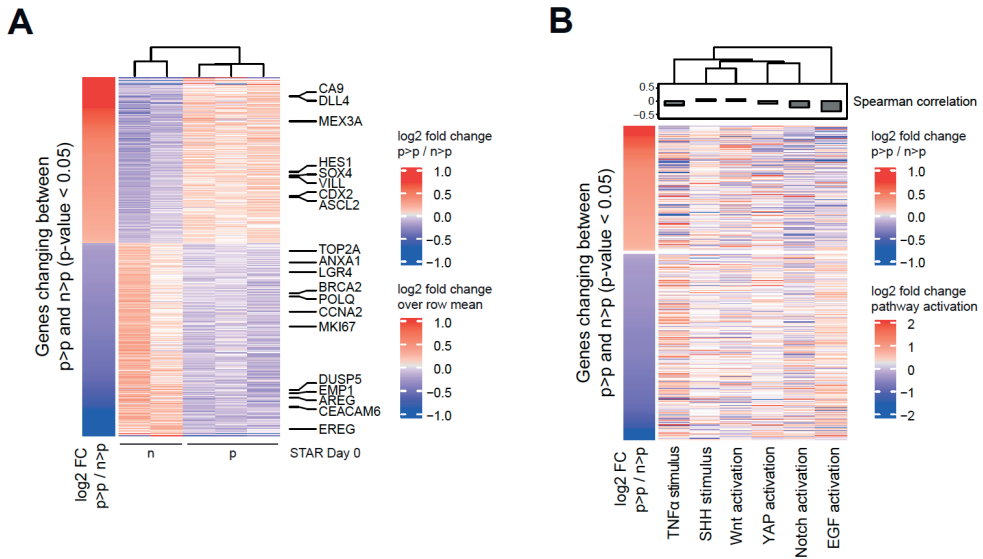


Figure 4: Early dedifferentiation events display upregulation of EGF pathway activity

A. Comparison of dedifferentiation genes across all A/K/P/S organoids samples at Day 5. Left: Log2 fold change of gene expression levels between the two conditions p>p / n>p with p and n denoting STAR⁺ and STAR⁻ fate at Day 0 > Day 5, respectively (p-value < 0.05). Right: Gene expression of genes as log2 fold change over row mean. **B.** Comparison of dedifferentiation genes across pathway signatures. Left: Log2 fold change of gene expression levels between the two conditions p>p / n>p with p and n denoting STAR⁺ and STAR⁻ fate at Day 0 > Day 5, respectively (p-value < 0.05). Right: Gene expression upon pathway perturbations of genes as log2 fold change over row mean. Top: For each pathway, Spearman correlation coefficients when compared to dedifferentiation signature (left).

Mature organoids display AP-1 transcriptional activity

We next turned to significant features at Day 12, the time point at which CRC organoids demonstrate most cell type diversity. In fact, pathway analysis suggested an upregulation of YAP-induced target genes on Day 12 (Fig 3A), which was a surprise considering the previously reported YAP activity during the first two days of PDO outgrowth (5). Nonetheless, YAP target genes were significantly enriched on Day 12 (Fig 5A) with 36 % of the predicted YAP target genes (FC in public signature > 1.5) upregulated on Day 12, compared to only 17 % on Day 5 (Fig 5B).

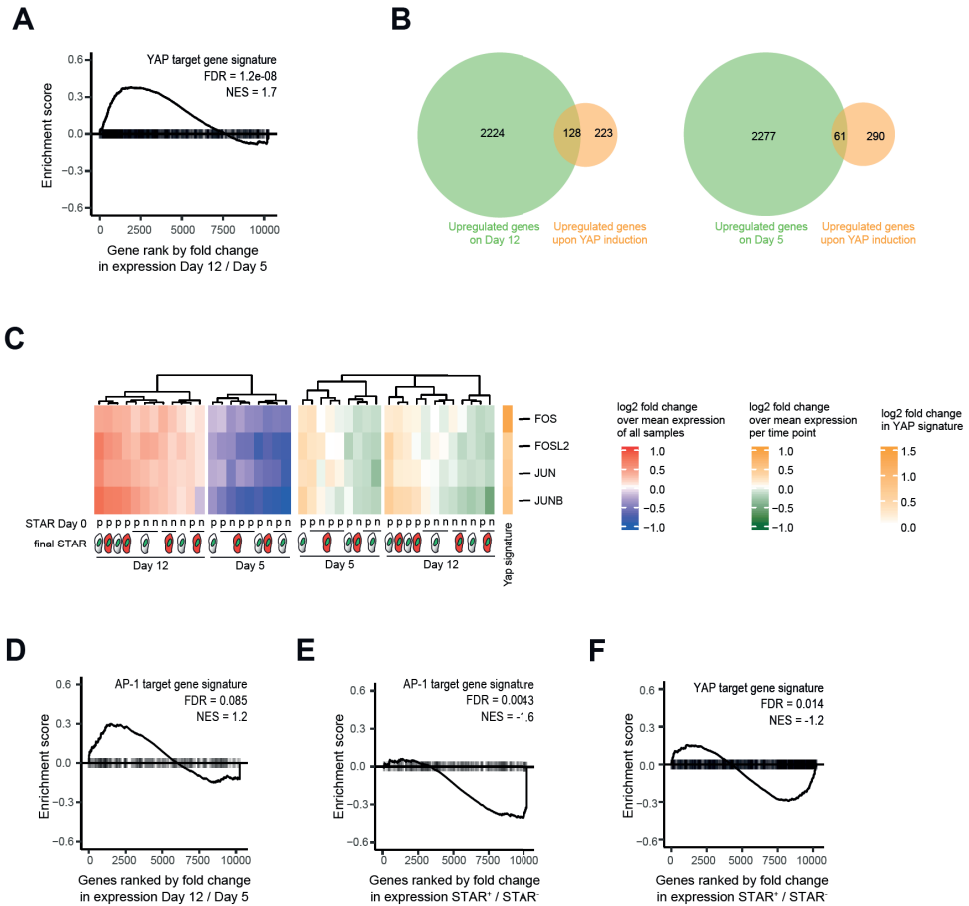


Figure 5: Mature organoids display AP-1 transcriptional activity

A. GSEA on ranked gene expression of Day 12 versus Day 5 with YAP target gene signature, derived from (32). **B.** Venn diagrams depicting the overlap between YAP-induced genes of a public signature (FC > 1.5, derived from (32)) and differentially upregulated genes on Day 5 (top) or Day 12 (bottom) in A/K/P/S organoids. **C.** Heatmap of selected genes upregulated YAP target genes in public signature (FC > 1.5, derived from (32)) and differential expression on Day 12 versus Day 5 in A/K/P/S organoids (FDR < 0.01). **D-E.** GSEA on ranked gene expression of (D) Day 12 versus Day 5 and (E) STAR⁺ versus STAR⁻ cells with expression signature of predicted AP-1 transcriptional targets, derived from (51). **F.** GSEA on ranked gene expression of STAR⁺ versus STAR⁻ cells with YAP target gene signature, derived from (32).

While the transcriptional activator YAP cannot bind DNA itself, it frequently binds the TFs TEAD1-4 to direct their activity. Yet, hyperaccessible chromatin sites with TEAD motifs were enriched at Day 5 (Fig 1E). Conversely, YAP can also serve as coactivator to the dimeric transcription complex AP-1 (26,27), whose subunits belong to the c-FOS, c-JUN, and ATF families (28). These binding sites, in contrast to those of the TEADs, were hyperaccessible

on Day 12 (Fig 1E), suggesting that YAP might be promoting a different transcriptional programme on Day 12 than during the earliest stages of organoid outgrowth.

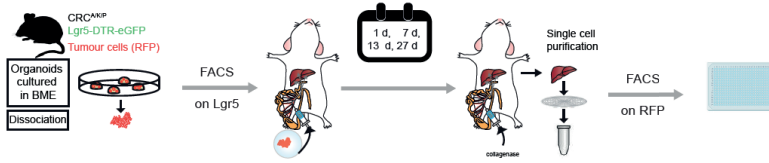
It has previously been described that YAP can induce expression of AP-1 subunits (29). Accordingly, we found AP-1 subunit expression to be enhanced on Day 12 (Fig 5C). AP-1 transcriptional targets are highly context dependent and can involve many cellular processes such as proliferation, survival, and differentiation depending on the composition of the hetero- or homodimer in the complex (28). Nonetheless, we found a set of AP-1 transcriptional targets to be enriched at Day 12 (yet not to statistical significance, p-value = 0.085) (Fig 5D). In particular, we found AP-1 binding sites to be more accessible in STAR⁺ cells (Fig 2C) and likewise target gene sets for both AP-1 and YAP were significantly enriched in STAR⁺ cells on RNA level (Fig 5E-F).

Thus, we propose that during organoid outgrowth the YAP transcriptional program changes from an initial regenerative / developmental-like program (on Days 1-2) towards a late-stage AP-1-mediated program, that is of particular importance in STAR⁺ cells in heterogeneous organoids.

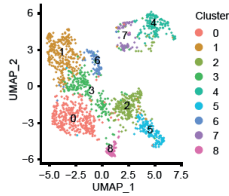
Confirmation of findings in CRC metastasis

So far, our analyses on the outgrowth of CRC organoids has demonstrated a dramatic change in gene expression over time with a pronounced proliferative phase in young organoids, upregulation of MAPK signalling in dedifferentiating cells, and a YAP/AP-1 target gene signature in mature organoids. Having previously reported on the similarity between organoid outgrowth and *in vivo* liver metastasis formation, we set out to validate whether the transcriptomic changes phenocopy the metastatic setting and could thus be used to infer more detailed aspects of epithelial self-organisation in metastasis.

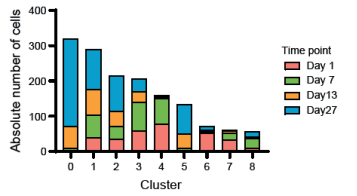
A



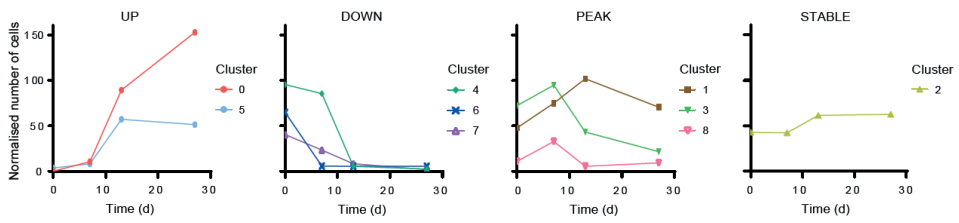
B



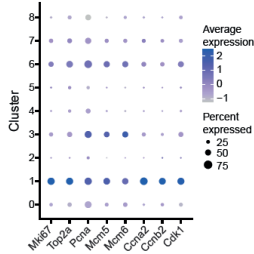
C



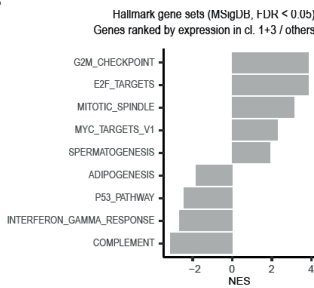
D



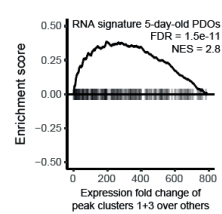
E



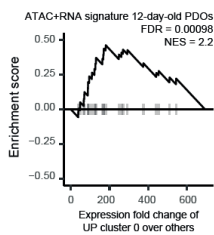
F



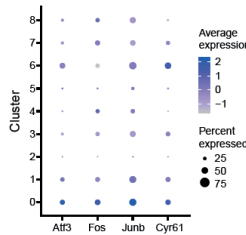
G



H



I



◀Figure 6: Confirmation of findings in CRC metastasis

A-C. Data information: These figure panels were previously published in (5) and were partially adapted.

A. Schematics of experimental set-up. Lgr5⁺ or Lgr5⁻ cells were isolated from the RFP⁺ mouse A/K/P CRC organoids by FACS and injected into the portal vein. After 1, 7, 13, and 27 days, metastatic cells were isolated from the livers and sorted by FACS and processed for scRNA-seq. **B.** UMAP representation of scRNA-seq data colour-coded by clusters resulting from unsupervised hierarchical clustering. **C.** Absolute number of analysed cells per cluster, colour-coded by the time of harvest. **D.** Scaled number of cells per cluster over time of scRNA-seq metastasis time-course dataset. Number of cells was scaled by total number of cells sequenced per time point / average number of cells sequenced per time point. Clusters were grouped based on temporal pattern demonstrating increase (UP), decrease (DOWN), peak pattern (PEAK) or no pattern (STABLE) over time. **E.** Normalized expression data of selected genes differentially expressed in clusters 1+3 over all non-peak clusters (FDR < 0.01, |FC| > 1.5). **F.** Normalised enrichment score of Hallmark gene sets registered at MolSigDB (FDR < 0.05) when analysing ranked gene expression of clusters 1+3 / non-peak clusters. **G.** GSEA of cluster 1+3 versus non-peak cluster genes with expression signature of 5-day-old A/K/P/S organoids (Signature: FDR < 0.01 and FC < 1.5 in Day 12 / Day 5 comparison; GSEA: FDR = 1.5e-11, NES = 2.8). **H.** GSEA of cluster 0 versus non-up cluster genes with ATAC+RNA expression signature of 12-day-old A/K/P/S organoids (GSEA: FDR = 9.8e-4, NES = 2.2). **I.** Normalized expression data of selected genes differentially expressed in cluster 0 over all non-up clusters (FDR < 0.01, |FC| > 1.5).

For this purpose, we re-analysed single cell RNA-seq (scRNA-seq) data from a CRC liver metastasis formation time-course experiment (5), in which metastases, originating from either Lgr5⁺ or Lgr5⁻ CRC cells of a murine *Apc*, *Kras*, *Tp53*-mutant cancer model (2), were analysed after 1, 7, 13, and 27 days (Fig 6A). Unsupervised hierarchical clustering had previously been performed and 9 distinct clusters were identified (5) (Fig 6B-C). While re-analysing the scRNA-seq dataset with respect to time, we noticed that all but one cluster are dominated by cells harvested on individual time points. For instance, clusters 4, 6, and 7 are dominated by cells from the first day, while clusters 0 and 5 are enriched for cells from the last day (Fig 6D). Conversely, clusters 1, 3, and 8 depict an expression pattern peaking at Days 7-13. In total, 86 % of all sequenced cells belong to these clusters, underlining the nature of a dynamically changing transcriptome during CRC metastasis outgrowth.

In this model of metastasis formation, we have previously demonstrated that the expression signatures of Lgr5⁺ and Lgr5⁻ cells become more pronounced and diverge from each other over the course of 4 weeks (5). Thus, while existent both *in vitro* during organoid and *in vivo* during metastasis outgrowth, this process is either slowed down or proceeds to more advanced levels in CRC metastases. In analogy to the pronounced proliferative phase of 5-day-old CRC organoids, we performed DGE analysis for clusters peaking in abundance after 7-13 days. 75 genes are significantly upregulated in clusters 1+3 (FDR < 0.01 and |FC| > 1.5) among which many cell cycle-related genes can be found (Fig 6E, Fig S6A). Accordingly, GSEA for Hallmark and Kegg signatures at MSigDB confirmed this observation (Fig 6F, Fig S6B). In addition, we derived a gene expression signature of the highly-proliferative 5-day-old organoids from our transcriptomic *in vitro* dataset. GSEA

showed that a strong enrichment of this signature in 7-13-day-old metastatic cells (Fig 6G, Fig S6C), highlighting the overlap of upregulated genes in organoids and in metastases.

Conversely, cluster 8, the last cluster with a peak pattern (enriched for 7-day-old cells), demonstrates upregulation of differentiation markers commonly associated with the secretory lineage (e.g. *Ang4*, *Tff3*, *Muc2*, *Mmp7*, *Agr2*, *Atoh1*) (Fig S6D). While this finding is very different to the findings in clusters 1+3, cluster 8 only comprises 3.7 % of all cells and thus this might well be a result of having injected secretory progenitor cells that were already committed to differentiating within this lineage. Taken together, the analysis of clusters with peak pattern reveals a strong proliferative behaviour of 7-13-day-old CRC metastases.

To confirm the upregulation of YAP/AP-1-mediated transcription, we performed DGE analysis on clusters most enriched for 27-day-old metastatic cells. Accordingly, we found a positive correlation between the gene expression profile of cluster 0 cells and both ATAC and ATAC+RNA signatures derived from Day 12 PDOs (Fig 6H, Fig S6E). Additionally on RNA level, we found significant upregulation of multiple AP-1 complex members (*Atf3*, *Fos*, *Junb*) as well as some YAP target genes (*Cyr61*) in cluster 0 (Fig 6I, Fig S6F), similar to the expression data in mature organoids. However, the most classical YAP targets are more strongly expressed by cells in cluster 6 (Fig S6G), which is almost exclusively comprised of 1-day-old metastatic cells which is furthermore in line with an early-stage YAP/TEAD program.

DISCUSSION

Transcriptomic profiling of the earliest stages of metastatic outgrowth is challenging due to limited material and, in case of spontaneous metastasis formation, due to asynchronous seeding. Thus, for actual mapping of gene expression patterns at this critical moment in time, models of metastasis formation are required that circumvent these problems. While scRNA-seq can be well exploited to work around limitations in material and to resolve heterogeneous responses in individual cells, sequencing depth is limited. We have therefore used CRC organoid outgrowth as a model for metastatic outgrowth to gain detailed insights into the earliest transcriptomic changes, and have subsequently confirmed our findings in scRNA-seq data of a metastasis time-course formation experiment.

Considering recent literature, we now propose the following cascade for metastatic liver colonisation: Disseminating tumour cells are vastly devoid of classical CSC markers (2), either because non-SCs are more motile or because YAP activity, which counteracts

intestinal stemness, enhances survival of individual CRC cells (5,10,24). Upon arrival in the liver, YAP activity is rapidly lost (5). Instead, a proliferative response is initiated in the vast majority of cells. Subsequently, dedifferentiation leads to the *de novo* appearance of CSCs in which MAPK target genes (including two developmental MAPK ligands) are upregulated. This event marks the transition into the main unrestricted growth phase into clinically detectable lesions, among others driven by the activity of Lgr5⁺ CSCs (1,2).

Analysis of 'open' chromatin in 5-day-old CRC organoids by means of ATAC-seq has revealed hyperaccessibility of sites containing binding motifs for TFs of the TEAD and HOX family. This finding could relate to the previously described YAP activity during the first 1-2 days of CRC organoid outgrowth, which is important for the survival of single CRC cells. Similarly, HOX and E2F activity have been described to suppress apoptosis in the model systems *C. elegans* (30). Nonetheless, translating this finding to human cancers has proven difficult, as HOX genes control multiple aspects of human tumour biology, including differentiation, invasion, and apoptosis (31). Furthermore, the outcome is highly context-dependent and might vary both with the individual HOX genes involved and the tissue in question. Thus, the hyperaccessibility of HOX binding sites at Day 5 of PDO outgrowth is difficult to interpret and warrants further investigation.

Alternatively, the accessibility of HOX and TEAD binding sites is a result of a regenerative / developmental response initiated in isolated intestinal cells (5,7). During regeneration, YAP activity only transiently suppresses Wnt activity, eventually resulting in the reappearance of intestinal SCs (32). Accordingly, we found Wnt activation to be enriched in 5-day-old PDOs. The fact that many of the Wnt-responsive genes include cell cycle regulators is in line with intestinal biology, as, for instance, physiological Wnt activity is required for the maintenance of the crypt compartment (33), while overactivation of the Wnt pathway results in hyperproliferation and adenoma formation (34–37). Along these lines, various cell cycle-associated genes and transcription factors were generally upregulated in 5-day-old PDOs and in 7-13-day-old metastasis. Among those, we found the family of E2F TFs whose expression and activity is incidentally controlled by the Wnt target gene *MYC* (38–40). As *MYC* was also upregulated in the PDOs, it is conceivable that the Wnt-driven upregulation of *MYC* results in the pronounced proliferative response observed at this time point. Evidence further adding to this idea are the fact that *E2F1* expression can be a potent inducer of proliferation, even working in quiescent cells (41).

Having reported on cell type maturation during metastasis formation before (5), we now show that cell type markers used to identify distinct cell populations were only

differentially expressed in PDOs at Day 12. This indicates that before cells mature reaching a state similar to a homeostatic setting, they transition from the early YAP^{high} state via an intermediate, proliferative, WNT^{high} setting. Maturation over time is further reflected in the hyperaccessibility of chromatin sites associated with HNF4 and the PPAR subfamilies in STAR⁺ cells (primarily at Day 12), both of which having been implicated in enterocyte differentiation (8,20).

Additionally, we noted hyperaccessible chromatin sites with AP-1 binding motifs in mature organoids (Day 12) and an enrichment for AP-1 subunits in 27-day-old metastases. For instance, JUN-associated AP-1 targets involve proliferation- and apoptosis-related genes (28). While AP-1 sites and target gene expression were generally more associated with STAR⁺ cells, the speculation of AP-1 targets involving pro-proliferative programs in cells with less active Wnt signalling than CSCs is tempting. Expression levels of JUN and FOS proteins are indirectly regulated through active p38/JNK and ERK kinases, respectively (28). As they are differentially upregulated in both 12-day-old PDOs and in 27-day-old metastases, the initiation of a late-stage AP-1 target gene program might involve multiple steps and stimuli controlled by MAPK, JUNK and possible more pathways working in concert at a certain point in time. We further propose that the resulting target gene program shares many traces with YAP activity, presumably as YAP can further amplify AP-1 transcriptional activity. Assuming that the result involves pro-proliferative effects, this could also explain why YAP/TAZ serve as a negative prognostic marker for CRC (42,43).

Lastly, our dataset enables the analysis of early fate changes during CRC PDO outgrowth. Our findings suggest that dedifferentiation involves a proliferative state that is different from a regenerative response. Instead, it is a TA-like state with active proliferation and upregulation of MAPK-related ligands. In analogy to the signalling gradients in intestinal crypts, this might constitute the final state before reaching the CSC state that is linked to even higher Wnt activity (25). While these changes are picked-up in our dataset, they are at the verge of statistical significance (p -value < 0.05, FDR < 0.5), which further justifies the use of (*in vitro*) model systems with higher sequencing depth to study such questions. Indeed, when attempting similar analyses on the scRNA-seq dataset, expression changes with FDR < 0.5 were basically non-existent (data not shown).

The upregulation of the ErbB family ligands *AREG* and *EREG* in dedifferentiated cells fits to the enhanced MAPK activity. In fact, these ligands are among a set of YAP/TAZ-regulated genes (32,44,45) and expression might thus be induced or enhanced downstream of

YAP activation in single cells. On top of this, both ligands have pro-proliferative effects that can also influence neighbouring cells, seeing that these ligands are secreted by the producing cells (32,44,45). The first dedifferentiating cells could therefore exert both cell-autonomous and non-cell autonomous effects, starting to repopulate the SC pool and sending pro-proliferative signals to surrounding cells to rapidly accumulate a critical cell mass before re-establishing a proliferation equilibrium.

ACKNOWLEDGEMENTS

We would like to thank the entire Snippert lab for continuous support and fruitful discussions. Financial support came from the Dutch Cancer Society (KWF fellowship, UU 2013–6070) and the ERC (ERC Starting Grant, IntratumoralNiche - 803608) with both grants being awarded to H.J.G. Snippert. This work is part of the Onco Institute (co-financed by the Dutch Cancer Society).

AUTHOR CONTRIBUTIONS

M.C.H and K.C.O have performed the sample collection for the RNA-ATAC sequencing experiment. M.C.H and L.v.V. have processed the samples. R.L. and M.C.H. have performed the analysis. M.C.H. has performed the remaining *in vitro* experiments and their analysis. M.C.H., M.V., and H.J.G.S have conceived the study and M.C.H. and H.J.G.S have written the manuscript.

DECLARATIONS OF INTEREST

The authors declare no potential conflict of interests.

MATERIAL AND METHODS

Organoid cultures

Cancer organoid lines were grown in Matrigel (Corning) and cultured in Advanced DMEM/F12 (Invitrogen), supplemented with 1% HEPES (Invitrogen), 1% GlutaMax (Invitrogen), 1% Penicillin-Streptomycin (Lonza), 1x B27 supplement (Invitrogen), 1.25 mM N-Acetyl-Cystein (Sigma-Aldrich), 10 mM Nicotinamide (Sigma-Aldrich), 500 nM A-83 (Tocris), and 10 μ M SB202190 (Gentaur). For SMAD4 WT lines, 10% Noggin CM was added as well. In general, PDOs were cultured with 10% Noggin CM, 10% R-Spondin-1 CM, and 50 ng/mL human EGF (PeproTech).

Organoid lines were passaged by trypsinisation to single cells using Trypsin/EDTA (Sigma-Aldrich), while trypsinisation was stopped using trypsin inhibitor (Sigma-Aldrich) at a 1:1 ratio. For experiments, cells were plated at a density of 500-1,000 cells / μ l Matrigel.

Organoids were equipped with the STAR reporter as previously described (14,15). A STAR design of 4 binding sites for *ASCL2* was used with downstream TagBFP2, IRES, and blasticidin selection cassette which is available (among others) on Addgene.

The identity of the lines and the absence of microplasm was repeatedly confirmed using targeted PCR and sequencing.

FACS of STAR lines

Prior to FACS, organoid lines were trypsinized to single cells and strained using a 40 μ m cell culture strainer (VWR). Cells were kept in culture media with 100 μ g/mL primocin (InvivoGen) and 1.5 μ M Draq7 (Cell Signaling Technology). Single, alive cells were isolated based on forward and side scattering properties and Draq7-negativity. STAR-negative gate was defined after running the corresponding parental line without STAR. Cells were collected in organoid media with 100 μ g/mL primocin and 2 % v/v Matrigel. Samples for sequencing were collected in technical duplicates or triplicates of 15-20 k cells each for bulk RNA-seq and 75-100 k cells for bulk ATAC-seq, then snap-frozen.

Fixation of organoids inside Matrigel

Organoids was washed with PBS for 5 min at RT. For fixation, PBS with 4% PFA (VWR) and 0.25 % glutaraldehyde (Sigma-Aldrich) was incubated for 15 min at RT. Quenching of background signal was performed by three washing steps with 1 % sodium borohydride (Sigma-Aldrich) for 10 min at RT each. Samples were kept in PBS at 4°C until use.

EdU incorporation assay

Organoids were treated with 500 nM EdU for 16 h overnight, then fixed in Matrigel. EdU incorporation was visualised according to the manufacturer's instructions using a 647 nm dye (Click-iT™ EdU Cell Proliferation Kit for Imaging, ThermoFisher).

EdU quantification

Organoids were scanned on a Leica SP8X confocal microscope using a 40X water objective (HC PL APO CS2; NA 1.1). Image processing was performed in Fiji (<https://imagej.nih.gov/ij/>). For each image, the sum of H2B and EdU signal intensities was calculated and the ratio of EdU over H2B signal was computed as measure of the fraction of EdU⁺ cells.

Bulk RNA-seq sample preparation

RNA was isolated using the Qiagen RNeasy kit. Sequencing libraries were prepared as previously described (5,8). In short, RNA sequencing libraries were generated using the KAPA RNA HyperPrep Kit with RiboErase (HMR, KAPA Biosystems) according to protocol. NextFlex DNA barcodes (Bioo Scientific) were used for adapter ligation. Library size and concentration was assessed using the High Sensitivity DNA bioanalyzer (Agilent Technologies) and the KAPA Library Quantification Kit (KAPA Biosystems), respectively. 50-bp paired-end reads were sequenced with an Illumina NextSeq 500.

Bulk ATAP-seq sample preparation

ATAC samples were processed as previously described (8). In short, cells were lysed and DNA was extracted after performing the transposition reaction with a Tn5 enzyme for 30 min at 37°C. Subsequently, the reaction was stopped through addition of 44 mM EDTA, 131 mM NaCl, 0.3 % SDS, and 600 µg/mL proteinase K. DNA was extracted using the Qiagen MinElute PCR Purification Kit.

Transposed DNA fragments were amplified using Custom Nextera PCR Primers 1 and 2 together with 10 µl DNA input. Subsequent clean-up was performed using reverse 0.65x SPRI beads (AMPure). An Illumina NextSeq 500 was used for sequencing of 50 bp paired-end reads.

Bulk RNA-seq analysis

Reads were mapped to the pre-indexed hg38 genome assembly. PCR duplicates were removed from analysis. The R package DESeq2 (46) was used for differential gene expression analysis (Wald test with Benjamini-Hochberg correction). Data was rlog transformed and normalized by row mean expression prior to generating heatmaps using the ComplexHeatmap package (47).

Gene set enrichment analyses were run using the fgsea package (48). Signatures derived from public data include: intestinal stem cells (49,50), TA cells (50), enterocytes (50), Paneth cells (50), intestinal regeneration (24), intestinal foetal cells (24), brush border genes (17), and predicted AP-1 targets (51). (The latter was accessed through the website https://maayanlab.cloud/Harmonizome/gene_set/AP-1/MotifMap+Predicted+Transcription+Factor+Targets, 15th June 2022). Pathway scores were derived from the following perturbation studies: YAP (32), Wnt (52), EGF (53), SHH (54), Notch (GSE111127), TNF α (GSM3112129). For a fair comparison between lines of genes dynamically expressed in time, equal number of samples were used per line and condition (N=10 / line).

Bulk ATAC-seq analysis

Sequencing reads were aligned to the human reference genome hg19 using BWA-MEM. PCR duplicates were removed from the analysis using picard (version 1.129). Reads were further filtered for a quality score of at least 1 and for not mapping to the mitochondrial chromosome. Accessible sites were identified in each sample with macs2 (FDR-adjusted p-value < 0.001). A union of all identified peaks was used for subsequent analyses.

Differential site accessibility was performed with DESeq2 package (46). Significantly accessible sites were called after Wald test followed by correction for multiple testing (Benjamini-Hochberg method). Data visualisation was performed upon normalisation, log₂ transformation, and noise-stabilisation using the rlogTransformation function of the DESeq2 package (46). Heatmaps were generated using the R package ComplexHeatmap (47).

Fluorescent image analysis

Fluorescent images were processed with Fiji (<https://imagej.nih.gov/ij/>), applying background subtraction, smoothing, cropping and rotating, and linear contrast adjustment, when necessary.

Quantification and statistical analysis

Non-sequencing-related statistics were performed using GraphPad Prism (software version 9). P-values < 0.05 were considered statistically significant. Significance levels of < 0.05, < 0.01, and < 0.001 were indicated by (*), (**), and (***), respectively.

Data and code availability

The bulk sequencing data is available on Gene Expression Omnibus under the accession number GSE207071 with the following subseries: GSE207068 for ATAC data of A/K/P/S as well as GSE207069 and GSE207070 for RNA data of A/K/P/S and A/K/P, respectively.

REFERENCES

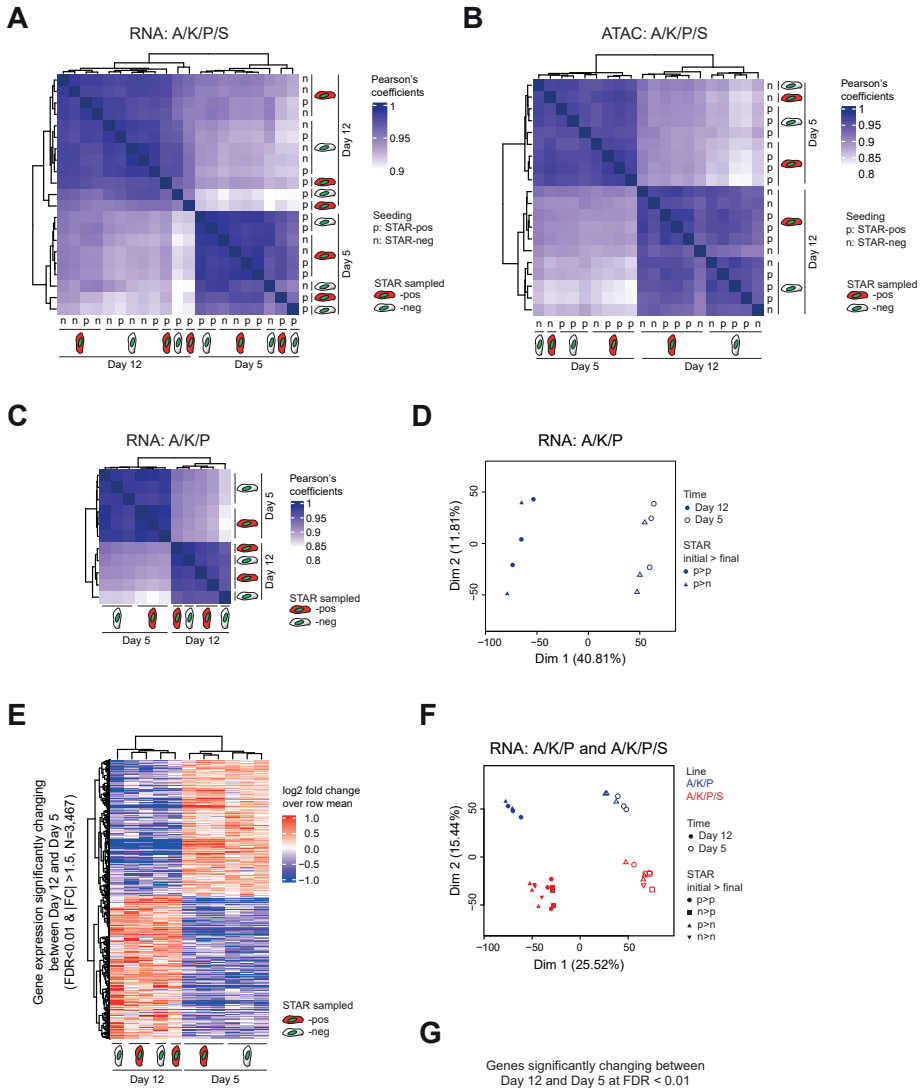
1. De Sousa E Melo F, Kurtova A V., Harnoss JM, Kljavin N, Hoeck JD, Hung J, et al. A distinct role for Lgr5 + stem cells in primary and metastatic colon cancer. *Nature* [Internet]. Nature Publishing Group; 2017;543:676–80. Available from: <http://www.nature.com/doi/10.1038/nature21713>
2. Fumagalli A, Oost KC, Kester L, Morgner J, Bornes L, Bruens L, et al. Plasticity of Lgr5-Negative Cancer Cells Drives Metastasis in Colorectal Cancer. *Cell Stem Cell* [Internet]. Elsevier Inc.; 2020;26:569-578.e7. Available from: <https://doi.org/10.1016/j.stem.2020.02.008>
3. Obenauf AC, Massagué J. Surviving at a Distance: Organ-Specific Metastasis. *Trends in Cancer* [Internet]. Elsevier Ltd; 2015;1:76–91. Available from: <http://dx.doi.org/10.1016/j.trecan.2015.07.009>
4. Massagué J, Obenauf AC. Metastatic colonization by circulating tumour cells. *Nature*. 2016. page 298–306.
5. Heinz MC, Peters NA, Oost KC, Lindeboom RGH, van Voorthuijsen L, Fumagalli A, et al. Liver Colonization by Colorectal Cancer Metastases Requires YAP-Controlled Plasticity at the Micrometastatic Stage. *Cancer Res* [Internet]. American Association for Cancer Research; 2022 [cited 2022 May 16];82:1953–68. Available from: <https://aacrjournals.org/cancerres/article/82/10/1953/696332/Liver-Colonization-by-Colorectal-Cancer-Metastases>
6. Clevers H. Modeling Development and Disease with Organoids. *Cell*. Cell Press; 2016;165:1586–97.
7. Serra D, Mayr U, Boni A, Lukonin I, Rempfler M, Challet Meylan L, et al. Self-organization and symmetry breaking in intestinal organoid development. *Nature* [Internet]. Springer US; 2019;569:66–72. Available from: <http://dx.doi.org/10.1038/s41586-019-1146-y>
8. Lindeboom RG, Voorthuijsen L van, Oost KC, Rodríguez-Colman MJ, Luna-Velez M V, Furlan C, et al. Integrative multi-omics analysis of intestinal organoid differentiation. *Mol Syst Biol* [Internet]. 2018;14:e8227. Available from: <http://msb.embopress.org/content/14/6/e8227>
9. Beumer J, Puschhof J, Bauzá-Martinez J, Martínez-Silgado A, Elmentaite R, James KR, et al. High-Resolution mRNA and Secretome Atlas of Human Enteroendocrine Cells. *Cell*. 2020;181:1291–306.
10. Cheung P, Xiol J, Dill MT, Yuan WC, Panero R, Roper J, et al. Regenerative Reprogramming of the Intestinal Stem Cell State via Hippo Signaling Suppresses Metastatic Colorectal Cancer. *Cell Stem Cell* [Internet]. 2020;27:590-604.e9. Available from: <http://www.ncbi.nlm.nih.gov/pubmed/32730753>
11. Drost J, van Jaarsveld RH, Ponsioen B, Zimmerlin C, van Boxtel R, Buijs A, et al. Sequential cancer mutations in cultured human intestinal stem cells. *Nature* [Internet]. 2015;521:43–7. Available from: <http://dx.doi.org/10.1038/nature14415>
12. Fumagalli A, Drost J, Suijkerbuijk SJE, Van Boxtel R, De Ligt J, Offerhaus GJ, et al. Genetic dissection of colorectal cancer progression by orthotopic transplantation of engineered cancer organoids. *Proc Natl Acad Sci U S A* [Internet]. 2017;114:E2357–64. Available from: <http://www.pnas.org/lookup/doi/10.1073/pnas.1701219114>
13. Schuijers J, Junker JP, Mokry M, Hatzis P, Koo BK, Sasselli V, et al. Ascl2 acts as an R-spondin/wnt-responsive switch to control stemness in intestinal crypts. *Cell Stem Cell* [Internet]. Elsevier Inc.; 2015;16:158–70. Available from: <http://dx.doi.org/10.1016/j.stem.2014.12.006>
14. Oost KC, van Voorthuijsen L, Fumagalli A, Lindeboom RGH, Sprangers J, Omerzu M, et al. Specific Labeling of Stem Cell Activity in Human Colorectal Organoids Using an ASCL2-Responsive Minigene. *Cell Rep* [Internet]. Elsevier Company.; 2018;22:1600–14. Available from: <https://doi.org/10.1016/j.celrep.2018.01.033>

15. Heinz MC, Oost KC, Snippert HJG. Introducing the Stem Cell ASCL2 Reporter STAR into Intestinal Organoids. STAR Protoc [Internet]. The Author(s); 2020;100126. Available from: <https://doi.org/10.1016/j.xpro.2020.100126>
16. Johnson JE, Birren SJ, Saito T, Anderson DJ. DNA binding and transcriptional regulatory activity of mammalian achaete-scute homologous (MASH) proteins revealed by interaction with a muscle-specific enhancer. Proc Natl Acad Sci USA [Internet]. 1992;89:3596–600. Available from: <http://www.pubmedcentral.nih.gov/articlerender.fcgi?artid=48915&tool=pmcentrez&rendertype=abstract>
17. Chen L, Luo S, Dupre A, Vasoya RP, Parthasarathy A, Aita R, et al. The nuclear receptor HNF4 drives a brush border gene program conserved across murine intestine, kidney, and embryonic yolk sac. Nat Commun [Internet]. Nature Publishing Group; 2021 [cited 2022 May 18];12:1–15. Available from: <https://doi.org/10.1038/s41467-021-22761-5>
18. Girard R, Tremblay S, Noll C, St-Jean S, Jones C, Gélinas Y, et al. The transcription factor hepatocyte nuclear factor 4A acts in the intestine to promote white adipose tissue energy storage. Nat Commun 2022 131 [Internet]. Nature Publishing Group; 2022 [cited 2022 Apr 27];13:1–14. Available from: <https://www-nature-com.proxy.library.uu.nl/articles/s41467-021-27934-w>
19. Colin S, Briand O, Touche V, Wouters K, Baron M, Pattou F, et al. Activation of intestinal peroxisome proliferator-activated receptor- α increases high-density lipoprotein production. Eur Heart J [Internet]. Inserm; 2013 [cited 2022 May 17];34:2566. Available from: </pmc/articles/PMC3984589/>
20. Necela BM, Thompson EA. Pathophysiological roles of PPAR γ in gastrointestinal epithelial cells. PPAR Res. 2008;
21. Bracken AP, Ciro M, Cocito A, Helin K. E2F target genes: Unraveling the biology. Trends Biochem Sci. 2004;29:409–17.
22. Beck F. Homeobox genes in gut development. Gut [Internet]. BMJ Publishing Group; 2002 [cited 2022 May 17];51:450. Available from: </pmc/articles/PMC1773336/>
23. Wu Z, Guan KL. Hippo Signaling in Embryogenesis and Development. Trends Biochem Sci. Elsevier Current Trends; 2021;46:51–63.
24. Yui S, Azzolin L, Maimets M, Pedersen MT, Fordham RP, Hansen SL, et al. YAP/TAZ-Dependent Reprogramming of Colonic Epithelium Links ECM Remodeling to Tissue Regeneration. Cell Stem Cell [Internet]. Elsevier Inc.; 2018;22:35-49.e7. Available from: <https://doi.org/10.1016/j.stem.2017.11.001>
25. Kabiri Z, Greicius G, Zaribafzadeh H, Hemmerich A, Counter CM, Virshup DM. Wnt signaling suppresses MAPK-driven proliferation of intestinal stem cells. J Clin Invest. American Society for Clinical Investigation; 2018;128:3806–12.
26. He L, Pratt H, Gao M, Wei F, Weng Z, Struhl K. Yap and taz are transcriptional co-activators of ap-1 proteins and stat3 during breast cellular transformation. Elife. eLife Sciences Publications Ltd; 2021;10.
27. Zanconato F, Forcato M, Battilana G, Azzolin L, Quaranta E, Bodega B, et al. Genome-wide association between YAP/TAZ/TEAD and AP-1 at enhancers drives oncogenic growth. Nat Cell Biol. 2015;17:1218–27.
28. Eferl R, Wagner EF. AP-1: A double-edged sword in tumorigenesis. Nat Rev Cancer. European Association for Cardio-Thoracic Surgery; 2003;3:859–68.
29. Koo JH, Plouffe SW, Meng Z, Lee D-H, Yang D, Lim D-S, et al. Induction of AP-1 by YAP/TAZ contributes to cell proliferation and organ growth. 2020; Available from: <http://www.genesdev.org/cgi/doi/10.1101/gad.331546.119>.

30. Winn J, Carter M, Avery L, Cameron S. Hox and a Newly Identified E2F Co-repress Cell Death in *Caenorhabditis elegans*. *Genetics* [Internet]. Oxford University Press; 2011 [cited 2022 May 16];188:897. Available from: [/pmc/articles/PMC3176086/](https://pubmed.ncbi.nlm.nih.gov/26503053/)
31. Shah N, Sukumar S. The Hox genes and their roles in oncogenesis. *Nat Rev Cancer* 2010 105 [Internet]. Nature Publishing Group; 2010 [cited 2022 May 17];10:361–71. Available from: <https://www-nature-com.proxy.library.uu.nl/articles/nrc2826>
32. Gregorieff A, Liu Y, Inanlou MR, Khomchuk Y, Wrana JL. Yap-dependent reprogramming of Lgr5+ stem cells drives intestinal regeneration and cancer. *Nature* [Internet]. 2015;526:715–8. Available from: <http://www.ncbi.nlm.nih.gov/pubmed/26503053>
33. Korinek V, Barker N, Moerer P, Van Donselaar E, Huls G, Peters PJ, et al. Depletion of epithelial stem-cell compartments in the small intestine of mice lacking Tcf-4. *Nat Genet* [Internet]. Nature Publishing Group; 1998 [cited 2022 Apr 28];19:379–83. Available from: https://www-nature-com.proxy.library.uu.nl/articles/ng0898_379
34. Kim KA, Kakitani M, Zhao J, Oshima T, Tang T, Binnerts M, et al. Mitogenic Influence of Human R-Spondin1 on the Intestinal Epithelium. *Science*. 2005;309:1256–9.
35. van de Wetering M, Sancho E, Verweij C, de Lau W, Oving I, Hurlstone A, et al. The beta-catenin/TCF-4 complex imposes a crypt progenitor phenotype on colorectal cancer cells. *Cell*. United States; 2002;111:241–50.
36. Su LK, Kinzler KW, Vogelstein B, Preisinger AC, Moser AR, Luongo C, et al. Multiple Intestinal Neoplasia Caused by a Mutation in the Murine Homolog of the APC Gene. *Science* [Internet]. American Association for the Advancement of Science ; 1992 [cited 2022 Apr 28];256:668–70. Available from: <https://www.science.org/doi/abs/10.1126/science.1350108>
37. Sansom OJ, Reed KR, Hayes AJ, Ireland H, Brinkmann H, Newton IP, et al. Loss of Apc in vivo immediately perturbs Wnt signaling, differentiation, and migration. *Genes Dev*. 2004;18:1385–90.
38. Leung JY, Ehmann GL, Giangrande PH, Nevins JR. A role for Myc in facilitating transcription activation by E2F1. *Oncogene* 2008 2730 [Internet]. Nature Publishing Group; 2008 [cited 2022 May 17];27:4172–9. Available from: <https://www-nature-com.proxy.library.uu.nl/articles/onc200855>
39. Leone G, DeGregori J, Sears R, Jakoi L, Nevins JR. Myc and Ras collaborate in inducing accumulation of active cyclin E/Cdk2 and E2F. *Nature* [Internet]. Nature Publishing Group; 1997 [cited 2022 May 17];387:422–6. Available from: <https://www-nature-com.proxy.library.uu.nl/articles/387422a0>
40. Leone G, Sears R, Huang E, Rempel R, Nuckolls F, Park CH, et al. Myc requires distinct E2F activities to induce S phase and apoptosis. *Mol Cell*. Cell Press; 2001;8:105–13.
41. Johnson DG, Schwarz JK, Cress WD, Nevins JR. Expression of transcription factor E2F1 induces quiescent cells to enter S phase. *Nature*. 1993;365:349–52.
42. Yuen HF, McCrudden CM, Huang YH, Tham JM, Zhang X, Zeng Q, et al. TAZ Expression as a Prognostic Indicator in Colorectal Cancer. *PLoS One*. 2013;8.
43. Xu Z, Wang H, Gao L, Zhang H, Wang X. YAP levels combined with plasma CEA levels are prognostic biomarkers for early-clinical-stage patients of colorectal cancer. *Biomed Res Int*. 2019;2019.
44. Yang N, Morrison CD, Liu P, Miecznikowski J, Bshara W, Han S, et al. TAZ induces growth factor-independent proliferation through activation of EGFR ligand amphiregulin. *Cell Cycle* [Internet]. Taylor & Francis; 2012 [cited 2022 May 17];11:2922–30. Available from: [/pmc/articles/PMC3419062/](https://pubmed.ncbi.nlm.nih.gov/26503062/)

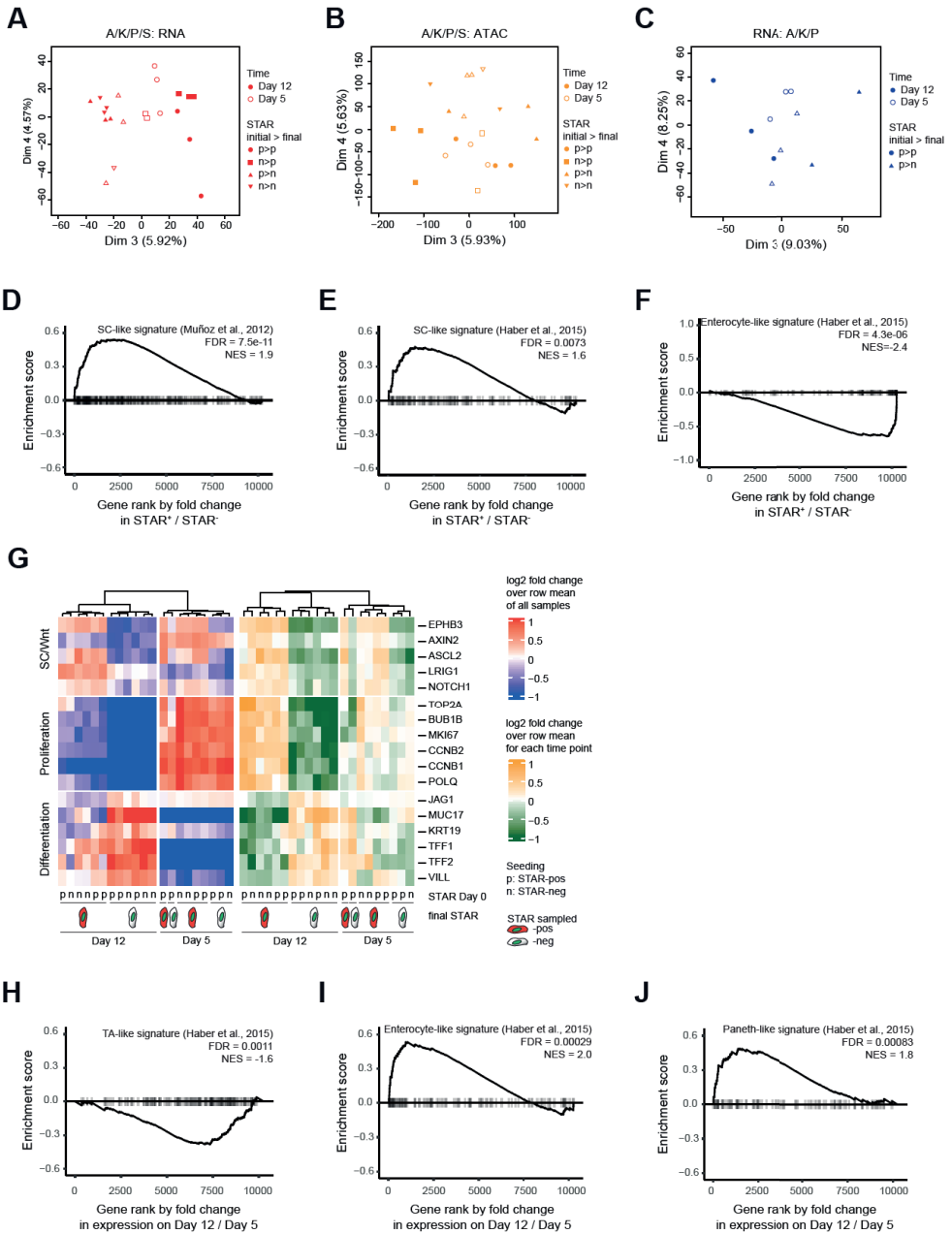
45. Zhang J, Ji JY, Yu M, Overholtzer M, Smolen GA, Wang R, et al. YAP-dependent induction of amphiregulin identifies a non-cell-autonomous component of the Hippo pathway. *Nat Cell Biol* [Internet]. Nature Publishing Group; 2009 [cited 2022 May 17];11:1444–50. Available from: <https://www-nature-com.proxy.library.uu.nl/articles/ncb1993>
46. Love MI, Huber W, Anders S. Moderated estimation of fold change and dispersion for RNA-seq data with DESeq2. *Genome Biol.* 2014;15:1–21.
47. Gu Z, Eils R, Schlesner M. Complex heatmaps reveal patterns and correlations in multidimensional genomic data. *Bioinformatics.* 2016;32:2847–9.
48. Korotkevich G, Sukhov V, Budin N, Shpak B, Artyomov MN, Sergushichev A. Fast gene set enrichment analysis. *bioRxiv* [Internet]. 2021;60012. Available from: <http://biorxiv.org/content/early/2021/02/01/060012.abstract>
49. Muñoz J, Stange DE, Schepers AG, Van De Wetering M, Koo BK, Itzkovitz S, et al. The Lgr5 intestinal stem cell signature: Robust expression of proposed quiescent ' +4' cell markers. *EMBO J.* 2012;31:3079–91.
50. Haber AL, Biton M, Rogel N, Herbst RH, Shekhar K, Smillie C, et al. A single-cell survey of the small intestinal epithelium. *Nature* [Internet]. Nature Publishing Group; 2017;551:333–9. Available from: <http://dx.doi.org/10.1038/nature24489>
51. Rouillard AD, Gundersen GW, Fernandez NF, Wang Z, Monteiro CD, McDermott MG, et al. The harmonizome: a collection of processed datasets gathered to serve and mine knowledge about genes and proteins. *Database* [Internet]. Oxford Academic; 2016 [cited 2022 Jul 15];2016. Available from: <https://academic.oup.com/database/article/doi/10.1093/database/baw100/2630482>
52. Michels BE, Mosa MH, Grebbin BM, Yepes D, Darvishi T, Hausmann J, et al. Human colon organoids reveal distinct physiologic and oncogenic Wnt responses. *J Exp Med.* 2019;216:704–20.
53. Malik A, Pal R, Gupta SK. EGF-mediated reduced miR-92a-1-5p controls HTR-8/SVneo cell invasion through activation of MAPK8 and FAS which in turn increase MMP-2/-9 expression. *Sci Rep* [Internet]. Nature Publishing Group UK; 2020;10:1–15. Available from: <https://doi.org/10.1038/s41598-020-68966-4>
54. Everson JL, Fink DM, Chung HM, Sun MR, Lipinski RJ. Identification of sonic hedgehog-regulated genes and biological processes in the cranial neural crest mesenchyme by comparative transcriptomics. *BMC Genomics.* BMC Genomics; 2018;19:1–11.

SUPPLEMENTARY MATERIAL



◀Figure S1: Related to Figure 1

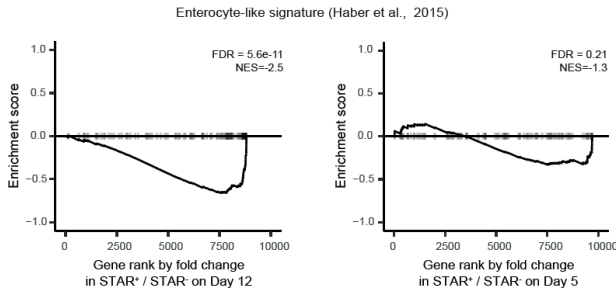
A-C. Sample similarities represented as Heatmap of Pearson's coefficients for (A) A/K/P/S RNA-seq, (B) A/K/P/S ATAC-seq, and (C) A/K/P RNA-seq samples. **D.** Principal component analysis of A/K/P RNA-seq samples. STAR⁺ (p) and STAR⁻ (n) populations of days 5 and 12 are depicted by different symbols. **E.** Heatmap of dynamically expressed genes between Day 12 and Day 5 in A/K/P organoid samples (FDR < 0.01, |FC| > 1.5). Data is represented as log₂ fold change over row mean. **F.** Principal component analysis of pooled A/K/P/S (red) and A/K/P (blue) RNA-seq samples. STAR⁺ (p) and STAR⁻ (n) populations of Day 0 (initial) and of Day 5/12 (final) are depicted by different symbols. **G.** Venn diagram representing the number of differentially expressed genes over time for A/K/P/S (red) and A/K/P (blue) organoids. For a fair comparison, equal numbers of samples per time point were used for each line (N = 10 each, FDR < 0.01).



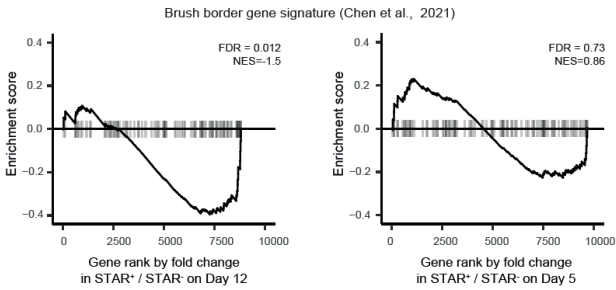
◀**Figure S2: Related to Figure 2**

A-C. PCA depicting dimensions 3 and 4 of (A) A/K/P/S RNA-seq, (B) A/K/P/S ATAC-seq, and (C) A/K/P RNA-seq samples. STAR⁺ (p) and STAR⁻ (n) populations of Day 0 (initial) and of Day 5/12 (final) are depicted by different symbols. **D-F.** GSEA of ranked gene expression in STAR⁺ / STAR⁻ samples with (D) SC-like signature extracted from (49), (E) SC-like signature extracted from (50), and (F) enterocyte-like signature extracted from (50). **G.** Heatmap of selected genes reflecting SC/Wnt-, proliferation-, and differentiation-related genes in A/K/P/S organoids. Stemness and proliferation markers are increased in STAR⁺ cells, while differentiation genes are upregulated in STAR⁻ cells (FDR < 0.01). Data is depicted as row mean over all samples (left) or over all samples of each time point (right). **H-J.** GSEA of ranked gene expression on Day 12 versus Day 5 with (H) TA-like, (I) enterocyte-like, and (J) Paneth-like signature, all extracted from (50).

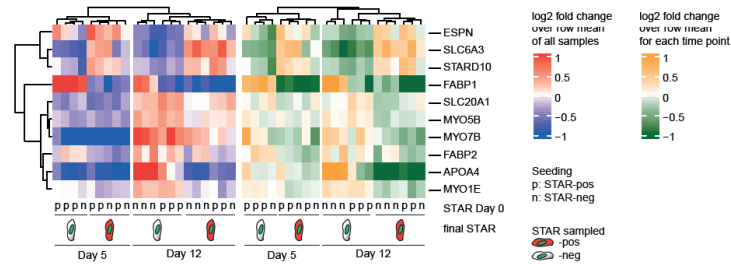
A



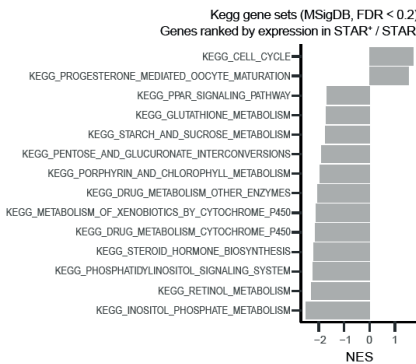
B



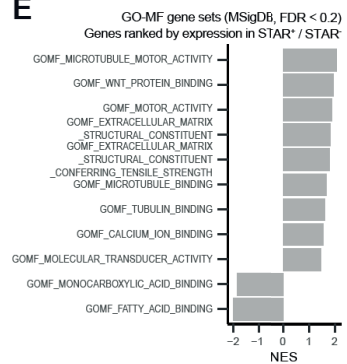
C



D



E



◀**Figure S3: Related to Figure 2**

A-B. GSEA of ranked gene expression in STAR⁺ / STAR⁻ samples of Day 12 (left) and Day 5 (right) with (A) enterocyte-like signature extracted from (50) and (B) brush border signature extracted from (17). **C.** Heatmap of enterocyte-related genes in A/K/P/S organoids that are differentially expressed between STAR⁺ and STAR⁻ cells on Day 12 (FDR < 0.05). Data is depicted as row mean over all samples (left) or over all samples of each time point (right). **D-E.** Normalised enrichment score (NES) of (D) Kegg and (E) gene ontology molecular function (GO-MF) gene sets registered at MolSigDB when analysing ranked gene expression in STAR⁺ versus STAR⁻ cells of A/K/P/S organoids (FDR < 0.2).

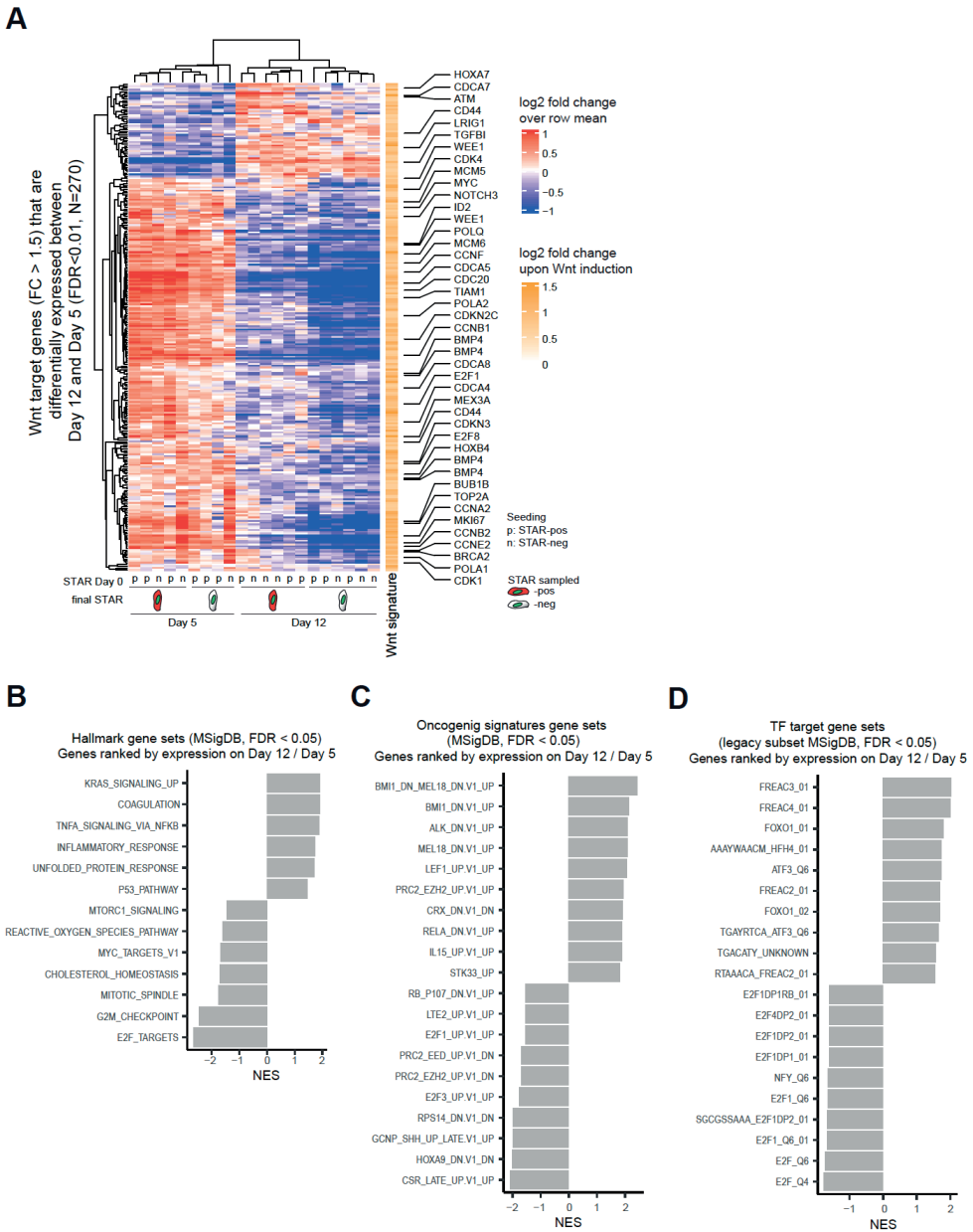


Figure S4: Related to Figure 3

A. Heatmap of Wnt target genes upregulated in public signature ($FC > 1.5$) filtered for differential expression on Day 12 versus Day 5 in A/K/P/S organoids (FDR < 0.01). **B-D.** Normalised enrichment score (NES) of top and bottom 5-10 gene sets of (B) Hallmark, (C) Oncogenic signatures, (D) Transcription factor target gene sets registered at MolSigDB when analysing ranked gene expression on Day 12 versus Day 5 in A/K/P/S organoids (FDR < 0.05).

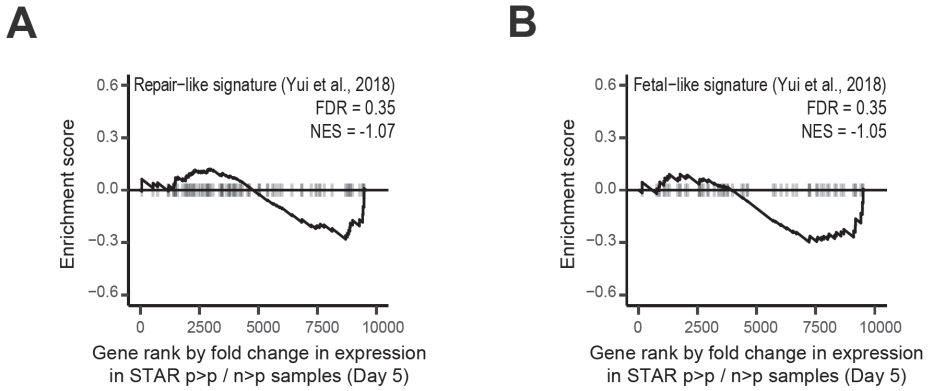
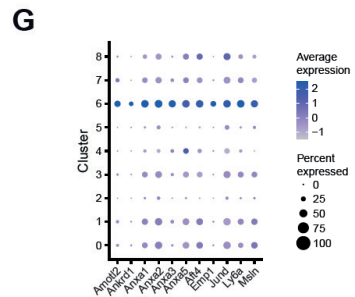
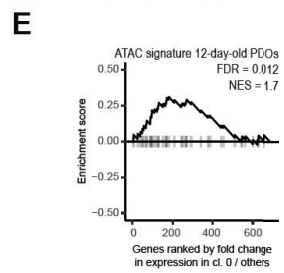
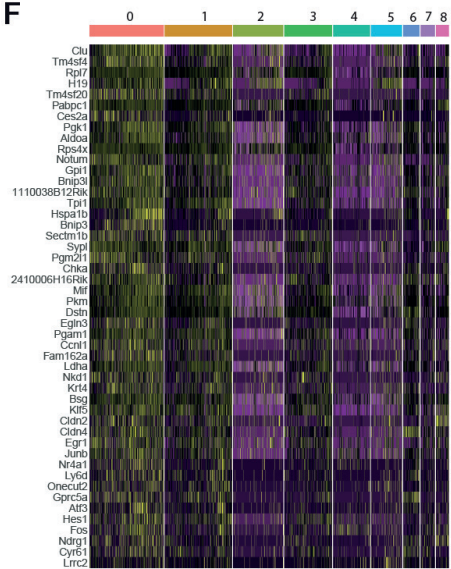
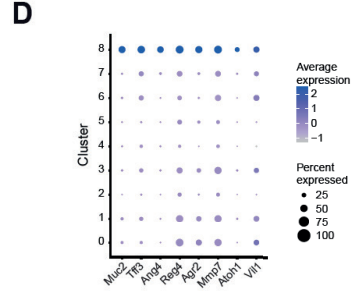
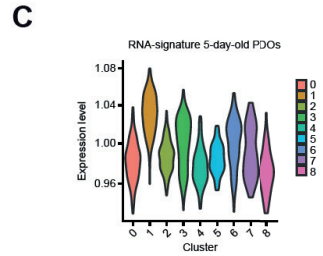
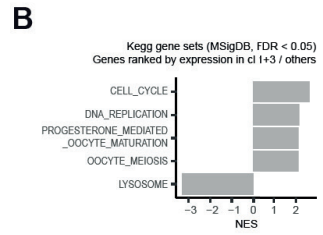
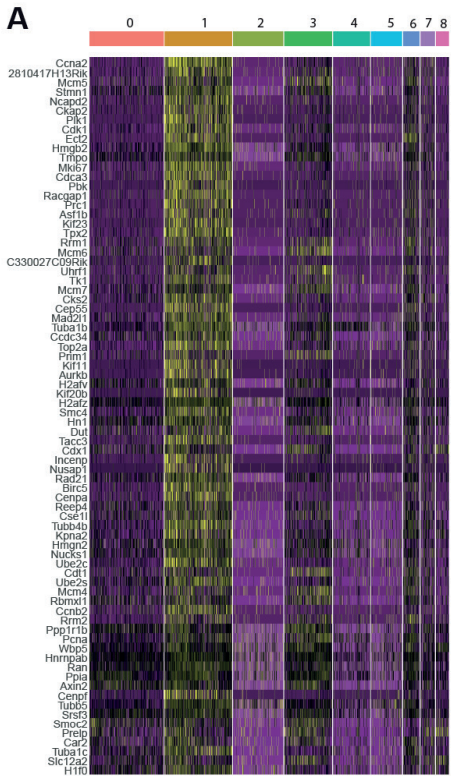


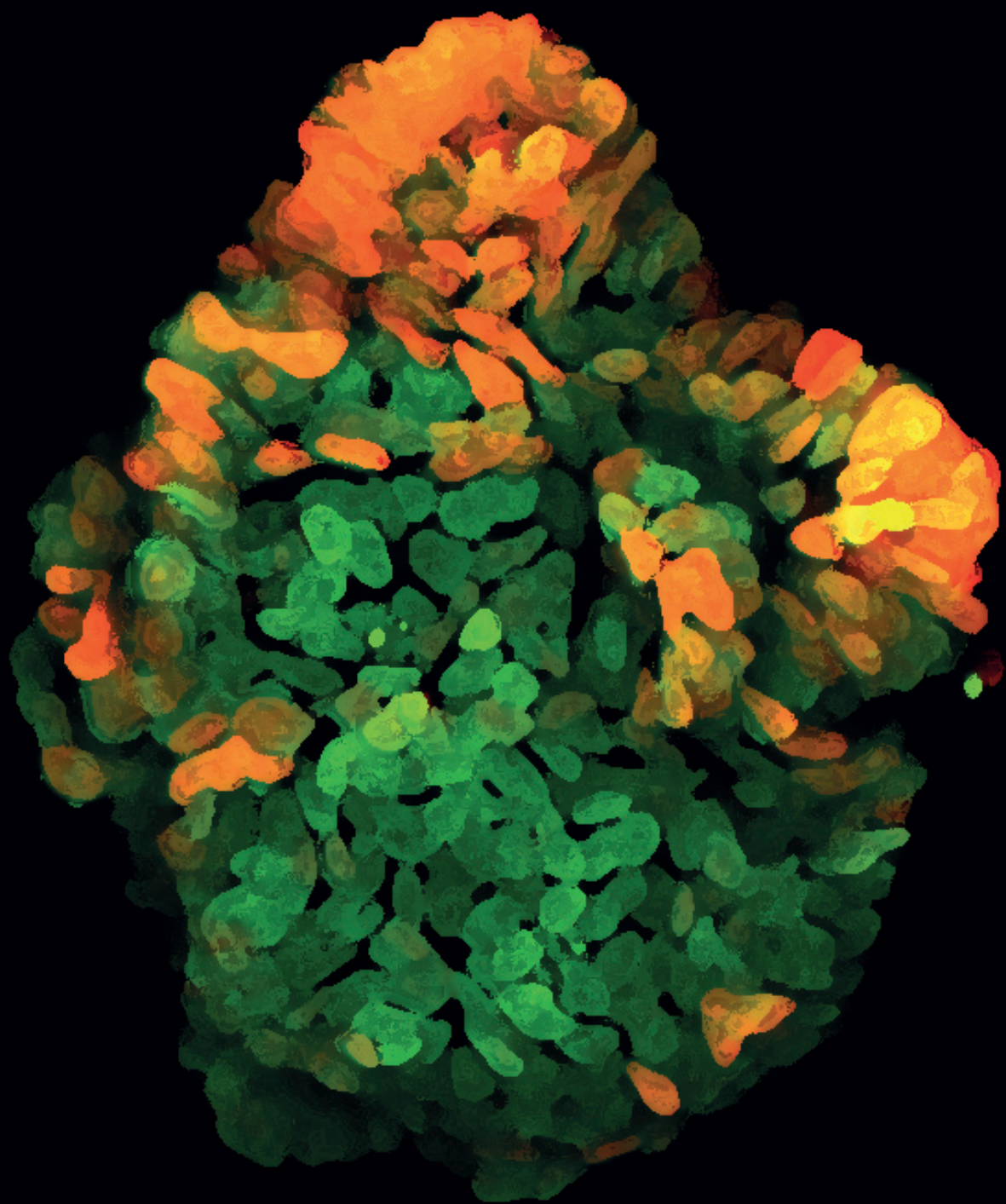
Figure S5: Related to Figure 4

A-B. GSEA on ranked gene expression of STAR samples p>p and n>p on Day 5 (p and n denoting STAR⁺ and STAR⁻ cells, respectively) with a gene set for (A) intestinal regeneration and (B) intestinal development, both derived from (24).



◀Figure S6: Related to Figure 6

A. Heatmap of differentially upregulated genes in cluster 1+3 over all *non-peak* clusters (FDR < 0.01, |FC| > 1.5). **B.** Normalised enrichment score of Kegg gene sets registered at MolSigDB (FDR < 0.05) when analysing ranked gene expression of clusters 1+3 / *non-peak* clusters. **C.** Expression level of 5-day-old A/K/P/S organoid signature over clusters. **D.** Normalized expression data of selected genes differentially expressed in cluster 8 over all *non-peak* clusters (FDR < 0.01, |FC| > 1.5). **E.** GSEA of cluster 0 versus *non-up* cluster genes with ATAC expression signature of 12-day-old A/K/P/S organoids (Signature: FDR < 10e-8, FC > 1.5, distance to TSS < 5 kb, in Day 12 / Day 5 comparison; GSEA: FDR = 0.012, NES = 1.7). **F.** Heatmap of differentially upregulated genes in cluster 0 over all *non-up* clusters (FDR < 0.01, |FC| > 1.5). **G.** Normalized expression data of selected genes differentially expressed in cluster 6 over all other clusters (FDR < 0.01, |FC| > 1.5).



CHAPTER

Quiescent Cells in Colorectal Cancer
Liver Micro- and Macrometastases
are Transcriptionally Distinct

Niek A. Peters^{1*}, Maria C. Heinz^{2,3*}, Emre Kucukkose¹, Bas
Viergever¹, Matthijs Baars², Andre Verheem¹, Yvonne
Vercoulen², Hugo Snippert^{2,3#}, Inne H.M. Borel Rinkes^{1#},
Onno Kranenburg^{1#}

1 Lab Translational Oncology, Division of Imaging and
Cancer, University Medical Center Utrecht, Utrecht
University, Utrecht, the Netherlands.

2 Center for Molecular Medicine, University Medical
Center Utrecht, Utrecht, the Netherlands.

3 Oncode Institute, the Netherlands.

*: Equal contribution.

#: Lead contact.

In preparation.

SUMMARY

Metastatic latency describes the phenomenon of cancer recurrence months or years after surgical removal of the primary tumor. Causal for this are micrometastases that had already formed in distant organs at the time of surgery, but stayed quiescent during this lag time. However, they constitute a major threat to the patient's health once they transition to efficient growth and start to colonize the organ. Although clinically relevant, micrometastases are difficult to detect due to their sporadic and dormant nature as well as their small size. Due to these reasons and the absence of accurate model systems, micrometastasis are poorly understood.

To better understand the difference between micro- and macrometastasis, we here present an isolation protocol of CRC liver metastases grown in mice that includes a separation based on size. Using xenotransplantation of patient-derived CRC organoids (PDOs), we find that liver macrometastases are characterized by TNF α signaling and epithelial-to-mesenchymal transition traits, while micrometastases are metabolically distinct.

To further address dormancy of micrometastases, we have adapted a P27-based reporter to mark quiescent cells in PDOs *in vitro* and *in vivo*. *In vivo* analyses revealed that micrometastases can be either cycling or quiescent, while macrometastases contain both populations of cells. In-depth analyses of quiescent cells obtained from either micro- or macrometastases revealed that the key transcriptional differences associated with differently sized metastases is also reflected by the quiescent subpopulations. This suggests that the epithelial traits connected to macrometastases are not limited to the proliferating subpopulation and it is thus conceivable that the microenvironment might be instructive in metastatic outgrowth and might change along the outgrowth trajectory.

INTRODUCTION

Colorectal cancer (CRC) is one of the most common malignancies (1) with about 25% of patients eventually suffering from metastatic disease (2). Metastases are seeded by circulating tumor cells (CTCs) that are lodged at a distant site in the body, extravasate out of the bloodstream and into the parenchyma and start to colonize the organ (3). This last step of the metastatic cascade, the step of *metastatic colonization*, is the rate-limiting step of the metastatic cascade and can take up to months or even years (3). This latency effect is the result of micrometastases that can remain dormant on a population level without any net gain in absolute cell number for long periods of time (4). Cellular quiescence, a non-proliferative state that retains the cell's ability to reenter the cell cycle upon certain stimuli (5), is one possible cause for growth stagnation in micrometastases (3). Alternatively, steady metastatic size can be achieved when the amount of proliferation is balanced equal cell loss, for instance due to immune-mediated eradication (3). While both cellular quiescence and active immune-surveillance are believed to contribute to metastatic latency (6,7), our basic understanding of micrometastasis remains limited due to their small size and sporadic nature as well as a lack of adequate model systems.

We have recently demonstrated that liver micrometastasis of CRC patients are devoid of intestinal stem cell markers (8) and that *de novo* emergence of Lgr5⁺ CSC marks the transition point towards overt outgrowth and organ colonization. Within these efficiently growing metastases, Lgr5⁺ cancer stem cells are at the apex of cellular hierarchy and are essential to maintain and fuel metastatic growth (9). However, it is less clear which factors contribute to and/or determine the duration of the latency period. While our previous work indicates that prolongation of the early transitory YAP activity can trigger growth stagnation *in vitro*, it is less clear which epithelial and microenvironmental factors enforce population dormancy over long periods of time.

Patient-derived cancer organoids have emerged as key tool to study inter- and intra-patient disease heterogeneity due to their accuracy in phenocopying tissue physiology, high efficiency to establish, and their suitability for functional studies and genetic engineering (10,11). Moreover, clonal outgrowth of patient tumor organoids phenocopy metastasis formation to close extent, including changes in phenotypic and transcriptional states with a close-up on epithelial biology (8). In addition, we have here utilized organoids in xenotransplantation studies metastasis formation in the context of the complex microenvironment.

To better understand the nature of population dormancy in micrometastases, we have adapted and exploited a reporter for cellular quiescence that is based on expression

levels of the CDK inhibitor p27 (12). By integrating the quiescence reporter in xenograft models of patient-derived CRC organoids, we could monitor and isolate these cells along the evolutionary trajectory of metastasis formation and growth. While quiescent cells are detected both in micro- and in macrometastases, the cells are transcriptionally distinct, suggesting that their transcriptional state is subject to epithelial and microenvironmental changes during the micro- to macrometastasis transition.

RESULTS

Liver micrometastases of human colorectal cancers are devoid of fibrotic components in the tumor microenvironment

Recent data suggests accumulation of α -smooth muscle actin-positive (α -SMA⁺) cells and collagen deposition in the formation of liver metastases (25). To study the tumor microenvironment (TME) of CRC micro- and macrometastases in our model system, we orthotopically transplanted PDOs in the cecum of NSG mice from where they spontaneously metastasize (**Figure 1a**). Using immunohistochemistry (IHC) against human CEA, we could accurately detect formed liver metastases of different sizes (N=35, with micrometastases being $< 1,000\mu\text{m}^2$). Subsequently, consecutive slides were used to assess their proliferative nature (Ki67), fibrotic components (α -SMA) and presence of collagen deposition (Sirius Red) (**Figure 1b**). In all micrometastases analyzed, we found neither signs of proliferation, α -SMA⁺ fibroblasts nor of collagen deposition which was in contrast to macrometastases (**Figure 1c**). To ensure that the lack of marker expression in micrometastases is not due to the fact that these tiny metastases were not present anymore on the consecutive slides, we set out to confirm these findings using Imaging Mass Cytometry™ (IMC) that enables high multiplex antibody staining on the same tissue sections (**Figure 1d**).

First, whole slide scanning was performed to detect immunofluorescence against CEA that identifies the locations of micro- and macro-metastases (N=28). Next, metastatic regions (CEA⁺) were analyzed for the presence of Histone 3, pan-Keratin, Ki67, α -SMA, and Collagen I. Thus, we could confirm that micrometastases were generally non-proliferative and lacked both α -SMA⁺ fibroblasts and deposition of collagen when compared to their macrometastatic counterparts (**Figure 1e**).

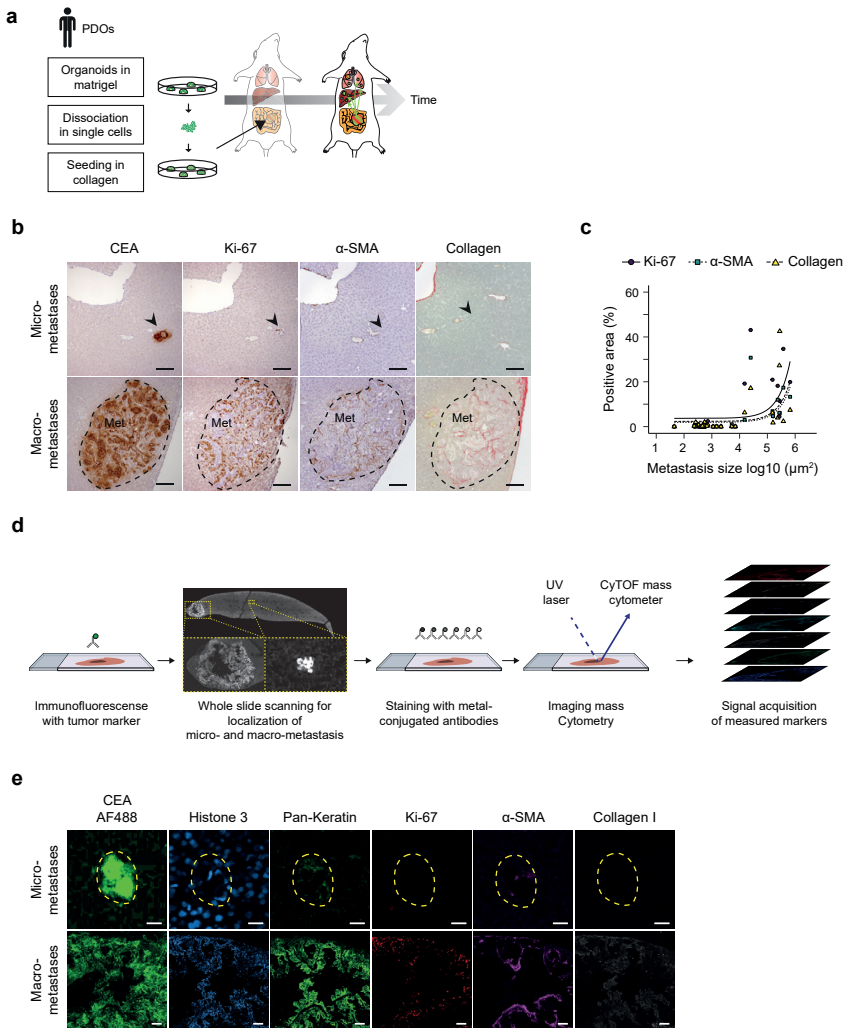


Figure 1. Liver micrometastases of human colorectal cancers are devoid of fibrotic components in the tumor microenvironment

a. Experimental setup: Patient-derived organoids (PDOs) are cultured in Matrigel. Organoids are harvested, dissociated into single cells and seeded in 8 μl collagen spheres. The collagen spheres are surgically transplanted under the serosa layer of the mouse cecum, where they grow into a primary tumor and from where they can over time metastasize to the liver, lungs, and peritoneum. **b.** Immunohistochemistry of micro- and macrometastases for CEA, Ki67, and α-SMA. Histological staining for collagen using Sirius Red. Arrow indicates location of micrometastasis. Scale bar, 100 μm. **c.** Scatterplot of the relationship between metastasis size (μm²) and relative area of metastases positive for Ki67, α-SMA, and collagen. **d.** Experimental setup for combining immunofluorescence and IMC for the multi-parameter analysis of micro- and macrometastases on the same tissue section. Immunofluorescence using antibodies against CEA is used identify the location of metastases. Sections are then stained with metal-conjugated antibodies and processed in the Hyperion IMC system. **e.** IMC result using metal-conjugated antibodies against Histone 3, pan-Keratin, Ki67, α-SMA, and Collagen I. Scale bar, 20 μm in micrometastasis and 100 μm in macrometastasis.

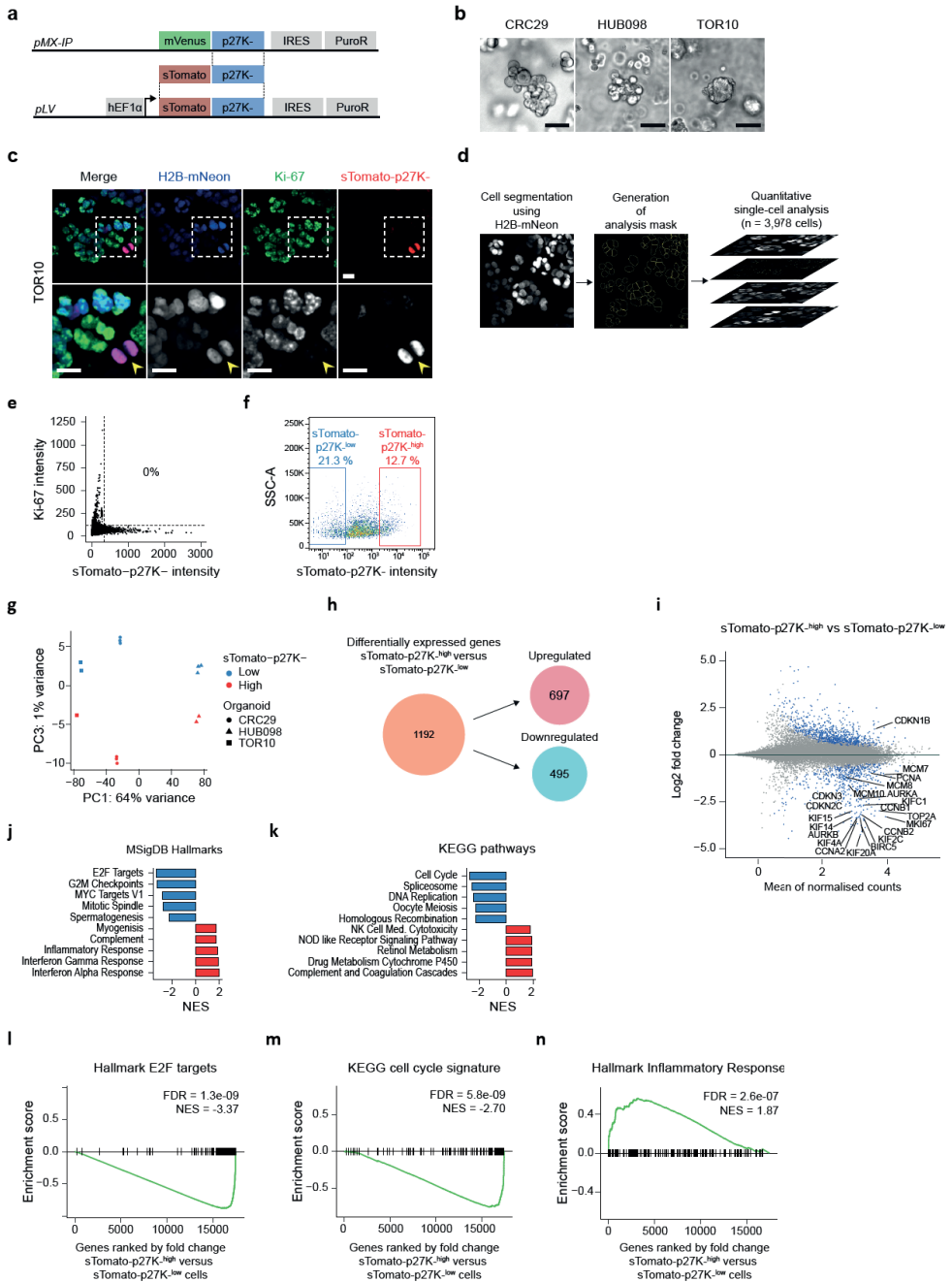
Quiescent cell cycle indicator sTomato-p27K- marks non-proliferative tumor cells *in vitro*

To study the non-proliferative dormancy phenotype of micrometastasis, we exploited a previously published reporter that labels quiescent (G0) cells (12). This reporter system is based on a fusion protein between a fluorescent protein and a mutant version of the CDK inhibitor p27 (p27K-), as p27 expression is higher in quiescent G0 cells than in cycling cells (12,26,27). The mutant p27K- is incapable of inhibiting CDKs and consequently does not influence the cell cycle. The quiescence reporter, adapted for our purposes and now combining sTomato with p27K- under the control of the ubiquitously active human promoter EF1a (**Figure 2a**), was stably integrated into the genome of three different CRC PDOs: CRC29, HUB098, and TOR10 (**Figure 2b**).

To test the functionality of the quiescence reporter in PDOs *in vitro*, we compared Ki67 and sTomato-p27K- levels in single cells through immunofluorescence. Using a custom-made Fiji macro, the analysis of 3,978 single cells of three PDO lines demonstrated that Ki67 positivity and sTomato-p27K^{high} expression were mutually exclusive features (**Figure 2c-e** and **Figure S1a-b**). While live cell imaging revealed that reporter activity can also be observed in mitotic cells, it was at reduced levels (sTomato-p27K^{low}), which is in line with the varying expression patterns of p27 during the cell cycle (12,26,27) (**Figure S2c** and **Movie 1**). Next, we isolated sTomato-p27K^{low} and sTomato-p27K^{high} subpopulations through fluorescent-activated cell sorting (FACS) and performed transcriptomic analysis through RNA-sequencing (RNA-seq) (**Figure 2f**). Principal component analysis (PCA) of all samples revealed that PDO identity is the most contributing factor to biological variance (**Figure S2a**), followed by reporter activity in the third principle component (**Figure 2g**).

Differential gene expression analysis between sTomato-p27K^{high} and sTomato-p27K^{low} cells resulted in 697 up- and 495 downregulated genes (1,192 genes, absolute fold change > 1.5, FDR < 0.01, **Figure 2h**, **Table S1**). In line with the principle of the quiescence reporter, the sTomato-p27K^{low} population was strongly enriched for cell cycle-related genes (such as *MKI67*, *PCNA*, *AURKA*, *AURKB*, *CCNA2*, *CCNB2*), while the sTomato-p27K^{high} population showed next to p27 itself (*CDKN1B*) increased expression of differentiation markers and inflammatory cytokines (such as *KRT19*, *KRT20*, *MUC2*, *IL6*, *IL32*, **Figure 2i**).

Unbiased analysis of the differentially expressed genes was performed using gene set enrichment analysis (GSEA) with gene sets registered at Molecular Signature Database (MSigDB). Both Hallmark and Kegg signature analysis confirmed that sTomato-p27K^{low} cells were highly enriched for cell cycle-related pathways (e.g. E2F Targets, G2M Checkpoints, MYC Targets V1), while sTomato-p27K^{high} cells were enriched for interferon pathway and inflammatory response (**Figure 2j-n** and **Figure S2b**). Taken together, this data demonstrates that the quiescence reporter is faithfully marking a population of non-proliferating, sTomato-p27K^{high} cells in CRC PDOs *in vitro*.



◀Figure 2. Quiescent cell cycle indicator sTomato-p27K- marks non-proliferative tumor cells *in vitro*

a. Schematic of the sTomato-p27K- lentiviral reporter. The sTomato-p27K- fusion protein is cloned into a lentiviral backbone in which the fusion protein is driven by a human EF1a promoter (hEF1a). Other elements: internal ribosome entry site (IRES), puromycin selection cassette (PuroR). **b.** Representative snapshots of PDOs (CRC29, HUB098, and TOR10) in culture. Scale bar, 50 μm . **c.** Immunofluorescence staining against Ki67 (green) and sTomato (red) in TOR10 organoids constitutively expressing the fusion protein H2B-mNeon (blue). Close-ups, white boxes. Yellow arrows, sTomato-p27K⁻ cells. Scale bar, 20 μm . **d.** Single cell quantification strategy of immunofluorescence (c) using cell segmentation based on H2B-mNeon expression. In total, 3,978 cells were analyzed. **e.** Scatterplot of 3,978 cells demonstrating sTomato-p27K- and Ki-67 expression levels as quantified in (d). **f.** FACS scatterplot sTomato-p27K- reporter levels with gating strategy for sTomato-p27K^{low} and sTomato-p27K^{high} subpopulations. **g.** Principal component analysis with PDO line identity indicated by symbols and sTomato-p27K- levels indicated by color. **h.** Venn diagram depicting differentially expressed genes across sTomato-p27K- populations (FDR < 0.01 and fold-change > 1.5). **i.** MA-plot of differentially expressed genes between sTomato-p27K^{high} and sTomato-p27K^{low} cells (FDR < 0.01). **j-k.** Bar graph showing the five most significantly enriched gene sets (j) of the MSigDB Hallmarks and (k) from the Kegg pathways database in sTomato-p27K^{low} and sTomato-p27K^{high} cells. **l-m.** GSEA demonstrating the similarity of sTomato-p27K^{low} cells with pathways resembling proliferation: (l) E2F targets and (m) KEGG cell cycle. **n.** GSEA demonstrating the similarity of sTomato-p27K^{high} cells with inflammatory response signature.

5

Micrometastasis contain either cycling or quiescent cells, while macrometastasis are heterogeneous

To assess the presence of quiescent cells during metastasis formation and growth, we orthotopically transplanted the three PDO quiescence reporter lines into mice (**Figure 3a**). All three PDOs spontaneously metastasized to the liver, yielding CRC liver metastases of different sizes (micro- and macrometastases, **Figure 3b**). Fluorescence multiplex IHC using antibodies against human Nucleoli (hNucleoli), sTomato (RFP), and Ki67 was performed to evaluate their proliferative / quiescent nature. A total of 13,148 hNucleoli⁺ metastatic cells could be identified for analysis (**Figure 3c**). Similar to our *in vitro* analysis, cells with simultaneous expression of both Ki67 and intermediate or high levels of sTomato-p27K- were extremely rare (0.05%, **Figure 3d**), demonstrating the suitability of the quiescence reporter for CRC metastasis studies.

Next, analysis of quiescent cells at different stages of metastatic outgrowth revealed three distinct phenotypes (**Figure 3e**). Micrometastases were either entirely quiescent (sTomato-p27K^{high} / Ki67^{low}) or entirely proliferative (sTomato-p27K^{low} / Ki67^{high}), while macrometastases generally comprised a mixed population of proliferating and quiescent cells. This finding indicates that there is heterogeneity in the cycling behavior across micro-metastases in our model systems.

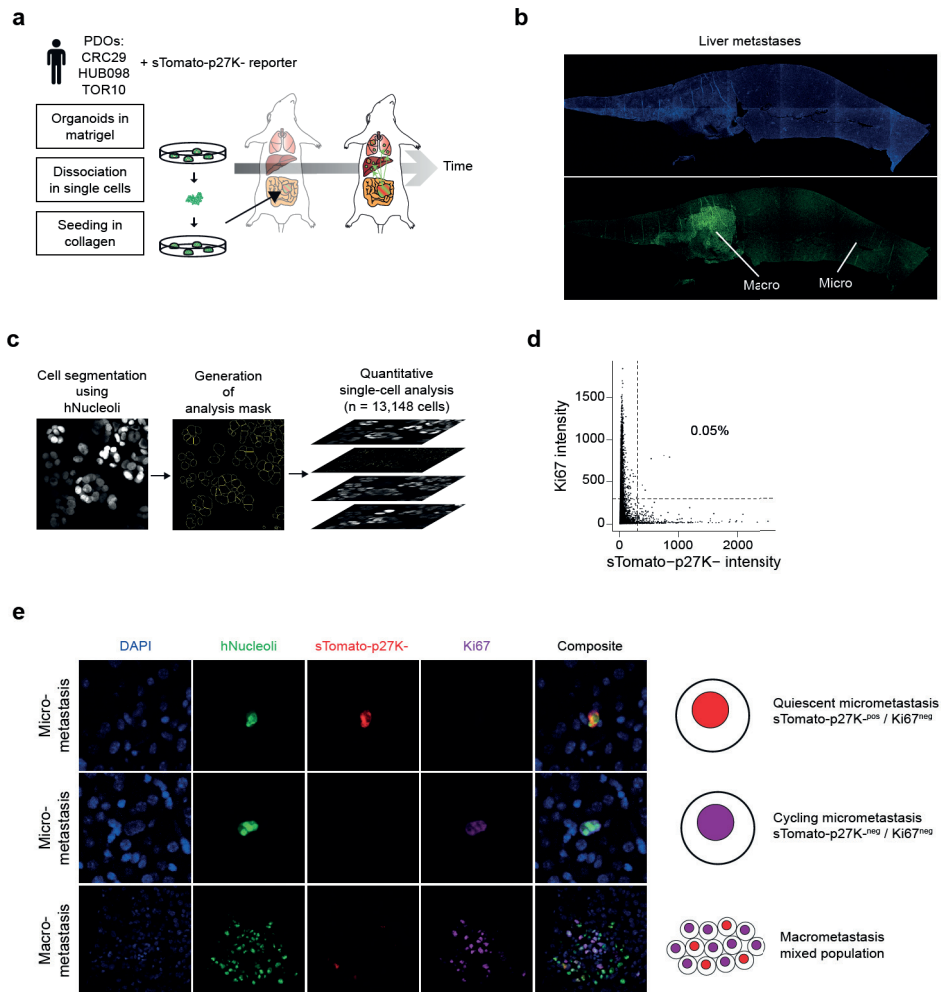


Figure 3. Micrometastases consist either of cycling or quiescent cells while macrometastases contain both subpopulations

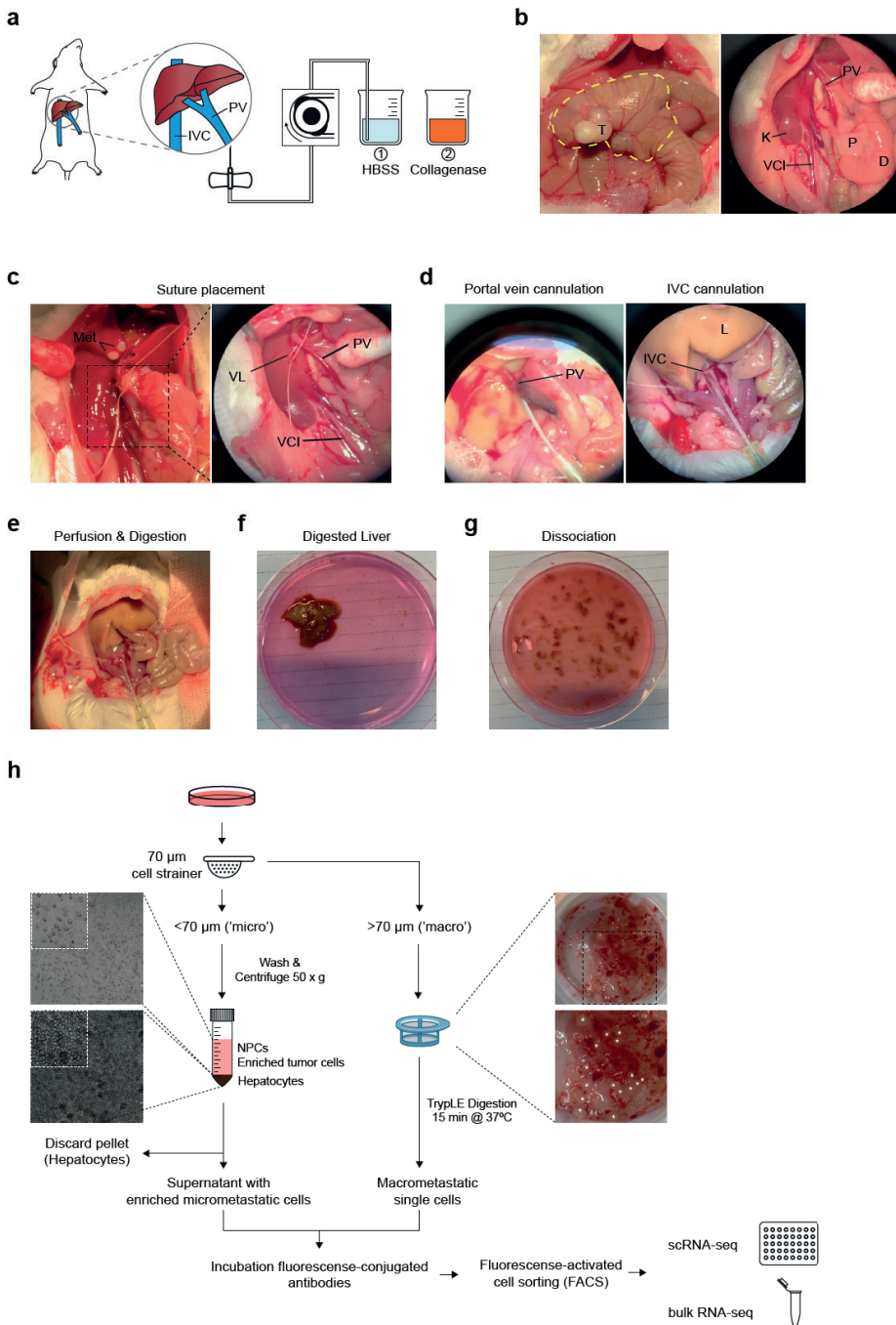
a. Experimental setup: PDOs with integrated quiescence reporter sTomato-p27K- were transplanted in the cecum of mice (identical to Figure 1A). **b.** Confocal imaging overview of DAPI (blue) and human Nucleoli (green, hNucleoli) demonstrating a mouse liver section with a micro- and macrometastasis. **c.** Single-cell quantification strategy of immunofluorescence using cell segmentation based on hNucleoli expression in the mouse liver. In total 13,148 metastatic cells were analyzed. **d.** Scatterplot of 10,148 cells demonstrating sTomato-p27K- and Ki-67 expression levels in liver metastatic cells. **e.** Fluorescence multiplex immunohistochemistry (mIHC) using antibodies against hNucleoli (green), sTomato (red), Ki67 (magenta).

Isolation of micro- and macro-metastasis using collagenase liver perfusion with subsequent size separation

We next designed a strategy to isolate sTomato-p27K^{high} cells from *in vivo* grown liver micro- and macrometastasis for subsequent analysis. The underlying isolation and enrichment methods are based on using *in-situ* collagenase liver perfusion followed by steps of centrifugation and size-based filtration (**Figure 4a**).

First, a midline incision is used to open the intraperitoneal cavity, exposing the orthotopically-transplanted tumor inside the cecum. The intestines are rotated laterally, exposing the portal vein (PV) and the subhepatic inferior vena cava (IVC) (**Figure 4b**). Depending on the anatomy of the specific mouse (for example strenuous surgical anatomy due to adhesions), either the PV (first choice) or the subhepatic IVC (second choice) can be used as cannulation site and subsequent liver perfusion. When the subhepatic IVC is used, the suprahepatic vena cava needs to be additionally clamped to ensure adequate retrograde perfusion of the liver. After successful cannulation of either vein (**Figure 4d**), the cannula can be fixed using a suture (**Figure 4c**) and the liver can be successively perfused with HBSS perfusion medium and collagenase digestion medium (**Figure 4e**). After successful liver digestion (**Figure 4f**) and opening of the liver's capsule allowing its contents into suspension, the vastly dissociated content of the liver should be visible (**Figure 4g**).

Next, the liver suspension is subjected to a metastasis enrichment protocol (**Figure 4h**). After multiple washing steps, the cell suspension is filtered over a 70 μm cell strainer, yielding a macrometastasis fraction in the strainer and a flow-through with hepatocytes, stroma and micrometastatic cells. Single cell suspensions of these fractions can be stained for cellular markers and FACS-based isolation methods for single-cell or bulk RNA-seq analysis (**Figure 4h**).



◀Figure 4. Isolation strategy of micro- and macrometastases using collagenase liver perfusion with subsequent size separation

a. Graphical representation in-situ collagenase liver perfusion. The portal vein (PV) or the subhepatic inferior vena cava (IVC) is cannulated and secured using a suture. First, the liver is perfused with HBSS and subsequently perfused with digestion medium containing collagenase type IV. **b.** Left: Image of the mouse caecum (yellow polygon) with a primary CRC tumor (T) 4 weeks after orthotopic transplantation of PDOs. Right: Enlarged photograph of portal vein (PV) and subhepatic inferior vena cava (IVC). K, kidney. P, pancreas. D, duodenum. **c.** Images demonstrating the application of a suture around the portal vein (PV) to be used as vessel loop for fixation of the vessel canula. VL, vessel loop suture. VCI, vena cava inferior. **d.** Images showing cannulation of the portal vein (PV) on the left and cannulation of the subhepatic inferior vena cava (IVC) on the right. L, liver. **e.** Image showing in-situ liver perfusion and digestion of the mouse liver. **f-g.** Image of a digested liver in a collection dish (f) before and (g) after dissociation. **h.** Strategy for the separation of micro- and macrometastases using size separation and centrifugation. The liver suspension is first filtered over a 70 μm cell strainer, resulting in two fractions ($< 70 \mu\text{m}$ and $> 70 \mu\text{m}$). The $< 70 \mu\text{m}$ fraction is repeatedly centrifuged at 50 x g to pellet and discard hepatocytes from the sample and enrich the sample for micrometastatic tumor cells. The $> 70 \mu\text{m}$ fraction in the filter contains macrometastases (*) and is subsequently enzymatically dissociated into a single-cell suspension. Both subcultures can then be further processed for downstream analyses.

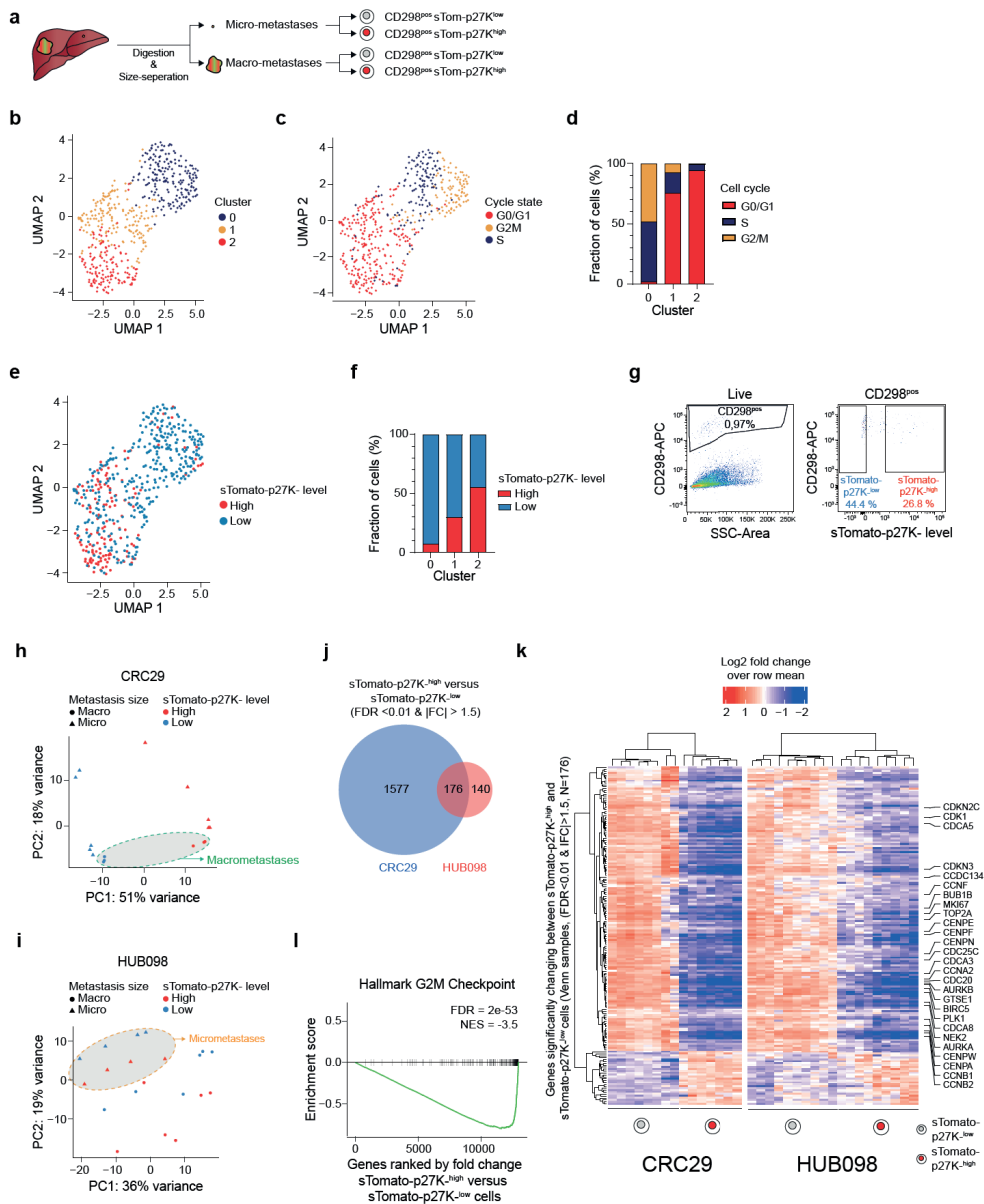
5

Quiescent cell cycle indicator sTomato-p27K- marks non-proliferative metastatic tumor cells in the mouse liver

We next used this extended isolation strategy on liver metastases of the xenotransplanted CRC29 p27K- reporter organoids to perform single-cell RNA-seq (scRNA-seq) (**Figure 5a-b**). Seurat-based cell cycle analysis revealed that the variance in this dataset is mainly driven by the cells' cell cycle state (**Figure 5c-d**, **Figure S3a-b**). Accordingly, of the three clusters identified through unsupervised hierarchical clustering (**Figure 3b**), cluster 0 mainly consists of cycling cells identified to be in S-phase or G2M-phase and is significantly enriched for cell cycle-related genes (such as *MKI67*, *TOP2A*, and *CDK1*). On the other hand, cluster 2 which mainly consists of cells in G0/G1-phase, is enriched for the cell cycle inhibitors p21, p57 and p15 (*CDKN1A*, *CDKN1C* and *CDKN2B*, resp.) as well as the differentiation marker *KRT20* (**Figure S3b**).

We next correlated the transcriptional cell cycle status to the reporter levels recorded during FACS. Reassuringly, sTomato-p27K^{low} cells constitute the vast majority of the highly proliferative cluster 0 and were generally enriched for cell cycle-related genes, while sTomato-p27K^{high} cells were enriched in the non-proliferative cluster 2 (**Figure 5e-f**, **Figure S3b**).

Surprisingly, we noted no major influence of the size of the metastasis on the transcriptome (**Figure S3a**). As we reasoned that this might be related to the sequencing depth associated with single cell analysis, we performed bulk RNA-seq on similar cell populations of CRC29 and HUB098 metastatic cells (**Figure 5g**).



◀Figure 5. Single-cell and bulk RNA-seq reveal that the quiescence reporter marks non-proliferative CRC cells *in vivo*

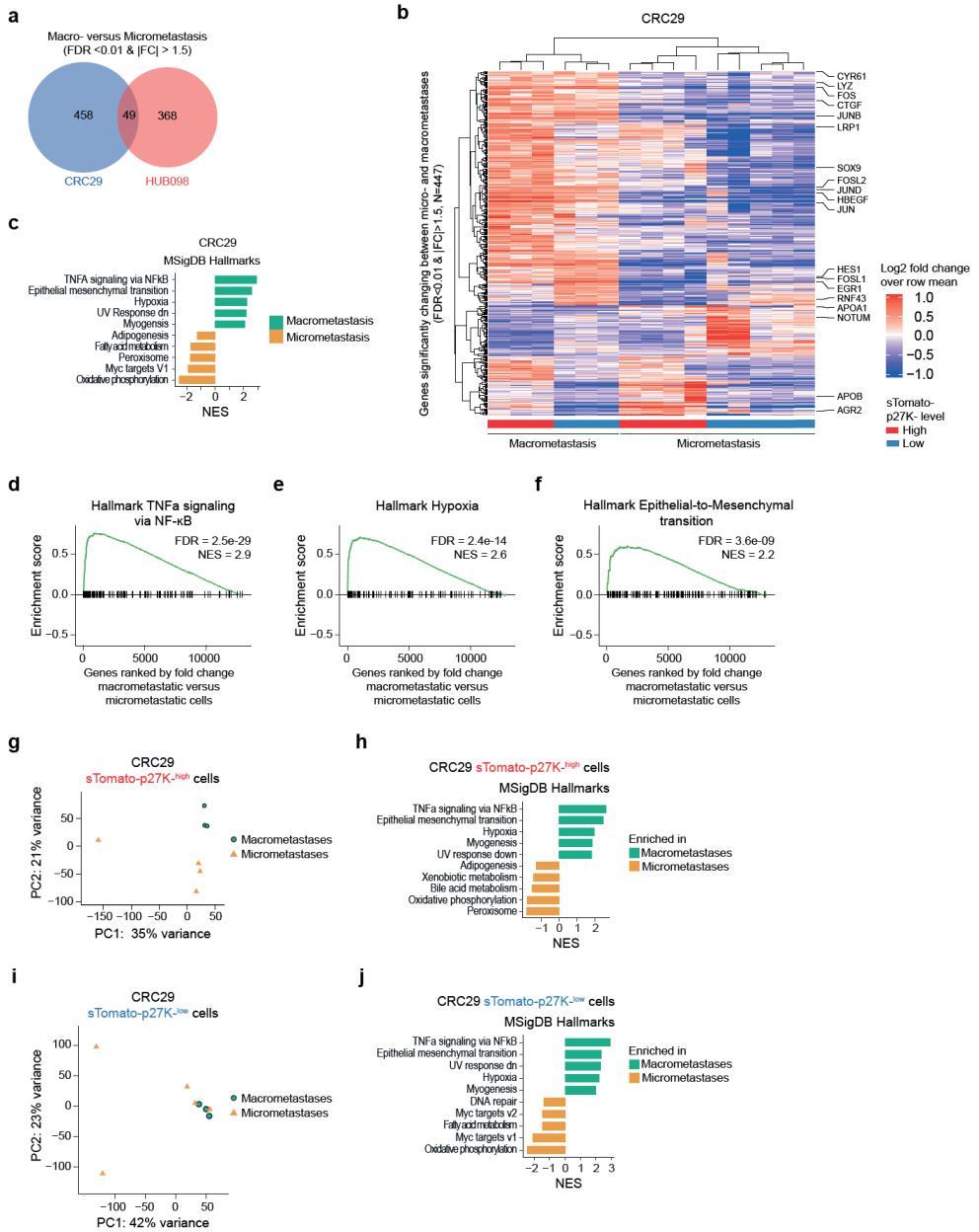
a. Schematic of experimental setup for the isolation of human CRC cells from micro- and macrometastases in the mouse liver. After digestion, metastases are size-separated using a cell strainer. sTomato-p27K^{high} and sTomato-p27K^{low} human CRC cells (hCD298⁺) are isolated using FACS. **b.** UMAP of scRNA-seq data color-coded by Seurat clusters resulting from unsupervised hierarchical clustering. **c.** UMAP of scRNA-seq data color-coded by cell cycle state (G0/G1, G2/M, and S) identified by Seurat. **d.** Bar graph showing the cell cycle distribution per cluster. **e.** UMAP of scRNA-seq data color-coded by FACS-based sTomato-p27K- expression levels, classified to be either sTomato-p27K^{high} or sTomato-p27K^{low}. **f.** Bar graph depicting FACS sTomato-p27K- expression levels per cluster. **g.** Gating strategy for the isolation of CD298⁺ sTomato-p27K^{low} and CD298⁺ sTomato-p27K^{high} cells. **h-i.** PCA depicting sTomato-p27K- populations (color) and metastasis size (symbol) for (h) CRC29 and (i) HUB098. **j.** Venn diagram depicting differentially expressed genes across sTomato-p27K- populations in CRC29 and HUB098 (FDR < 0.01 and fold-change > 1.5). **k.** Heatmap showing all 176 differentially expressed genes between sTomato-p27K^{high} (quiescent) and sTomato-p27K^{low} cells (absolute fold change > 1.5, FDR < 0.01) in CRC29 and HUB098. **l.** GSEA demonstrating sTomato-p27K^{low} cells enriched for the proliferation associated Hallmark G2M Checkpoint gene set (NES = -3.5, FDR = 2⁻⁵³).

Now, for CRC29, PCA showed that the main contributing factor for biological variance is associated with P27K- expression levels, directly followed by metastatic size (**Figure 5h**). For HUB098, on the other hand, the reporter influence is less pronounced with samples primarily clustering according to metastatic size. Nonetheless, within each size-based cluster, a clear separation by quiescence reporter activity can be observed (**Figure 5i**). Thus, this data suggests for both lines a difference in biology between (i) micro- and macrometastases, and (ii) sTomato-p27K^{low} and sTomato-p27K^{high} metastatic cells.

Transcriptome analysis of sTomato-p27K^{high} versus sTomato-p27K^{low} cells demonstrated 1,753 and 316 differentially expressed genes in CRC29 and HUB098 cells, respectively (FDR < 0.01 & absolute fold change > 1.5, **Figure 5j**), with a 176 gene overlap (**Figure 5k**). As expected, many cell cycle and proliferation-related genes were among the differentially expressed genes (such as *CDK1*, *MKI67*, *AURKA*, *AURKB*, *CCNB1*, *TOP2A*, and *CCNA1*). Indeed, GSEA demonstrates that sTomato-p27K^{low} cells of both CRC29 and HUB098 were enriched for pathways related to proliferation, while interferon responses were enriched in sTomato-p27K^{high} cells (**Figure 5l**, **Table S2**).

Micrometastases are biologically distinct from macrometastases

We next investigated the transcriptional differences between micro- and macrometastasis. Differential gene expression analysis between the subcultures yielded 507 and 419 dynamically expressed genes for CRC29 and HUB098, respectively (**Figure 6a**). In both lines, macrometastases were enriched for genes associated with extracellular matrix



◀Figure 6. Micrometastases are biologically distinct from macrometastases

a. Venn diagram depicting differentially expressed genes across micro- and macrometastases in CRC29 and HUB098 (fold change > 1.5, FDR < 0.01). **b.** Heatmap showing the differentially expressed genes between macro- and micrometastases in CRC29 (absolute fold change > 1.5, FDR < 0.01). **c.** Bar graph showing the five most significantly enriched gene sets of the MSigDB Hallmarks in macro- versus micrometastases in CRC29. **d-f.** GSEA demonstrating CRC29 macrometastases to be enriched for the MSigDB Hallmark gene sets (d) TNF α signaling via NF- κ B, (e) Hypoxia, and (f) Epithelial to Mesenchymal Transition. **g-j.** Subanalysis on all (g-h) CRC29 sTomato-p27K^{high} and (i-j) CRC29 sTomato-p27K^{low} samples. (g/i) PCA indicating metastasis size (symbol, color). (h/j) Bar graph showing the five most significantly enriched MSigDB Hallmarks gene sets for in macro- versus micrometastases.

remodeling, and fibrosis (such as *CYR61*, *CTGF*, *LRP1*, **Figure 6b** and **Figure S4a**). Furthermore, TNF α signaling and hypoxia pathways are among the upregulated gene sets in macrometastases of both lines (**Figure 6c-e**, **Figure S4b**, and **Table S3**). For CRC29 specifically, the gene set epithelial-to-mesenchymal transition was also significantly upregulated in macrometastases (NES = 2.2, $p = 3.6^{-09}$, **Figure 6c, f**). Conversely, micrometastases were characterized by alterations in their metabolism (such as oxidative phosphorylation, peroxisome, and fatty acid metabolism, **Figure 6c**). Unfortunately, presumably due to the overall different phenotype of CRC29 vs HUB098, we found minor similarities on the individual gene level.

In a next step, we assessed the transcriptional variation within quiescent or proliferating cancer subpopulations and found the size of metastases to be a major contributor to the variance of the data set (**Figure 6g, i**, **Figure S5a-b**). For both subpopulations, GSEA revealed next to cell cycle-related signatures TNF α signaling, hypoxia and epithelial-to-mesenchymal transition gene sets to be enriched in macrometastases (**Figure 6h, j**, **Figure S5c-d**, **Tables S4-S5**) (except for epithelial-to-mesenchymal transition markers in the HUB098 sTomato-p27K^{low} subpopulation). On the other hand, micrometastases were characterized by a distinct metabolic state (**Figure 6c, h, j**). Thus, the overall transcriptional differences in gene expression between micro- and macrometastases are reflected in both sTomato-p27K^{high} and sTomato-p27K^{low} subpopulations.

While the two analyzed CRC lines were overall very different in gene expression (**Figure 2g**), we nevertheless found shared differences between micro- and macrometastases across the lines. While micrometastases were characterized by a distinct metabolic state, macrometastases demonstrated some mesenchymal traits and upregulated signaling indicative of a hypoxic and fibrotic environment. This is in line with the previous IMC analysis of tissues slides that has demonstrated fibrotic markers to be present in the tumor microenvironment of macrometastases specifically (**Figure 1e**).

DISCUSSION

Metastatic colonization of the liver by CRC cells is a highly inefficient process (3). After tumor cells have extravasated into the liver parenchyma, they can persist as micrometastases in a dormant state from months up to years. This process is accountable for the clinical phenomenon of metastatic latency in which recurrent disease may manifest several years after removal of the primary tumor. Unfortunately, the dormant state of micrometastases and their outgrowth into overt clinical macrometastases are poorly understood and extremely hard to study due to their sporadic occurrence and small size.

In this study, we investigated micrometastatic disease of CRC with a focus on cellular quiescence. Using a combination of techniques including xenograft transplantation models of PDOs, metastasis isolation protocols using in-situ collagenase liver perfusion, metastatic size-separation and fluorescent labeling of quiescent cells (12), we provide novel insights into dormancy of CRC liver metastases.

In-situ liver perfusion protocols have previously been used to isolate the highly abundant hepatocytes as single cell suspension (16,17,28–31). However, metastatic cells are rare in comparison to hepatic cells. To be able to isolate CRC metastases from the liver, we have therefore modified the original protocol that now allows for the enrichment of metastatic cells, while additionally separating metastases by size using cell culture strainers. Coupled to FACS-based isolation of metastatic cells, this strategy has revealed fundamental differences in the transcriptome of micro- and macrometastases. The pronounced differences also support the view that the technical procedure generates highly enriched samples, as the limited number of micrometastatic cells per liver would have easily been outnumbered by numerous cells from macrometastases in case of cross-contamination.

To study if latent micrometastases are quiescent on a single cell as opposed to on a population level, we adapted the mVenus-p27K- quiescent cell cycle indicator (12) for our purposes and integrated it into three different PDOs using lentiviruses. We have shown that the reporter can be used to faithfully detect quiescent cells in G0 in both micro- and macrometastases when isolating cells with high reporter levels. In particular, this subpopulation demonstrated mutual exclusivity with the proliferation marker Ki67 both *in vitro* and *in vivo*. Yet, it should be noted that while we have focused on p27, the CDK inhibitors p21 and p57 can also promote quiescence (5). While usually all three proteins are highly expressed in quiescent cells (5) and while they were all enriched in the sTomato-p27K^{high} population on scRNA-seq, we have not formally excluded the existence of quiescent cells beyond the sTomato-p27K^{high} population.

Using the quiescence reporter, we have revealed that in our model systems micrometastases are either entirely cycling or entirely quiescent. While this suggests cellular quiescence to be implicated in the formation of micrometastases in our model systems, we cannot address the role of the immune system in population dormancy, given that the xenotransplantations were performed in immunocompromised mice. In addition, having performed spontaneous metastasis formation assays, the actual age of the metastases is unknown. Thus, we cannot tell which lesions have recently formed and if the quiescent micrometastases are reflective of metastatic latency. To address this, future studies with induced metastasis formation assays are required.

Nonetheless, we observed fundamental transcriptomic differences between micro- and macrometastatic disease. While macrometastases were generally characterized by TNF α signaling, hypoxia, and epithelial-to-mesenchymal transition, micrometastases showed upregulation of genes associated with metabolic pathways. As these differences were also apparent when analyzing subpopulations (such as quiescent cells), this hints at a remodeling of the cancer cells state during metastatic outgrowth as well as changes in the tumor microenvironment.

The combination of methodologies presented in this study will be instrumental for future research aiming to improve our understanding of micrometastases. Open questions for instance comprise the duration by which cells can retain in a quiescent state, if the relative abundance of quiescent cells changes over time, and if the propensity to form dormant micrometastases correlates with the presence of cellular quiescence, genomic landscape and/or tumor subtypes. In addition, our toolbox offers the possibility to separately collect metastatic cells from either micro- or macroscopic lesions for comparative analyses, such as testing their metastatic outgrowth potential in a serial transplantation experiments. A difference would imply genomic and/or epigenetic traits to be instrumental for the transition towards successful outgrowth. Furthermore, these underlying causes could be in-depth analyzed using newly established organoid lines from the *in vivo*-selected metastatic lesions with the aim to identify vulnerabilities in micrometastases that might be therapeutically exploitable in the context of adjuvant CRC treatment.

MATERIAL AND METHODS

Mouse experiments

All mouse experiments were performed in accordance with protocols approved by the Institutional Animal Care and Use Committee of Utrecht University. Animals were housed

at animal facilities of the Central Laboratory Animal Research Facility (Gemeenschappelijk Dierenlaboratorium, GDL).

Mouse experiments with orthotopic transplantation of colorectal cancer organoids were performed as previously described (8,13). In brief, 8-12 week old male and/or female NOD.Cg-PrkdcSCID Il2rgtm1Wjl/SzJ mice, obtained from Charles River were used. When the research end point or humane end point was reached, mice were euthanized for organ collection or liver perfusion (see below).

For transplantation experiments using organoids with the sTomato-p27K- reporter, a total of 15 mice was used (n = 5 mice per cell lines, 3 cell lines total).

Immunohistochemistry

Specimens were formalin fixed and paraffin embedded and subsequently cut into 4 μ m sections. Then, sections were deparaffinized by immersion in xylene and subsequently rehydrated in a graded alcohol series (100% ethanol to 70% ethanol). Epitope retrieval was carried out in 10 mM sodium citrate (pH 6.0). Endogenous peroxidase was blocked using a PBS H₂O₂ buffer. Tissues were incubated overnight at 4°C using antibodies against CEA (1:600, ab75685, Abcam), Ki67 (1:1000, NCL-Ki67p, Novacastra), and α -SMA (1:300, ab5694, Abcam). Goat-anti-Rb-poly-HRP or Mouse-anti-Rb-poly-HRP was used to as secondary antibody and signal amplification, as appropriate. Sections were then developed with diaminobenzidine (DAB) followed by a hematoxylin counterstaining. Sections were then air dried and cover slipped.

Immunofluorescence

Immunofluorescence on colorectal cancer organoids was performed on 15-well Ibidi u-slide Angiogenesis slides. Organoids dissociated with TrypLE. Matrigel were plated into the bottom of the well with organoid medium placed on top. Organoids were allowed to grow for 7-10 days after which the organoids were fixed using 4% paraformaldehyde. PBDBT buffer (PBS / 1% BSA / 1% DMSO / 0.2% Triton-X100) is used as washing buffer and used for the dilution of primary and secondary antibodies. Wells were incubated with primary antibodies using antibodies against Ki67 (1:500, NCL-Ki67p, Novacastra). Images were then generated on the Zeiss LSM550 Confocal Laser Scanning Microscope.

Fluorescence multiplex immunohistochemistry

Tyramide multiplex immunohistochemistry (mIHC) using was performed as previously described (8). In brief, mIHC enables the simultaneous detection of multiple proteins of interest on the same tissue section using fluorophore-conjugated tyramide molecules serving as the substrate for HRP-conjugated secondary antibodies. Serial heat-mediated stripping of the primary/secondary antibody pair, while preserving the fluorescent signal makes this process amenable to multiple rounds of staining in a sequential fashion on the same tissue slide without crosstalk between same host species antibodies.

For the mIHC experiments, the Alexa Fluor 488 Tyramide SuperBoost Kit (B40922, Invitrogen, ThermoFisher) was used. Sections were incubated with antibodies against human Nucleoli (1:500, ab190710, Abcam), RFP (1:500, Rockland 600-401-379), Ki67 (1:1000, NCL-Ki67p, Novacastra).

Histopathological quantification

Confocal scanned images were analyzed using QuPath v0.3.0 (14). Cells were detected using the 'cell detection' function using the H2B-mNeon or human Nucleoli detection channel. The detected cells were subsequently used as an analysis mask to quantify the expression of additional markers within the detected cell using the 'export detection measurements' function.

Imaging Mass Cytometry

Imaging Mass Cytometry™ (IMC) was performed on the Hyperion™ Imaging System using metal-conjugated antibodies enabling multiparameter analysis on a single section (15). First, sections were subjected to normal immunofluorescence using antibodies against tumor marker CEA (1:600, ab75685, Abcam). Slides were scanned using a NanoZoomer fluorescent Digital Slide Scanner (Hamamatsu). The sections were then stained using a panel of metal-conjugated antibodies against the following targets: α -SMA (3141017D, Fluidigm), Collagen type I (3169023D, Fluidigm), Histone H3 (3176023D, Fluidigm), Ki67 (3168022D, Fluidigm), Pan-Keratin (3148020D, Fluidigm).

The scans were used to identify the location of metastases which are subsequently UV laser ablated using the Hyperion™ system. The CYTOF mass cytometer generated multiple parameter image files which were then aligned with the fluorescent image scan.

In-situ collagenase liver perfusion

For the isolation of micro- and macrometastatic CRC cells, we have adopted and modified an existing liver perfusion protocol (16,17) which has been previously described (8).

First, the mouse abdomen is opened with a midline incision. Then, the portal vein (PV) and subhepatic inferior vena cava (IVC) are exposed. At this stage it is essential to evaluate the anatomy of both veins to maximize the probability for successful cannulation. Before cannulation of the PV, a suture with a knot is placed around the hepatic pedicle which can be tied down after successful cannulation to fixate the canula. When cannulation fails, it is pivotal that hemostasis is achieved to allow for a subsequent attempt in the non-cannulated PV or IVC.

The PV or the IVC are cannulated with a 24G IV catheter (BD Insyte Autoguard Shielded IV catheter; BD 381412) after which the canula is fixated in the vein with a suture. The catheter is then connected with fluidic system driven by a peristaltic pump to enable the in-situ perfusion and digestion of the liver. If the portal vein is cannulated, the subhepatic IVC is cut to allow drainage of the perfusate. When the subhepatic IVC is chosen as perfusion site, the suprahepatic IVC is clamped with a bulldog clamp and the portal-vein is cut to allow retro-grade perfusion of the liver.

First, 70 mL HBSS 70 mL HBSS (Gibco) with 0.5 mmol/L EGTA and 25 mmol/L HEPES (pH-adjusted to 7.4 at 37°C by NaOH) is perfused with a speed of 7-9 mL/min, making the liver to blanch. Then the liver is digested using 80 mL digestion medium consisting of DMEM-low glucose (Corning) with 15 mmol/L HEPES, Penicillin-Streptomycin, collagenase type IV (Gibco) in sufficient quantity for 120 Collagenase Digestive Units (CDU)/mL at 37°C. After successful digestion, the liver is carefully excised while care should be taken not to rupture Glisson's capsule to prevent the liver falling apart while still in situ.

The liver is placed in a 15-cm petri dish with 10 mL digestion medium and subsequently dissociated by carefully opening Glisson's capsule. The liver suspension containing intact macrometastases is resuspended in 25 mL ice-cold isolation medium (DMEM-High/F-12, Gibco with 10% FBS) and filtered through a 70 µm cell strainer. While the flow-through (< 70 µm fraction) contains micrometastatic cells, macrometastases are caught in the strainer (> 70 µm fraction, visible with the naked eye) and are subsequently collected. Both fractions are then processed for further analysis.

The micrometastatic fraction is washed three times using 25 mL isolation medium using low-speed centrifugation at 50 x g to pellet hepatocytes. The supernatant containing the CRC cells is processed further each time. The macrometastatic fraction is first trypsinized using Liberase™ (Roche) for 10-15 minutes at 37°C. The resulting single cell suspension is then washed once.

Both fractions are stained using APC anti-human CD298 antibodies (341706, Biolegend) and SyTOX blue for live-dead cell discrimination. Single, alive, hCD298⁺ cells were collected by FACS for scRNA-seq, while hCD298⁺-sTomato-p27K^{low} and hCD298⁺-sTomato-p2K^{high} cell populations were collected for bulk RNA-seq.

Organoid culture

Organoid cultures were cultured in Matrigel (Corning) using conditions as previously described (10,18).

Bulk RNA-seq analysis

For the generation of the bulk RNA-seq data from *in vitro* organoids, library preparation and Next Generation Sequencing (NGS) was performed at USEQ (Utrecht Sequencing Facility, Utrecht, The Netherlands). To generate the libraries, Truseq RNA stranded polyA (Illumina) was used. Then, libraries were sequenced on the Illumina NextSeq500 platform on the High Output 1 x 75bp configuration. This resulted in a minimal sequencing depth of 23 million reads per sample. Sequencing reads were mapped to the pre-indexed hg37 genome assembly.

For the generation of the *in vivo* bulk RNA-seq data, samples were transported to Single Cell Discoveries (SCD, Hubrecht Institute, Utrecht, The Netherlands) for low-input RNA sequencing (n = 500 – 8000 cells per sample). CEL-seq2 style barcodes are used to allow pooling of multiple samples into one sequencing library.

Dimension reduction and differential gene expression analysis (Wald test with Benjamini-Hochberg correction) was performed using the DESeq2 R-package on bioconductor (19). Gene set enrichment analysis (GSEA) was performed using the fgsea R-package (20) with the Hallmark and Kegg gene sets registered at Molecular Signature Database (MSigDB) (21). Unless indicated otherwise, the top 5 significantly enriched gene sets are depicted. Heatmaps were generated with rlog-transformed and row-normalized expression data using ComplexHeatmap R-package (22).

Single-cell RNA sequencing and analysis

scRNA-seq was performed in line with the SORT-seq protocol (23). Reads were mapped to the hg38 genome assembly including sTomato-p27K- reporter transcripts. Analysis was performed using the R-package Seurat (24), including cells with > 1,000 reads and < 40 % mitochondrial content.

Quantification and statistical analysis

Statistical analysis was performed using R statistical program version 4.1.1 for Mac (R Foundation for Statistical Computing, Vienna, Austria; <http://www.R-project.org>) or GraphPad Prism (software version 9). Results with p-values < 0.05 were considered statistically significant, unless indicated otherwise.

REFERENCES

1. Siegel RL, Miller KD, Fuchs HE, Jemal A. Cancer statistics, 2022. *CA Cancer J Clin* [Internet]. American Cancer Society; 2022 [cited 2022 Aug 11];72:7–33. Available from: <https://onlinelibrary-wiley-com.proxy.library.uu.nl/doi/full/10.3322/caac.21708>
2. Okholm C, Mollerup TK, Schultz NA, Strandby RB, Achiam MP, Med D, et al. Synchronous and metachronous liver metastases in patients with colorectal cancer. *Dan Med J*. 2018;65:1–6.
3. Massagué J, Obenauf AC. Metastatic colonization by circulating tumour cells. *Nature*. 2016. page 298-306.
4. Obenauf AC, Massagué J. Surviving at a Distance: Organ-Specific Metastasis. *Trends in Cancer* [Internet]. Elsevier Ltd; 2015;1:76–91. Available from: <http://dx.doi.org/10.1016/j.trecan.2015.07.009>
5. Marescal O, Cheeseman IM. Cellular Mechanisms and Regulation of Quiescence. *Dev Cell*. Cell Press; 2020;55:259–71.
6. Lawson DA, Bhakta NR, Kessenbrock K, Prummel KD, Yu Y, Takai K, et al. Single-cell analysis reveals a stem-cell program in human metastatic breast cancer cells. *Nature*. 2015;526:131–5.
7. Malladi S, Macalinao DG, Jin X, He L, Basnet H, Zou Y, et al. Metastatic Latency and Immune Evasion through Autocrine Inhibition of WNT. *Cell*. 2016;165:45–60.
8. Heinz MC, Peters NA, Oost KC, Lindeboom RGH, van Voorthuijsen L, Fumagalli A, et al. Liver Colonization by Colorectal Cancer Metastases Requires YAP-Controlled Plasticity at the Micrometastatic Stage. *Cancer Res* [Internet]. American Association for Cancer Research; 2022 [cited 2022 May 16];82:1953–68. Available from: <https://aacrjournals.org/cancerres/article/82/10/1953/696332/Liver-Colonization-by-Colorectal-Cancer-Metastases>
9. De Sousa E Melo F, Kurtova A V., Harnoss JM, Kljavin N, Hoek JD, Hung J, et al. A distinct role for Lgr5 + stem cells in primary and metastatic colon cancer. *Nature* [Internet]. Nature Publishing Group; 2017;543:676–80. Available from: <http://www.nature.com/doi/finder/10.1038/nature21713>
10. Van De Wetering M, Francies HE, Francis JM, Bounova G, Iorio F, Pronk A, et al. Prospective Derivation of a Living Organoid Biobank of Colorectal Cancer Patients. *Cell*. Cell Press; 2015;161:933–45.
11. Clevers H. Modeling Development and Disease with Organoids. *Cell*. Cell Press; 2016;165:1586–97.
12. Oki T, Nishimura K, Kitaura J, Togami K, Maehara A, Izawa K, et al. A novel cell-cycle-indicator, mVenus-p27K -, identifies quiescent cells and visualizes G0-G1 transition. *Sci Rep*. 2014;4.
13. Fumagalli A, Suijkerbuijk SJE, Begthel H, Beerling E, Oost KC, Snippert HJ, et al. A surgical orthotopic organoid transplantation approach in mice to visualize and study colorectal cancer progression. *Nat Protoc* [Internet]. Nature Publishing Group; 2018;13:235–47. Available from: <http://www.nature.com/doi/finder/10.1038/nprot.2017.137>
14. Bankhead P, Loughrey MB, Fernández JA, Dombrowski Y, McArt DG, Dunne PD, et al. QuPath: Open source software for digital pathology image analysis. *Sci Reports* 2017 71 [Internet]. Nature Publishing Group; 2017 [cited 2022 Aug 11];7:1-7. Available from: <https://www-nature-com.proxy.library.uu.nl/articles/s41598-017-17204-5>
15. Giesen C, Wang HAO, Schapiro D, Zivanovic N, Jacobs A, Hattendorf B, et al. Highly multiplexed imaging of tumor tissues with subcellular resolution by mass cytometry. *Nat Methods* 2014 114 [Internet]. Nature Publishing Group; 2014 [cited 2022 Aug 11];11:417–22. Available from: <https://www-nature-com.proxy.library.uu.nl/articles/nmeth.2869>

16. Charni-Natan M, Goldstein I. Protocol for Primary Mouse Hepatocyte Isolation. *STAR Protoc. Elsevier*; 2020;1:100086.
17. Klaunig JE, Goldblatt PJ, Hinton DE, Lipsky MM, Trump BF. Mouse Liver Cell Culture . I. Hepatocyte Isolation. *In Vitro*. 1981;17:913–25.
18. Küçükköse E, Peters NA, Ubink I, van Keulen VAM, Daghighian R, Verheem A, et al. KIT promotes tumor stroma formation and counteracts tumor-suppressive TGF β signaling in colorectal cancer. *Cell Death Dis* 2022 137 [Internet]. Nature Publishing Group; 2022 [cited 2022 Aug 11];13:1–10. Available from: <https://www-nature-com.proxy.library.uu.nl/articles/s41419-022-05078-z>
19. Love MI, Huber W, Anders S. Moderated estimation of fold change and dispersion for RNA-seq data with DESeq2. *Genome Biol*. 2014;15:1–21.
20. Korotkevich G, Sukhov V, Budin N, Shpak B, Artyomov MN, Sergushichev A. Fast gene set enrichment analysis. *bioRxiv* [Internet]. 2021;60012. Available from: <http://biorxiv.org/content/early/2021/02/01/060012.abstract>
21. Subramanian A, Tamayo P, Mootha VK, Mukherjee S, Ebert BL, Gillette MA, et al. Gene set enrichment analysis: A knowledge-based approach for interpreting genome-wide expression profiles. *Proc Natl Acad Sci U S A* [Internet]. National Academy of Sciences; 2005 [cited 2022 Aug 11];102:15545–50. Available from: <https://www.pnas.org/doi/abs/10.1073/pnas.0506580102>
22. Gu Z, Eils R, Schlesner M. Complex heatmaps reveal patterns and correlations in multidimensional genomic data. *Bioinformatics*. 2016;32:2847–9.
23. Muraro MJ, Dharmadhikari G, Grün D, Groen N, Dielen T, Jansen E, et al. A Single-Cell Transcriptome Atlas of the Human Pancreas. *Cell Syst. Cell Press*; 2016;3:385-394.e3.
24. Hao Y, Hao S, Andersen-Nissen E, Mauck WM, Zheng S, Butler A, et al. Integrated analysis of multimodal single-cell data. *Cell. Cell Press*; 2021;184:3573-3587.e29.
25. Correia AL, Guimaraes JC, Auf der Maur P, De Silva D, Trefny MP, Okamoto R, et al. Hepatic stellate cells suppress NK cell-sustained breast cancer dormancy. *Nat* 2021 5947864 [Internet]. Nature Publishing Group; 2021 [cited 2022 Aug 11];594:566–71. Available from: <https://www-nature-com.proxy.library.uu.nl/articles/s41586-021-03614-z>
26. Susaki E, Nakayama K, Nakayama KI. Cyclin D2 Translocates p27 out of the Nucleus and Promotes Its Degradation at the G 0 -G 1 Transition . *Mol Cell Biol* [Internet]. American Society for Microbiology; 2007 [cited 2022 Aug 12];27:4626–40. Available from: <https://journals.asm.org/doi/10.1128/MCB.00862-06>
27. Malek NP, Sundberg H, McGrew S, Nakayama K, Kyriakidis TR, Roberts JM. A mouse knock-in model exposes sequential proteolytic pathways that regulate p27Kip1 in G1 and S phase. *Nat* 2001 4136853 [Internet]. Nature Publishing Group; 2001 [cited 2022 Aug 12];413:323–7. Available from: <https://www-nature-com.proxy.library.uu.nl/articles/35095083>
28. Jung Y, Zhao M, Svensson KJ. Isolation, culture, and functional analysis of hepatocytes from mice with fatty liver disease. *STAR Protoc. Elsevier*; 2020;1:100222.
29. Choi WM, Eun HS, Lee YS, Kim SJ, Kim MH, Lee JH, et al. Experimental Applications of in situ Liver Perfusion Machinery for the Study of Liver Disease. *Mol Cells* [Internet]. Korean Society for Molecular and Cellular Biology; 2019 [cited 2022 Aug 11];42:45. Available from: [/pmc/articles/PMC6354060/](https://pmc/articles/PMC6354060/)
30. Li WC, Ralphs KL, Tosh D. Isolation and culture of adult mouse hepatocytes. *Methods Mol Biol* [Internet]. Humana Press; 2010 [cited 2022 Aug 12];633:185–96. Available from: https://link-springer-com.proxy.library.uu.nl/protocol/10.1007/978-1-59745-019-5_13

31. Cabral F, Miller CM, Kudrna KM, Hass BE, Daubendiek JG, Kellar BM, et al. Purification of Hepatocytes and Sinusoidal Endothelial Cells from Mouse Liver Perfusion. *J Vis Exp* [Internet]. MyJoVE Corporation; 2018 [cited 2022 Aug 12];2018:56993. Available from: [/pmc/articles/PMC5894826/](#)

SUPPLEMENTARY MATERIAL

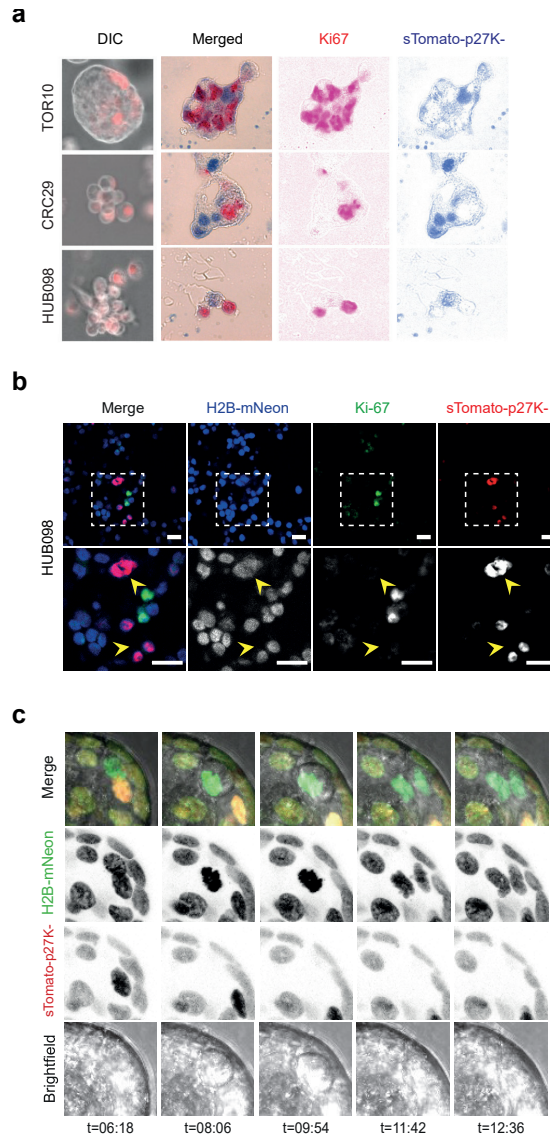


Figure S1: Related to Figure 2

a. Immunohistochemistry on paraffin embedded organoids (TOR10, CRC29, and HUB098) using antibodies against Ki67 and sTomato using Vector Blue and Liquid Permanent Red. **b.** Immunofluorescence staining against Ki67 (green) and sTomato (red) in HUB098 organoids constitutively expressing the fusion protein H2B-mNeon (blue). Close-ups, white boxes. Yellow arrows, sTomato-p27K⁻ cells. Scale bar, 20 μ m. **c.** Selected stills from confocal live cell imaging showing dividing mitotic cells to be negative for the quiescence reporter sTomato-p27K⁻.

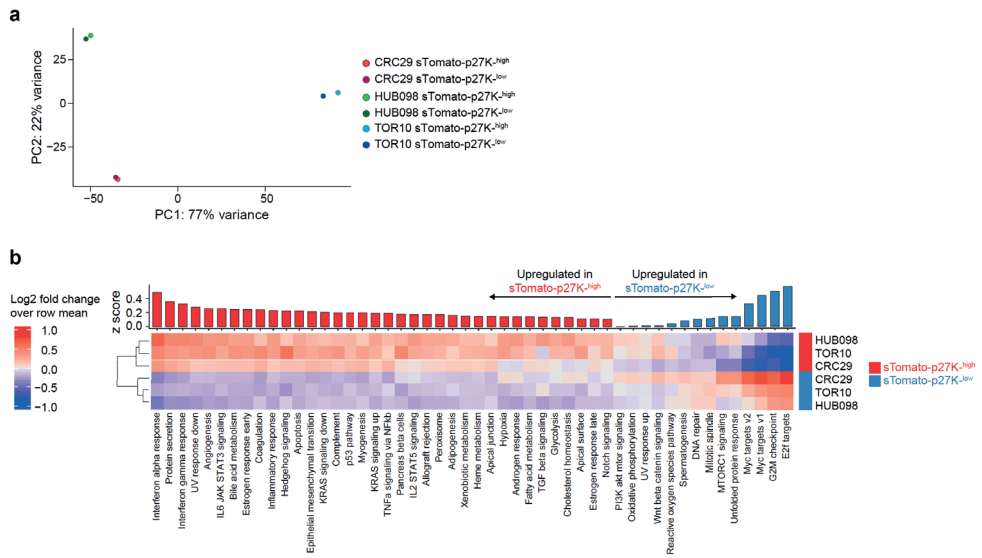


Figure S2: Related to Figure 2

a. PCA with PDO line identity and sTomato-p27K- levels (high or low) indicated by color. **b.** Z-scores of Hallmark signatures for sTomato-p27K^{high} cells and sTomato-p27K^{low} cells.

5

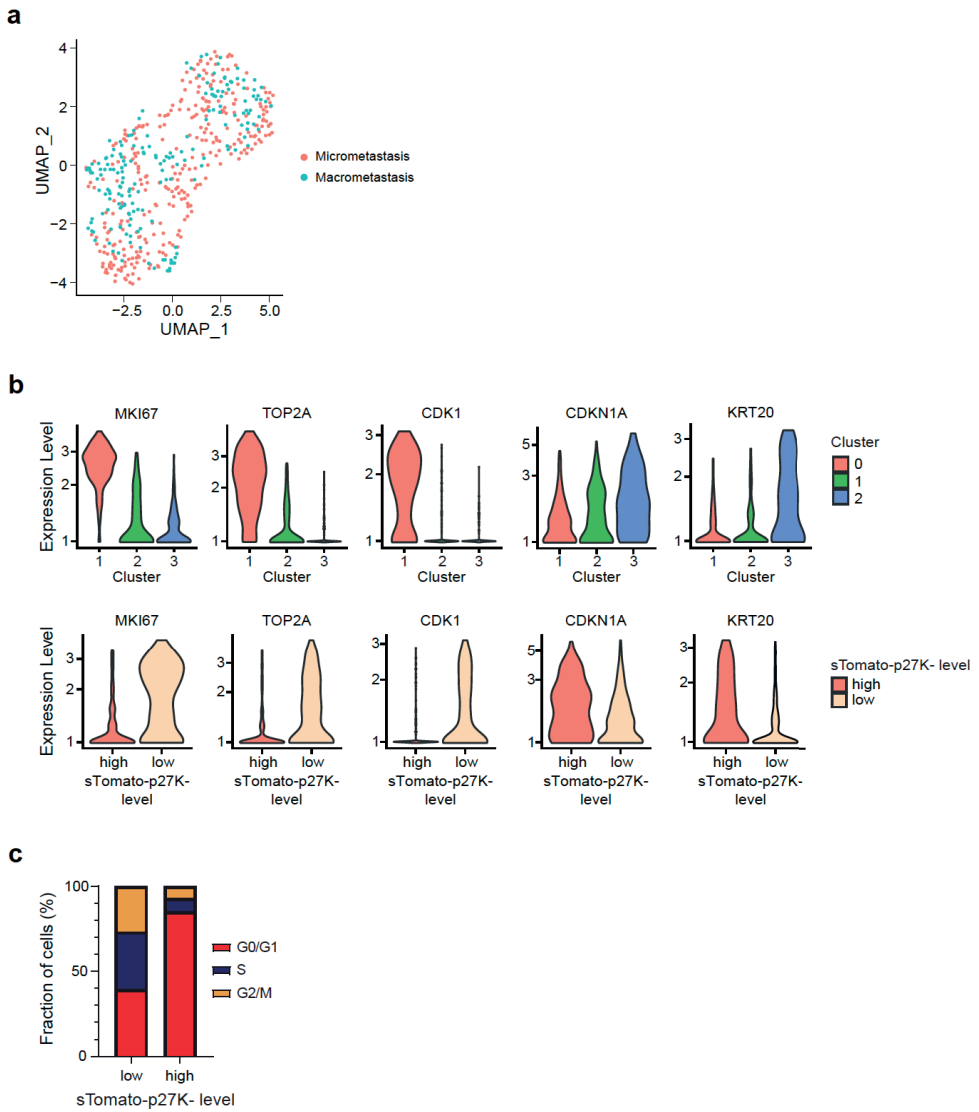


Figure S3: Related to Figure 5

a. UMAP of scRNA-seq data color-coded by metastasis size. **b.** Expression levels of *MKI67*, *TOP2A*, *CDK1*, *CDKN1B*, and *KRT20* across (top) Seurat clusters (top) and (bottom) sTomato-p27K- expression levels. **c.** Bar graph showing cell cycle distributions within sTomato-p27K^{-high} and sTomato-p27K^{-low} cells.

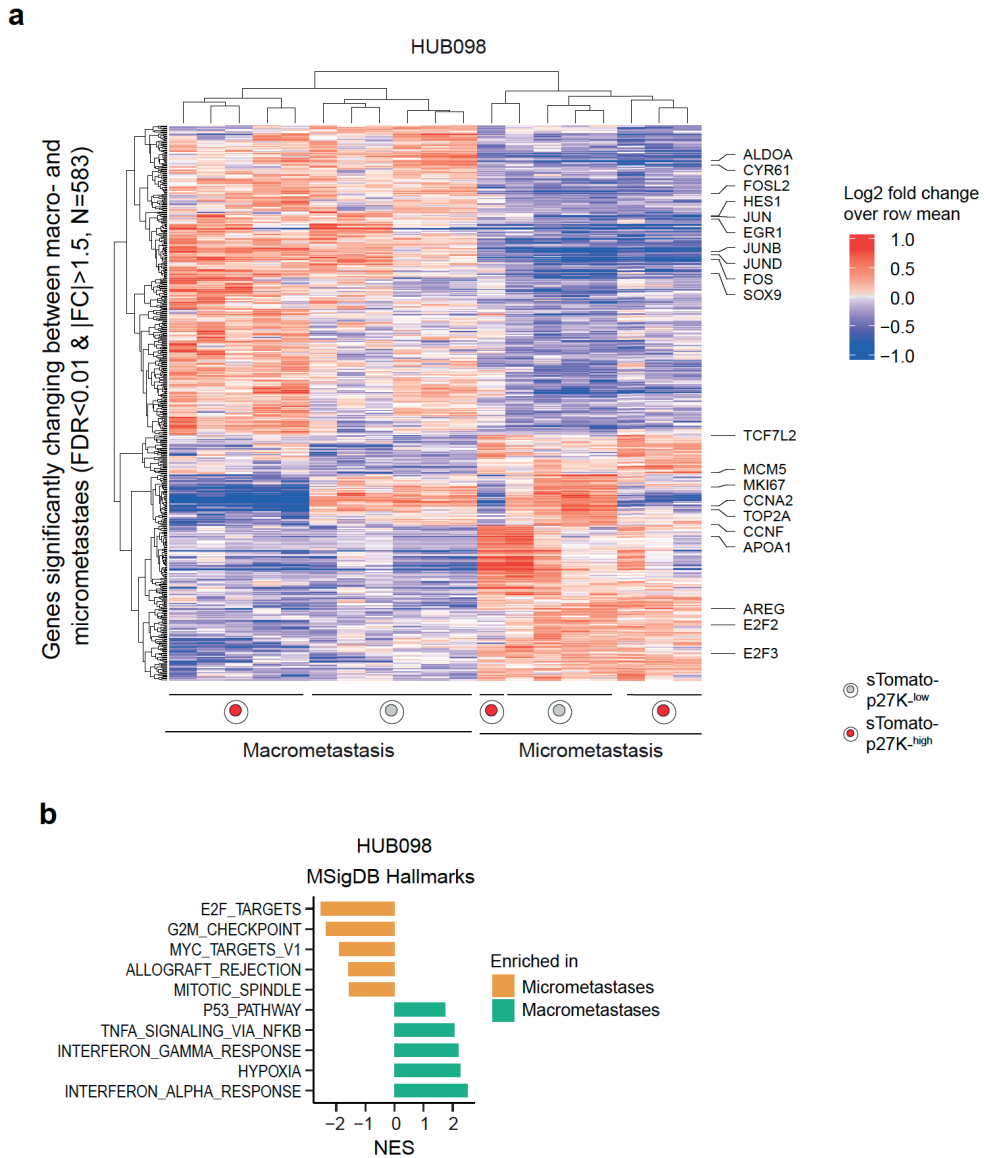


Figure S4: Related to Figure 6

a. Heatmap showing the differentially expressed genes between macro- and micrometastases in HUB098 (absolute fold change > 1.5, FDR < 0.01). **b.** Bar graph showing the five most significantly enriched gene sets of the MSigDB Hallmarks in macro- versus micrometastases in HUB098.

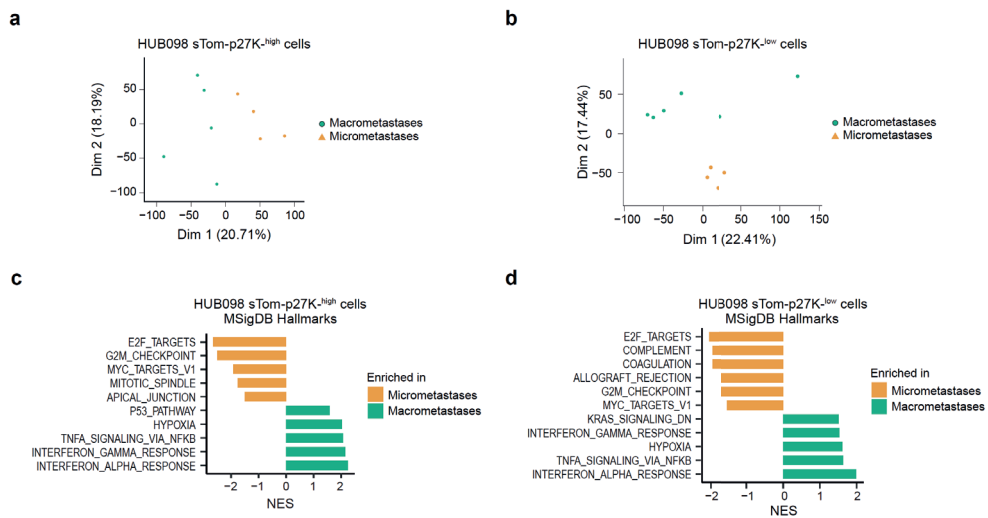


Figure S5: Related to Figure 6

a-b. PCA of all (a) sTomato-p27K^{high} and (b) sTomato-p27K^{low} samples of HUB098 with metastasis size indicated by color/symbol. **c-d.** Bar graph showing the five most significantly enriched gene sets of the MSigDB Hallmarks in HUB098 macro- versus micrometastases within (c) sTomato-p27K^{high} and (d) sTomato-p27K^{low} cells.

Ensembl Gene ID	External Gene Name	Base Mean	Log2 Fold Change	LfcSE	Stat	pvalue	padj
ENSG00000125538	IL1B	115.32	5.25	0.81	6.06	1.32E-09	8.95E-08
ENSG00000163762	TM4SF18	37.27	4.56	0.37	11.53	8.91E-31	2.17E-27
ENSG00000091972	CD200	18.45	4.14	0.50	7.66	1.79E-14	3.75E-12
ENSG00000231645	KRT17P6	13.87	4.05	0.57	6.59	4.51E-11	4.41E-09
ENSG00000027644	INSRR	10.41	4.05	0.84	4.44	9.01E-06	2.51E-04
ENSG00000159625	DRC7	4.20	3.80	0.82	4.26	2.05E-05	5.22E-04
ENSG00000226321	CROCC2	5.00	3.75	0.96	3.59	3.37E-04	5.94E-03
ENSG00000131885	KRT17P1	244.10	3.71	0.23	14.61	2.45E-48	1.20E-44
ENSG00000069122	ADGRF5	2.31	3.42	0.80	3.89	1.02E-04	2.15E-03
ENSG00000108691	CCL2	13.24	3.39	0.53	5.76	8.60E-09	4.83E-07
ENSG00000136960	ENPP2	17.70	3.38	0.74	4.16	3.15E-05	7.65E-04
ENSG00000260532		5.32	3.31	0.69	4.31	1.65E-05	4.30E-04
ENSG00000187908	DMBT1	85.43	3.22	0.24	11.86	1.93E-32	5.37E-29
ENSG00000160401	CFAP157	14.81	3.15	0.52	5.39	7.15E-08	3.26E-06
ENSG00000167653	PSCA	71.63	3.14	0.55	5.17	2.39E-07	9.80E-06
ENSG00000070985	TRPM5	18.79	3.12	0.43	6.51	7.37E-11	6.84E-09
ENSG00000211892	IGHG4	27.66	3.08	0.44	6.22	4.87E-10	3.74E-08
ENSG00000169064	ZBBX	7.14	3.08	0.61	4.53	6.03E-06	1.75E-04
ENSG00000167889	MGAT5B	6.68	2.98	0.74	3.59	3.32E-04	5.88E-03
...							
ENSG00000166851	PLK1	1832.22	-3.53	0.42	-7.69	1.46E-14	3.19E-12
ENSG00000168078	PBK	1096.58	-3.56	0.52	-6.24	4.35E-10	3.38E-08
ENSG00000142945	KIF2C	1873.58	-3.56	0.50	-6.45	1.12E-10	1.01E-08
ENSG00000111665	CDCA3	779.19	-3.57	0.31	-10.51	7.41E-26	1.20E-22
ENSG00000178999	AURKB	1088.68	-3.63	0.47	-7.07	1.58E-12	2.26E-10
ENSG00000066279	ASPM	1865.46	-3.63	0.46	-7.24	4.36E-13	6.96E-11
ENSG00000115163	CENPA	443.03	-3.74	0.46	-7.46	8.75E-14	1.54E-11
ENSG00000135451	TROAP	1191.54	-3.79	0.44	-7.87	3.65E-15	9.37E-13
ENSG00000143228	NUF2	764.95	-3.86	0.48	-7.32	2.40E-13	4.01E-11
ENSG00000089685	BIRC5	1547.27	-3.92	0.52	-6.96	3.48E-12	4.52E-10
ENSG00000117650	NEK2	883.37	-3.93	0.54	-6.69	2.30E-11	2.43E-09
ENSG00000129195	PIMREG	745.41	-3.94	0.43	-8.35	6.84E-17	2.47E-14
ENSG00000075218	GTSE1	899.28	-3.95	0.55	-6.65	2.90E-11	2.97E-09
ENSG00000182572	NA	6.04	-4.02	0.79	-4.70	2.62E-06	8.37E-05
ENSG00000183856	IQGAP3	2060.03	-4.04	0.54	-6.95	3.55E-12	4.59E-10
ENSG00000140451	PIF1	311.81	-4.14	0.38	-10.11	4.81E-24	5.87E-21
ENSG00000163810	TGM4	9.18	-4.20	0.61	-6.38	1.75E-10	1.50E-08
ENSG00000126787	DLGAP5	1623.17	-4.24	0.52	-7.54	4.58E-14	8.59E-12
ENSG00000112984	KIF20A	1454.81	-4.40	0.51	-8.00	1.29E-15	3.48E-13
ENSG00000166535	A2ML1	19.04	-5.61	0.68	-7.76	8.30E-15	1.93E-12

Table S1: Related to Figure 2

Significantly changing genes between sTomato-p27K^{high} and sTomato-p27K^{low} cells of CRC29, HUB098 and TOR10 samples combined (FDR < 0.01, absolute fold change > 1.5). Depicted here: top 20 and bottom 20 genes.

Table S2: CRC29 results

Pathway	pvalue	padj	log2err	ES	NES	size
HALLMARK_TNFA_SIGNALING_VIA_NFKB	5.06E-31	2.53E-29	1.446	0.757	2.905	168
HALLMARK_EPITHELIAL_MESENCHYMAL_TRANSITION	9.64E-16	2.41E-14	1.018	0.707	2.592	117
HALLMARK_HYPOXIA	2.88E-10	3.60E-09	0.814	0.588	2.238	160
HALLMARK_UV_RESPONSE_DN	1.82E-08	1.82E-07	0.734	0.597	2.191	119
HALLMARK_MYOGENESIS	4.51E-07	3.76E-06	0.675	0.579	2.111	112
HALLMARK_HEDGEHOG_SIGNALING	7.71E-04	3.51E-03	0.477	0.682	1.902	27
HALLMARK_TGF_BETA_SIGNALING	4.76E-03	1.25E-02	0.407	0.562	1.777	48
HALLMARK_IL6_JAK_STAT3_SIGNALING	3.58E-03	1.01E-02	0.432	0.540	1.741	53
HALLMARK_INFLAMMATORY_RESPONSE	3.01E-03	9.41E-03	0.432	0.467	1.700	110
HALLMARK_KRAS_SIGNALING_UP	1.64E-03	6.31E-03	0.455	0.462	1.699	122
HALLMARK_P53_PATHWAY	2.93E-04	1.63E-03	0.498	0.439	1.690	175
HALLMARK_APOPTOSIS	1.82E-03	6.49E-03	0.455	0.456	1.688	126
HALLMARK_MITOTIC_SPINDLE	6.64E-04	3.32E-03	0.477	0.429	1.672	193
HALLMARK_COAGULATION	7.61E-03	1.90E-02	0.407	0.488	1.652	76
HALLMARK_KRAS_SIGNALING_DN	1.05E-02	2.51E-02	0.381	0.465	1.609	84
HALLMARK_COMPLEMENT	2.38E-03	7.93E-03	0.432	0.426	1.599	144
HALLMARK_IL2_STAT5_SIGNALING	3.65E-03	1.01E-02	0.432	0.422	1.594	148
HALLMARK_ESTROGEN_RESPONSE_EARLY	1.20E-02	2.74E-02	0.381	0.389	1.491	167
HALLMARK_FATTY_ACID_METABOLISM	2.76E-04	1.63E-03	0.498	-0.391	-1.675	130
HALLMARK_PEROXISOME	1.39E-03	5.78E-03	0.455	-0.427	-1.732	85
HALLMARK_MYC_TARGETS_V1	1.33E-06	9.52E-06	0.644	-0.417	-1.898	193
HALLMARK_OXIDATIVE_PHOSPHORYLATION	3.63E-15	6.04E-14	0.997	-0.562	-2.530	183

Table S2: HUB098 results

Pathway	pvalue	padj	log2err	ES	NES	size
HALLMARK_INTERFERON_ALPHA_RESPONSE	9.35E-14	1.56E-12	0.955	0.697	2.513	88
HALLMARK_HYPOXIA	3.18E-11	3.98E-10	0.851	0.571	2.259	157
HALLMARK_INTERFERON_GAMMA_RESPONSE	1.83E-10	1.83E-09	0.827	0.557	2.194	151
HALLMARK_TNFA_SIGNALING_VIA_NFKB	6.38E-09	5.32E-08	0.761	0.516	2.066	169
HALLMARK_P53_PATHWAY	4.79E-05	3.00E-04	0.557	0.432	1.740	172
HALLMARK_CHOLESTEROL_HOMEOSTASIS	3.89E-03	1.77E-02	0.432	0.477	1.618	62
HALLMARK_GLYCOLYSIS	1.33E-03	6.64E-03	0.455	0.380	1.521	168
HALLMARK_INFLAMMATORY_RESPONSE	1.30E-02	4.66E-02	0.381	0.388	1.437	103
HALLMARK_COMPLEMENT	7.64E-03	2.94E-02	0.407	-0.390	-1.484	136
HALLMARK_MITOTIC_SPINDLE	7.71E-04	4.28E-03	0.477	-0.392	-1.564	191
HALLMARK_ALLOGRAFT_REJECTION	6.53E-03	2.72E-02	0.407	-0.434	-1.578	96
HALLMARK_MYC_TARGETS_V1	1.32E-06	9.43E-06	0.644	-0.475	-1.897	193
HALLMARK_G2M_CHECKPOINT	4.20E-14	1.05E-12	0.965	-0.593	-2.359	189
HALLMARK_E2F_TARGETS	6.31E-18	3.15E-16	1.096	-0.632	-2.530	194

Table S2: Related to Figure 5

GSEA result of ranked gene expression between sTomato-p27K^{high} and sTomato-p27K^{low} cells in CRC29 and HUB098 with the MolSigDB Hallmark gene sets.

Table S3: CRC29 results

Pathway	pvalue	padj	log2err	ES	NES	size
HALLMARK_TNFA_SIGNALING_VIA_NFKB	3.78E-22	1.89E-20	1.221	0.725	2.587	167
HALLMARK_EPITHELIAL_MESENCHYMAL_TRANSITION	3.95E-15	9.88E-14	0.997	0.732	2.442	108
HALLMARK_HYPOXIA	1.17E-06	1.96E-05	0.644	0.552	1.939	154
HALLMARK_MYOGENESIS	4.16E-05	4.16E-04	0.557	0.555	1.852	106
HALLMARK_UV_RESPONSE_DN	6.27E-05	5.23E-04	0.538	0.534	1.800	116
HALLMARK_HEDGEHOG_SIGNALING	8.19E-03	3.72E-02	0.381	0.645	1.692	25
HALLMARK_APOPTOSIS	1.67E-03	1.05E-02	0.455	0.472	1.615	126
HALLMARK_P53_PATHWAY	3.89E-03	2.16E-02	0.432	0.430	1.540	175
HALLMARK_TGF_BETA_SIGNALING	1.29E-02	4.97E-02	0.381	0.517	1.527	49
HALLMARK_MITOTIC_SPINDLE	7.07E-03	3.53E-02	0.407	0.414	1.496	191
HALLMARK_COMPLEMENT	1.19E-02	4.94E-02	0.381	0.424	1.466	137
HALLMARK_OXIDATIVE_PHOSPHORYLATION	2.39E-05	2.99E-04	0.576	-0.417	-1.758	183
HALLMARK_PEROXISOME	5.51E-04	3.94E-03	0.477	-0.473	-1.781	84

Table S3: HUB098 results

Pathway	pvalue	padj	log2err	ES	NES	size
HALLMARK_INTERFERON_ALPHA_RESPONSE	3.54E-08	3.47E-07	0.720	0.611	2.236	89
HALLMARK_INTERFERON_GAMMA_RESPONSE	9.49E-09	1.55E-07	0.748	0.544	2.153	152
HALLMARK_TNFA_SIGNALING_VIA_NFKB	1.27E-08	1.56E-07	0.748	0.518	2.072	167
HALLMARK_HYPOXIA	2.28E-07	1.60E-06	0.690	0.507	2.020	156
HALLMARK_P53_PATHWAY	9.01E-04	4.91E-03	0.477	0.395	1.585	173
HALLMARK_APICAL_JUNCTION	6.85E-03	3.36E-02	0.407	-0.402	-1.507	121
HALLMARK_MITOTIC_SPINDLE	1.86E-05	1.14E-04	0.576	-0.440	-1.758	189
HALLMARK_MYC_TARGETS_V1	1.66E-07	1.36E-06	0.690	-0.481	-1.919	193
HALLMARK_G2M_CHECKPOINT	5.69E-17	1.39E-15	1.057	-0.630	-2.508	188
HALLMARK_E2F_TARGETS	7.54E-23	3.69E-21	1.238	-0.664	-2.651	194

Table S3: Related to Figure 6

GSEA result of ranked gene expression between macro- and micrometastatic CRC29 and HUB098 cells with the MolSigDB Hallmark gene sets.

Table S4: CRC29 results

Pathway	pvalue	padj	log2err	ES	NES	size
HALLMARK_TNFA_SIGNALING_VIA_NFKB	3.78E-22	1.89E-20	1.221	0.725	2.587	167
HALLMARK_EPITHELIAL_MESENCHYMAL_TRANSITION	3.95E-15	9.88E-14	0.997	0.732	2.442	108
HALLMARK_HYPOXIA	1.17E-06	1.96E-05	0.644	0.552	1.939	154
HALLMARK_MYOGENESIS	4.16E-05	4.16E-04	0.557	0.555	1.852	106
HALLMARK_UV_RESPONSE_DN	6.27E-05	5.23E-04	0.538	0.534	1.800	116
HALLMARK_HEDGEHOG_SIGNALING	8.19E-03	3.72E-02	0.381	0.645	1.692	25
HALLMARK_APOPTOSIS	1.67E-03	1.05E-02	0.455	0.472	1.615	126
HALLMARK_P53_PATHWAY	3.89E-03	2.16E-02	0.432	0.430	1.540	175
HALLMARK_TGF_BETA_SIGNALING	1.29E-02	4.97E-02	0.381	0.517	1.527	49
HALLMARK_MITOTIC_SPINDLE	7.07E-03	3.53E-02	0.407	0.414	1.496	191
HALLMARK_COMPLEMENT	1.19E-02	4.94E-02	0.381	0.424	1.466	137
HALLMARK_OXIDATIVE_PHOSPHORYLATION	2.39E-05	2.99E-04	0.576	-0.417	-1.758	183
HALLMARK_PEROXISOME	5.51E-04	3.94E-03	0.477	-0.473	-1.781	84

Table S4: HUB098 results

Pathway	pvalue	padj	log2err	ES	NES	size
HALLMARK_INTERFERON_ALPHA_RESPONSE	3.54E-08	3.47E-07	0.720	0.611	2.236	89
HALLMARK_INTERFERON_GAMMA_RESPONSE	9.49E-09	1.55E-07	0.748	0.544	2.153	152
HALLMARK_TNFA_SIGNALING_VIA_NFKB	1.27E-08	1.56E-07	0.748	0.518	2.072	167
HALLMARK_HYPOXIA	2.28E-07	1.60E-06	0.690	0.507	2.020	156
HALLMARK_P53_PATHWAY	9.01E-04	4.91E-03	0.477	0.395	1.585	173
HALLMARK_APICAL_JUNCTION	6.85E-03	3.36E-02	0.407	-0.402	-1.507	121
HALLMARK_MITOTIC_SPINDLE	1.86E-05	1.14E-04	0.576	-0.440	-1.758	189
HALLMARK_MYC_TARGETS_V1	1.66E-07	1.36E-06	0.690	-0.481	-1.919	193
HALLMARK_G2M_CHECKPOINT	5.69E-17	1.39E-15	1.057	-0.630	-2.508	188
HALLMARK_E2F_TARGETS	7.54E-23	3.69E-21	1.238	-0.664	-2.651	194

Table S4: Related to Figure 6

GSEA result of ranked gene expression between sTomato-p27K^{high} macro- and micrometastatic CRC29 and HUB098 cells with the MolSigDB Hallmark gene sets.

Table S5: CRC29 results

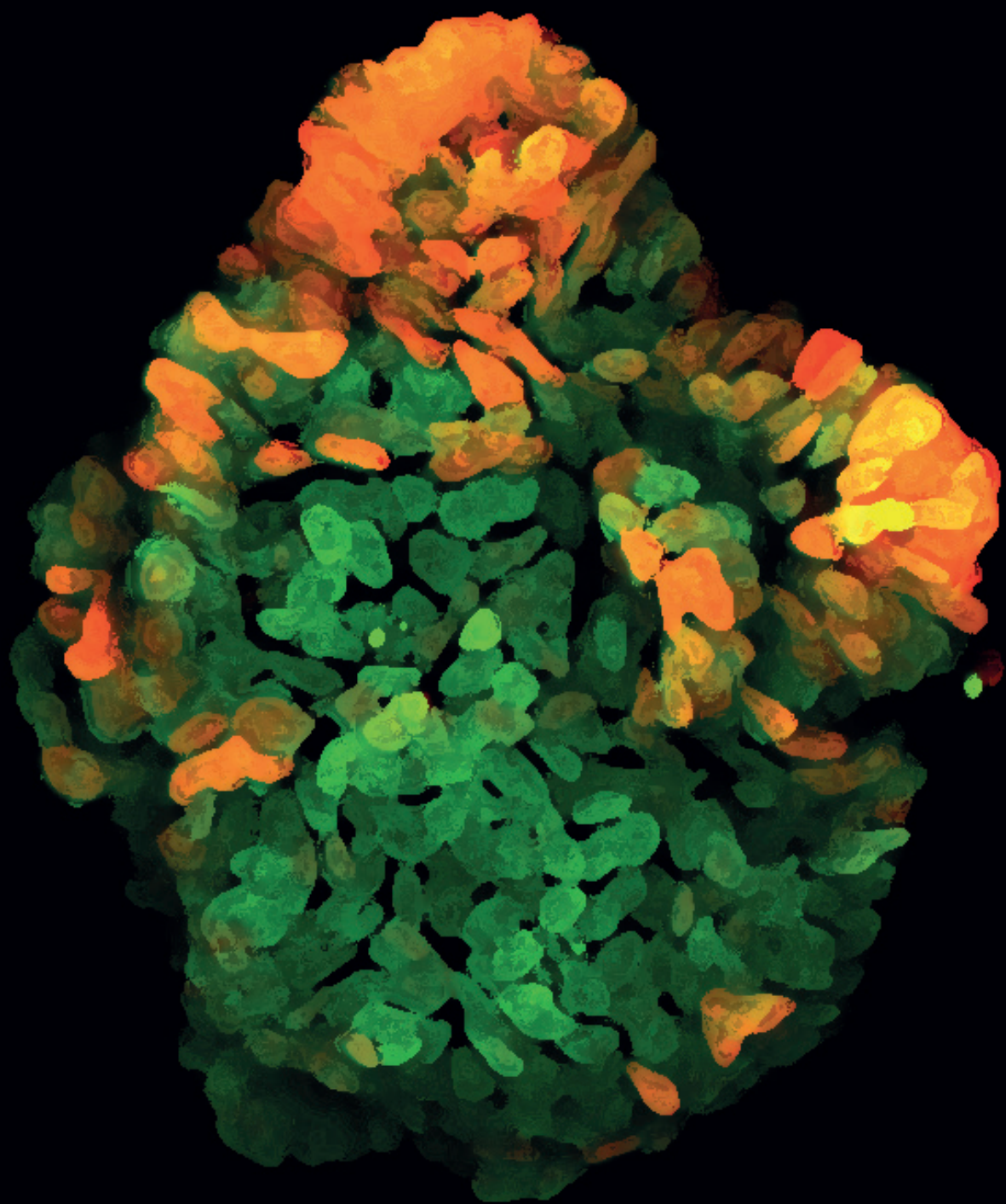
Pathway	pvalue	padj	log2err	ES	NES	size
HALLMARK_TNFA_SIGNALING_VIA_NFKB	5.04E-27	2.52E-25	1.350	0.704	2.935	167
HALLMARK_EPITHELIAL_MESENCHYMAL_TRANSITION	9.54E-11	1.59E-09	0.839	0.594	2.336	114
HALLMARK_UV_RESPONSE_DN	9.41E-10	1.18E-08	0.788	0.586	2.315	118
HALLMARK_HYPOXIA	2.38E-09	2.38E-08	0.775	0.535	2.215	158
HALLMARK_MYOGENESIS	4.23E-06	3.02E-05	0.611	0.513	2.001	110
HALLMARK_KRAS_SIGNALING_UP	7.54E-05	4.71E-04	0.538	0.464	1.845	120
HALLMARK_TGF_BETA_SIGNALING	1.44E-03	5.98E-03	0.455	0.542	1.808	48
HALLMARK_HEDGEHOG_SIGNALING	3.02E-03	1.16E-02	0.432	0.599	1.778	27
HALLMARK_INFLAMMATORY_RESPONSE	7.12E-04	3.24E-03	0.477	0.439	1.702	107
HALLMARK_MITOTIC_SPINDLE	2.84E-04	1.58E-03	0.498	0.391	1.662	192
HALLMARK_APICAL_SURFACE	1.23E-02	3.43E-02	0.381	0.553	1.640	27
HALLMARK_P53_PATHWAY	6.29E-04	3.14E-03	0.477	0.388	1.623	174
HALLMARK_KRAS_SIGNALING_DN	6.55E-03	2.07E-02	0.407	0.438	1.619	78
HALLMARK_COAGULATION	6.62E-03	2.07E-02	0.407	0.439	1.595	73
HALLMARK_COMPLEMENT	3.62E-03	1.29E-02	0.432	0.377	1.539	141
HALLMARK_APOPTOSIS	1.40E-02	3.67E-02	0.381	0.378	1.518	127
HALLMARK_IL2_STAT5_SIGNALING	7.11E-03	2.09E-02	0.407	0.360	1.494	148
HALLMARK_ESTROGEN_RESPONSE_EARLY	1.86E-02	4.43E-02	0.352	0.334	1.390	163
HALLMARK_FATTY_ACID_METABOLISM	1.60E-02	3.99E-02	0.352	-0.353	-1.485	126
HALLMARK_MYC_TARGETS_V1	7.43E-08	6.19E-07	0.705	-0.471	-2.097	193
HALLMARK_OXIDATIVE_PHOSPHORYLATION	1.48E-13	3.69E-12	0.944	-0.556	-2.458	184

Table S5: HUB098 results

Pathway	pvalue	padj	log2err	ES	NES	size
HALLMARK_INTERFERON_ALPHA_RESPONSE	2.09E-06	5.24E-05	0.627	0.627	1.987	87
HALLMARK_TNFA_SIGNALING_VIA_NFKB	9.20E-04	5.95E-03	0.477	0.473	1.628	168
HALLMARK_HYPOXIA	1.27E-03	7.07E-03	0.455	0.472	1.613	159
HALLMARK_INTERFERON_GAMMA_RESPONSE	2.91E-03	1.46E-02	0.432	0.450	1.530	154
HALLMARK_XENOBIOTIC_METABOLISM	5.91E-03	2.69E-02	0.407	-0.401	-1.526	128
HALLMARK_MYC_TARGETS_V1	9.51E-04	5.95E-03	0.477	-0.388	-1.530	193
HALLMARK_BILE_ACID_METABOLISM	1.12E-02	4.67E-02	0.381	-0.444	-1.537	75
HALLMARK_G2M_CHECKPOINT	6.96E-05	6.96E-04	0.538	-0.431	-1.712	189
HALLMARK_ALLOGRAFT_REJECTION	8.42E-04	5.95E-03	0.477	-0.475	-1.747	100
HALLMARK_COAGULATION	3.08E-05	3.85E-04	0.557	-0.556	-1.952	80
HALLMARK_COMPLEMENT	3.44E-06	5.74E-05	0.627	-0.506	-1.953	139
HALLMARK_E2F_TARGETS	1.08E-08	5.39E-07	0.748	-0.517	-2.041	194

Table S5: Related to Figure 6

GSEA result of ranked gene expression between sTomato-p27K^{low} macro- and micrometastatic CRC29 and HUB098 cells with the MolSigDB Hallmark gene sets.



CHAPTER

6

Dissecting the Role of Hedgehog Signalling in Advanced Colorectal Cancer

Maria C. Heinz^{1,2}, Ingrid Verlaan-Klink^{1,2}, Hugo J. G. Snippert^{1,2,#}

¹ Center for Molecular Medicine, University Medical Center
Utrecht, Utrecht, the Netherlands.

² Oncode Institute, the Netherlands.

#: Lead Contact.

In preparation.

SUMMARY

In the adult intestine, Hedgehog ligands are produced in the epithelium and signal toward the mesenchyme to promote enterocyte differentiation and to restrict the immune response. Yet, the role of Hedgehog signalling in colorectal cancer (CRC) is more elusive. Conflicting data have suggested both tumour-suppressive and tumour-promoting roles. Furthermore, the debate on the exact nature of Hedgehog signalling is still ongoing, questioning whether Hedgehog signalling is solely paracrine or possibly also autocrine via a non-canonical Hedgehog pathway.

To address the role of Hedgehog signalling and its nature in advanced CRC *in vitro* and *in vivo*, we have used engineered and patient-derived CRC organoids to recapitulate the heterogeneity of the disease. We show that *in vitro*, Hedgehog ligands are produced by all cells but most strongly by non-stem-like cells. Pharmacological pathway perturbations using agonists and antagonists did not reveal any signs of autocrine signalling in purely epithelial CRC organoids. To study Hedgehog signalling using genetic manipulations, we have generated a Hedgehog ligand knock-out library through CRISPR/Cas9 technology. Experiments with genetically deleted Hedgehog ligands confirmed the previous drug-based observations. Moreover, xenotransplantation studies suggested similar metastasis formation capacity in the presence or absence of Hedgehog ligands, suggesting that paracrine Hedgehog signalling does not affect the initial stages of CRC metastatic growth.

INTRODUCTION

The Hedgehog signalling molecules are classically known for their key roles as morphogens during embryogenesis, patterning developing tissues and cell fates as a function of their concentration. More recent studies in mice have now also demonstrated their significance for tissue homeostasis during adulthood. In the intestine, Hedgehog ligands are produced by different epithelial cell types that are distributed along the crypt-villus axis. While the crypt compartments comprise *Lgr5*⁺ intestinal stem cells, epithelial niche cells, and highly proliferative transit-amplifying cells (located towards the isthmus), the intestinal villi are made up of functionally specialized, post-mitotic cells. Of the three Hedgehog ligands, Sonic Hedgehog (SHH) is expressed in the epithelial crypt regions (1,2), while Indian Hedgehog (IHH) expression spreads over the entire length of the villi (3,4). The third Hedgehog ligand, Desert Hedgehog (DHH), is very lowly expressed and no role is yet described for adult intestinal biology.

While the effects of the different Hedgehog ligands are understood to varying levels, they have in common that they all signal towards the mesenchyme in a paracrine manner (4,5). The main responsive cell types are α -smooth muscle actin-positive (α -SMA⁺) myofibroblasts (4,6). The secreted Hedgehog ligands bind the transmembrane protein Patched (*PTCH1-2*) which otherwise exerts an inhibitory function towards the receptor Smoothed (*SMO*) (7). Active SMO results in downstream signalling with activation of the GLI family of transcription factors (*GLI1-3*) (7). Through this cascade, IHH regulates the number of α -SMA⁺ cells (3). Additionally, Hedgehog signalling leads to an increase in BMP expression in the stroma, thereby instructing the formation of a BMP gradient along the crypt-villus axis. Thus, Hedgehog signalling indirectly supports enterocyte differentiation through BMP signalling, while restricting proliferation and WNT levels (4,8).

The role of Hedgehog signalling in colorectal cancer (CRC) and its mode of action is more controversial (9). Analyses of paired normal and malignant samples of the same patient frequently demonstrate upregulation of SHH and IHH in the diseased setting (10–14). Along these lines, some studies have suggested different Hedgehog pathway players to serve as negative prognostic factors for CRC survival (SHH, *PTCH1*, *GLI*, *SMO* (12,15)), however other studies failed to validate these findings (16,17). In addition, multiple studies report Hedgehog signalling to exert tumour growth-promoting effects in CRC (2,10,14,18), for instance through *Ihh*-mediated signalling in mice heterozygous for the tumour suppressor gene *Apc* (14). However, these findings seem to be context-dependent as other studies demonstrated tumour-suppressive roles for Hedgehog

signalling in CRC, either directly or indirectly through modulation of Wnt targets and ErbB family ligand expression (19,20). Strikingly, even on the cellular level there is an ongoing debate about the signalling mode in CRC. As expected from Hedgehog signalling in tissue development, many recent studies point at paracrine signalling from CRC cells towards the mesenchyme (14,18,19), however, some studies have reported autocrine, non-canonical Hedgehog signalling leading to the activation of GLIs (21) in CRC.

While enhanced expression of SHH and IHH in CRCs seems to be a widely accepted notion, few key questions remain unaddressed. First, are there differential effects between the individual Hedgehog ligands on human CRC growth and metastasis formation? Second, is Hedgehog signalling in advanced CRC solely paracrine towards the mesenchyme?

To study these questions with a reductionist approach, we have used patient-derived and CRISPR/Cas9-engineered CRC organoids which are known to reflect the epithelial side of highly advanced CRC biology, including accurate response towards anti-cancer therapies (22,23). We have recently reported that cellular and transcriptomic changes occurring during organoid formation, phenocopy the processes during early liver metastasis formation. Here, we have now assessed the temporal expression pattern of Hedgehog ligands and downstream pathway activation during organoid formation, while perturbing their function either pharmacologically or genetically. In line with classic literature on Hedgehog signalling during tissue development, we find no evidence for autocrine signalling in human CRC organoids. Second, we observed no significant effect on CRC liver metastasis formation *in vivo* in samples that are deficient for HH ligands.

RESULTS

CRC organoid outgrowth mimics epithelial characteristics during metastasis outgrowth

We have previously demonstrated that different cell types are formed in micrometastatic lesions (24) and likewise that the transcriptome of developing metastases changes from a developmental state towards expression patterns resembling more mature intestinal stem and non-stem cells (25). In parallel, we could show that a similar level of epithelial self-organisation takes place during the outgrowth of CRC organoids: Cellular diversity is established at the multicellular stage through so-called *epithelial self-organisation*, as assessed by the fluorescent stem cell reporter (STAR) that reflect transcriptional activity of the stem cell regulator ASCL2 (25,26) (Chapter 4) (Fig 1A-B): In short, single STAR⁺ (or STAR⁻) cells first display high YAP activity for 1-2 days, while subsequently growing into multicellular, phenotypically homogeneous structures. These organoids are highly proliferative when the

first cell fate changes can be observed about 5 days after plating. Subsequently, organoids continue to grow with both STAR⁺ and STAR⁻ compartments increasing over time, to finally display a stem cell-driven cellular hierarchy with diverse mature cell types at Day 12 (Fig 1A) (27,28). Conversely when epithelial self-organisation does not take place and no cell fate changes are observed, organoids become growth restricted (Fig 1B).

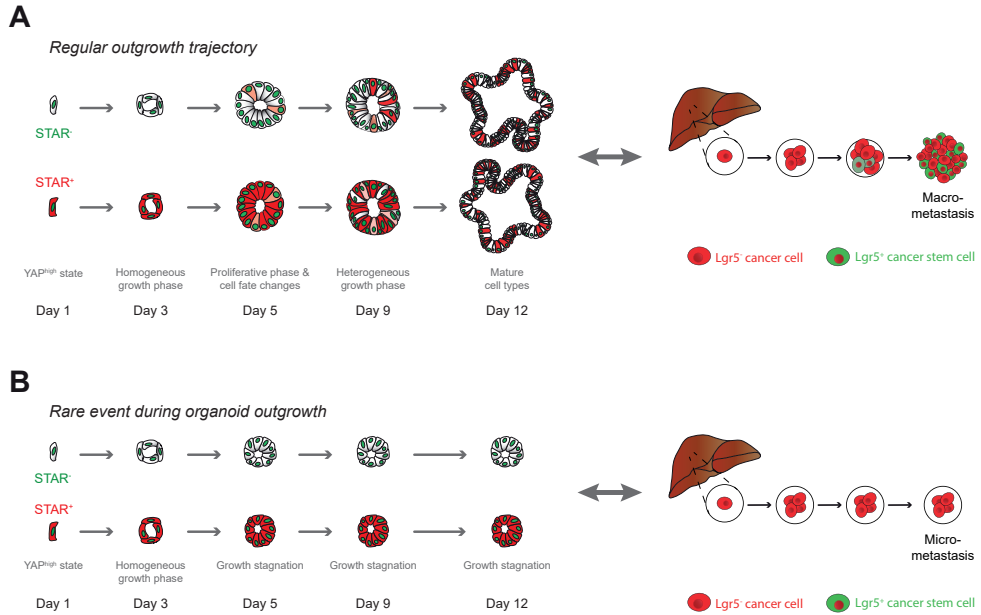
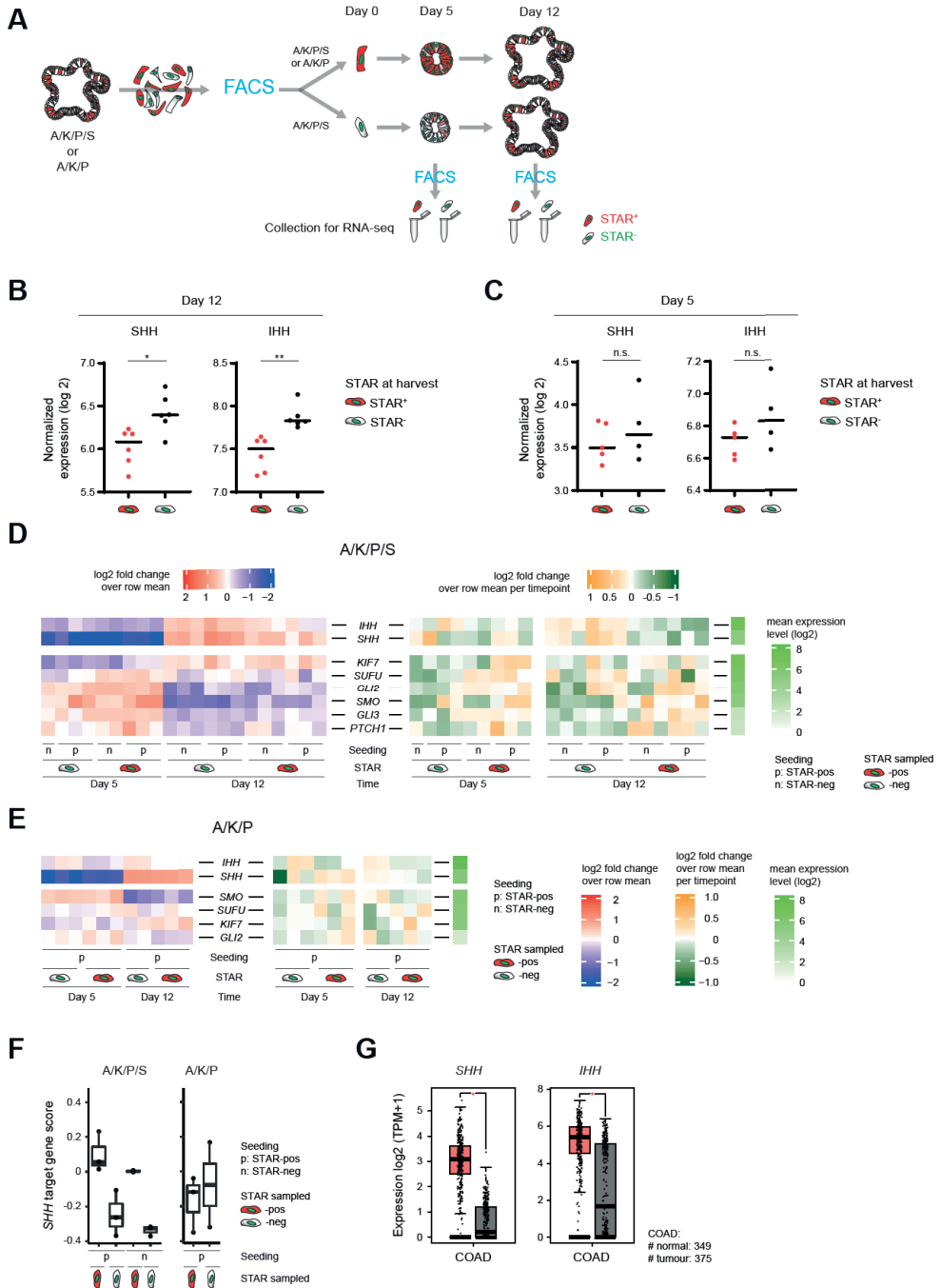


Figure 1: CRC organoid outgrowth mimics epithelial characteristics during metastasis outgrowth

CRC organoid outgrowth mimics the early steps of metastatic colonisation in terms of cellular composition and states. While there is increasing evidence that most metastases are seeded by cancer non-stem cells, *in vitro* both STAR⁻ and STAR⁺ cells can form organoids. In all cases, single cells first display high YAP activity and initially proliferate into a homogeneous, multicellular structure. Only then, cellular heterogeneity arises in the case of successful outgrowth with maturation of cell types over time **A**. Conversely, persistent YAP activity correlates with a homogeneous composition and growth stagnation **B**. This overview is based on data previously generated (25)(Chapter 4).

Hedgehog signalling is upregulated in advanced CRC

The observation that homogeneous STAR⁺ organoids are compromised in growth (25) made us question whether in advanced CRC, non-stem cells still have a supportive role towards the stem cells, in analogy to the role of niche-resident Paneth cells in the healthy intestine. To address this question, we analysed transcriptomic data of heterogeneous, 12-day-old A/K/P/S organoids (Fig 2A). Our interest was sparked by the Hedgehog ligands *SHH* and *IHH* as they were more strongly expressed by STAR⁻ than by STAR⁺ cells (Fig 2B). Moreover, their overall expression level and difference in expression pattern became more pronounced as organoids aged (Fig 2B-C, Fig S1A).



◀Figure 2: Hedgehog ligand expression is upregulated in advanced CRC

A. Schematic overview of the experimental setup used to generate bulk RNA-seq data (Chapter 4). STAR⁺ and STAR⁻ A/K/P/S and A/K/P CRC cells were collected by FACS and plated as single cells. After 5 and 12 days, organoids were dissociated to single cells and STAR⁺ and STAR⁻ cells were collected in technical duplicates or triplicates for both bulk RNA-seq (15-20 k cells each). **B-C.** Normalized expression data of *SHH* and *IHH* in STAR⁺ (red) and STAR⁻ (black) cells of A/K/P/S organoids, analysed after (B) 12 days and (C) 5 days of outgrowth. Two-tailed Student's t-test was used to assess statistical significance between the STAR populations in these plots. Gene expression differences between STAR populations on Day 12 are also significantly altered after correcting for multiple testing during the bulk RNA-seq analysis. **D-E.** (D) A/K/P/S and (E) A/K/P organoid expression data of selected Hedgehog-related genes as log₂ fold change over row mean of (left) all samples and (right) all samples per time points. STAR identity at the time of seeding (Day 0) is indicated as STAR⁺ (p) and STAR⁻ (n). STAR levels at the time of harvest (Day 5 or Day 12) are denoted as STAR-pos and STAR-neg. Additionally, the mean normalized log₂ expression level of each gene is plotted next to the Heatmap (green). **F.** Expression value of *SHH* target gene score derived from publically available data set (30), for STAR⁺ and STAR⁻ cells of A/K/P/S and A/K/P organoids. **G.** Expression data of the Hedgehog ligands *SHH* and *IHH* in patient samples registered in TCGA data base. The colon adenocarcinoma (COAD) cohort including the GTEx colon set was analysed. Expression levels are indicated as log₂ of transcripts per million (TPM) +1. Statistically significant changes in gene expression are indicated by asterisks.

Conversely, core components of the Hedgehog signalling pathway, being *PTCH1*, *SMO*, and *GLI2/3*, were enriched at Day 5 (Fig 2D). Their temporal expression pattern is not entirely unexpected but rather in line with Hedgehog signalling being a developmental pathway, given that young organoids were previously described to reside in an immature state (25,29). Despite the anti-correlative expression pattern of *PTCH1*, *SMO*, and *GLI2/3* versus the Hedgehog ligands, the downstream pathway components were present at detectable levels at Day 12. Even more, unlike the STAR⁻ cell-enriched ligands, they showed enhanced expression in STAR⁺ cells (Fig 2D). As this observation would fit to the idea of paracrine cross-talk between epithelial cell types, we decided to expand the range of Hedgehog target genes in this analysis. We computed a Hedgehog target gene expression score based on publically available data (30) and found that STAR⁺ cells in 12-day-old organoids have a stronger signature of this pathway score than corresponding STAR⁻ cells (Fig 2F), indicating that STAR⁺ cells might conduct (enhanced) Hedgehog signalling.

In a next step, we checked if the same expression pattern can be detected in A/K/P organoids. We could confirm both the upregulation of the Hedgehog ligands over time and enhanced expression in STAR⁻ cells at Day 12 (Fig 2E, Fig S1B). While some Hedgehog pathway components like *SUFU* and *KIF7* were enriched in STAR⁺ cells (Fig 2E), the unbiased Hedgehog target score was comparable between STAR populations (Fig 2F).

As A/K/P/S and A/K/P organoids are CRISPR-engineered cancers, we next assessed the temporal expression pattern of Hedgehog ligands in three different patient-derived CRC organoids. Upregulation over time could be confirmed for the two CRC lines P9T and P19Tb (Fig S1B). Just for line P16T, this pattern could not be observed (Fig S1B).

Nonetheless, when comparing the expression levels of Hedgehog ligands in patient biopsies of normal and colon adenocarcinoma samples registered at TCGA database, we found a statistically significant upregulation of *SHH* and *IHH* in the malignant samples (Fig 2G), arguing for the need to evaluate their function in more depth. *DHH*, on the other hand, demonstrated overall limited expression levels in both populations (Fig S1C).

Autocrine Hedgehog signalling is not detectable in A/K/P/S CRC organoids

Previous observations have indicated that there is autocrine Hedgehog signalling in CRC. However, as not all classic pathway components seemed to be involved, it was declared to be non-canonical (21). To test the necessity for and nature of Hedgehog signalling in CRC, we assessed the response of purely epithelial CRC organoids to pharmacological perturbations of the Hedgehog signalling cascade.

Having determined suitable drug doses in Hedgehog-responsive systems through qRT-PCR (Fig S2), we used the following Hedgehog activating drugs on CRC organoids: recombinant SHH or IHH (recSHH / recIHH) or a small molecule agonist of SMO (SAG). However, we did not notice any convincing effect on the expression of known Hedgehog targets (Fig 3A). For instance, only the context dependent Hedgehog targets *HES1* and *VEGFA* were upregulated (fold change (FC) > 1.5) upon recSHH administration, while well-known Hedgehog targets such as *GLI1*, *GLI2*, and *PTCH2* were not reliably picked up. Accordingly, no changes in CRC organoid morphology were observed, even 96 h after addition of the drugs (Fig 3B-C). Likewise, when assessing functional effects by analysing organoid outgrowth behaviour through CellTiter-Glo, supplementation of the culture media with either recSHH or recIHH did not result in any measurable differences (Fig 3D, Fig S3A). Only the combined treatment with recSHH + recIHH led to a statistically significant, yet small increase in biomass. These results could not be confirmed upon pathway activation with SAG (Fig 3D).

Thus, in our experiments, we did not detect any effect upon extra stimulation of the Hedgehog pathway. As endogenous Hedgehog levels could potentially be sufficient to drive maximum pathway activity, we exploited multiple drugs to affect Hedgehog signalling in a negative manner, either by blocking the activating receptor SMO (Vismodegib), the downstream transcription factors GLI1/2 (GANT61), or by inhibiting the Hedgehog acetyltransferase HHAT (RU-SKI43) which is required for the posttranslational modification of Hedgehog ligands prior to their secretion (31).

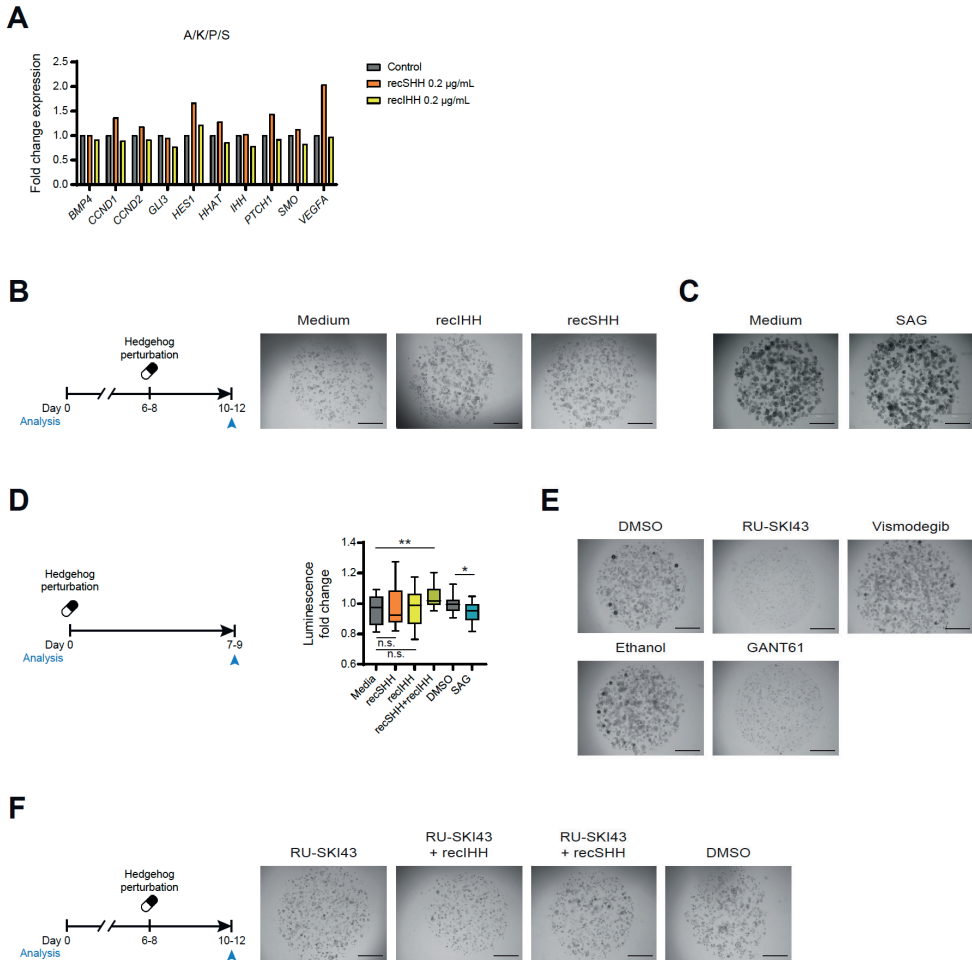


Figure 3: Autocrine Hedgehog signalling is not detectable in A/K/P/S CRC organoids

A. Gene expression of putative Hedgehog target genes in A/K/P/S CRC organoids upon 48 h of Hedgehog activation through drugs as measured by qPCR. Expression values were normalized to housekeeping genes and are represented as fold change to their respective controls. The following genes were not reliably picked up (cycle number > 33): *GLI1*, *GLI2*, *PTCH2*. **B-C.** A/K/P/S organoids grown for (B) 6 days and (C) 7 days from single cells were treated with (B) 0.2 µg/mL recSHH or recIHH and (C) 1 µM SAG or DMSO for 96 h prior to morphological inspection at the microscope. Scale bars, 100 µm. **D.** A/K/P/S organoids were grown from single cells for 7 days in the presence of 0.2 µg/mL recSHH, recIHH or both, or 1 µM SAG. Then, CellTiter-Glo was used to assess the viable biomass through luminescent imaging. Data is represented after normalization to respective control condition. Two-tailed Student's t-test was used to assess significance levels. **E.** Example pictures of organoids grown from single cells for 7-days in the presence of 10 µM RU-SKI43, 10 µM Vismodegib, 10 µM GANT61 or the respective controls (DMSO and ethanol). Scale bars, 100 µm. **F.** 6-day-old A/K/P/S organoids were treated with 10 µM RU-SKI43 in the presence or absence of 2 µg/mL recSHH or recIHH. Pictures indicate organoid formation capacity in the given conditions. Scale bars, 100 µm.

A/K/P/S organoid morphology was unchanged 96 h after addition of the drugs (Fig S3B). However, long-term incubation with the drugs GANT-61 and RU-SKI43 was highly toxic to CRC organoids when grown from single cells (Fig 3E, Fig S3C). To test if Hedgehog pathway activity is essential during the outgrowth of A/K/P/S organoids or if we are dealing with off-target toxicity, we attempted to rescue the phenotype of HHAT inhibition through supplementation with recombinant Hedgehogs. Again, similar levels of toxicity were observed even in the presence of recSHH or reclHH and at a higher concentration than strictly necessary (Fig 3F). Taken together, pharmacological perturbation of Hedgehog signalling has not revealed any convincing evidence for autocrine, CRC-intrinsic signalling in our model system.

Generation of a Hedgehog ligand knockout library

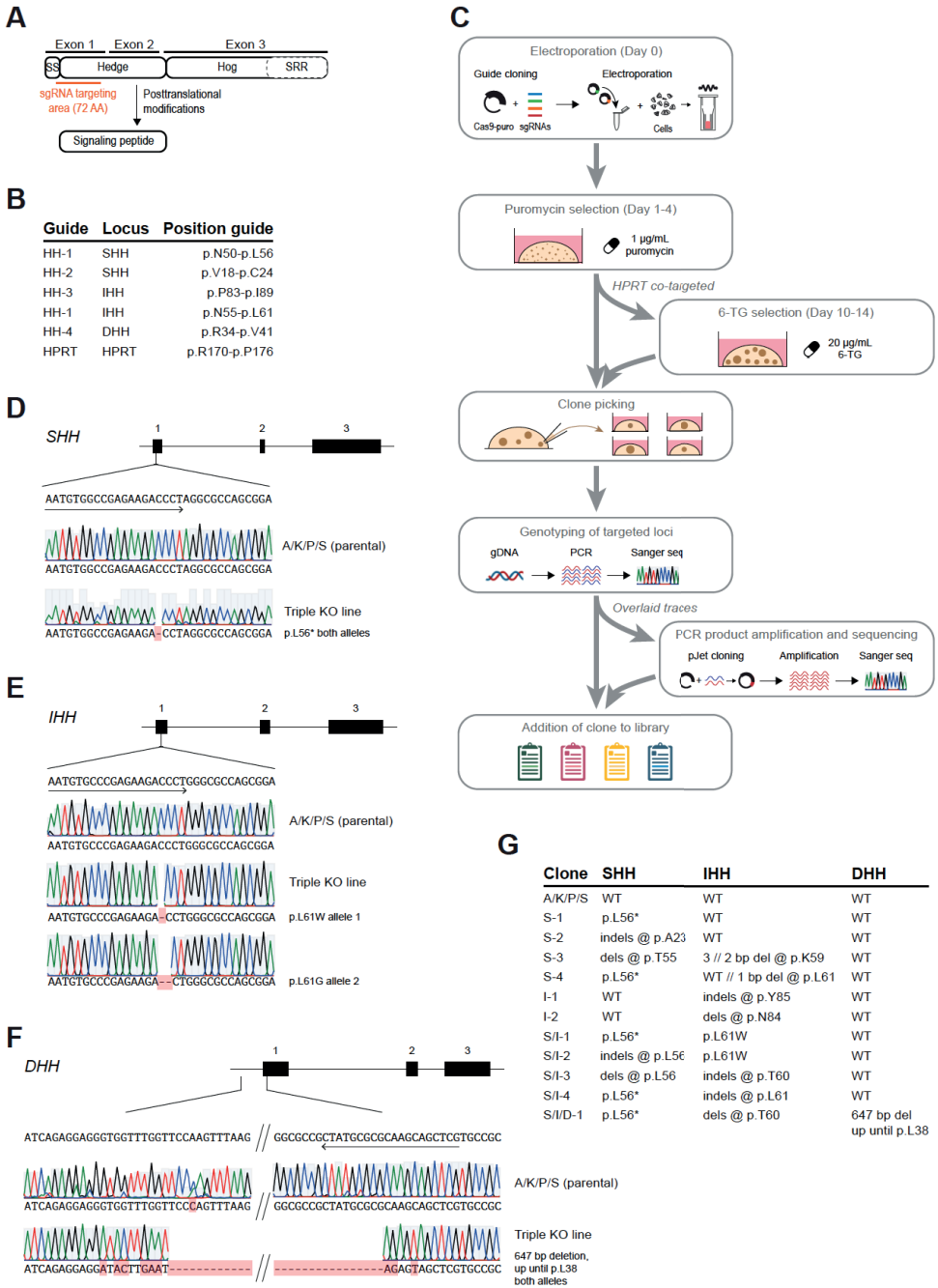
To circumvent the problem of possible undesired drug-related toxicities, we decided to generate a series CRC organoid knock-out (KO) lines in which we deplete either individual Hedgehog ligands or combinations thereof through CRISPR-Cas9 technology.

Hedgehog proteins undergo extensive posttranslational modifications. While the hog domain at the C-terminus is important for initial autocleavage reactions, additional lipid modifications are conducted while being in the endoplasmic reticulum for which the signal sequence (SS) at the N-terminus is essential (32,33). The resulting dually lipidated, active signalling molecule is encoded by exons 1-2. We thus decided to target the first exons of *SHH*, *IHH*, and *DHH* with wild type Cas9 to disrupt gene function by generating double-strand breaks and subsequently select for defective repair products with stochastic base pair (bp) insertions and/or deletions (small indels) (Fig 4A). For each genetic locus, one to two guides were designed and selected based on their predicted on-target efficiency and unlikelihood for off-targets beyond the Hedgehog ligands using benchling (Fig 4B, Table S2). Electroporated A/K/P/S organoids were selected for their uptake of the targeting vector (through puromycin resistance), and subsequently hand-picked and genotyped through targeted PCR and sequencing (Fig 4C). If multiple traces were overlaid, the corresponding PCR amplicons of that locus were cloned into pJet vectors, amplified in DH5 α competent bacteria, and multiple mono-allelic DNA strands were sequenced again (Fig 4C).

Having used combinations of different guides, the first round of electroporation yielded multiple double KO clones for *IHH* and *SHH* as well as a single KO clone for *SHH* (clone S-1). In a subsequent step, a triple KO clone was generated by targeting the *IHH* and *DHH* loci in clone S-1. Additionally, single *IHH* KO clones were derived from the parental A/K/P/S line by co-targeting the *HPRT* locus. This strategy allows to select for CRISPR/

Cas9 activity rather than for targeting vector uptake, as the drug 6-TG will kill off cells with intact (non-targeted) *HPRT* (34) (Fig 4C).

Ultimately, we obtained a Hedgehog KO clone library containing multiple single KO clones for *SHH* (S) and *IHH* (I), double KO clones for *SHH* and *IHH* (S/I), and a triple KO clone for all Hedgehog proteins (S/I/D) (Fig 4G, Table S1). The triple KO clone contains a premature stop in *SHH* through a 1 bp deletion (Fig 4D), 1 and 2 bp deletions in *IHH* (Fig 4E), and a 647 bp deletion in the *DHH* locus, resulting in a loss of the coding sequence up until AA 38 (Fig 4F). The sequencing results of the other clones prior to and, if applicable, after pJet cloning are presented in Fig S4A-C and Fig S5A-B, respectively.



◀Figure 4: Generation of a Hedgehog ligand knockout library

A. Schematic make-up of Hedgehog proteins: Coding sequence is spanned over three exons. Posttranslational modifications involving the Hog domain and the signalling sequence (SS) are required to turn the protein into a peptide capable of inducing signalling. Targeting region of different single guide RNAs (sgRNAs) is indicated in orange. **B.** Overview of the sgRNAs used to target the different Hedgehog ligands and for *HPRT*. **C.** Workflow of Hedgehog KO clone generation through CRISPR/Cas9 targeting. sgRNAs were cloned into a Cas9 vector co-expressing puromycin resistance cassette. Organoids were electroporated together with various guide combinations to generate indels. Selection was performed using 1 µg/mL puromycin for 3 days and, in case of co-targeting *HPRT*, with additional 6-TG for about 4 days. Surviving clones were hand-picked and expanded for genotyping by targeted PCR and Sanger sequencing. In case of overlaying traces, PCR products were cloned into a pJet expression vector and PCR molecules were amplified upon transformation in DH5α competent bacteria before sequencing again. Clones with confirmed indels were added to the library. **D-F.** Sequencing results Hedgehog loci of both the parental line and the triple KO clone. sgRNA and its orientation is indicated by an arrow. (D) SHH: Triple KO clone demonstrates 1 bp deletion resulting in a premature STOP at p.L56*. (E) IHH: Triple KO clone demonstrates 1 bp and 2 bp deletion resulting in a frame-shifts and p.L61W and p.L61G, respectively. (F) DHH: Triple KO clone demonstrates 647 bp deletion ranging from the intron into the first exon up until codon 38. **G.** Overview of the Hedgehog KO library with clone name and summary of genotype for each of the three Hedgehog ligands: *SHH*, *IHH*, and *DHH*.

Triple KO organoids are not responsive to recombinant Hedgehogs *in vitro*

Having these genetic knock-out models in hand, we next made use of them to reinvestigate previous pharmacological findings. We reasoned that if the small but significant outgrowth advantage of *A/K/P/S* organoids when cultured with recSHH + recIHH (Fig 3D) is due to genuine autocrine Hedgehog signalling, we should be able to rescue potential growth delay in KO clones. We therefore repeated the assay using the triple KO clone and analysed growth after 7 days through CellTiter-Glo. In contrast to the previous observation, we did not see any growth advantage upon addition of recombinant Hedgehog ligands or through treatment with SAG (Fig S5C). Nor did the organoid show any morphological change upon drug treatment (Fig S5C). When comparing the outgrowth behaviour of the triple KO clone to the parental line side-by-side through CellTiter-Glo, we could observe a significant increase in growth in the triple KO clone (Fig S5D). However, as supplementation with recombinant Hedgehog proteins did not impede outgrowth of the triple KO line (Fig S5C), we suspect that this effect is rather a technical artefact due to inequality in plating densities or clonal differences.

Thus, also when using a genetic approach, we could not find consistent indications for autocrine Hedgehog signalling in CRC organoids.

Mouse weight was measured during the course of the experiment (Fig S6A), as a drop may indicate progressed disease. Yet, the results between both lines did not indicate any major differences between the lines (Fig S6B). In parallel, tumour load was measured biweekly using magnetic resonance imaging (MRI). This revealed that metastasis formed in all mice and were generally detectable after 5 weeks in both conditions (Fig 5B). The number of metastasis formed across mice was comparable between the parental A/K/P/S and the triple KO line (Fig 5C). In addition, when investigating the size of the individual lesions, we observed no statistically significant difference (p-value = 0.052, Fig 5D). While a trend towards bigger metastases in the triple KO line was observed, experimental and logistic complications in our set-up have resulted in limited mouse numbers that hamper us from drawing firm conclusions.

DISCUSSION

Intestinal organoids constitute a great model system to study the consequence of cellular heterogeneity within epithelia due to their propensity to self-organise into structures with different intestinal cell types, a principle which is (at least in part) preserved in CRC organoids (25,29). This trait is also reflected by changes in overall gene expression patterns during the outgrowth of single cells into organoids, transitioning from a more foetal (regenerative) program towards stem cell and differentiation features in distinct subpopulations (25). Here, we have used CRC organoids to profile Hedgehog-related gene expression in advanced CRCs and have found Hedgehog ligands and pathway players to be upregulated in mature, heterogeneous organoids. The expression pattern of these genes fits well our and other groups' additional analysis on TCGA data and previous publications reporting an upregulation of Hedgehog ligands and pathway players in CRC when compared to paired normal biopsy material (12,14,19). We further found that the Hedgehog ligands *SHH* and *IHH* in particular are more strongly expressed by STAR⁺ cells in mature organoids, suggesting that non-stem cells are the main source of Hedgehog ligands in CRC. This finding is reminiscent of intestinal biology in adulthood where functionally differentiated cells on the villi are the main source of *IHH* (35). Although at first glance this finding seems to be contradicting a report that Hedgehog ligands are enriched in CD133⁺ tumour-initiating cells (10), the authors themselves acknowledged that their CD133⁺ cell population comprises many stromal cells which, not expressing any Hedgehog ligands, might severely reduce the average expression levels of the ligands.

A major question concerning Hedgehog signalling in CRC is whether it acts purely paracrine towards the mesenchyme or can also act autocrine on the same cells, or

even between different subpopulations of the same tumour. Using organoid models we studied dynamic Hedgehog expression patterns in patient material (22). Starting with pharmacological perturbations, we have utilised Hedgehog activating and inhibiting proteins/drugs on A/K/P/S CRC organoids. As target genes of Hedgehog signalling are mostly context-dependent, we have tested a wide range of putative targets in organoids, including targets that respond to these drugs in Hedgehog-responsive LX-2 and HepG2 cell lines. Yet, the addition of neither recSHH, recIHH nor SAG led to a convincing change in gene expression in CRC organoids. Neither did we see a change in organoid morphology even when treated up to 7 days. Likewise, the treatment with the SMO antagonist (SAG) failed to produce significant results. Next, to circumvent any possible off-target effect of the drugs, we utilised a genetic approach and generated a library of CRISPR/Cas9 KO clones with various combination of Hedgehog ligand KOs. Foremost, the triple Hedgehog KO organoids showed no growth delay *in vitro* and demonstrated no response upon external addition of recombinant Hedgehogs.

In contrast to our data, there is one study in which the authors claim the existence of non-canonical, autocrine Hedgehog signalling in patient-derived CRC organoids that only involves the pathway components *SHH* and *PTCH1* (21). In this study, Hedgehog signalling is downregulated through knockdown or inhibition of *HHAT*, which results in cellular toxicity and reduced spheroid formation but could be rescued through addition of recSHH. In our hands though, addition of recSHH on top of HHAT inhibition did not rescue the induced toxicity of RU-SKI43, not even when used at identical concentrations. If this discrepancy is linked to different genetic background warrants further investigation. Thus, we do not find clear signs of cell-autonomous Hedgehog signalling in CRC organoids with an A/K/P/S mutational background. This notion is further shared by many other *in vivo*-based studies which claim no existence for autocrine Hedgehog signalling in CRCs in mice (18,19,36).

We next wondered if paracrine Hedgehog signalling would influence CRC metastasis formation in the liver. While the number of metastases was comparable between the triple KO and the parental A/K/P/S line, the size of the metastases indicated a trend towards bigger lesions in the triple KO clone. Of note, this finding did not reach statistical significance. Additional caution is warranted concerning the size distributions as individual time-course MRI data indicated that close-by metastasis have fused over time (data not shown), resulting in non-representative lesions (in terms of size) that are indistinguishable from clonal metastases at the last day of imaging. Thus, further experiments are required to address the question as to whether Hedgehog signalling contributes to metastasis formation.

For more detailed studies, it will be of importance to confirm the integrity of the KO on protein level. So far, this proved challenging on Western Blot due to the fact that the ligands are lowly abundant, highly modified with lipids (31) and probably secreted. Alternatively, pull-down assays or ELISAs could be considered to rule out that any residual Hedgehog variants, transcribed from alternative start sites, were secreted into the medium.

Next to these technical considerations, genetic, transcriptional, and immune-related differences between cancers could explain the lack of a clear *in vivo* phenotype. First, mutations could render cancer cells less sensitive to mesenchymal-derived factors. For instance, epithelial BMP signalling has shown to be altered upon loss of SMAD4, resulting in a pro-tumorigenic effect in CRC cell lines (37). Alternatively, the mesenchymal response to Hedgehog ligands could be diminished in CRC (despite increased ligand expression in the tumour), as previously observed for a colitis-associated CRC model (19). Along these lines, epithelial BMP signalling, which is induced in the stroma by epithelial-derived IHH and exerts a pro-differentiation effect during intestinal homeostasis, is downregulated in CRCs (38).

Next to BMP signalling, Wnt signalling is also altered in response to Hedgehog pathway perturbation. While some studies suggest that Hedgehog signalling negatively regulates Wnt signalling in homeostasis and disease (tumour-suppressive role) (4,8,19,21,39), others have reported a positive correlation between Hedgehog activity and tumour proliferation (tumour-promoting role) (14,18). This further underlines the high context dependency and suggests that many confounding factors are yet to be understood, like timing, signalling levels, as well as the exact response of the immune system.

In fact, during homeostasis, Hedgehog signalling is important for the suppression of an acute immune response (3,6,40,41). In line with this, inflammatory bowel disease is associated with reduced Hedgehog activity (40,42). Unfortunately, here we could not address the questions as to whether Hedgehog ligand expression can still elicit an immune response in advanced CRC, given that the transplantation experiments were performed in immunocompromised mice.

Despite facing similar problems, preclinical studies on Hedgehog pathway inhibition in mice through SMO inhibitors have yielded promising results (18). Yet, when translated into a clinical trial for patients with advanced CRC, no additional benefit could be observed when administered together with 5-FU-based chemotherapy regimens (43), while showing promising results for basal-cell carcinoma (44,45). While plasma levels of

all drugs were at expected levels (43), it seems that existing metastatic lesions in CRCs patients were insensitive to targeting of Hedgehog signalling. Based on the transcriptional dynamics of Hedgehog pathway component during organoid growth, we hoped to detect a role for Hedgehog signalling during the earliest stages of metastasis formation but were so far unable to do so. This could suggest that the underlying genetic and resulting transcriptional changes in the A/K/P/S CRC model have led to an alteration in the paracrine Hedgehog signalling cascade at least at one critical node. It would therefore be of interest to dissect if and in what way paracrine Hedgehog signalling changes during colorectal carcinogenesis in a bottom-up approach, taking into account different CRC (driver) mutations as well as the change in the tumour microenvironment (stromal composition and immune response).

ACKNOWLEDGEMENTS

We thank Marieke van de Ven, Natalie Proost, Manon Boeije, and everybody involved at the Animal Laboratory Mouse Cancer Clinic (NKI, Amsterdam) for conducting the transplantation experiments. In addition, we are grateful to everybody who has provided scientific input during project discussion. This project was financially supported by the Dutch Cancer Society by means of a KWF fellowship (UU 2013–6070) and the ERC through an ERC Starting Grant (IntratatumoralNiche - 803608) both awarded to H.J.G. Snippert. This project is part of the Oncode Institute with is partly financed by the Dutch Cancer Society.

AUTHOR CONTRIBUTIONS

M.C.H. and H.J.G.S. conceived the study. M.C.H. performed all experiments and analyses. I.V. helped in generating and genotyping the Hedgehog knock-out clone library. M.C.H. and H.J.G.S. wrote the manuscript.

DECLARATION OF INTEREST

The authors declare no potential conflict of interests.

MATERIAL AND METHODS

Organoid cultures

The following engineered and patient-derived CRC organoid lines (PDOs), derived as previously described (22,46), were used in this study: Engineered A/K/P/S ($APC^{KO/KO}$; $KRAS^{G12D/-}$; $TP53^{KO/KO}$; $SMAD4^{KO/KO}$) and A/K/P ($APC^{KO/KO}$; $KRAS^{G12D/-}$; $TP53^{KO/KO}$) as well as

PDO P19Tb (COSMIC: I2L-P19Tb-Tumor-Organoid, ID 2433500), P16T (COSMIC: I2L-P16-Tumor-Organoid, ID 2433496), and P9T (COSMIC: I2L-P9-Tumor-Organoid, ID 2433492).

Organoids were maintained in Matrigel (Corning, Cat.No. 356231) and cultured as previously described (25) in Advanced DMEM/F12 (Invitrogen, Cat# 12634-028) supplemented with 10 mM Hepes (Invitrogen, Cat# 15630-056), 1% GlutaMAX (Invitrogen, Cat# 35050-038), 1% Penicillin-Streptomycin (Lonza, Cat# DE17-602E) as well as 1x B27 supplement (Invitrogen, Cat# 17504001), 1.25 mM N-Acetyl-L-cysteine (Sigma-Aldrich, Cat# A9165), 10 mM Nicotinamide (Sigma-Aldrich, Cat# N0636), 500 nM A83-01 (Tocris, Cat# 2939/10), 10 μ M SB202190 (Gentaur, Cat# A1632), 10 % R-Spondin1 conditioned medium, 10 % Noggin conditioned medium, and 50 ng/mL human EGF (PeproTech). A/K/P and A/K/P/S organoids were cultured in the absence of EGF, R-Spondin1, and, in case of A/K/P/S, Noggin (25).

Organoids were passaged by Matrigel degradation using Dispase II (Life Technologies, Cat.No. 17105041) and enzymatic digestion to single cells or small clumps using Trypsin/EDTA (Sigma-Aldrich, Cat# 25200056) as described previously (25). Subsequently, culture media was supplemented with 10 μ M Y-27632 (Gentaur, Cat.No. A3008) for 2 days if cells were plated for maintenance but not for experimental purposes. Experiments were performed at a plating density of 250-1,000 cells / 1 μ L Matrigel.

Identity of the lines was regularly confirmed using targeted PCRs and subsequent sequencing of identifying loci.

Cell line cultures

The human liver stellate cell line LX-2 was cultured in Dulbecco's Modified Eagle's Medium (DMEM) (Sigma, D6429) supplemented with 10 % Foetal Bovine Serum (FBS) (Sigma, F7524). The human hepatocellular carcinoma cell line HepG2 was cultured in DMEM supplemented with 10 % FBS, 1% Penicillin-Streptomycin (Lonza, DE17-602E), and 1 % L-Glutamine (Lonza, BE17-605E). Media was refreshed every 2-3 days.

Cell lines were cultured in 10 cm dishes for maintenance and passaged by washing the cells twice with 4 mL PBS prior to incubation with 3 mL Trypsin/EDTA (Sigma, T3924) for 5-10 min at 37°C. Cells were collected into 50 mL tubes and trypsin was deactivated with 27 mL culture media. Cells were pelleted by spinning at 350xg for 4 min and split in a 1:4 ratio.

For qPCR experiments, LX-2 and HepG2 cells were plated into 6-well plates and drug-treated for 24 h and 48 h, respectively. Cells were harvested and frozen in 350 μ L RLT buffer at -80°C until processed.

Drug overview

The following drugs were used in the experiments: GANT61 (Bio Connect, Cat.No. S8075_10mg, 10 mM stock in ethanol), recombinant IHH (recIHH, R&D Systems, 1705-HH-025, 200 µg/mL stock in 0.1%BSA/PBS), recombinant SHH (recSHH, R&D Systems, 1845-SH-025, 200 µg/mL stock in 0.1%BSA/PBS), RU-SKI 43 hydrochloride (R&D Systems, 4886/10, 10 mM in DMSO), smoothed agonist hydrochloride (SAG, Bio Connect, S7779_2mg, 10 mM in DMSO), Vismodegib (Bio Connect, S1082_5mg, 10 mM in DMSO).

Generation of Cas9 expression vectors

Cas9 gRNA expression vectors were assembled according to a published protocol(47). Guides sequences were selected based on their on- and off-target score as predicted by Benchling. High off-target probabilities were only allowed within Hedgehog coding sequences (Table S2). For each guide, single-stranded, complementary oligonucleotides were annealed with T4 ligase and the resulting double-stranded sgRNA was cloned into the Cas9 vector (SpCas9(BB)-2A-Puro, Addgene #48139) upon 6 cycles of repeated *BbsI* digestion and ligation, followed by transformation in Stbl3 competent bacteria. The integrity of Cas9 vectors was confirmed using targeted sequencing of the U6 promoter and following sgRNA.

Generation of Hedgehog knockout clones

To generate Hedgehog knockout clones, A/K/P/S organoids harvested and dissociated to small clumps (as described above) and counted. Cells were split over multiple tubes to obtain approximately 1 million cells per tube. Cells were electroporated in 100 µL BTXpress electroporation solution containing (Fisher Scientific, Cat.No. 15417350) a total of 10-30 µg DNA of multiple Cas9 vectors (Table S2) with a NEPA21 Super Electroporator (Nepagene) and settings previously described(48). Cells were recovered in 400 µL PBS with 10 µM Y-27632 (Sigma, Y0503) for 20 min on ice, then plated in Matrigel.

After 1 day, 1 µg/mL puromycin (Sigma, Cat.No. P8833) was added to the cultures for 48-72 h (based on puromycin-sensitive control) to select for Cas9 vector transfer into cells. In case of co-targeting of the HPRT1 locus, 20 µg/mL 6-Thioguanine (6-TG) was added for 7 days to well-grown organoids to select for Cas9 activity in cells (34). For drug release, organoids were replated into new Matrigel.

Single, surviving organoids were picked manually and subcultured into 2 wells of a 48-well plate, to allow for fast genotyping while maintaining the line in culture.

Genotyping of candidate Hedgehog knockout clones

DNA was isolated using the QIAamp DNA Micro Kit (Qiagen, Cat.No. 56204). Targeted PCRs were performed using the DNA polymerase phusion high fidelity kit (Bioke, Cat.No. NEB M0530L) in 25 μ L reactions followed by purification of the 15 μ L of the PCR product on a 1% agarose gel and Sanger sequencing. For clear, single bands, Sanger sequencing was performed using 0.5 μ L of the PCR product, otherwise DNA isolated from cut agarose gel blocks using the QIAquick gel extraction kit (Qiagen, Cat.No. 28706) was sequenced.

When overlapping reads per locus were detected after the Cas9 cut site, PCR products were cloned into a pJET1.2 vector (ThermoFisher, Cat.No. K1231) using DH5 α competent bacteria and 4-8 bacteria colonies were amplified, DNA was isolated, and loci sequenced to resolve single alleles at high resolution. PCR and sequencing primers are listed in Table S3.

Quantitative RT-PCR analysis (qRT-PCR)

RNA was extracted using the RNAeasy Mini Kit (Qiagen) according to the manufacturer's protocol with DNaseI treatment (Quiagen). 1 μ g of RNA was reverse transcribed using the iScript™ cDNA Synthesis Kit (Bio-Rad). RT-PCRs were run in 384-well plates (Biorad, Cat. No. HSP3801) with 5 μ L FastStart Universal SYBR Green Master (Sigma-Aldrich), 4 μ L cDNA, and 0.5 μ M forward and reverse primer each (Table S3) per well. Mean expression of the following housekeeping genes was used for normalization: LX-2 cells (B2M, RPLPO), HepG2 cells (ACTB, B2M), CRC organoids (ACTB, B2M). Data is represented as mean + SEM.

CellTiter-Glo assays

Organoids were dissociated to single cells and counted. Organoids were plated at a density of 2,000 cells / 10 μ L Matrigel into white-walled 96-well tissue culture plates (Merck). Drugs were added at indicated concentrations. After 7 days, 50% v/v CellTiter-Glo Luminescent Cell Viability Reagent (Promega, Cat.No. G7572) was added to each well. After shaking the plate vigorously for 30 min, luminescent readout was performed using a SpectraMax M5 microplate reader (Molecular Devices). Reads from cell-free wells used to derive background levels, which were subtracted from all reads. For each drug, reads were normalized to the corresponding control wells.

Flow cytometry analysis

Organoids were harvested and dissociated to single cells using Trypsin/EDTA. For viability measurements, samples were incubated with DAPI for 15 min on ice prior to analysis.

Samples were run on a BD FACSCelesta™ flow cytometer. Single, DAPI-negative cells of 3 independent experiments were considered to be alive and used for the quantification of viability.

TCGA data analysis

The colon adenocarcinoma cohort (COAD) containing 273 tumour and 41 normal samples was selected and, to increase the number of normal tissue samples by 308, pooled with the colon dataset of GTEx. Analysis was performed with the browser-based GEPIA2 tool (49). The integrated one-way ANOVA test was used to compare gene expression between samples and p-values smaller than 0.01 were considered statistically significant (*).

Mouse experiments

Animal experiments were performed in accordance with protocols approved by the Institutional Animal Care and Use Committee of the Netherlands Cancer Institute. Animals were kept at the Mouse Cancer Clinic of the Netherlands Cancer Institute.

NOD.Cg-Prkdc^{SCID} Il2rg^{tm1Wjl}/SzJ mice (NSG) were purchased from The Jackson Laboratory and were used at an age of 6-8 weeks as acceptor mice for *in vivo* studies.

Mesenteric vein injections into mice

Organoids were passaged 4 days prior to start of the experiment. On the day of injection, organoids were isolated from Matrigel and trypsinized to single cells as described above. Cells were counted and the appropriate amount was pelleted and resuspended in PBS. 250,000 cells resuspended in 100 μ L PBS were injected into the mesenteric vein of NSG mice as previously described (25,50). Unfortunately, 5 out of 12 mice had to be sacrificed shortly after injection due to health complaints. The conditions of the remaining mice were monitored by weight every 2-3 days and metastasis formation was monitored through biweekly MRI, starting at week 1. Mice were sacrificed after 13 weeks (except for one mouse of the parental line that was sacrificed after 10.5 weeks).

Statistical analyses

Statistical tests were performed using GraphPad Prism (software version 9.3.1). Significance levels smaller than 0.05, 0.001, and 0.001 were considered significant and outlined by (*), (**), and (***) , respectively unless indicated otherwise.

REFERENCES

1. Van den Brink GR, Hardwick JCH, Nielsen C, Xu C, Ten Kate FJ, Glickman J, et al. Sonic hedgehog expression correlates with fundic gland differentiation in the adult gastrointestinal tract. *Gut*. 2002;51:628–33.
2. Varnat F, Zacchetti G, Ruiz i Altaba A. Hedgehog pathway activity is required for the lethality and intestinal phenotypes of mice with hyperactive Wnt signaling. *Mech Dev*. 2010;127:73–81.
3. Van Dop WA, Heijmans J, Büller NVJA, Snoek SA, Rosekrans SL, Wassenberg EA, et al. Loss of Indian hedgehog activates multiple aspects of a wound healing response in the mouse intestine. *Gastroenterology* [Internet]. Elsevier Inc.; 2010;139:1665-1676.e10. Available from: <http://dx.doi.org/10.1053/j.gastro.2010.07.045>
4. van Dop WA, Uhmman A, Wijgerde M, Sleddens-Linkels E, Heijmans J, Offerhaus GJ, et al. Depletion of the Colonic Epithelial Precursor Cell Compartment Upon Conditional Activation of the Hedgehog Pathway. *Gastroenterology* [Internet]. AGA Institute American Gastroenterological Association; 2009;136:2195-2203.e7. Available from: <http://dx.doi.org/10.1053/j.gastro.2009.02.068>
5. Kolterud Å, Grosse AS, Zacharias WJ, Walton KD, Kretovich KE, Madison BB, et al. Paracrine Hedgehog Signaling in Stomach and Intestine: New Roles for Hedgehog in Gastrointestinal Patterning. *Gastroenterology* [Internet]. AGA Institute American Gastroenterological Association; 2009;137:618–28. Available from: <http://dx.doi.org/10.1053/j.gastro.2009.05.002>
6. Westendorp BF, Büller NVJA, Karpus ON, van Dop WA, Koster J, Versteeg R, et al. Indian Hedgehog Suppresses a Stromal Cell–Driven Intestinal Immune Response. *Cmgh* [Internet]. Elsevier Inc; 2018;5:67-82.e1. Available from: <https://doi.org/10.1016/j.jcmgh.2017.08.004>
7. Kong JH, Siebold C, Rohatgi R. Biochemical mechanisms of vertebrate hedgehog signaling. *Development*. 2019;146.
8. van den Brink GR, Bleuming SA, Hardwick JCH, Schepman BL, Offerhaus GJ, Keller JJ, et al. Indian Hedgehog is an antagonist of Wnt signaling in colonic epithelial cell differentiation. *Nat Genet*. 2004;36:277–82.
9. Papadopoulos V, Tsapakidis K, Riobo Del Galdo NA, Papandreou CN, Del Galdo F, Anthony A, et al. The Prognostic Significance of the Hedgehog Signaling Pathway in Colorectal Cancer. *Clin Colorectal Cancer*. Elsevier; 2016;15:116–27.
10. Varnat F, Duquet A, Malerba M, Zbinden M, Mas C, Gervaz P, et al. Human colon cancer epithelial cells harbour active HEDGEHOG-GLI signalling that is essential for tumour growth , recurrence , metastasis and stem cell survival and expansion. *EMBO Mol Med*. 2009;1:338–51.
11. Oniscu A, James RM, Morris RG, Bader S, Malcomson RDG, Harrison DJ. Expression of Sonic hedgehog pathway genes is altered in colonic neoplasia. *J Pathol*. 2004;203:909–17.
12. Xu M, Li X, Liu T, Leng A, Zhang G. Prognostic value of hedgehog signaling pathway in patients with colon cancer. *Med Oncol* [Internet]. Springer; 2012 [cited 2022 Apr 20];29:1010–6. Available from: <https://link.springer.com/article/10.1007/s12032-011-9899-7>
13. Monzo M, Moreno I, Artells R, Ibeas R, Navarro A, Moreno J, et al. Sonic hedgehog mRNA expression by real-time quantitative PCR in normal and tumor tissues from colorectal cancer patients. *Cancer Lett*. 2006;233:117–23.
14. Büller NVJA, Rosekrans SL, Metcalfe C, Heijmans J, Van Dop WA, Fessler E, et al. Stromal Indian hedgehog signaling is required for intestinal adenoma formation in mice. *Gastroenterology* [Internet]. Elsevier, Inc; 2015;148:170-180.e6. Available from: <http://dx.doi.org/10.1053/j.gastro.2014.10.006>

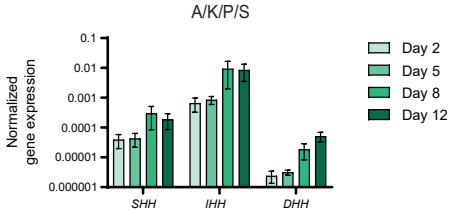
15. Ding YL, Zhou Y, Xiang L, Ji ZP, Luo Z hong. Expression of glioma-associated oncogene homolog 1 is associated with invasion and postoperative liver metastasis in colon cancer. *Int J Med Sci*. 2012;9:334–8.
16. Yoshikawa K, Shimada M, Miyamoto H, Higashijima J, Miyatani T, Nishioka M, et al. Sonic hedgehog relates to colorectal carcinogenesis. *J Gastroenterol*. 2009;44:1113–7.
17. Li T, Liao X, Lochhead P, Morikawa T, Yamauchi M, Nishihara R, et al. SMO Expression in Colorectal Cancer: Associations with Clinical, Pathological, and Molecular Features. *Ann Surg Oncol* [Internet]. Springer Science and Business Media, LLC; 2014 [cited 2022 Apr 20];21:4164–73. Available from: <https://link.springer.com/article/10.1245/s10434-014-3888-y>
18. Yauch RL, Gould SE, Scales SJ, Tang T, Tian H, Ahn CP, et al. A paracrine requirement for hedgehog signalling in cancer. *Nature*. 2008;455:406–10.
19. Gerling M, Büller NVJA, Kirn LM, Joost S, Frings O, Englert B, et al. Stromal Hedgehog signalling is downregulated in colon cancer and its restoration restrains tumour. *Nat Commun*. 2016;7.
20. Westendorp F, Karpus ON, Koelink PJ, Vermeulen JLM, Meisner S, Koster J, et al. Epithelium-derived Indian Hedgehog restricts stromal expression of ErbB family members that drive colonic tumor cell proliferation. *Oncogene* [Internet]. Springer US; 2021; Available from: <http://dx.doi.org/10.1038/s41388-020-01633-0>
21. Regan JL, Schumacher D, Staudte S, Steffen A, Haybaeck J, Keilholz U, et al. Non-Canonical Hedgehog Signaling Is a Positive Regulator of the WNT Pathway and Is Required for the Survival of Colon Cancer Stem Cells. *Cell Rep*. 2017;21:2813–28.
22. van de Wetering M, Francies HE, Francis JM, Bounova G, Iorio F, Pronk A, et al. Prospective Derivation of a Living Organoid Biobank of Colorectal Cancer Patients. *Cell* [Internet]. Elsevier Inc.; 2015;161:933–45. Available from: <http://dx.doi.org/10.1016/j.cell.2015.03.053>
23. Kawasaki K, Toshimitsu K, Matano M, Fujita M, Fujii M, Togasaki K, et al. An Organoid Biobank of Neuroendocrine Neoplasms Enables Genotype-Phenotype Mapping. *Cell*. Cell Press; 2020;183:1420-1435.e21.
24. Fumagalli A, Oost KC, Kester L, Morgner J, Bornes L, Bruens L, et al. Plasticity of Lgr5-Negative Cancer Cells Drives Metastasis in Colorectal Cancer. *Cell Stem Cell* [Internet]. Elsevier Inc.; 2020;26:569-578.e7. Available from: <https://doi.org/10.1016/j.stem.2020.02.008>
25. Heinz MC, Peters NA, Oost KC, Lindeboom RGH, van Voorthuijsen L, Fumagalli A, et al. Liver Colonization by Colorectal Cancer Metastases Requires YAP-Controlled Plasticity at the Micrometastatic Stage. *Cancer Res* [Internet]. American Association for Cancer Research; 2022 [cited 2022 May 16];82:1953–68. Available from: <https://aacrjournals.org/cancerres/article/82/10/1953/696332/Liver-Colonization-by-Colorectal-Cancer-Metastases>
26. Oost KC, van Voorthuijsen L, Fumagalli A, Lindeboom RGH, Sprangers J, Omerzu M, et al. Specific Labeling of Stem Cell Activity in Human Colorectal Organoids Using an ASCL2-Responsive Minigene. *Cell Rep* [Internet]. ElsevierCompany.; 2018;22:1600–14. Available from: <https://doi.org/10.1016/j.celrep.2018.01.033>
27. De Sousa E Melo F, Kurtova A V., Harnoss JM, Kljavin N, Hoeck JD, Hung J, et al. A distinct role for Lgr5 + stem cells in primary and metastatic colon cancer. *Nature* [Internet]. Nature Publishing Group; 2017;543:676–80. Available from: <http://www.nature.com/doifinder/10.1038/nature21713>
28. Shimokawa M, Ohta Y, Nishikori S, Matano M, Takano A, Fujii M, et al. Visualization and targeting of LGR5 + human colon cancer stem cells. *Nature* [Internet]. Nature Publishing Group; 2017;545:187–92. Available from: <http://www.nature.com/doifinder/10.1038/nature22081>

29. Serra D, Mayr U, Boni A, Lukonin I, Rempfler M, Challet Meylan L, et al. Self-organization and symmetry breaking in intestinal organoid development. *Nature* [Internet]. Springer US; 2019;569:66–72. Available from: <http://dx.doi.org/10.1038/s41586-019-1146-y>
30. Everson JL, Fink DM, Chung HM, Sun MR, Lipinski RJ. Identification of sonic hedgehog-regulated genes and biological processes in the cranial neural crest mesenchyme by comparative transcriptomics. *BMC Genomics*. BMC Genomics; 2018;19:1–11.
31. Chen MH, Li YJ, Kawakami T, Xu SM, Chuang PT. Palmitoylation is required for the production of a soluble multimeric Hedgehog protein complex and long-range signaling in vertebrates. *Genes Dev*. 2004;18:641–59.
32. Pereira J, Johnson WE, O'Brien SJ, Jarvis ED, Zhang G, Gilbert MTP, et al. Evolutionary genomics and adaptive evolution of the hedgehog gene family (Shh, Ihh and Dhh) in vertebrates. *PLoS One*. 2014;9:1–35.
33. Hardy RY, Resh MD. Identification of N-terminal residues of sonic hedgehog important for palmitoylation by Hedgehog acyltransferase. *J Biol Chem*. 2012;287:42881–9.
34. Liao S, Tammamo M, Yan H. Enriching CRISPR-Cas9 targeted cells by co-targeting the HPRT gene. *Nucleic Acids Res*. 2015;43:4–11.
35. Büller NVJA, Rosekrans SL, Westerlund J, van den Brink GR. Hedgehog signaling and maintenance of homeostasis in the intestinal epithelium. *Physiology*. 2012;27:148–55.
36. Geyer N, Gerling M. Hedgehog Signaling in Colorectal Cancer: All in the Stroma? *Int J Mol Sci* 2021, Vol 22, Page 1025 [Internet]. Multidisciplinary Digital Publishing Institute; 2021 [cited 2022 Apr 20];22:1025. Available from: <https://www.mdpi.com/1422-0067/22/3/1025/htm>
37. Voorneveld PW, Kodach LL, Jacobs RJ, Liv N, Christiaan Zonneville A, Hoogenboom JP, et al. Loss of SMAD4 alters BMP signaling to promote colorectal cancer cell metastasis via activation of Rho and ROCK. *Gastroenterology* [Internet]. Gastroenterology; 2014 [cited 2022 Jun 27];147. Available from: <https://pubmed.ncbi.nlm.nih.gov/24704720/>
38. Kodach LL, Bleuming SA, Musler AR, Peppelenbosch MP, Hommes DW, Van Den Brink GR, et al. The bone morphogenetic protein pathway is active in human colon adenomas and inactivated in colorectal cancer. *Cancer*. 2008;112:300–6.
39. Madison BB, Braunstein K, Kuizon E, Portman K, Qiao XT, Gumucio DL. Epithelial hedgehog signals pattern the intestinal crypt-villus axis. *Development*. 2005;132:279–89.
40. Lees CW, Zacharias WJ, Tremelling M, Noble CL, Nimmo ER, Tenesa A, et al. Analysis of Germline GLI1 Variation Implicates Hedgehog Signalling in the Regulation of Intestinal Inflammatory Pathways. *PLOS Med* [Internet]. Public Library of Science; 2008 [cited 2022 Jun 29];5:e239. Available from: <https://journals.plos.org/plosmedicine/article?id=10.1371/journal.pmed.0050239>
41. Zacharias WJ, Li X, Madison BB, Kretovich K, Kao JY, Merchant JL, et al. Hedgehog Is an Anti-Inflammatory Epithelial Signal for the Intestinal Lamina Propria. *Gastroenterology*. W.B. Saunders; 2010;138:2368-2377.e4.
42. Xie Z, Zhang M, Zhou G, Lin L, Han J, Wang Y, et al. Emerging roles of the Hedgehog signalling pathway in inflammatory bowel disease. *Cell Death Discov* 2021 71 [Internet]. Nature Publishing Group; 2021 [cited 2022 Jun 29];7:1–9. Available from: <https://www-nature-com.proxy.library.uu.nl/articles/s41420-021-00679-7>
43. Berlin J, Bendell JC, Hart LL, Firdaus I, Gore I, Hermann RC, et al. A randomized phase II trial of vismodegib versus placebo with FOLFOX or FOLFIRI and bevacizumab in patients with previously untreated metastatic colorectal cancer. *Clin Cancer Res*. 2013;19:258–67.

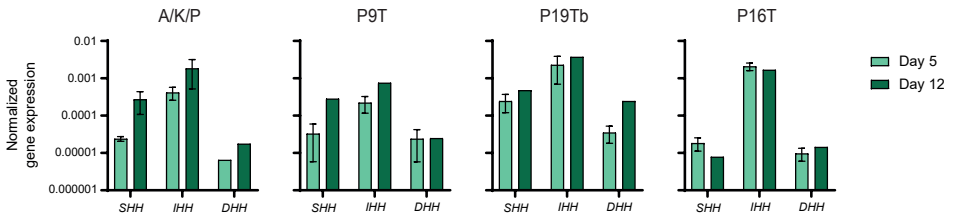
44. LoRusso PM, Rudin CM, Reddy JC, Tibes R, Weiss GJ, Borad MJ, et al. Phase I trial of hedgehog pathway inhibitor vismodegib (GDC-0449) in patients with refractory, locally advanced or metastatic solid tumors. *Clin Cancer Res* [Internet]. American Association for Cancer Research; 2011 [cited 2022 Jun 29];17:2502–11. Available from: <https://aacrjournals.org/clincancerres/article/17/8/2502/12113/Phase-I-Trial-of-Hedgehog-Pathway-Inhibitor>
45. Sekulic A, Migden MR, Oro AE, Dirix L, Lewis KD, Hainsworth JD, et al. Efficacy and Safety of Vismodegib in Advanced Basal-Cell Carcinoma. *N Engl J Med* [Internet]. Massachusetts Medical Society; 2012 [cited 2022 Jun 29];366:2171–9. Available from: <https://www.nejm.org/doi/10.1056/NEJMoa1113713>
46. Drost J, van Jaarsveld RH, Ponsioen B, Zimmerlin C, van Boxtel R, Buijs A, et al. Sequential cancer mutations in cultured human intestinal stem cells. *Nature* [Internet]. 2015;521:43–7. Available from: <http://dx.doi.org/10.1038/nature14415>
47. Ran FA, Hsu PD, Wright J, Agarwala V, Scott DA, Zhang F. Genome engineering using the CRISPR-Cas9 system. *Nat Protoc*. 2013;8:2281–308.
48. Fujii M, Matano M, Nanki K, Sato T. Efficient genetic engineering of human intestinal organoids using electroporation. *Nat Protoc* [Internet]. Nature Publishing Group; 2015;10:1474–85. Available from: <http://dx.doi.org/10.1038/nprot.2015.088>
49. Tang Z, Kang B, Li C, Chen T, Zhang Z. GEPIA2: an enhanced web server for large-scale expression profiling and interactive analysis. *Nucleic Acids Res* [Internet]. Oxford Academic; 2019 [cited 2022 Apr 21];47:W556–60. Available from: <https://academic.oup.com/nar/article/47/W1/W556/5494747>
50. van der Bij GJ, Bögels M, Otten MA, Oosterling SJ, Kuppen PJ, Meijer S, et al. Experimentally induced liver metastases from colorectal cancer can be prevented by mononuclear phagocyte-mediated monoclonal antibody therapy. *J Hepatol* [Internet]. Elsevier; 2010;53:677–85. Available from: <https://doi.org/10.1016/j.jhep.2010.04.023>

SUPPLEMENTARY MATERIALS

A



B



C

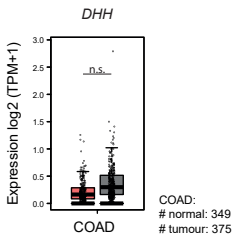


Figure S1: Related to Figure 2

A-B. Relative gene expression of all three Hedgehog ligands over time as measured by qPCR for (A) A/K/P/S organoids (Days 2, 5, 8, 12) and (B) A/K/P, P9T, P19Tb, and P16T organoids (Days 5, 12). Data was normalized to the expression of housekeeping genes and is represented as mean + SEM (if applicable). **C.** Expression data of the Hedgehog ligand *DHH* in patient samples registered in TCGA data base. The colon adenocarcinoma (COAD) cohort including the GTEx colon set was analysed. Expression levels are indicated as log₂ of transcripts per million (TPM) +1. Statistically significant changes in gene expression are indicated by asterisks.

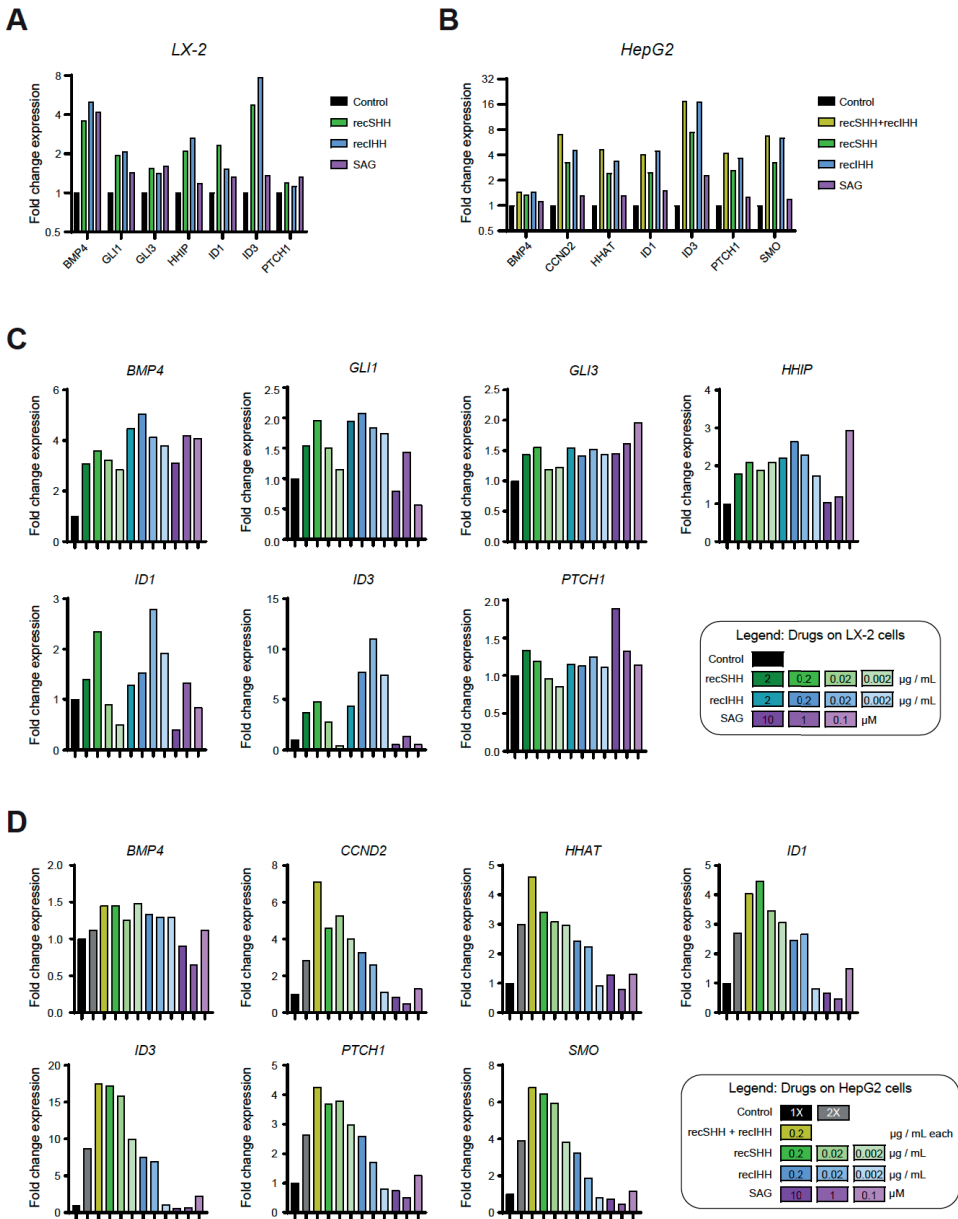


Figure S2: Related to Figure 3

A-D. Gene expression of putative Hedgehog target genes upon Hedgehog activation as measured by qPCR. Drugs were added for 24 h at indicated concentrations. Data is plotted as expression fold change compared to control. Experiment was performed in (A,C) LX-2 liver stellate cells and (B,D) HepG2 liver hepatocellular carcinoma cells. Panels A and B summarize data depicted in panels C and D, respectively, by depicting the best drug concentrations. (A-B) recSHH and reciHH were used at 0.2 $\mu\text{g} / \text{mL}$ (each). SAG was used at 1 μM .

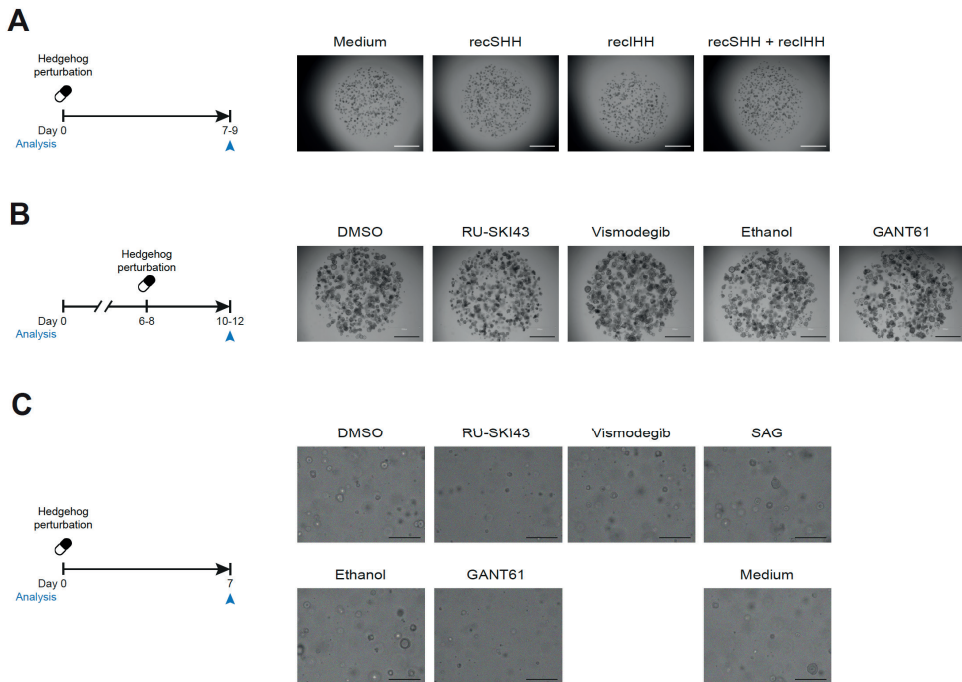


Figure S3: Related to Figure 3

A. Representative images of A/K/P/S organoids grown for 7 days from single cells in the presence of 0.2 $\mu\text{g}/\text{mL}$ recSHH, recIHH, or both. Scale bars, 100 μm . **B.** Representative images of 10-day-old A/K/P/S organoids grown treated for the last 4 days with 10 μM RU-SKI43, 10 μM Vismodegib, 10 μM GANT61 or DMSO and ethanol as controls. Scale bars, 100 μm . **C.** Close-ups of A/K/P/S organoids grown for 7 days from single cells in the presence of 10 μM RU-SKI43, 10 μM Vismodegib, 1 μM SAG, 10 μM GANT61 or control conditions (DMSO, ethanol, medium). Scale bars, 25 μm .

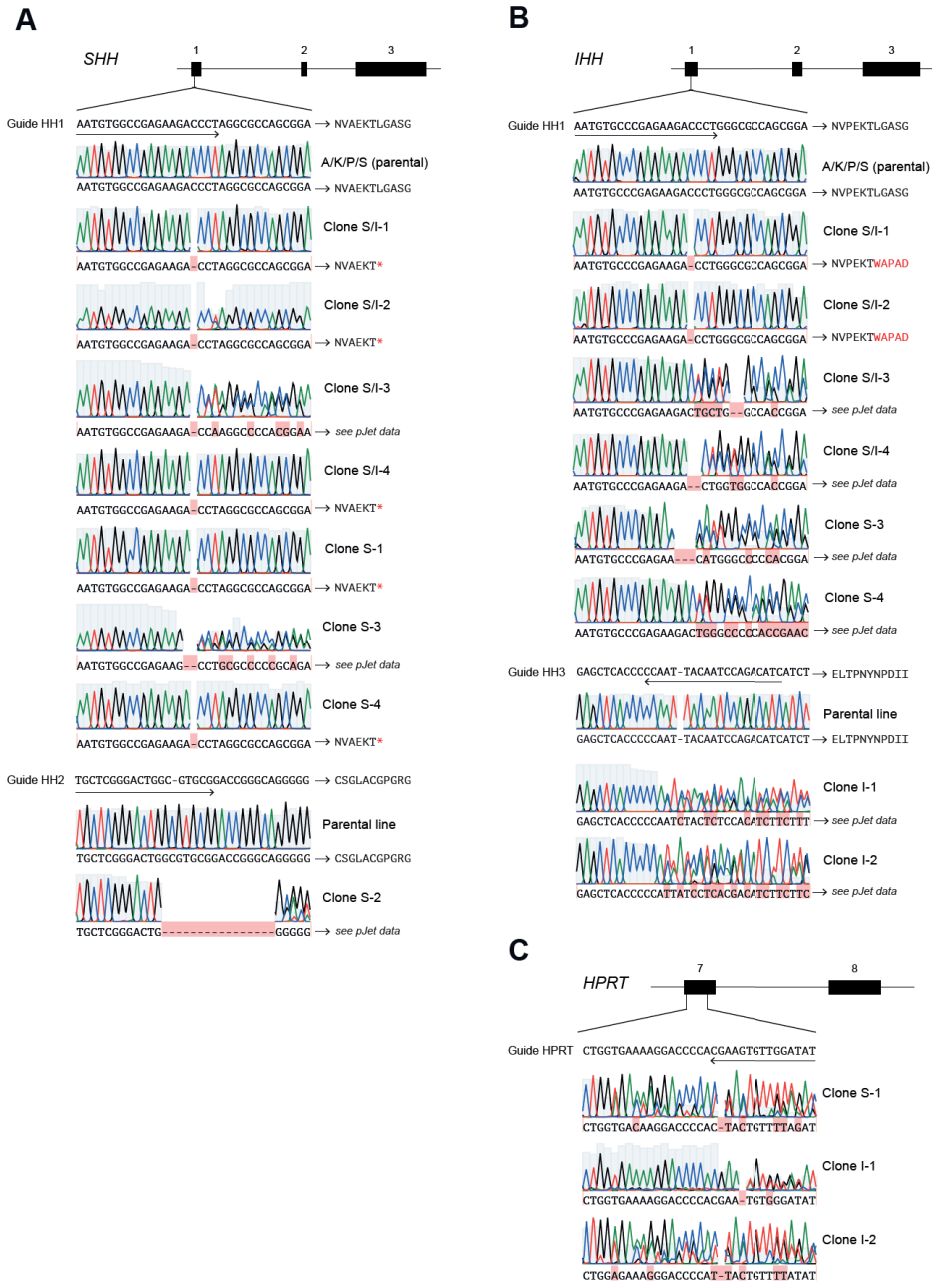


Figure S4: Related to Figure 4

A-C. Sequencing results of clones registered in KO library for loci (A) *SHH*, (B) *IHH* and, if co-targeted, (C) *HPRT*. sgRNAs and their orientation are indicated by a black arrow. Misalignments are highlighted by red background. Resulting changes in amino acids are depicted in red. Corresponding pJet data is depicted in Figure S5A-B. (A-B) Traces of parental line are identical to traces represented in Figure 4D-E, respectively.

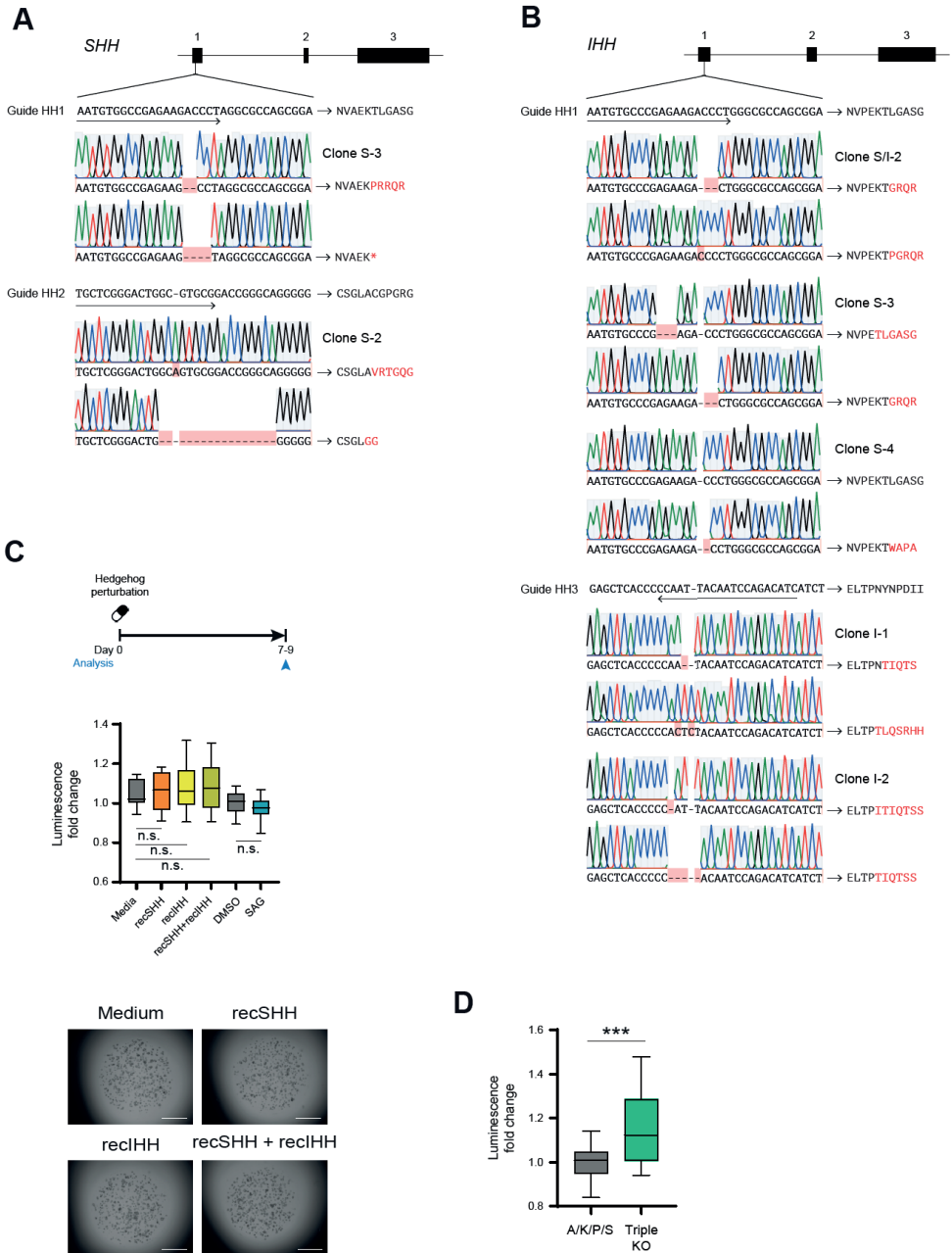


Figure S5: Related to Figure 4

A-B. Sequencing results after cloning PCR products of loci (A) *SHH* and (B) *IHH* into pJet vectors. sgRNAs and their orientation are indicated by a black arrow. Mismatches are highlighted by red background. Resulting changes in amino acids are depicted in red. **C.** Triple KO organoids were

grown from single cells for 7 days in the presence of 0.2 $\mu\text{g}/\text{mL}$ recSHH, recIHH, recSHH + recIHH or 1 μM SAG. CellTiter-Glo was performed and luminescent reads were normalized to respective control condition. Two-tailed Student's t-test was used test for significance. Representative images of organoids after 7 days are depicted. Scale bars, 100 μm . **D.** A/K/P/S organoids and triple KO organoids were plated as single cells and grown for 7 days prior to performing CellTiter-Glo. Luminescent reads were normalized to the levels of A/K/P/S organoids. Two-tailed Student's t-test was used to assess the difference in growth.

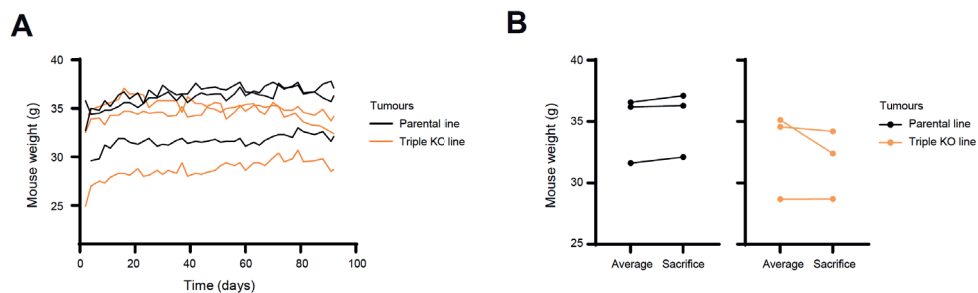


Figure S6: Related to Figure 5

A-B. Mouse weight after mesenteric vein injection of parental (A/K/P/S, black) and triple KO line (orange). (A) Mouse weight over time. (B) Average mouse weight compared to weight at last measurement day.

Clone	Derived from line	SHH			IHH			DHH			HPRT	
		#	allele 1	allele 2	#	allele 1	allele 2	#	allele 1	allele 2	targeted?	disrup-ted?
A/K/P/S	NA	1	WT	NA	1	WT	NA	1	WT	NA	n	NA
S-1	A/K/P/S	1	1 bp del > p.L56*	NA	1	WT	NA	1	WT	NA	n	NA
S-2	A/K/P/S	2	1 bp ins > p.C24V	16 bp del > p.A23G	1	WT	NA	1	WT	NA	y	y
S-3	A/K/P/S	2	2 bp del > p.T55P	4 bp del > p.T55*	2	3 bp del > p.K59T	2 bp del > p.L61G	1	WT	NA	n	NA
S-4	A/K/P/S	1	1 bp del > p.L56*	NA	2	WT	1 bp del > p.L61	1	WT	NA	n	NA
I-1	A/K/P/S	1	WT	NA	2	1 bp del > p.Y85T	1 bp ins > p.Y85L	1	WT	NA	y	y
I-2	A/K/P/S	1	WT	NA	2	1 bp del > p.N84I	4 bp del > p.N84T	1	WT	NA	y	y
S/I-1	A/K/P/S	1	1 bp del > p.L56*	NA	1	1 bp del > p.L61W	NA	1	WT	NA	n	NA
S/I-2	A/K/P/S	2	1 bp del > p.L56*	1 bp del > L56Q	1	1 bp del > p.L61W	NA	1	WT	NA	n	NA
S/I-3	A/K/P/S	2	1 bp del > p.L56K	2 bp del > p.L56W	2	1 bp ins > p.L61P	2 bp del > p.L61G	1	WT	NA	n	NA
S/I-4	A/K/P/S	1	1 bp del > p.L56*	NA	2	1 bp ins > p.L61P	2 bp del > p.L61G	1	WT	NA	n	NA
S/I/D-1	Clone S1	1	1 bp del > p.L56*	NA	2	1 bp del > p.L61W	2 bp del > p.L61G	1	647 bp del up until p.L38	NA	n	NA

Table S1: Overview of mutations in Hedgehog KO library

Sequenced-verified Hedgehog KO clones are listed alongside with their mutational status of the three Hedgehog loci, indicating, if applicable, the extent of indels and the resulting first non-silent amino acid change. Number of alleles (#) refers to the number of visible alleles during PCR-amplified sequencing of the loci. The last two columns indicate if the HPRT allele was co-targeted and if so it was disrupted, too. Abbreviations: WT: wild type; y: yes; n: no; NA: not applicable.

Plasmid	Target	Guide sequence	PAM	On-target Efficiency Score	Off-target Specificity Score	Off-targets with score > 2.0	Fw oligo sequence	Rv oligo sequence
HH1	SHH, IHH	AATGTGGCCG AGAAGACCT	AGG	67.04	49.02	IHH (68.3)	caccgAATGTGGC CGAGAAGACCT	aaacAGGGTCTTC TCGGCCACATTC
HH2	SHH	GTATGCTCGG GACTGGCGTG	CGG	62.96	85.46	NA	caccgTATGCTCG GGACTGGCGTG	aaacCACGCCAG TCCCAGCATACTC
HH3	IHH	GATGTCTGGA TTGTAATTGG	GGG	75.33	67.15	SHH (3.6)	caccgATGTCTG GATTGTAATTGG	aaacCCAATTACA ATCCAGACATC
HH4	DHH	CGAGCTGCTT GCGCGCATAG	CGG	62.46	97.93	NA	caccgCGAGCTGC TTGCGCGCATAG	aaacCTATGCGCG CAAGCAGCTCGC
HPRT	HPRT	GGCTTATATC CAACACTTCG	TGG	43.86	88.16	chr13:+530 46108 (2.0)	caccgGGCTTATA TCCAACACTTCG	aaacCCGAATATA GGTTGTGAAGC

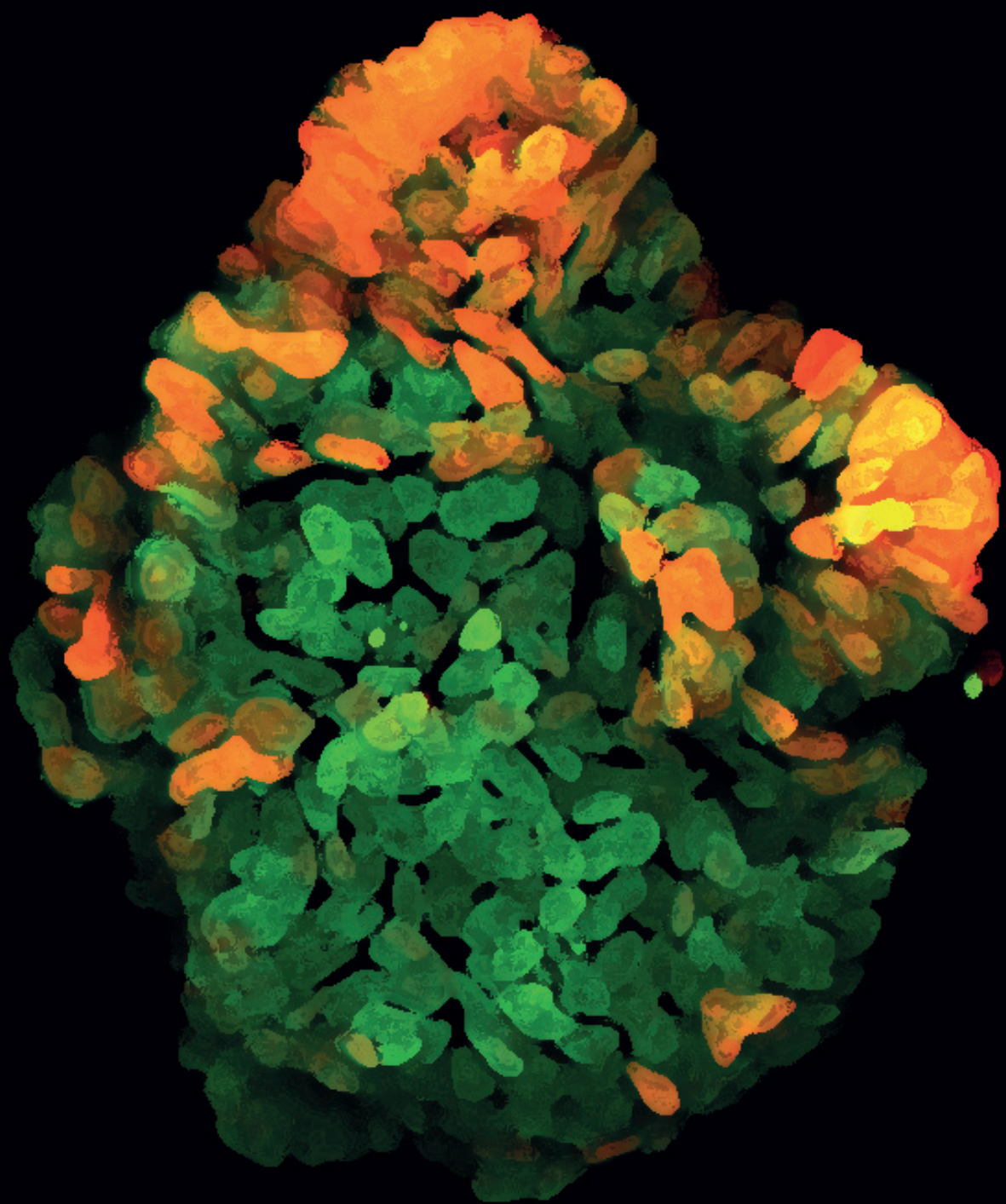
Table S2: sgRNA overview

Overview of sgRNAs selection used to target the loci *SHH*, *IHH*, *DHH*, and *HPRT*. The sequence of the guide is indicated together with the oligo sequences used for cloning the guide into the Cas9 expression vector (Addgene #48139). On-target and off-target specificity scores are indicated for each guide as predicted by Benchling, while for both higher values are generally preferable (maximum of 100). Individual loci with an off-target score > 2.0 are depicted. High off-target scores within other Hedgehog loci were considered favourable for the generation of double or triple KO clones.

Assay	Target	Fw primer sequence	Rev primer sequence	Product size	Seq primer (if applicable)
Genotyping	SHH	AAGGCAGCCTCT CTCACAAAGCT	CAGCTGGACCC TTGACCTCCAT	849 b	CAGACTCTTTTTGT CTTTTGATT
Genotyping	SHH	AAGGCAGCCTCT CTCACAAAGCT	GCTCTGCGATA CAGCCAGCC	1,289 b	CAGACTCTTTTTGT CTTTTGATT
Genotyping	IHH	cgccgcGTTGCCA AAACAAA	TCTCCTCCGGG CTTGGGGAT	808 b	GCTCAGAGTCGAGGCG
Genotyping	IHH	cgccgcGTTGCCA AAACAAA	ACTCCTTCCCG TCCCCAC	1,316 b	GCTCAGAGTCGAGGCG
Genotyping	DHH	ACTTCTGGATG ACAGCGGAGG	CTGGGCTGCCA TAGGAAAACGG	991 b	ACCAGCAGTGACC GGCTAG
Genotyping	DHH	CAGGTGGGCAG TGTTGGGA	CCCCTGTCCCA GCCCTTTT	1,921 b	AATTGGACGTGTTGCCCTC
Genotyping	HPRT	GATGCTCACCTC TCCCACAC	GAAGTGCACC CTAGCCTGG	892 b	CCCTTCCTAGTAATC CCCATAA
qRT-PCR	ACTB	CATTCAAATAT GAGATGCGTTGT	TGTGGACTTGG GAGAGGACT	103 b	
qRT-PCR	B2M	GAGGCTATCCA GGTACTCCA	CGGCAGGCAT ACTCATCTTTT	248 b	
qRT-PCR	RPLPO	GGCGTCTCGT GGAAGTGAC	GCCTTGCGCAT CATGGTGT	255 b	
qRT-PCR	BMP4	ACCGAATGCTG ATGGTCGTT	CAGAAGTGTGCG CCTCGAAGT	173 b	
qRT-PCR	CCND1	GCCCCAGGAG CTGCTGCAA	ATCGTGCGGG GTCATTGCGG	79 b	
qRT-PCR	GLI1	CTCGCCACCT CTTCCAAAT	CCCAATCCGAG AGGTTTGT	70 b	
qRT-PCR	GLI2	CATGGAGCACT ACCTCCGTTT	CGAGGGTCATC TGGTGTAAT	173 b	
qRT-PCR	GLI3	GAAGTGTCCA CTCGAACAGA	GTGGCTGCATA GTGATTGCG	125 b	
qRT-PCR	HHAT	CCACCTCGATG CTGATCCTG	GCCAGCCTTGT ATGAAGATCCT	93 b	
qRT-PCR	HHIP	TCTCAAAGCC TGTTCCACTCA	GCCTCGGCAAG TGTAAGAAGAA	108 b	
qRT-PCR	PTCH1	CCAGAAAGTAT ATGCACTGGCA	GTGCTCGTACA TTTGCTTGGG	134 b	
qRT-PCR	SMO	GAAGTGCCTT GGTTCGGA	GCAGGGTAGC GATTGAGTT	212 b	
qRT-PCR	CCND2	GCCACCTGGAT GCTGGAGTCT	AGTCGGGACC CCAGCCAAGA	102 b	
qRT-PCR	ID1	CTGCTCTACGA CATGAACGG	GAAGGTCCCTG ATGTAGTCGAT	124 b	
qRT-PCR	ID3	GAGAGGCACTC AGCTTAGCC	TCCTTTTGTGCG TTGGAGATGAC	170 b	
qRT-PCR	PTCH2	GCTTCGTGCTT ACTTCCAGGG	CATGCGGAGA CCTAATGCCA	121 b	
qRT-PCR	GLI2	CTGCCTCCGAG AAGCAAGAAG	GCATGGAATG GTGGCAAGAG	157 b	
qRT-PCR	HES1	AGGCGGACATT CTGGAAATG	CGGTACTTCCC CAGCACACTT	103 b	
qRT-PCR	IHH	AACTCGCTGGC TATCTCGGT	GCCCTCATAA TGCAGGGACT	111 b	
qRT-PCR	SHH	CCAAGGCACA TATCCACTGCT	GTCTCGATCAG TAGAAGACCT	241 b	
qRT-PCR	VEGFA	CTCACCAAGG CCAGCACATA	TACCGGGATTT CTTGCGCTT	148 b	
qRT-PCR	DHH	CACCACGCTC AGGATTCACTC	CAACCATACT TGTTGCGGTC	84 b	

Table S3: Primer overview

Overview of oligonucleotides used for genotyping KO clones or for assessing mRNA levels through qRT-PCR. For genotyping of loci, a nested sequencing primer is listed.



CHAPTER

Discussion

7

INTRODUCTION

During my PhD, I have studied several aspects of colorectal cancer (CRC) metastasis formation. Together with my colleagues, we have investigated epithelial characteristics and cell fate changes during successful and failed liver colonisation (**Chapter 3**) and zoomed more closely into transcriptional changes during successful outgrowth in **Chapter 4**. In addition, we have assessed the different nature of quiescent cells in CRC micro- and macrometastasis in **Chapter 5**. Finally, we have investigated in how far Hedgehog signalling activity affects CRC metastasis formation (**Chapter 6**). All of our studies are based on adult stem cell-derived organoid technology that provides a better reflection of cellular heterogeneity and self-organisation than cell lines. We have primarily used patient-derived CRC organoids (PDOs) and human engineered CRC organoids but have made use of CRC organoids derived from genetically-engineered mouse models (GEMMs) when advantageous, to mimic CRC metastasis formation *in vitro* (with a close-up on epithelial biology) and to study its more complex biology *in vivo*.

In this Chapter, I review the current view and emerging novel perspectives on the different steps of the metastatic cascade with a focus on CRC and discuss the relation to my PhD work. I conclude by highlighting possible novel therapeutic concepts that are currently being tested for their suitability in treating metastatic CRC.

COLORECTAL CANCER

Cancer cells display adaptive behaviour throughout the metastatic cascade, being both challenged and instructed by the respective microenvironment. Local invasion of cancer cells at the primary tumour site is followed by intravasation into the blood or lymph vessels, circulation through the body, arrest and extravasation at a distant site, and finally growth first into a microscopic lesion with subsequent colonisation of the target organ. While all steps by themselves are inefficient, metastasis formation in advanced CRC is far from rare. About 20% of patients present in the clinic with stage IV metastatic disease at the time of diagnosis and some further 35-45% of patients with localised stage II-III disease will relapse within 3-5 years (1). Being the second and third most common type of cancer in men and women worldwide (2), respectively, the numbers of CRC-related mortality caused by metastasis are devastating (being the 4th most common cause of cancer-related death worldwide in 1990-2013 (3)). Thus, we need to work tirelessly to improve screening programs and encourage people to participate in order to try and catch CRC at its earliest stages, when the likelihood for dissemination is much reduced and the chance for cure by surgery is high (the risk for relapse is around 5%, 10-12%, and 30% for stage I, II, and III, respectively) (4).

Since 2003, population-wide screening for CRC in individuals aged between 50 and 74 years of age is recommended by the EU council. Encouragingly, first positive trends are already detectable in European countries having pioneered CRC screening, with a reduction in mortality that exceeds the general decline in mortality observed in developed countries since 1980 (5). Nonetheless, screening methods are not flawless and might be more sensitive for some CRC subtypes than for others (e.g. colonoscopy being easier for left-sided than for right-sided lesions) (5,6). In addition, a worrying rise in the number of early-onset CRCs (patients < 50 years of age) has been observed in the past 30 years for yet unknown reasons (2,7) (currently accounting for about 10% of all cases). This increase in incidence slowly starts to result in increased mortality, too (8). As the clinical features of early-onset CRC are somewhat different from later-onset disease (8), the rise in incidence is unlikely to be a result of increased screening (which anyway usually only starts at the age of 45-50 years).

Thus, despite efficient screening options available to date, it is to be expected that the absolute numbers of advanced (metastatic) CRC will stay high over the next decades. Thus, while trying to prevent the disease, we need to continuously do research to better understand the disease and the complex process of metastasis formation that underlies fatality and aim at developing novel therapeutic approaches to further reduce CRC-related mortality in the future.

PRIMARY TUMOUR GROWTH AND LOCAL INVASION

Invasion of cancer cells at the primary tumour site requires breaking down the basement membrane (for instance through matrix metalloproteinases) which results in the release of previously tethered growth factors that in turn can further promote tumour growth (9). In addition, cancer cells can further modify their environment to facilitate invasion, for instance through bundling of collagen (10,11) or the recruitment of certain types of macrophages (12). In the case of CRC, the ability to invade allows lesions which previously have grown outwards into the lumen of the intestine to now expand into the submucosa, the underlying muscle layers, and finally into the (sub-)serosa.

While primary cancer growth can be well studied in general, profiling of invading CRC cells at the primary tumour site is technically challenging. It either requires multi-region sampling of the primary tumour to get a static snapshot representing the heterogeneity of a single tumour or intravital microscopy (IVM) which can be applied to xenograft models to visualise and track individual cancer cells over time. From a cell type perspective, it has recently been shown by IVM that the majority of migratory cells that detach from

the primary tumour (approx. 90 %) are negative for the stem cell marker Lgr5. However, as a substantial fraction of CRC cells is Lgr5⁺ (15), it would be of great interest to further characterise these invading cancer cells. For instance, the quiescence reporter described in **Chapter 5** could be utilised to assess their proliferative nature. In addition, it would be of great interest to assess the epithelial to-mesenchymal transition (EMT) status of invading cancer cells, as EMT has been implicated in this process (16). In particular, evidence is recently accumulating for a *partial or hybrid* EMT state in metastasis formation that only involves some of the full EMT markers and might even be dynamically changing during dissemination (17,18). Thus, tissue slices of primary tumours that have metastasized (generated during orthotopic transplantation studies performed in **Chapter 3** and **Chapter 5**) could be used to analyse the expression levels of individual EMT markers and their spatial distribution in order to address the following open questions: Which EMT players are involved in the invasion of CRC? Is there inter-patient heterogeneity in the EMT state? And, at what stage of invasion do EMT markers appear?

In a previous study on invasion of CRC, single cell invasion outnumbered collective invasion (a small connected group of invading cells) (19). Together with the fact that in this study the vast majority of circulating tumour cells was Lgr5⁺, the assumption that the cell-of-origin of metastasis formation is Lgr5⁺ is tempting. However, as Lgr5⁺ CRC cells form metastases more efficiently than Lgr5⁻ cells when injected into mice (19), we cannot rule out that Lgr5⁺ cells are the seeding clone of (at least some) metastases. While our experiments were not tailored at addressing this question, the study of later events of the metastatic cascade presented in **Chapter 3** and **Chapter 4** might well be influenced by the identity of the seeding clone. We have therefore generally accounted for the different possibilities by performing (organoid and metastasis) outgrowth experiments with both cancer stem and non-stem cells as starting population.

INTRAVASATION AND THE ROUTE OF DISSEMINATION

The entrance of locally invaded cancer cells into the circulation is called *intravasation*. While this can refer to both the vasculature as well as the lymph system, lymphatic vessels seem to allow easier entrance due to a lack of a protective pericyte layer and less tight junctions. This could also explain why lymph node metastasis are an early marker for dissemination in many cancer types (20). Despite of this early event, the notion prevails that distant organs are generally reached via the blood system (21). Two milestone studies in 2018 have demonstrated the ability of cancer cells residing in lymph nodes to enter the blood system (22,23), suggesting the involvement of both systems in a single dissemination process. In

line with this, subsequent work on melanoma has indicated that the exposure to lymph reduces the cancer cells' risk of ferroptosis in the blood (24), providing a molecular reason for the more complex, sequential lymph-to-blood-route of dissemination.

Validating this hypothesis in patients is challenging, yet it would be interesting to see if CRC cells also metastasize more efficiently when injected into lymph nodes rather than into the blood stream. Thus, a side-by-side comparison of intranodal versus portal / mesenteric vein injection (the latter being used in **Chapter 3** and **Chapter 6**) in mice could be an interesting step to assess if the exposure to lymph confers a pro-metastatic effect to CRC cells both in an immunocompromised and an immunocompetent cancer model. Furthermore, genome sequencing-based studies have evolved into a major tool to reconstruct phylogenies of tumours at different sites in individual patients, providing insights into clonal relationships and seeding potential (25). In this context, the UK-based national autopsy program PEACE deserves particular attention, collecting multi-region samples of deceased, non-small-cell lung cancer patients and thus providing a full picture of disease progression in the form of multiple case studies. Preliminary data presented by Mariam Jamal-Hanjani at the EMBL|EMBO Metastasis conference in 2022 (currently 18 patients with > 200 samples) indicates that no subsequent seeding originates from local (surgical) lymph node metastases in this cancer type. Intriguingly and conversely, however, distant lymph node metastases were identified (among others) as sources for subsequent seeding. This finding from a hitherto unseen study design adds granularity to the previous perspective of dissemination routes, highlighting the potential of lymph node metastasis to further propagate the disease (either through the lymphatic or the blood system) and suggesting ongoing adaptive processes in already disseminated cancer cells that further influence their subsequent seeding behaviour. Such studies are unfortunately not easily possible, not even in mice. For instance, disease burden might accumulate too fast to allow for subsequent seeding, as (presumably) in case of the cancer models used in this thesis (**Chapter 3** and **Chapter 5**). In addition, the multi-step adaptation processes in the context of different therapeutic treatments would require experiments presumably lasting years with a very refined monitoring of the mice and understanding of the drug-induced side-effects.

In addition, while it had been a long-held believe that cancer cells are constantly shed throughout the day, it has now been demonstrated for breast cancer that both the number and the potential for successful seeding of disseminated cancer cells is affected by the circadian rhythm with pro-metastatic traits related to the rest phase (26). If such principles also apply to CRC is still unknown. To assess this, sophisticated isolation strategies of circulating tumour cells at different time points during the day would be required for a side-by-side comparison.

Intravasation and the route of dissemination are generally topics beyond the scope of this thesis. While they take place during liver metastasis formation after orthotopic transplantation (**Chapter 3** and **Chapter 5**), no analysis was performed concerning the intermediate steps of the metastatic cascade. Conversely, in induced (synchronous) metastasis formation experiments, the metastatic steps from invasion to intravasation are skipped entirely. For these assays, we have chosen the blood system as travelling medium (**Chapter 3** and **Chapter 6**), having injected cancer cells into the mesenteric or portal vein, both of which drain directly into the liver.

FROM CIRCULATING TUMOUR CELLS TO EXTRAVASATION

Once inside the circulation, cancer cells have to survive additional threats such as anoikis (cell death due to loss of anchorage), shear forces, and immune detection, before arresting at a distant site and extravasating into the target organ parenchyma (9). To increase the chance for survival and decrease the risk for immune-mediated killing in one go, cancer cells can hijack platelets and hide inside a microthrombus formed by the clotting/coagulation machinery in the blood (12). The formation of such a larger structure additionally facilitates the lodging at a distant site due to physical constraints (12). The choice of the distant target site is certainly influenced by anatomic properties, such as the route of circulation and the size restrictions imposed by smaller vessels, while ongoing research is investigating to what extent tissue-specific interactions between the luminal wall of vasculature and cancer cells can also influence organ tropism (9). While intravasation into the circulation is facilitated through cancer-induced (lymph-) angiogenesis which results in the formation of new, yet corrupted vessels with less tight endothelial cell junctions (20,27,28), vessels encountered during extravasation are usually intact and thus impose a stronger barrier. Cells can either grow intraluminally until the vessel bursts or nonetheless cross the endothelial and pericyte layers to enter the organ parenchyma (29).

For CRC, there is good evidence that the liver constitutes the prime organ for metastasis due to the portal vein directly draining into the liver where CRC cells easily get trapped (21). Additionally, extravasation into the liver is facilitated by fenestrated vessels which constitute a much lower obstacle than in many other organs (30). Thus, we have focused on liver metastasis outgrowth in our studies. When analysing patient liver tissue sections, we have found several multicellular micrometastatic lesions that were presumably located inside vessels based on their morphology (31) (**Chapter 3**), suggesting growth inside the vasculature in CRC patients. Based on the intestinal stem cell marker OLFM4, we found that all micrometastatic lesions (vessel co-opted included) are negative for intestinal stem cell markers.

In our work, the cancer cells' journey through the circulation only takes place in spontaneous metastasis formation experiments, yet in immunocompromised mice due to a focus on human CRC. While intact immune surveillance would probably not affect these particular steps of the metastatic cascade more than reducing the number of surviving cells, I consider the lack of such as not very relevant to the circulating tumour cells' state in our experiments (**Chapter 3** and **Chapter 5**).

Conversely, induced (synchronous) metastasis formation experiments have several drawbacks considering the state of the resulting circulating tumour cells (**Chapter 3** and **Chapter 6**): First, most of these experiments were conducted with *in vitro*-grown organoids as starting material. Thus, these cells are derived from a growth-promoting environment entirely lacking mesenchymal features and are therefore transcriptionally different to orthotopically transplanted CRC cells. Yet, even when performing injection experiments with transplanted organoids as isolation material, *in vitro* dissociation to single cells is required prior to injection. We therefore need to keep in mind that this processing step might well interfere with the transcriptional state of the seeding cells (for instance through enzymatic digestion and the loss of epithelial cell-cell contacts). However, there are no good alternatives yet for performing metastasis formation experiments while knowing the age of the arising metastases. Due to the single cell nature of CTCs in induced metastasis formation experiments, they best represent metastatic outgrowth starting from single cells. Yet, in many cancers, cell clusters are superior in metastasis formation compared to single cells and their presence correlates with worse prognosis (26,32–34). As there is now also emerging evidence for collective invasion in CRC (Eduard Batlle laboratory personal communication), it would be of great interest to assess if the epithelial characteristics of early (or failed) metastatic outgrowth we have described in this work also apply to cell cluster-derived metastases.

In addition, we generally assume that these experiments best model the seeding of primary tumour clones into the liver (assumption based on the time they take), where cancer cells again have to adapt to survive and thrive in this hostile environment. Yet, we cannot rule out metastasis-to-metastasis seeding events to take place inside the liver as previously described for CRC (35), which might be initiated by cells with a different cellular state and could be a confounding factor in our results. While the chance of metastasis-to-metastasis seeding is probably very low our experiments due to relatively short time spans (several weeks), we still need to be cautious with generalising our findings to metastases in patients that have formed over years and might thus have been subjected to multiple rounds of adaptation in different places inside the human body (as illustrated

by the PEACE study discussed earlier in this Chapter). Considering that many CRC patients present with multiple metastases of undefined origin (location), it would be of great importance to better understand if the clonal origin of metastasis influences their state and in particular their response to therapeutic interventions.

LIVER COLONISATION

Upon reaching the distant site, disseminated cancer cells first grow into micrometastases that can persist in a state of population dormancy for months up to decades before growing into macrometastases and overtaking the organ. This lag time is known as *metastatic latency* during which micrometastases are virtually clinically undetectable and efficient growth is prevented by epithelial, mesenchymal, or immune-related causes (36).

In the case of CRC, metastatic latency is usually short, limited to up to 5 years, while most relapses happen within 1-3 years after diagnosis. The most frequent metastatic sites are the liver and the lungs, followed by the peritoneum, distant lymph nodes, and bones (37). The reason for the relatively short latency time in CRC compared to other diseases is still to be elucidated, yet it seems to suggest the traits required for colonisation are (re-)acquired more easily or that the environment is less hostile. Promoting factors could include growth factor independence typically gained by CRC cells during carcinogenesis through driver mutations or the inherent plasticity of the intestinal tract that enables fast and flexible cell fate changes (for instance during regeneration, reviewed in **Chapter 1**).

In **Chapter 3**, we have demonstrated a high similarity between organoid and metastatic outgrowth that is rooted in the cells' nature to self-organise and establish a kind of tissue architecture, even when cultured *in vitro*. Using the transcriptional *ASCL2* reporter STAR and the *Lgr5-DTR-eGFP* allele in human and mouse lines, as readouts for stem-like cells, respectively, we could show that outgrowth trajectories *in vivo* and *in vitro* are phenotypically alike. Single cells first proliferate for a few days in the absence of cell fate changes (at the resolution of STAR or *Lgr5*). If, in a next step, cellular heterogeneity is established, growth can continue, generating many more cancer stem and non-stem cells and eventually resulting in macrometastasis (macro-organoids). Conversely, failure to generate cell type heterogeneity is linked to growth stagnation (*in vitro*) which resembles the dormant nature of micro-metastasis (*in vivo*).

The study described in **Chapter 3** has added granularity to adaptive behaviour of CRC cells during metastatic outgrowth. While we have previously published in a collaborative project the cellular patterning of metastasis of different sizes (19), we now have provided

a time-resolved trajectory of metastatic outgrowth using IVM. While IVM enabled the tracking of individual lesions over time on consecutive days, it is a low-throughput, resource-intensive assay that requires some luck of finding lesions beneath the imaging window. As circulating CRC cells are vastly Lgr5⁺ (19), the IVM study was therefore performed upon injecting Lgr5⁺ CRC cells. While the *in vitro* outgrowth studies of CRC organoids have nicely complemented this assay and could be conducted in much higher numbers starting with both cancer stem and non-stem cells, this study resolves the outgrowth patterns irrespective of the metastasis-initiating cell clone.

As micrometastasis are virtually undetectable in CRC patients and as the transition from micrometastatic disease to organ colonisation usually happens over several dozens of months, the study of this process is technically challenging. While we could analyse micrometastases of CRC patients (**Chapter 3**), liver specimen were obtained after the patients had progressed to macrometastatic disease. Thus, the micrometastases available for analysis are biased towards long-term latency and it is impossible to know if these lesions would ever have started to colonise the livers. However, the finding that micrometastasis are devoid of CSCs easily fits to the idea that most circulating CRC cells are devoid of stemness (19) and suggests that the re-appearance of CSCs has not yet happened. Alternatively, CSCs might have formed in these lesions but have died off since, a possibility in line with the concept of population dormancy rather than cellular quiescence. In fact, cGAS-STING mediated immune clearance in chromosomally unstable cancer cells that have recently started to cycle and have ended up with cytosolic DNA after chromosome missegregation (38) could biologically substantiate such an idea.

The cellular state and the cycling behaviour of micrometastasis could be further investigated with the tools presented in **Chapter 5**. Here, we have adapted a quiescence reporter based on high expression level of P27 (*CDKN1B*) and validated its reliability in labelling non-cycling cells. In addition, we have extended a liver perfusion protocol used for the isolation of metastatic cells by some additional steps that allow separating macrometastasis from micrometastasis. Transcriptomic analysis of differently sized metastases has demonstrated various differences with micrometastasis being enriched for oxidative phosphorylation, while macrometastasis process more inflammatory and fibrotic stimuli. While this size separation has clearly demonstrated key differences, there are two key risks for sample contamination with this protocol. The liver preceding liver perfusion comprises a collagenase cocktail that efficiently dissociated hepatic tissue and micrometastasis, while macrometastasis were detected as intact structures. Thus, when subsequently using a 70 µm pore cell culture strainer, there is a chance that individual

dissociated cells from macrometastasis contaminate the micrometastasis sample. Additionally, so far we are blind for the size cut-off at which metastasis are still efficiently digested by collagenase and for their corresponding metastatic states. It would therefore be very interesting to validate the initial findings in a next step on a liver tissue strip with metastases being embedded in their environment.

A possible confounding factor in this study was the age of the metastasis. As the experiments were performed after orthotopic transplantation (**Chapter 5**), metastasis of microscopic size could have either just arrived in the liver or represent non-efficient outgrowth. Along these lines, we found micrometastasis to be either entirely cycling or non-cycling, yet a direct correlation is not possible. It would therefore be of great interest to couple our harvesting strategy to a metastasis model with synchronous seeding to study the nature of latent micrometastasis and, for instance, assess their change in transcriptomic state over time.

We have contributed further knowledge to the fields of metastatic latency and colonisation by profiling the transcriptional changes during (failed) metastatic outgrowth using both organoid-derived bulk sequencing data as well as single-cell RNA-sequencing data from a metastasis time-course formation experiment (**Chapter 3**). Concerning metastatic latency, we have revealed that micro-organoids have high levels of YAP transcriptional activity. However, this finding could not be confirmed in micrometastasis (data not shown). Conversely, YAP activity during the first days of outgrowth was detectable both *in vitro* and *in vivo*. Thus, YAP activity in micro-organoids could be an artefact of the culture system, be specific to only some CRC subtypes, or micrometastasis when profiled might be beyond the YAP state and might face additional hurdles on their way to colonisation.

Concerning liver colonisation, we could show in **Chapter 4** that initial YAP activity is followed by a highly proliferative phase involving E2F family members during organoid and metastasis outgrowth, while late-stage organoids and metastasis display activity of AP-1 family members, suggesting YAP to serve as co-activator to this transcriptional complex, driving a different transcriptional program. The analysis of earliest phases of metastatic growth is inherently limited by little material and thus was conducted through single-cell RNA-sequencing in our studies. To not be confounded by metastases at different stages of outgrowth, such assays require synchronous seeding and are therefore subjected to aforementioned limitations. Additionally, while most of this thesis is focused on human CRC, the metastasis time-course experiment was conducted using murine CRC cells due to their much higher engraftment rate. However, as the transcriptional findings were overall

very similar between murine metastasis and human organoids, general concepts are very likely transferrable. On the other hand, using the well scalable organoid system *in vitro*, profiling could be performed at a much higher sequencing depth at transcriptomic and chromatin level on human tissue. This has allowed to also interrogate the transcriptomic changes in recently formed CSCs during the outgrowth of non-stem cells into organoids which was linked to EGF pathway activation. The question as to whether EGFP pathway upregulation is correlative or essential should be further investigated.

In **Chapter 6**, we have assessed the role of Hedgehog signalling on CRC metastasis formation. To this end, we have generated a knock-out (KO) line of all three Hedgehog ligands through CRISPR/Cas9 technology in the background of an advanced CRC organoid line. However, we did not see any significant difference between the Hedgehog KO and the parental line in liver metastasis formation. The insensitivity to Hedgehog signalling fits to the clinical observation that inhibition of Hedgehog signalling in combination with chemotherapy for metastatic CRC has no beneficial effect (39). Nevertheless and fundamentally-speaking, it would be interesting to disentangle the Hedgehog cross-talk between the epithelium and the mesenchyme, to ultimately resolve at which stage CRCs become insensitive to Hedgehog signalling. Such future studies should address if CRC cells produce functional ligands (correct post-translational modifications and intact secretion), if the microenvironment is still responsive to Hedgehog stimuli (presence and activity of responsive subpopulations), and if cancer cells are still affected by the mesenchymal response to the Hedgehog ligands. In particular, the latter step could be impeded by CRC driver mutations. For instance, the pro-differentiation effect normally induced by *IHH* through BMP production in the mesenchyme could be reduced in *SMAD4*-mutated CRC cells. Alternatively, the loss of *APC* which generates hyperactivity of the Wnt pathway could mask pro-proliferative effects otherwise exerted by GLI1⁺ crypt-based mesenchymal cells (13), even if their number is positively regulated by Hedgehog ligands (as in the case of villus-based GLI1⁺ myofibroblasts in the intestine (14)). However, the chance for therapeutic benefit based on these studies might be low, considering that early-stage CRC is usually surgically resected with high chances for cure.

Next to these general considerations, I would like to now highlight some thoughts directly concerning the liver environment. Hedgehog signalling is critical for liver development and large scale regeneration (after partial hepatectomy) (40). It acts in a paracrine manner with ligands being produced by hepatocytes or bile duct cells and secreted towards hepatic stellate cells, leading to the formation of progenitor cells during regeneration. In inflammatory liver diseases, Hedgehog signalling is furthermore linked to fibrosis and

matrix remodelling (40). It would thus be conceivable that metastasis residing in the liver can modulate their environment by engaging Hedgehog signalling. While the fact that a clinical trial targeting Hedgehog signalling in metastatic CRC did not show any benefit (39), could have been explained by insufficient drug concentrations at the site of the disease, the hypothesis of CRC cells remodelling the liver microenvironment should have resulted in a phenotype when comparing KO line versus parental line metastasis. The lack of such suggests either compromised Hedgehog signalling or insensitivity of the advanced CRC cells to intact signalling.

ORGAN-TROPISM IN METASTASIS FORMATION

While the liver constitutes the prime target for metastasis formation in CRC, other organs are also regularly affected. Next to physiological reasons (the portal vein draining from the intestine into the liver), the nature of the vasculature in the liver (fenestrated, less well protected) facilitates the extravasation of cancer cells into the liver compared to many other organs. In contrast, the vasculature of the lungs or the brain (both being other important sites of CRC metastasis) is less 'leaky' with additional protective layers around endothelial cells and thus constitutes a greater obstacle (29). Upon arrival of the cancer cells, organ colonisation is heavily influenced by the microenvironment on multiple levels. For instance, the 'soil' generally provides very different signalling cues compared to the original organ. While most cancers are considered (vastly) growth factor independent, the activation of pathways not engaged in the original tissue can still impact on the cancer cells' behaviour. For CRC, evidence is now emerging that liver metastases are in a Wnt-high, more stem-like state than metastases in different organs (Frederic de Sauvage laboratory personal communication). This suggests that the liver provides less of a hostile soil to CRC cells, given that Wnt activity is linked to proliferation in the intestinal tract.

A second key difference comprises the local immune response. Many primary cancers evade immune detection for instance through inactivation or exclusion of immune cells from their surroundings or by transforming them to exert tumour-promoting effects (12,27). While direct mechanisms such as the cancer cells' secretion of cytokines that paralyse infiltrating immune cells (21), might be preserved in disseminated cancer cells, indirect mechanisms involving the recruitment of immunosuppressive cells (41) might not be immediately active at the metastatic site. In line with this, it has been demonstrated that natural killer cells can actively repress metastatic disease of brain and lung cancers to a micrometastatic extent in immunocompetent mouse models (42).

Within the framework of this thesis, we have studied in-depth liver colonisation by CRC cells. It would be very interesting to extend the range of tissues used and investigate if the conceptual underpinnings of the metastasis outgrowth trajectory described in **Chapter 3** and **Chapter 4**, are similar in different target organs or even for other cancer types. Similarly, the influence of different target organs on the propensity of extravasating cancer cells to readily proliferate or to (transiently) enter a state of quiescence could be compared using the quiescence reporter introduced in **Chapter 5**. For instance, we have noticed that upon integration of the STAR reporter into patient-derived P19Tb CRC organoids, the parental line known to efficiently generate liver metastases had turned into a line now predominantly forming macrometastases in the lungs with micrometastatic disease in the liver (data not shown). Assuming that this observation is caused by the integration of STAR into a subclone of the P19Tb parental line, it would be very interesting to exploit the combination of the highly-related parental and STAR reporter line to study the differences in the 'seed' associated with different metastatic locations as well as the difference in cycling behaviour.

The study of the behaviour of human cancer cells *in vivo* was performed in immunocompromised mice. While this clearly affects the composition of the microenvironment, I think that for the epithelial-focused studies we have conducted, the immunocompromised setting is justified and unlikely to majorly influence the general conclusions. However, it should be noted that in particular for the transition from micrometastatic growth to liver colonisation (**Chapter 3**), we have not described additional hurdles likely to be implied by the immune system, as previously described for other cancer types (42), but instead focus on the underlying epithelial biology.

TARGETING CRC METASTASIS

The challenge in treating cancer consists in eradicating as many of the diseased cells as possible while reducing normal tissue toxicity. It thus follows that surgery with curative intent that allows excising the entire tumour in one procedure is frequently the best approach, if the cancer has not already spread to distant organs and if the risk of surgery-induced serious, lasting handicaps is not too high. In case of CRC, surgery is curative in about 70% of stage I-III CRC (4). To reduce the risk for relapse, patients presenting with local lymph node invasion usually receive adjuvant 5-fluorouracil (5-FU) + oxaliplatin-based chemotherapy after surgical removal of the primary tumour (6). For metastatic disease, 5-FU-based chemotherapy regimen are frequently applied, combined with either oxaliplatin, irinotecan or both. For more fragile patients, on the other hand, the single-agent fluoropyrimidine can be applied, being less efficacious yet easier to tolerate (6).

Next to chemotherapy, targeted therapies have proven efficacious for a subset of CRC patients, yet are so far only applied for metastatic disease and typically in combination with chemotherapy. One main target for CRC is vascular endothelial growth factor A (*VEGFA*) that can be targeted through monoclonal antibodies (bevacizumab and ramucirumab), recombinant fusion proteins (ziv-aflibercept) or small-molecule-based kinase inhibitors (regorafenib) (6). Alternatively, in case of wild-type KRAS and NRAS, EGFR-targeted therapies can be considered (cetuximab and panitumumab) (43,44). Clinical studies using these various drugs had similar outcomes: they improved progression-free and/or overall survival by a few month compared to the control group (45–49). While this might sound like a small gain, it is interesting to note that most of these studies were performed on chemo-refractory tumours, thus, they can still be an option for second line treatment of metastatic CRC. Yet, not all cancers will respond to this treatment and as they are quite expensive, biomarkers predicting treatment response are badly needed.

Since 2017, immunotherapeutic agents are FDA-approved for metastatic CRCs with a high chance for neoantigen presentation, which means the subclasses deficient for mismatch repair pathway (dMMR) or microsatellite-*instable* (MSI) CRC (6). For these CRC subclasses, in particular the PD-1 inhibitor pembrolizumab has already been demonstrated to be superior to chemotherapy in a phase III clinical trial (50) and has therefore become standard of care for metastatic dMMR CRC (51). In addition, PD-1 inhibitors (nivolumab and dostarlimab) and CTLA-4 inhibitor (ipilimumab) are currently being investigated for their effectiveness when used alone or in combination (52–54). In addition, there is now increasing interest in using immunotherapy beyond (dMMR or MSI) metastatic CRC. An ongoing phase I/II clinical trial, the suitability of immunotherapy is being used in a neoadjuvant setting with subsequent surgical removal of the tumour with promising initial data (55). The pathological response rate of dMMR tumours is currently at 100% (20/20), while data on long-term benefit is pending. Intriguingly, however, 27% (4/15) of proficient MMR tumours also demonstrated pathological response and correlate with CD8⁺PD-1⁺ T cell infiltration. It will therefore be of great interest to further establish if the immunoscore can be predictive for immunotherapy response in proficient MMR tumours.

Another exciting new therapeutic strategy currently emerging involves the use of bispecific antibodies. With the idea to target the proliferation and survival pathways in CRC cells, the investigators Mark Throsby and Eduard Batlle have conducted a large screen of bispecific antibodies targeting EGFR together with either of the Wnt target surface receptors LGR4, LGR5, RNF43, and ZNRF3 (56). As CRCs are marked by hyperactivation

of the Wnt pathway, the choice for Wnt target surface receptors is expected to provide enhanced specificity for cancerous versus non-cancerous cells. In a two-step screening approach involving over 500 possible combinations of epitopes and up to 22 patient-derived CRC organoid lines, the antibody EGFR and LGR5 co-targeting antibody MCLA-158 was identified. MCLA-158 led to significant and synergistic growth inhibition in over 50% of all lines in an LGR5-dependent manner. Moreover, MCLA-158 was superior to the clinically used EGFR-targeting antibody cetuximab in reducing growth both *in vitro* and in xenograft model with an estimated 30-fold difference in IC50. Intriguingly, MCLA-158 also outperformed cetuximab in lines harbouring an oncogenic KRAS mutation, while the responsiveness of the lines was predictable by their expression level of LGR5. MCLA-158 is additionally provides a large therapeutic window affecting normal tissue only at much higher doses. Having further shown that the efficacy of MCLA-158 is not confined to CRC but can be extended to EGFR-high LGR5-high esophageal, gastric, as well as head and neck cancers, a phase I clinical trial has been launched with the aim to test MCLA-158 as single agent for advanced solid tumours (NCT03526835).

In a similar approach, different biotech companies and start-ups like Genentech and Laigo Bio are currently investigating the suitability of E3 ubiquitin ligases as one of the targets in bispecific antibodies to enhance the degradation of the antibody pair once internalised. For CRC, for instance, targeting ZNRF3 with IGF1R resulted as most promising combination for the treatment of CRC in a Genentech study, while sparing the healthy colon. The versatility of this novel therapeutic approach is now being exploited by Genentech in their search for antibody combinations for many different cancer types that rely on critical (growth factor) receptors and highly expressed E3 ubiquitin ligases specific to the cancer type in question (Frederic de Sauvage, EMBO | EMBL Symposium - Defining and Defeating Metastasis, June 2022, Heidelberg).

In analogy to expanding this treatment strategy to different cancer types, it would be of great interest to assess if this strategy could also be adapted to target cancer cells in different cellular states earlier during the metastatic cascade. For instance, adjuvant chemotherapy is frequently not curative, presumably as it is targeting proliferating cells, while latent cancer cells are in a distinct transcriptional state (**Chapter 3, Chapter 5, (57,58)**). Thus, it would be of particular interest to test the use of bispecific antibodies for the treatment of metastatic latency. To provide a therapeutic window, the potential pair of targets would have to include at least one receptor that is more strongly and/or more specifically expressed by latent metastatic cells compared to healthy tissues.

Another novel approach, yet less far established for CRC, includes the use of T-cell bispecific antibodies that are designed to bring T-cells into close proximity of cancer cells by co-binding a cancer-specific antigen, inducing subsequent T-cell mediated killing. For instance, the drug mosunetuzumab has already advanced to a phase III clinical trial for lymphoma (NCT04712097) and its exploitability for CRC is currently being investigated.

While most of these novel approaches are established using patient-derived primary CRC organoid lines or murine metastatic CRC models, they rarely reflect the treatment history of patients typically included into clinical trials. Yet, the treatment of cancer cells can transiently or durably change their cellular states and responsiveness to subsequent treatment regimen (58,59). Thus, there is a disconnect between the preclinical testing of novel therapeutics and the first essential tests for safety and efficacy in patients and thus a need for better model systems for highly advanced disease. Currently many laboratories are acquiring longitudinal samples of patients' disease progression including primary tumour and metastatic lines, with the aim of testing their different sensitivity to drugs typically applied in the clinic. This material will further be of great value in assessing if despite of inter-patient heterogeneity, common genetic or transcriptomic features are emerging in response to individual treatment options. In a subsequent step, it would be of interest to test if patient-derived CRC organoids can be used to accurately mimic drug-induced tumour evolution *in vitro*. More specifically, it will be intriguing to see if treatment-refractory lines can be generated in a dish by treating the primary tumour material with the same drugs the patient is receiving and used to subsequently test next-line treatment options and predict the patients' response. Another question that is of concern for the potential use of organoids for personalised medicine concerns the sampling size. What fraction of the tumour has to be sampled to reliably represent the different subclones of the disease? Similarly, for metastatic disease, how much inter-patient heterogeneity exists across different metastases inside a single or across multiple organs? In my opinion, these questions will be instrumental in advancing our understanding of metastatic CRC and of the heterogeneity of the disease.

REFERENCES

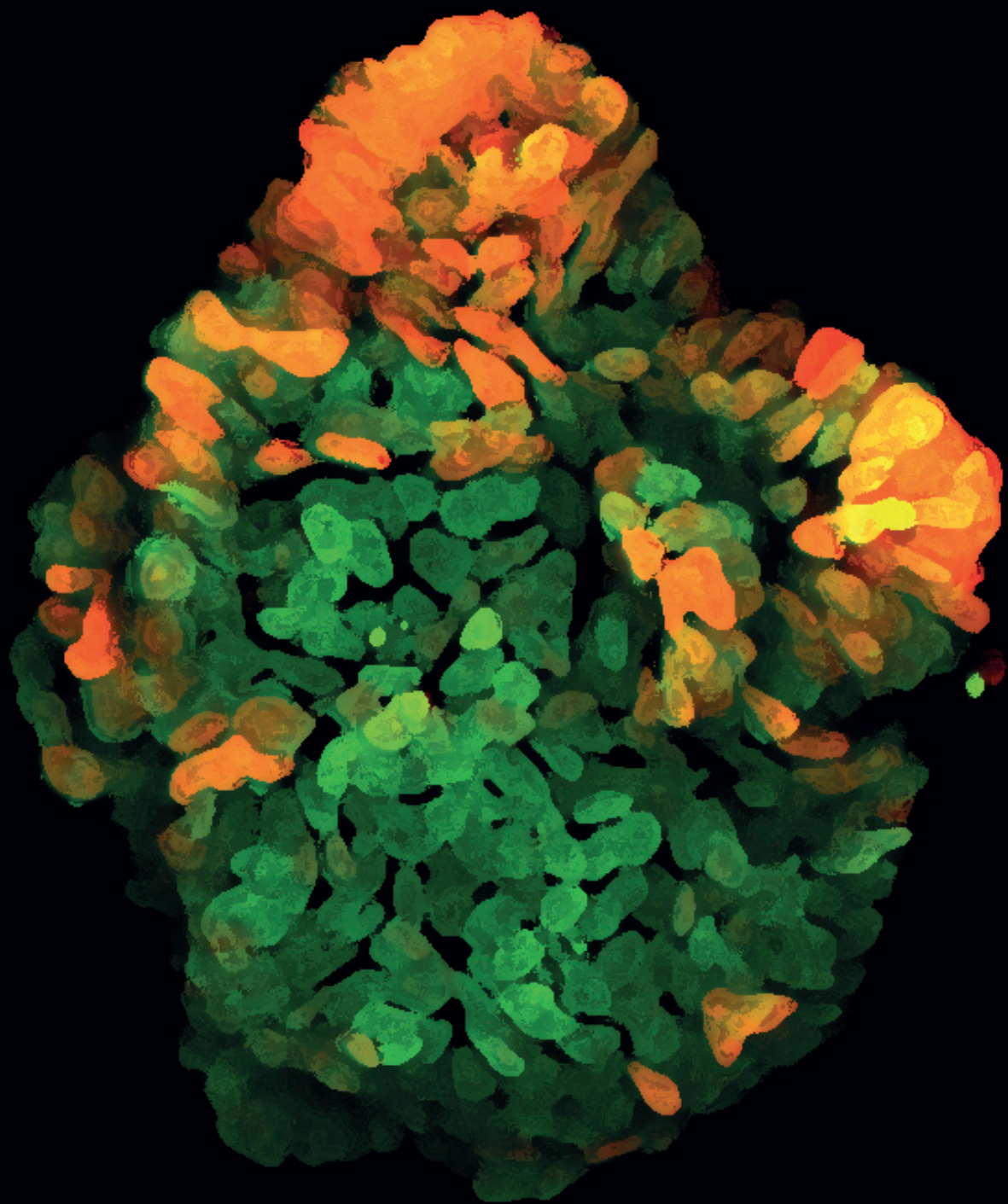
1. Tauriello DVF, Calon A, Lonardo E, Batlle E. Determinants of metastatic competency in colorectal cancer. *Mol Oncol*. 2017;11:97–119.
2. American Cancer Society. Colorectal Cancer Facts & Figures 2020-2022. Atlanta Am Cancer Soc. 2020;66:1–41.
3. Naghavi M, Wang H, Lozano R, Davis A, Liang X, Zhou M, et al. Global, regional, and national age-sex specific all-cause and cause-specific mortality for 240 causes of death, 1990-2013: A systematic analysis for the Global Burden of Disease Study 2013. *Lancet* [Internet]. Elsevier Ltd; 2015;385:117–71. Available from: [http://dx.doi.org/10.1016/S0140-6736\(14\)61682-2](http://dx.doi.org/10.1016/S0140-6736(14)61682-2)
4. Van Der Stok EP, Spaander MCW, Grünhagen DJ, Verhoef C, Kuipers EJ. Surveillance after curative treatment for colorectal cancer. *Nat Rev Clin Oncol* [Internet]. Nat Rev Clin Oncol; 2017 [cited 2022 Jul 5];14:297–315. Available from: <https://pubmed.ncbi.nlm.nih.gov/27995949/>
5. Cardoso R, Guo F, Heisser T, Hackl M, Ihle P, De Schutter H, et al. Colorectal cancer incidence, mortality, and stage distribution in European countries in the colorectal cancer screening era: an international population-based study. *Lancet Oncol*. Elsevier; 2021;22:1002–13.
6. Kuipers EJ, Grady WM, Lieberman D, Seufferlein T, Sung JJ, Boelens PG, et al. Colorectal cancer. *Nat Rev Dis Prim* 2015 11 [Internet]. Nature Publishing Group; 2015 [cited 2022 Jul 5];1:1–25. Available from: <https://www-nature-com.proxy.library.uu.nl/articles/nrdp201565>
7. Dekker E, Tanis PJ, Vleugels JLA, Kasi PM, Wallace MB. Colorectal cancer. *Lancet* [Internet]. Elsevier; 2019 [cited 2022 Jul 5];394:1467–80. Available from: <http://www.thelancet.com/article/S0140673619323190/fulltext>
8. Sinicrope FA. Increasing Incidence of Early-Onset Colorectal Cancer. *N Engl J Med* [Internet]. Massachusetts Medical Society; 2022 [cited 2022 Jul 11];386:1547–58. Available from: <https://www.nejm.org/doi/full/10.1056/NEJMra2200869>
9. Valastyan S, Weinberg RA. Tumor metastasis: Molecular insights and evolving paradigms. *Cell* [Internet]. Elsevier Inc.; 2011;147:275–92. Available from: <http://dx.doi.org/10.1016/j.cell.2011.09.024>
10. Koorman T, Jansen KA, Khalil A, Haughton PD, Visser D, Rätze MAK, et al. Spatial collagen stiffening promotes collective breast cancer cell invasion by reinforcing extracellular matrix alignment. *Oncogene* 2022 4117 [Internet]. Nature Publishing Group; 2022 [cited 2022 Jul 12];41:2458–69. Available from: <https://www-nature-com.proxy.library.uu.nl/articles/s41388-022-02258-1>
11. Cheung KJ, Gabrielson E, Werb Z, Ewald AJ. Collective invasion in breast cancer requires a conserved basal epithelial program. *Cell* [Internet]. Elsevier B.V.; 2013 [cited 2022 Jul 12];155:1639–51. Available from: <http://www.cell.com/article/S0092867413014803/fulltext>
12. Joyce JA, Pollard JW. Microenvironmental regulation of metastasis. *Nat Rev Cancer* 2009 94 [Internet]. Nature Publishing Group; 2008 [cited 2022 Jul 8];9:239–52. Available from: <https://www-nature-com.proxy.library.uu.nl/articles/nrc2618>
13. Degirmenci B, Valenta T, Dimitrieva S, Hausmann G, Basler K. Gli1-expressing mesenchymal cells form the essential Wnt-secreting niche for colon stem cells. *Nature* [Internet]. Springer US; 2018;558:449–53. Available from: <http://dx.doi.org/10.1038/s41586-018-0190-3>
14. Büller NVJA, Rosekrans SL, Westerlund J, van den Brink GR. Hedgehog signaling and maintenance of homeostasis in the intestinal epithelium. *Physiology*. 2012;27:148–55.

15. Shimokawa M, Ohta Y, Nishikori S, Matano M, Takano A, Fujii M, et al. Visualization and targeting of LGR5+ human colon cancer stem cells. *Nature* [Internet]. Nature Publishing Group; 2017 [cited 2022 Jul 28];545:187–92. Available from: <https://www-nature-com.proxy.library.uu.nl/articles/nature22081>
16. Vu T, Datta PK. Regulation of EMT in Colorectal Cancer: A Culprit in Metastasis. *Cancers (Basel)* [Internet]. Multidisciplinary Digital Publishing Institute (MDPI); 2017 [cited 2022 Jul 28];9. Available from: [/pmc/articles/PMC5742819/](https://pubmed.ncbi.nlm.nih.gov/35742819/)
17. Saxena K, Jolly MK, Balamurugan K. Hypoxia, partial EMT and collective migration: Emerging culprits in metastasis. *Transl Oncol* [Internet]. Neoplasia Press; 2020 [cited 2022 Jul 28];13. Available from: [/pmc/articles/PMC7419667/](https://pubmed.ncbi.nlm.nih.gov/3419667/)
18. Löönd F, Sugiyama N, Bill R, Bornes L, Hager C, Tang F, et al. Distinct contributions of partial and full EMT to breast cancer malignancy. *Dev Cell*. Cell Press; 2021;56:3203–3221.e11.
19. Fumagalli A, Oost KC, Kester L, Morgner J, Bornes L, Bruens L, et al. Plasticity of Lgr5-Negative Cancer Cells Drives Metastasis in Colorectal Cancer. *Cell Stem Cell* [Internet]. Elsevier Inc.; 2020;26:569–578.e7. Available from: <https://doi.org/10.1016/j.stem.2020.02.008>
20. Alitalo K, Tammela T, Petrova T V. Lymphangiogenesis in development and human disease. *Nat* 2005 4387070 [Internet]. Nature Publishing Group; 2005 [cited 2022 Jul 8];438:946–53. Available from: <https://www-nature-com.proxy.library.uu.nl/articles/nature04480>
21. Gupta GP, Massagué J. Cancer Metastasis: Building a Framework. *Cell*. Cell Press; 2006;127:679–95.
22. Brown M, Assen FP, Leithner A, Abe J, Schachner H, Asfour G, et al. Lymph node blood vessels provide exit routes for metastatic tumor cell dissemination in mice. *Science* [Internet]. American Association for the Advancement of Science; 2018 [cited 2022 Jul 8];359:1408–11. Available from: <https://www-science-org.proxy.library.uu.nl/doi/10.1126/science.aal3662>
23. Pereira ER, Kedrin D, Seano G, Gautier O, Meijer EFJ, Jones D, et al. Lymph node metastases can invade local blood vessels, exit the node, and colonize distant organs in mice. *Science* [Internet]. American Association for the Advancement of Science; 2018 [cited 2022 Jul 8];359:1403–7. Available from: <https://www-science-org.proxy.library.uu.nl/doi/10.1126/science.aal3622>
24. Ubellacker JM, Tasdogan A, Ramesh V, Shen B, Mitchell EC, Martin-Sandoval MS, et al. Lymph protects metastasizing melanoma cells from ferroptosis. *Nat* 2020 5857823 [Internet]. Nature Publishing Group; 2020 [cited 2022 Jul 8];585:113–8. Available from: <https://www-nature-com.proxy.library.uu.nl/articles/s41586-020-2623-z>
25. Rogiers A, Lobon I, Spain L, Turajlic S. The Genetic Evolution of Metastasis. *Cancer Res*. 2022;82:1849–57.
26. Diamantopoulou Z, Castro-Giner F, Schwab FD, Foerster C, Saini M, Budinjas S, et al. The metastatic spread of breast cancer accelerates during sleep. *Nat* 2022 [Internet]. Nature Publishing Group; 2022 [cited 2022 Jun 30];1–7. Available from: <https://www-nature-com.proxy.library.uu.nl/articles/s41586-022-04875-y>
27. Hanahan D, Weinberg RA. Hallmarks of Cancer: The Next Generation. *Cell*. Cell Press; 2011;144:646–74.
28. Carmeliet P, Jain RK. Principles and mechanisms of vessel normalization for cancer and other angiogenic diseases. *Nat Rev Drug Discov* 2011 106 [Internet]. Nature Publishing Group; 2011 [cited 2022 Jul 8];10:417–27. Available from: <https://www-nature-com.proxy.library.uu.nl/articles/nrd3455>
29. Obenauf AC, Massagué J. Surviving at a Distance: Organ-Specific Metastasis. *Trends in Cancer* [Internet]. Elsevier Ltd; 2015;1:76–91. Available from: <http://dx.doi.org/10.1016/j.trecan.2015.07.009>

30. Nguyen DX, Bos PD, Massagué J. Metastasis: from dissemination to organ-specific colonization. *Nat Rev Cancer* 2009 94 [Internet]. Nature Publishing Group; 2009 [cited 2022 Jul 8];9:274-84. Available from: <https://www-nature-com.proxy.library.uu.nl/articles/nrc2622>
31. Heinz MC, Peters NA, Oost KC, Lindeboom RG, van Voorthuisen L, Fumagalli A, et al. Liver Colonization by Colorectal Cancer Metastases Requires YAP-Controlled Plasticity at the Micrometastatic Stage. *Cancer Res* [Internet]. American Association for Cancer Research; 2022 [cited 2022 May 16];82:1953-68. Available from: <https://aacrjournals.org/cancerres/article/82/10/1953/696332/Liver-Colonization-by-Colorectal-Cancer-Metastases>
32. Cheung KJ, Ewald AJ. A collective route to metastasis: Seeding by tumor cell clusters. *Science* [Internet]. American Association for the Advancement of Science; 2016 [cited 2022 Jul 8];352:167-9. Available from: <https://www-science-org.proxy.library.uu.nl/doi/10.1126/science.aaf6546>
33. Aceto N, Bardia A, Miyamoto DT, Donaldson MC, Wittner BS, Spencer JA, et al. Circulating Tumor Cell Clusters Are Oligoclonal Precursors of Breast Cancer Metastasis. *Cell*. Cell Press; 2014;158:1110-22.
34. Hou JM, Krebs MG, Lancashire L, Sloane R, Backen A, Swain RK, et al. Clinical significance and molecular characteristics of circulating tumor cells and circulating tumor microemboli in patients with small-cell lung cancer. *J Clin Oncol*. 2012;30:525-32.
35. Dang HX, Krasnick BA, White BS, Grossman JG, Strand MS, Zhang J, et al. The clonal evolution of metastatic colorectal cancer. *Sci Adv* [Internet]. American Association for the Advancement of Science; 2020 [cited 2022 Jul 8];6. Available from: <https://www-sciadv.aay9691>
36. Sosa MS, Bragado P, Aguirre-Ghiso JA. Mechanisms of disseminated cancer cell dormancy: An awakening field. *Nat Rev Cancer*. Nature Publishing Group; 2014;14:611-22.
37. Hugen N, Van de Velde CJH, De Wilt JHW, Nagtegaal ID. Metastatic pattern in colorectal cancer is strongly influenced by histological subtype. *Ann Oncol*. Elsevier; 2014;25:651-7.
38. Kwon J, Bakhoun SF. The cytosolic DNA-sensing cGAS-sting pathway in cancer. *Cancer Discov* [Internet]. American Association for Cancer Research Inc.; 2020 [cited 2022 Jul 26];10:26-39. Available from: <https://aacrjournals.org/cancerdiscovery/article/10/1/26/2314/The-Cytosolic-DNA-Sensing-cGAS-STING-Pathway-in>
39. Berlin J, Bendell JC, Hart LL, Firdaus I, Gore I, Hermann RC, et al. A randomized phase II trial of vismodegib versus placebo with FOLFOX or FOLFIRI and bevacizumab in patients with previously untreated metastatic colorectal cancer. *Clin Cancer Res*. 2013;19:258-67.
40. Gao L, Zhang Z, Zhang P, Yu M, Yang T. Role of canonical Hedgehog signaling pathway in liver. *Int J Biol Sci* [Internet]. Ivyspring International Publisher; 2018 [cited 2022 Jul 12];14:1636. Available from: [/pmc/articles/PMC6216024/](https://pmc/articles/PMC6216024/)
41. Kitamura T, Qian BZ, Pollard JW. Immune cell promotion of metastasis. *Nat Rev Immunol* [Internet]. NIH Public Access; 2015 [cited 2022 Jul 12];15:73. Available from: [/pmc/articles/PMC4470277/](https://pmc/articles/PMC4470277/)
42. Malladi S, Macalinao DG, Jin X, He L, Basnet H, Zou Y, et al. Metastatic Latency and Immune Evasion through Autocrine Inhibition of WNT. *Cell*. 2016;165:45-60.
43. Amado RG, Wolf M, Peeters M, Van Cutsem E, Siena S, Freeman DJ, et al. Wild-type KRAS is required for panitumumab efficacy in patients with metastatic colorectal cancer. *J Clin Oncol*. American Society of Clinical Oncology; 2008;26:1626-34.

44. Douillard J-Y, Oliner KS, Siena S, Tabernero J, Burkes R, Barugel M, et al. Panitumumab-FOLFOX4 Treatment and RAS Mutations in Colorectal Cancer. *N Engl J Med* [Internet]. New England Journal of Medicine (NEJM/MMS); 2013 [cited 2022 Jul 11];369:1023–34. Available from: <https://www.nejm.org/doi/10.1056/NEJMoa1305275>
45. Hurwitz H, Fehrenbacher L, Novotny W, Cartwright T, Hainsworth J, Heim W, et al. Bevacizumab plus Irinotecan, Fluorouracil, and Leucovorin for Metastatic Colorectal Cancer. <https://doi.org/10.1056/NEJMoa032691> [Internet]. Massachusetts Medical Society; 2004 [cited 2022 Jul 11];350:2335–42. Available from: <https://www.nejm.org/doi/10.1056/NEJMoa032691>
46. Cunningham D, Humblet Y, Siena S, Khayat D, Bleiberg H, Santoro A, et al. Cetuximab Monotherapy and Cetuximab plus Irinotecan in Irinotecan-Refractory Metastatic Colorectal Cancer. <https://doi.org/10.1056/NEJMoa033025> [Internet]. Massachusetts Medical Society; 2004 [cited 2022 Jul 11];351:337–45. Available from: <https://www.nejm.org/doi/10.1056/NEJMoa033025>
47. Van Cutsem E, Peeters M, Siena S, Humblet Y, Hendlisz A, Neyns B, et al. Open-label phase III trial of panitumumab plus best supportive care compared with best supportive care alone in patients with chemotherapy-refractory metastatic colorectal cancer. *J Clin Oncol. American Society of Clinical Oncology*; 2007;25:1658–64.
48. Tabernero J, Yoshino T, Cohn AL, Obermannova R, Bodoky G, Garcia-Carbonero R, et al. Ramucirumab versus placebo in combination with second-line FOLFIRI in patients with metastatic colorectal carcinoma that progressed during or after first-line therapy with bevacizumab, oxaliplatin, and a fluoropyrimidine (RAISE): a randomised, double-blind, multicentre, phase 3 study. *Lancet Oncol. Elsevier*; 2015;16:499–508.
49. Grothey A, Van Cutsem E, Sobrero A, Siena S, Falcone A, Ychou M, et al. Regorafenib monotherapy for previously treated metastatic colorectal cancer (CORRECT): An international, multicentre, randomised, placebo-controlled, phase 3 trial. *Lancet* [Internet]. Elsevier B.V.; 2013 [cited 2022 Jul 11];381:303–12. Available from: <http://www.thelancet.com/article/S014067361261900X/fulltext>
50. André T, Shiu K-K, Kim TW, Jensen BV, Jensen LH, Punt C, et al. Pembrolizumab in Microsatellite-Instability-High Advanced Colorectal Cancer. *N Engl J Med* [Internet]. Massachusetts Medical Society; 2020 [cited 2022 Jul 11];383:2207–18. Available from: <https://www.nejm.org/doi/full/10.1056/NEJMoa2017699>
51. Kanani A, Veen T, Sørreide K. Neoadjuvant immunotherapy in primary and metastatic colorectal cancer. *Br J Surg* [Internet]. Oxford Academic; 2021 [cited 2022 Jul 11];108:1417–25. Available from: <https://academic.oup.com/bjs/article/108/12/1417/6409933>
52. Overman MJ, McDermott R, Leach JL, Lonardi S, Lenz HJ, Morse MA, et al. Nivolumab in patients with metastatic DNA mismatch repair-deficient or microsatellite instability-high colorectal cancer (CheckMate 142): an open-label, multicentre, phase 2 study. *Lancet Oncol. Elsevier*; 2017;18:1182–91.
53. Lenz HJ, Van Cutsem E, Luisa Limon M, Wong KYM, Hendlisz A, Aglietta M, et al. First-Line Nivolumab Plus Low-Dose Ipilimumab for Microsatellite Instability-High/Mismatch Repair-Deficient Metastatic Colorectal Cancer: The Phase II CheckMate 142 Study. *J Clin Oncol. NLM (Medline)*; 2022;40:161–70.
54. Cercek A, Lumish M, Sinopoli J, Weiss J, Shia J, Lamendola-Essel M, et al. PD-1 Blockade in Mismatch Repair-Deficient, Locally Advanced Rectal Cancer. *N Engl J Med* [Internet]. Massachusetts Medical Society; 2022 [cited 2022 Jul 11];386:2363–76. Available from: <https://www.nejm.org/doi/full/10.1056/NEJMoa2201445>

55. Chalabi M, Fanchi LF, Dijkstra KK, Van den Berg JG, Aalbers AG, Sikorska K, et al. Neoadjuvant immunotherapy leads to pathological responses in MMR-proficient and MMR-deficient early-stage colon cancers. *Nat Med* 2020 264 [Internet]. Nature Publishing Group; 2020 [cited 2022 Jul 11];26:566–76. Available from: <https://www-nature-com.proxy.library.uu.nl/articles/s41591-020-0805-8>
56. Herpers B, Eppink B, James MI, Cortina C, Cañellas-Socias A, Boj SF, et al. Functional patient-derived organoid screenings identify MCLA-158 as a therapeutic EGFR × LGR5 bispecific antibody with efficacy in epithelial tumors. *Nat Cancer* [Internet]. Springer US; 2022 [cited 2022 Jul 12];3:418–36. Available from: <https://www-nature-com.proxy.library.uu.nl/articles/s43018-022-00359-0>
57. Laughney AM, Hu J, Campbell NR, Bakhoun SF, Setty M, Lavallée VP, et al. Regenerative lineages and immune-mediated pruning in lung cancer metastasis. *Nat Med* [Internet]. Springer US; 2020;26:259–69. Available from: <http://dx.doi.org/10.1038/s41591-019-0750-6>
58. Álvarez-Varela A, Novellademunt L, Barriga FM, Hernando-Momblona X, Cañellas-Socias A, Cano-Crespo S, et al. Mex3a marks drug-tolerant persister colorectal cancer cells that mediate relapse after chemotherapy. *Nat Cancer* 2022 [Internet]. Nature Publishing Group; 2022 [cited 2022 Jul 1];1–19. Available from: <https://www-nature-com.proxy.library.uu.nl/articles/s43018-022-00402-0>
59. Haas L, Elewaut A, Gerard CL, Umkehrer C, Leindecker L, Pedersen M, et al. Acquired resistance to anti-MAPK targeted therapy confers an immune-evasive tumor microenvironment and cross-resistance to immunotherapy in melanoma. *Nat Cancer* 2021 27 [Internet]. Nature Publishing Group; 2021 [cited 2022 Jul 22];2:693–708. Available from: <https://www-nature-com.proxy.library.uu.nl/articles/s43018-021-00221-9>



APPENDIX

Dutch Summary
German Summary
List of Publications
Curriculum Vitae
Acknowledgements



NEDERLANDSE SAMENVATTING

Darmkanker is wereldwijd op de twee na meest voorkomende vormen van kanker. Indien vroegtijdig ontdekt, is er een goede kans op genezing door chirurgische verwijdering van het aangetaste deel van de dikke darm. Het gevaar schuilt in kankercellen die zich van de primaire tumor losmaken en door het menselijk lichaam migreren, aangezien zij kunnen leiden tot de vorming van nieuwe laesies in andere organen, wat *metastasering* wordt genoemd. Aangezien uitgezaaide colorectale kanker moeilijk te behandelen is, is veruit de beste toekomstige strategie in de strijd tegen darmkanker gebaseerd op screeningprogramma's die gericht zijn op vroegtijdige opsporing in groepen met een hoog risico. Aangezien colorectale kanker gewoonlijk gedurende een periode van enkele decennia ontwikkelt, kan een screeninginterval van 5-10 jaar voldoende zijn voor vroegtijdige opsporing. Hoewel de Europese Raad het potentieel van screening op colorectale kanker reeds heeft erkend en de invoering van screening op CRC heeft aanbevolen op bestuursniveau, moeten wij ons allen inspannen om het persoonlijke risico en de maatschappelijke last van colorectale kanker te verminderen. We mogen echter niet verwachten dat screening de enige oplossing is. Gebrek aan deelname door het daarmee gepaard gaande ongemak of de angst voor positieve resultaten, de kwaliteit van de screening en de ontwikkeling van de ziekte buiten de typische leeftijdsgroep zijn slechts enkele redenen waarom verbeterde behandelingsmogelijkheden voor gevorderde darmkanker nog steeds noodzakelijk zijn.

In deze studie hebben wij daarom de basisprincipes van metastasering bij darmkanker onderzocht. We hebben in het bijzonder de laatste stap van de metastatische cascade bestudeerd, wanneer kankercellen in andere organen zijn genesteld en daar een nieuwe tumor groeien. Deze uitzaaiingen groeien in sommige gevallen uit tot waarneembare laesies, terwijl ze in andere gevallen maanden tot tientallen jaren in organen schuilhouden als zogenaamde *micrometastasen*. Ook al hebben deze micrometastasen geen directe invloed op de gezondheid van de patiënt, toch zijn het risicofactoren die uiteindelijk opnieuw zullen gaan groeien en zich tot een macroscopische laesie zullen ontwikkelen. De observatie dat uitzaaiingen bij verschillende patiënten op verschillende momenten uitgroeien, illustreert dat elke kanker anders is. Niet alleen verschilt de combinatie van onderliggende veranderingen in het genoom die (deels) verantwoordelijk zijn voor het ontstaan van de ziekte van patiënt tot patiënt, zelfs binnen één tumor is er een grote heterogeniteit van cel tot cel. Deze heterogeniteit wordt gevonden in het genoom, alsmede bij de effectormoleculen van de cellen, de RNA's en de daaruit resulterende eiwitten. In deze studie hebben wij het fenomeen cellulaire heterogeniteit tussen, maar

vooral binnen, patiënten onderzocht door de *cellulaire toestanden*, samenstelling en veranderingen van tumorcel subpopulaties tijdens metastatische groei te onderzoeken.

Daartoe hebben wij gebruik gemaakt van een betrekkelijk nieuwe celkweekmethode van organoïden uit volwassen stamcellen (ontwikkeld in 2009), waarmee tumorcellen uit biopsies kunnen worden geïsoleerd en in het laboratorium voor onbepaalde tijd kunnen worden gekweekt, met behoud van belangrijke kenmerken van de individuele ziekte. Dit materiaal, dat groeit als *organoïden*, kan worden gecombineerd met reporter-systemen die kleurcodes geven aan specifieke subpopulaties van cellen op basis van hun cellulaire toestand. Met behulp van dergelijke *reporter-systemen* hebben wij onderscheid gemaakt tussen kankerstamcellen en niet-stamcellen, of tussen prolifererende en niet-prolifererende (in rust) cellen. De combinatie van patiënten afkomstige darmkanker organoïden met genetische manipulatie technieken (integratie van reporter systemen of wijziging van het genoom door CRISPR/Cas9 technologie) vormt de basis voor de meeste van de in dit werk uitgevoerde experimenten. In het laboratorium hebben wij darmkanker organoïden gebruikt om cellulaire heterogeniteit in detail en met hoge tijd resolutie te bestuderen, terwijl transplantaties van organoïden in muizen zijn uitgevoerd om vragen te beantwoorden in de context van een ontwikkelend organisme (b.v. metastatische groei in de lever).

In **hoofdstuk 1** geven wij een literatuuroverzicht van de algemene biologie van de darm en het colon. Wij concentreren ons op het regeneratiepotentieel van de darm en beschrijven wat er gebeurt wanneer cellen beschadigd raken en vervolgens verloren gaan. In het bijzonder kan het verlies van volwassen darmstamcellen op opmerkelijke wijze worden gecompenseerd door andere cellen die vervolgens van identiteit veranderen en de basistaken van darmstamcellen overnemen. Deze verwerving van stamceleigenschappen omvat onder meer het vermogen tot proliferatie en de productie van nieuwe stamcellen (zelfvernieuwing) en is daarom van bijzonder belang in de kankerbiologie, waar cellen stamachtige trekken aannemen en gekenmerkt worden door onbeperkte proliferatie. **Hoofdstuk 2** beschrijft het experimentele werk aan het STAR-reporter-systeem, dat tot doel heeft de cellulaire heterogeniteit tussen kankerstamcellen en gezonde darmstamcellen in vergelijking met niet-stamcellen te verduidelijken. Wij beschrijven enkele STAR-varianten die geschikt zijn voor verschillende experimentele opstellingen en geven aanwijzingen voor de integratie van STAR in organoïden.

Organoïden van darmkanker met de STAR-reporter worden in **hoofdstuk 3** gebruikt om de samenstelling van micro- en macrometastasen te onderzoeken. Wij tonen aan

dat in micrometastasen geen kankerstamcellen aanwezig zijn, terwijl macrometastasen zowel kankerstamcellen als niet-kankerstamcellen bevatten, hetgeen bevestigt dat kankerstamcellen belangrijk zijn voor metastatische groei. Verder tonen we aan dat de eerste metastatische cellen zich in een specifieke cellulaire (transcriptionele) toestand bevinden die wordt gekenmerkt door regeneratieve YAP-activiteit, wat belangrijk is voor de overleving van de geïsoleerde cellen. Door organoïdgroei te gebruiken als een model van metastatische groei, hebben we veranderingen in de cellulaire toestand van kankercellen in de tijd kunnen bestuderen. Er werd ontdekt dat verlenging van de initiële YAP status de vorming van cellulaire heterogeniteit en efficiënte groei kan verhinderen, wat suggereert dat deze YAP status één van de factoren kan zijn die de uitgroei van micrometastasen beperken.

Studies van organoïdgroei met behulp van de STAR-reporter worden voortgezet in **hoofdstuk 4** om meer gedetailleerd inzicht te verschaffen in de onderliggende processen van de verschillende cellulaire staten in de tijd. Wij gebruiken twee verschillende sequencing strategieën (RNA- en chromatine-gebaseerd) om de belangrijkste effectormoleculen van verschillende cellulaire staten te karakteriseren. Wij tonen aan dat de aanvankelijke YAP-status, zoals beschreven in hoofdstuk 3, wordt gevolgd door een zeer proliferatieve fase voordat de kankerstamcel- en de niet-stamcel-status uiteindelijk meer gedefinieerd worden. Verder onderzoeken we in meer detail hoe kankerstamcellen ontstaan binnen organoïden gevormd van niet-stamcellen, en presenteren we aanwijzingen dat de MAPK-signaalroute een essentiële rol speelt in dit proces. Wanneer deze bevinding wordt vertaald naar metastasen, kan redelijkerwijs worden aangenomen dat de activiteit van de MAPK-route vereist is voor de vorming van kankerstamcellen in voorheen stamcel-negatieve micrometastasen.

In **hoofdstuk 5** onderzoeken we de cellulaire toestand van prolifererende en niet-prolifererende cellen in micro- en macrometastasen met behulp van een reporter systeem in rust. We beschrijven hoe experimenteel geïnduceerde micrometastasen ofwel volledig cyclisch ofwel volledig niet-cyclisch zijn, terwijl macrometastasen beide subpopulaties bevatten. Om de verschillen tussen subpopulaties van metastasen van verschillende grootte te onderzoeken, is de rustreporter dan ook onvoldoende. In plaats daarvan zijn aanvullende methoden nodig om metastatische laesies op basis van hun grootte te onderscheiden. Hier beschrijven we een protocol om leverdissociatie uit te breiden met verschillende stappen die scheiding van metastasegrootte mogelijk maken. Met deze aanpak vinden verschillen tussen de cellulaire status (transcriptomen) van micro- en macrometastasen. Micrometastasen verschillen in hun metabolisme van

macrometastasen, terwijl de laatste meer tekenen vertonen van detectie van- en interactie met hun milieu. Aangezien deze verschillen ook tot uiting komen in de subpopulaties van kankercellen, zal het van groot belang zijn om te zien of de verschillende status van metastasen therapeutisch kan worden geëxploiteerd.

Hoofdstuk 6 richt zich op de rol van de Hedgehog signaalroute in darmkanker. Bij deze signaalroute zijn verschillende celpopulaties betrokken, aangezien de communicatie tussen ligand-producerende en ligand-ontvangende cellen betreft. Aangezien de beschikbare literatuur tegenstrijdige gegevens bevat over de effecten van de Hedgehog signaalroute in darmkanker en over de betrokken celtypes, hebben wij deze route op verschillende niveaus onderzocht. Wij tonen eerst aan dat Hedgehog liganden geproduceerd worden door darmkankercellen, vooral door de niet-stamcellen. Daar we geen signaaltransductie tussen verschillende tumor subpopulaties vinden, lijkt het erop dat, net als in de gezonde darm, de niet-epitheliale cellen de signaal-ontvangers zijn. Om deze hypothese te toetsen genereerden wij darmkanker organoïden die geen Hedgehog liganden kunnen produceren met CRISPR/Cas9 technologie, en vergelijken wij hun gedrag met dat van de Hedgehog ligand-competente lijn na transplantatie in muizen. Voorlopige resultaten suggereren dat Hedgehog liganden de groei van metastasen vertragen, maar verdere experimentele validatie is nodig.

Ten slotte vatten we de resultaten van dit werk samen in **hoofdstuk 7**, waarbij we de nadruk leggen op nieuwe bevindingen, experimentele tekortkomingen, de bredere literatuurcontext en toekomstperspectieven.

DEUTSCHE ZUSAMMENFASSUNG

Darmkrebs ist weltweit die dritthäufigste Krebsart. Bei frühzeitiger Erkennung bestehen gute Heilungschancen durch eine chirurgische Resektion des befallenen Teils des Dickdarms. Die Gefahr liegt in Krebszellen, die sich vom Primärtumor ablösen, durch den menschlichen Körper wandern und zur Bildung neuer Läsionen in anderen Organen führen können, was als *Metastasierung* bezeichnet wird. Da metastasierender Darmkrebs schwer zu behandeln ist, basiert die mit Abstand beste Zukunftsstrategie im Kampf gegen Darmkrebs auf Screening-Programmen, die auf die Früherkennung in Risikogruppen abzielen. Screening-Intervalle von 5-10 Jahre reichen dabei aus, da sich Darmkrebs in der Regel über eine Zeitspanne von einigen Jahrzehnten entwickelt. Auch wenn der Europäische Rat das Potenzial der Darmkrebsvorsorge bereits erkannt und die Implementierung einer solchen empfohlen hat, müssen wir alle daran mitwirken, das persönliche Risiko und die gesellschaftliche Belastung durch Darmkrebs zu verringern. Es ist jedoch nicht zu erwarten, dass die Darmkrebsvorsorge eine vollumfassende Lösung darstellt. Die mangelnde Teilnahme aufgrund der damit verbundenen Unannehmlichkeiten oder der Angst vor positiven Ergebnissen, die Qualität des Screenings und die Entwicklung der Krankheit außerhalb der typischen Altersspanne sind nur einige der Gründe, weshalb verbesserte Behandlungsmöglichkeiten für fortgeschrittene Darmkrebserkrankungen nach wie vor erforderlich sind.

In dieser Arbeit haben wir daher die grundlegenden Prinzipien der Metastasenbildung bei Darmkrebs untersucht, wobei wir uns auf den letzten Schritt der Metastasierungskaskade konzentriert haben; den Schritt wenn Krebszellen bereits in ein räumlich entferntes Organ eingedrungen sind und zu klinisch nachweisbaren Läsionen heranwachsen können, die dann die Funktion des Organs beeinträchtigen und somit einen negativen Einfluss auf die Gesundheit des Patienten haben.

Es ist bekannt, dass Metastasen manchmal auswachsen, während sie in anderen Fällen als sogenannte *Mikrometastasen* über Monate, Jahre oder sogar Jahrzehnte in Organen verweilen. Auch wenn diese Mikrometastasen die Gesundheit des Patienten zunächst nicht beeinträchtigen, stellen sie eine ständige Bedrohung dar, da es sein kann, dass sie irgendwann anfangen zu wachsen und sich zu einer makroskopischen Läsion entwickeln. Die Tatsache, dass sich Metastasen bei verschiedenen Patienten zu unterschiedlichen Zeitpunkten bilden, verdeutlicht dass jeder Krebs verschiedene Eigenschaften aufweist. Die Kombination der zugrunde liegenden Veränderungen im Genom, die (zumindest teilweise) für die Entwicklung der Krankheit ursächlich ist, ist von Patient zu Patient

unterschiedlich. Doch selbst innerhalb eines einzelnen Tumors gibt es von Zelle zu Zelle große Unterschiede. Diese Heterogenität betrifft die Ebene des Genoms, aber auch die Effektormoleküle der Zellen: RNAs und die daraus resultierenden Proteine. In dieser Arbeit liegt der Fokus auf der zellulären Heterogenität zwischen aber vor allem innerhalb von Patienten beschäftigt. Dazu haben wir die *zellulären Zustände*, das heißt die Zusammensetzung und die Veränderungen von Tumorzellsubpopulationen während des metastatischen Wachstums untersucht.

Hierzu haben wir eine relativ neue Zellkulturmethode (aus dem Jahr 2009) genutzt, mit deren Hilfe Tumorzellen aus Biopsien isoliert und im Labor unbegrenzt vermehrt werden können. Dieses als *Organoide* wachsende Material verkörpert wichtige Merkmale einer jeden individuellen Erkrankung. Organoide können mit *Reportersystemen* kombiniert werden, die bestimmte Subpopulationen von Zellen auf der Grundlage ihres zellulären Zustands farblich codieren. Mithilfe solcher Reportersysteme haben wir Krebsstammzellen von Nicht-Stammzellen oder sich teilende (*proliferierende*) von sich nicht-teilenden (*quieszenten*) Zellen unterschieden. Aus Patienten gewonnene Darmkrebsorganoide bilden in Kombination mit gentechnischen Verfahren (Integration von Reportersystemen oder Veränderung des Genoms durch CRISPR/Cas9-Technologie) die Grundlage bzw. das Ausgangsmaterial für die meisten im Rahmen dieser Arbeit durchgeführten Experimente. Im Labor haben wir Darmkrebsorganoide verwendet, um die zelluläre Heterogenität mit hoher zeitlicher Auflösung eingehend zu untersuchen. Zusätzlich wurden Transplantationen von Organoiden in Mäuse durchgeführt, um Fragen zu klären, die einen Organismus für eine angemessene Darstellung erfordern (z. B. metastatisches Wachstum in der Leber).

In **Kapitel 1** geben wir einen Literaturübersicht über die allgemeine Biologie des Darms. Wir konzentrieren uns auf das Regenerationspotenzial des Darms und beschreiben die Auswirkungen wenn Zellen beschädigt werden und anschließend absterben. Der Verlust von adulten Darmstammzellen kann bemerkenswerterweise durch andere Zellen kompensiert werden, die daraufhin ihre Identität ändern und die grundlegenden Aufgaben von Darmstammzellen übernehmen. Dieser Erwerb von Stammzeleigenschaften beinhaltet unter anderem das Potenzial, sich zu vermehren und weitere Stammzellen zu produzieren und ist daher von besonderem Interesse für die Krebsbiologie, in der Zellen stammzell-artige Eigenschaften annehmen und sich durch uneingeschränkte Vermehrung auszeichnen.

Kapitel 2 beschreibt die technische Arbeit am STAR-Reportersystem, das entwickelt wurde, um die zelluläre Heterogenität zwischen krebstartigen und gesunden Darmstammzellen

im Vergleich zu Nicht-Stammzellen auflösen zu können. Wir beschreiben verschiedene STAR-Varianten, die für unterschiedliche Versuchsaufbauten geeignet sind, und geben eine Anleitung zur Inkorporation von STAR in Organoide.

Darmkrebsorganoide mit dem STAR-Reporter werden in **Kapitel 3** verwendet, um die Zusammensetzung von Mikro- und Makrometastasen zu untersuchen. Wir zeigen, dass Mikrometastasen keine Krebsstammzellen aufweisen, während Makrometastasen sowohl Krebsstammzellen als auch Nicht-Stammzellen enthalten. Dies bestätigt, dass Krebsstammzellen für das metastatische Wachstum wichtig sind. Wir zeigen außerdem, dass sich die ersten metastatischen Zellen in einem bestimmten zellulären (Transkriptions-) Zustand befinden, der sich durch eine regenerative YAP-Aktivität auszeichnet, die für das Überleben der isolierten Zellen wichtig ist. Weiterhin verwenden wir Organoidwachstum als Annäherung für metastatisches Wachstum, um Veränderungen in den zellulären Zuständen von Krebszellen im Zeitablauf zu untersuchen. Dabei haben wir festgestellt, dass eine induzierte Verlängerung des anfänglichen YAP-Zustands die Bildung von zellulärer Heterogenität und effizientem Wachstum verhindern kann. Das deutet darauf hin, dass dieser YAP-Zustand einer der Gründe sein könnte, die das Wachstum von Mikrometastasen einschränken.

Die Studien zum Organoidwachstum mit dem STAR-Reporter werden in **Kapitel 4** weitergeführt, um detailliertere Einblicke in die zugrundeliegenden Prozesse der verschiedenen zellulären Zustände im Zeitablauf zu gewinnen. Wir verwenden zwei verschiedene Sequenzierungsstrategien (RNA- und Chromatin-basiert), um wichtige Effektmoleküle verschiedener zellulärer Zustände zu charakterisieren. Wir zeigen, dass auf den in Kapitel 3 beschriebenen anfänglichen YAP-Zustand eine hochgradig proliferative Phase folgt, bevor Krebsstamm- und Nicht-Stammzellzustände schließlich stärker ausgeprägt werden. Darüber hinaus untersuchen wir genauer, wie Krebsstammzellen in Nicht-Stammzell-Organoiden entstehen und präsentieren anfängliche Daten, die darauf hindeuten, dass der MAPK-Signalweg bei diesem Prozess eine wesentliche Rolle spielt. Überträgt man diese Erkenntnis auf die Metastasierung, kann hieraus abgeleitet werden, dass die Aktivität des MAPK-Signalwegs für die Bildung von Krebsstammzellen in bisher stammzellnegativen Mikrometastasen erforderlich ist.

In **Kapitel 5** untersuchen wir den zellulären Zustand von proliferierenden und nicht-proliferierenden Zellen in Mikro- und Makrometastasen mit Hilfe eines Quieszenz-Reportersystems. In experimentellen Metastasenmodellen stellen wir fest, dass in Mikrometastasen entweder alle Zellen proliferieren oder alle Zellen nicht-proliferieren,

während in Makrometastasen beide Subpopulationen enthalten sind. Um die Unterschiede zwischen den Subpopulationen in Metastasen unterschiedlicher Größe zu untersuchen, reicht der Quieszenz-Reporter während der Extrahierung metastatischer Zellen daher nicht aus. Stattdessen sind zusätzliche Methoden erforderlich, um metastatische Läsionen auf der Grundlage ihrer Größe zu isolieren. Wir erweitern ein Dissoziationsprotokoll für Lebergewebe um mehrere Schritte, welches die Trennung von Metastasen basierend auf ihrer Größe ermöglicht. Nach Anwendung dieser Methode finden wir heraus, dass die zellulären Zustände (Transkriptome) von Mikro- und Makrometastasen sehr unterschiedlich sind. Mikrometastasen unterscheiden sich von Makrometastasen in ihrem Stoffwechsel, während Makrometastasen Anzeichen dafür zeigen, dass sie ihre Mikroumgebung wahrnehmen und mit ihr interagieren. Da sich diese Unterschiede auch in den Subpopulationen der Krebszellen widerspiegeln, wäre es aufschlussreich zu untersuchen, ob der unterschiedliche zelluläre Zustand der Mikrometastasen therapeutisch genutzt werden kann.

Kapitel 6 befasst sich mit der Rolle des Hedgehog-Signalwegs bei Darmkrebs. An diesem Signalweg sind verschiedene Zellpopulationen beteiligt, da nur einige Zellen die Liganden produzieren, die in anderen Zellen eine Reaktion hervorrufen. Da die verfügbare Literatur widersprüchliche Daten über die Auswirkungen des Hedgehog-Signalwegs bei Darmkrebs und über die beteiligten Zelltypen enthält, haben wir diesen Signalweg auf mehreren Ebenen untersucht. Zunächst zeigen wir, dass Hedgehogliganden von Darmkrebszellen, insbesondere von Nicht-Stammzellen, produziert werden. Wir finden jedoch keine Hinweise auf eine Signalübertragung zwischen verschiedenen Subpopulationen eines Tumors, was darauf hindeutet, dass die reagierenden Zelltypen aus nicht-krebsartigen Zellen bestehen (wie im gesunden Darm). Daher stellen wir mit Hilfe der CRISPR/Cas9-Technologie Darmkrebsorganoide her, die nicht in der Lage sind, Hedgehogliganden zu produzieren. Als nächstes vergleichen wir in Transplantationsexperimenten deren Verhalten mit dem der ursprünglich Hedgehogliganden exprimierenden Organoide. Erste Daten deuten darauf hin, dass Hedgehogliganden das Wachstum von Metastasen verlangsamen. Allerdings sind weitere experimentelle Validierungen erforderlich.

Abschließend fassen wir die Ergebnisse dieser Arbeit in **Kapitel 7** zusammen, wobei wir neue Erkenntnisse, experimentelle Einschränkungen, den breiteren Literaturkontext und Zukunftsperspektiven diskutieren.

LIST OF PUBLICATIONS

(*: shared first, #: shared corresponding)

Liver Colonization by Colorectal Cancer Metastases Requires YAP-Controlled Plasticity at the Micrometastatic Stage. **Heinz MC***, Peters NA*, Oost KC, Lindeboom RGH, van Voorthuijsen L, Fumagalli A, van der Net MC, de Medeiros G, Hageman JH, Verlaan-Klink I, Borel Rinkes IHM, Liberali P, Gloerich M, van Rheenen J, Vermeulen M, Kranenburg O#, Snippert HJG#. *Cancer Research*. 2022 May 16; 82(10):1953-1968. doi: 10.1158/0008-5472.CAN-21-0933.

Introducing the Stem Cell ASCL2 Reporter STAR into Intestinal Organoids. **Heinz MC***, Oost KC*, Snippert HJG. *STAR Protocols*. 2020 Oct 8; 1(3):100126. doi: 10.1016/j.xpro.2020.100126. eCollection 2020 Dec 18.

Intestinal Regeneration Regulation by the Microenvironment. Hageman JH, **Heinz MC**, Kretzschmar K, van der Vaart J, Clevers H, Snippert HJG. *Developmental Cell*. 2020 Aug 24; 54(4):435-446. doi: 10.1016/j.devcel.2020.07.009.

Plasticity of Lgr5-Negative Cancer Cells Drives Metastasis in Colorectal Cancer. Fumagalli A*, Oost KC*, Kester L, Morgner J, Bornes L, Bruens L, Spaargaren L, Azkanaz M, Schelfhorst T, Beerling E, **Heinz MC**, Postrach D, Seinstra D, Sieuwerts AM, Martens JWM, van der Elst S, van Baalen M, Bhowmick D, Vrisekoop N, Ellenbroek SIJ, Suijkerbuijk SJE, Snippert HJ, van Rheenen J. *Cell Stem Cell*. 2020 Apr 2; 26(4):569-578.e7. doi: 10.1016/j.stem.2020.02.008 . Epub 2020 Mar 12.

Specific Labeling of Stem Cell Activity in Human Colorectal Organoids Using an ASCL2-Responsive Minigene. Oost KC, van Voorthuijsen L, Fumagalli A, Lindeboom RGH, Sprangers J, Omerzu M, Rodriguez-Colman MJ, **Heinz MC**, Verlaan-Klink I, Maurice MM, Burgering BMT, van Rheenen J, Vermeulen M, Snippert HJG. *Cell Reports*. 2018 Feb 6; 22(6):1600-1614. doi: 10.1016/j.celrep.2018.01.033.

Snake Venom Gland Organoids. Post Y*, Puschhof J*, Beumer J*, Kerckamp HM, de Bakker MAG, Slagboom J, de Barbanson B, Wevers NR, Spijkers XM, Olivier T, Kazandjian TD, Ainsworth S, Iglesias CL, van de Wetering WJ, **Heinz MC**, van Ineveld RL, van Kleef RGDM, Begthel H, Korving J, Bar-Ephraim YE, Getreuer W, Rios AC, Westerink RHS, Snippert HJG, van Oudenaarden A, Peters PJ, Vonk FJ, Kool J, Richardson MK, Casewell NR, Clevers H. *Cell*. 2020 Jan 23; 180(2):233-247.e21. doi: 10.1016/j.cell.2019.11.038.

CURRICULUM VITAE

Maria Christine Puschhof (née Heinz) was born on the 1st of April 1992 in Wiesbaden, Germany. She completed her A-levels at Stefan-George-Gymnasium in Bingen in 2010, majoring in Maths, Physics, and French. Maria next studied Physics at Heidelberg University, completing the Bachelor of Science in 2013 (research focus: particle physics) and the Master of Science in 2015 (research focus: medical physics), focusing on heavy ion radiotherapy. Pursuing this interest further, Maria enrolled in the interdisciplinary Radiation Biology programme at Oxford University providing insights into the physical, biological, and medical aspects of cancer radiotherapy from which she graduated (Master of Science, *with distinction*) in 2016. Since 2017, Maria has been working as PhD candidate in Hugo Snippert's group at the University Medical Center Utrecht. The results of the conducted research are presented in this thesis.

ACKNOWLEDGEMENTS

“The smallest act of kindness is worth more than the grandest intention.”

Oscar Wilde

My PhD has been a long journey with many different facets: intense and instructive, complex and creative, exhausting and exciting, challenging and collaborative, wild but worthwhile, fun and fascinating, unique and unforgettable. I am very grateful for the experience and for everybody along the way. I will never be able to put into words just how much the support of all of you has meant to me. Yet, reading Oscar Wilde, I at least want to try.

I thoroughly enjoyed the time in your group, **Hugo**. Thank you for your trust throughout all this time in experimental decisions and designs, small and pricy project decisions, presentations in-house and beyond, and in me despite having an unusual Physics + Radiation Biology educational background. Your trust in your lab allows everybody to grow into his or her role and I have learnt a great deal from this and from you. I very much appreciate that your door is always open and that in a “crisis”, you always look for the solution rather than for the culprit. It is amazing what you have achieved since starting your own lab and I am sure there is even more in the next decades to come...

Boudewijn, you are the master promoter of the former MCR with all its young research groups. Thank you for also supervising me in this role, for being available when I needed your support, and quite in general, for generating such a great atmosphere in the department.

Suz and **Marjo**, thank you for being such terrific friends. Being colleagues on top of that, you have cheered up every day. (Literally, every day with occasional weekend shifts, too...) There is a lot I will miss: at work, breaks with a fancy cappu or a Broodje Ben, project brainstorming, science or career discussions, and sharing the ups and downs of individual working days. And at least equally much the pre-work breakfast sessions, dinner parties at each others' places or in the city centre, and all these ours spent chatting about personal life, laughing, drinking, exchanging plans and dreams that have formed the foundation of our friendship. Let's keep it up! Suz, your talent of enacting scenes and Marjo, your dry humour are fantastic and made me crack up countless times. Thank you for always being there for me. And last but not least, thanks a lot for doing such an amazing job as my paranymphs.

Niek, I really enjoyed your positive nature and your attitude of making things possible in the lab. If it meant more mouse experiments, days that wouldn't end at the FACS machine

or all these endless stainings, you were always ready for action. We really pushed our publication together over the finish line. I wish you the best of luck with wrapping up your thesis, for your work in the clinic, and everything else.

Koen, you are the inventor of STAR and with this you have provided a tool that was not only perfectly designed to match my interest of intratumoral heterogeneity at the time of interviewing with Hugo but it also became a big part of many of my PhD projects. I thoroughly enjoyed planning and performing experiments with you for the 'movieSTAR' paper. Many thanks for your cheerful nature and for getting me started with STAR and quite general in the lab.

There is a lot to thank you for, **Ingrid**. In many of my projects you were busy with culturing, clone picking and genotyping, and on many Fridays with lentiviral transductions that have dragged on into the evening hours. Next to this, you are the tidy soul of the lab. Without you, freezers (and fridges as a matter of fact) would never be defrosted, at least half of our samples would forever be lost in liquid nitrogen, and if we were to make conditioned media ourselves, we would probably kill off all our organoids.

Bas, I will miss you random sounds, especially the duck-like one, your outbursts of Spanish, and your music replacing much-too-often-heard radio songs. Your love for cloning has generally infected the entire group, which is why we are having many cool reporter systems at hand but also way too many infusion primers and plasmids (at least I do). Having said this, keep up cloning!

Sander, you are a central element of a positive atmosphere in the Snippert group. You're literally always approachable and ready to help anywhere you can. You're the only Snippert who can reliably run a Western Blot (or even the only person world-wide?) which is just one example of where you contribute with expertise. Best of luck with wrapping up the current manuscript – I'll keep my fingers crossed.

My first student, **Joris**. I really enjoyed being your supervisor quite early during my PhD time. Your eagerness to learn and readiness to think along and question things are just two of the reasons why it's great to have you back on board as PhD. I will miss our spontaneous science discussions in the office for which half an hour is usually only a warm up and maybe even sometimes your Dutch bluntness.

Julian, thanks for all your positivity and the pleasant atmosphere you generate. I really enjoyed all the RNA-seq discussions, the coffee breaks to start the working day (or at any time of the day really), and the snacks to avoid an afternoon dip. I hope your tuft cells

won't continuously be tough cells to describe and I wish you all the luck for the next steps, both for and beyond your PhD life.

Why was the pun a bad comedian? He never got the *punchline* right. Right! This was my personal revenge... No, I'm kidding, **Michiel**, I really enjoyed your extrovert nature, always ready for the next joke. Additionally, your fun shirts, your willingness to help, and you being on top of departmental news (including the most recent gossip). You really are an asset to the department and it's awesome you stayed in CMM.

It's great to have you, **Maarten**, as bridge between the academic lab and the clinic. Your insights into clinical procedures have benefitted many discussions and are a good reminder as to why we are doing our jobs. It's impressive just how much coffee you can have on a daily basis, a frequency with which I just couldn't always keep up! I wish you all the luck both for your PhD and for shaping your future way as physician.

Nizar, you're always good for a random joke and you excel in finding a table in the canteen for group lunch. Now, that you have moved on, this hardly ever happens which shows that you were the main initiator of this. While I'm sure you won't miss lengthy organoid culturing too much, I am already missing the Nizar laugh. Best of luck for your professional and personal future!

Yannik, we (will) remember you as the person who has set up CRISPR/Cas9 in the department. Thanks for your curiosity about the different strategies of which we could all learn and for setting up such a flexible knock-in design of which we all profit. Having started at the same time as you, I still remember the beginnings of your PhD project and I think it was remarkable what risk you were willing to take, fighting against many sceptics during project discussions.

Many thanks, **Petra**, for supporting me with generating and genotyping of many, many Hedgehog clones. **Minco**, many thanks for working together with me during your internship time in the Snippert lab. I wish the two of you the best for your future together.

To our newbies, I'm sorry we didn't have more overlap in the lab. **Aśka**, I love to see some more British and international vibes in the department. **Sasha** and **Arne**, it's exciting to see you two building up the analysis branch of the lab. I wish the three of you the best of luck contributing with your unique expertise to the group and hope you'll enjoy the time as much as I have.

Mirjam, you're also almost there! I wish you all the best for finalizing your PhD and even

more so with your newborn family. I'm sure you'll pull it off! Many thanks also for your tip-off on the MST1 inhibitor. This one really saved our Cancer Research paper.

A big thank you to **all my collaborators** without whom the projects could not have reached their current form. Your work was invaluable.

Marianne and **Cristina**, thank you thank you thank you for always being available to help. **Marianne**, you constantly supported me with work-related matters such as shipments, administration and reimbursements just to mention a few. **Cristina**, the events for (CSnD) PhD students you have organized such as the yearly Masterclass and the Spetses summer school always were a highlight in the agenda.

I would also like to warmly thank everybody performing all the essential background tasks that ensure that all of us can work unimpeded and carefree. In particular, **Marjoleine**, **Cheuk**, and **Marcel** for taking care of all the ordering, deliveries, and the lab kitchen as well as our amazing **Stratenum IT department** who has neatly sorted out software- and password-related issues for me.

Many thanks to **everybody inside CMM and beyond** who has contributed to a pleasant working atmosphere and has advanced my projects by providing constructive feedback. Although I didn't always make it, I will miss the Friday 5 pm borrels.

Meine Heidelbuddies: Kaum zu glauben, dass wir uns inzwischen seit 12 Jahren kennen. Meiner Erinnerung nach mit viel Zufall am Anfang, **Martin** (#e-fellows), **Sascha** (#Lollifarbe), **Ole** (#Gruppenaufteilung zur Stadtralley nach Semesterticket ja/nein), stetiger Expansion kurz darauf, **Sven** und **Christian** und selektivem Zuwachs zu späterer Stunde **Maria** und **Svenja**. Danke für viele großartige Erinnerungen an die Heidelbergzeit sowohl in der Unteren Straße, im Eckstein oder im Zieglers als auch im Feld ob im Botanik, auf Dächern oder beim Zettel unter der Tür durchschieben. Die gemeinsamen Städtetrips sind unvergessen, genauso wie die jährlichen Camping Trips und gegenseitigen Besuche. Auf die nächsten 12 Jahre und auf den C.A.M.P.I.N.G. e.V.!

Viky, auch wir teilen viele schöne Erinnerungen an Heidelberg. Nicht etwa nur das stetige Zettel Rechnen, die Physikergrütze oder die Parties in der Physiker-WG, sondern auch die Zoobesuche, verquatschte Mädelsabende und Ausflüge wie auf den Weihnachtsmarkt in Straßburg. Vielen Dank für deine wertvolle Freundschaft und dafür, dass ich mit dir über alles reden kann.

An meine **Großfamilie**: Ich bin wirklich dankbar dafür, dass wir so ein gutes Verhältnis

haben. Ihr habt mich ein Leben lang schon begleitet und viele unvergessene Momente gestaltet. Ob spaßige Besuche bei den **Omas** und **Opas**, Frühstücken gehen mit dir, **Ursula**, und dabei den halben Tag quatschen oder die gemeinsamen Feiern und Feste. Es ist einfach immer schön!

Wie schön, dass wir Teil einer Familie seid, **Tini** und **Georg, Louise** und **Johanna** (nur schade, dass wir so weit auseinander wohnen). Das Wandern in Cornwall, nicht nur wegen des „Ausbrechen“ aus dem Campingplatz und die gemeinsamen Festivals waren wirklich Highlights, Tini. Auch der Segelturn ist unvergessen. Lieben Dank für viele schöne, gemeinsame Erlebnisse.

Für eure liebe Art und Unterstützung in allen Lebenslagen, **Iris** und **Frank**, ein ganz herzliches Dankeschön. Ihr seid immer an allem interessiert, was in meinem Leben passiert und bei euch fühlt man sich einfach zu Hause.

Matthias, danke dafür, dass du immer für mich da bist. Deine Hilfsbereitschaft und Loyalität sind wirklich herausragend. Ob gemeinsame Familienurlaube, Besuche in Utrecht oder Wochenenden in Weiler, es ist immer schön, gemeinsam mit die Zeit zu verbringen. Ich freue mich schon auf den nächsten Puzzle Day mit dir.

Mama und **Papa**, Danke für einfach Alles. Für so viele Jahre der endlosen Unterstützung, des Vertrauens, und der Liebe. Ich habe schon so viel von euch gelernt und trotzdem gibt es immernoch so viel, bei dem ich wieder und wieder euren Rat such und eure Hilfe brauche. Danke für euer unerschütterliches Vertrauen in mich und dafür, dass ihr all meine Entscheidungen mitgetragen habt.

Jens, du bist mein Fels in der Brandung. Du erkennst es immer, wenn ich dich brauche und gibst Dingen, die mir sehr wichtig sind, immer höchste Priorität. Deine Art Menschen zu begegnen, ist wirklich vereinnahmend und beeindruckend. Schon jetzt, haben wir eine wunderschöne, gemeinsame Geschichte. Beginnend in Heidelberg mit Zoobesuchen in der Freizeit aber auch gemeinsamen Arbeitsstunden auf dem Campus am Teich oder in Seminarräumen, Oxford als nächster Stopp mit gemeinsamen Collegedinnern und meinen vielen Biologie Fragen, in Utrecht die gemeinsame PhD Zeit mit all ihren Höhen und Tiefen, in denen du mich immer unterstützt hast, viele Strandbesuche und Wochenendtrips, unsere traumhafte Hochzeit, die für immer unvergessen bleiben wird und jetzt die Rückkehr nach Heidelberg. Wir teilen so viel an Lebenseinstellungen und -zielen und du hast so viel Empathie, dass ich in jeder Lage immer ich selbst sein kann. Danke für all deine Liebe und dafür, dass ich an deiner Seite leben darf.

